Universidade do Minho
Escola de Engenharia

Mohammad Mastali

Development of Innovative Hybrid DHCC-GFRP Sandwich Panels

July 2016

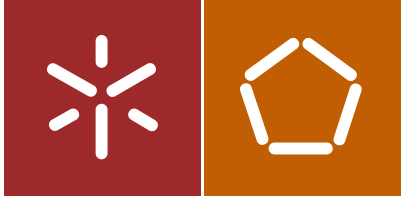

Universidade do Minho
Escola de Engenharia

Mohammad Mastali

Development of Innovative Hybrid DHCC-GFRP Sandwich Panels

Thesis of Doctoral in
Civil Engineering

Supervisors:
Professor Doutor Joaquim António Oliveira Barros
Doutora Maria Isabel Brito Valente

July 2016

STATEMENT OF INTEGRITY

I hereby declare having conducted my thesis with integrity. I confirm that I have not used plagiarism or any form of falsification of results in the process of the thesis elaboration.

I further declare that I have fully acknowledged the Code of Ethical Conduct of the University of Minho.

University of Minho, _____

Full name: Mohammad Nastali

Signature: 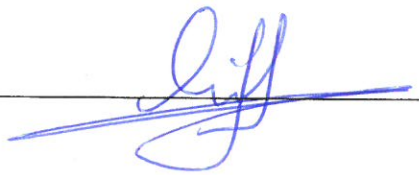

Acknowledgement

I would like to express my special appreciation and thanks to my supervisors: Professor Doctor Joaquim António Oliveira Barros and Doctor Maria Isabel Brito Valente, you have been tremendous mentors. I would like to thank you for encouraging my research and for allowing me to grow as a research scientist. Your advice on both research as well as on my career have been priceless. It was a pleasure working with you.

I would also like to acknowledge the scholarship “RehabGFRP - Rehabilitation of Building Floors with Lightweight High Performance GFRP Sandwich Panels”, with reference number of PTDC/ECM/113041/2009. Furthermore, I honestly appreciate the collaboration of the following labs: Civitest company for developing DHCC materials (Eng. Delfina Gonçalves), PIEP company for conducting VARTM process (Eng. Luis Oliveira) and structural lab of department of Civil Engineering of Minho University to execute the tests (Mr. Antonio Matos and Eng. Marco Jorge).

A special thanks to my family. Words cannot express how grateful I am to my family for all of the sacrifices that you have made on my behalf. Your prayer for me was what sustained me thus far. At the end, I would like express deeply appreciation to my friends who supported me in this program, and for their delightful friendship.

ABSTRACT

In this study, a new generation of composite sandwich slab is proposed as a solution for the rehabilitation of slabs in old masonry buildings. The innovative solution proposed includes four components: a Deflection Hardening Cement Composite (DHCC) layer on the top compression skin, a glass fiber reinforced polymer (GFRP) skin at the bottom tension surface, GFRP ribs to transfer shear from top to bottom layers, and foam core for thermal-insulation purposes. The DHCC layer contributes to the load carrying and deflection capacity due to its high stiffness, compressive strength and toughness. It also offers resistance to the occurrence of buckling phenomena in the GFRP ribs, improves the performance of this structural concept against impact and fire, and constitutes an excellent medium for the application of finishing materials, like ceramics or timber.

To evaluate the efficiency of the developed innovative slabs, different composite specimens, with various span lengths, were tested under different load conditions, including flexural loading, shear loading, and long term deformation. The obtained results from experimental tests are comprehensively analysed.

Advanced numerical simulations on the hybrid slabs are also developed. The influence of considering isotropic or orthotropic behaviour for the GFRP components and linear or nonlinear behaviour for the DHCC is investigated numerically. The results obtained during the experimental tests are used to appraise the performance of the constitutive models adopted in the FEM-based simulations and the quality of the meshes defined. In addition, some analytical models that consider the relation between force and deflection are proposed to evaluate the response of this structural system under static and long-term loadings.

RESUMO

Neste trabalho, desenvolve-se uma nova solução de painel sandwich a ser utilizado na substituição de pavimentos existentes em edifícios de alvenaria. A solução proposta consiste num painel sandwich que inclui quatro componentes principais: uma lâmina inferior tracionada, realizada em GFRP, uma camada superior comprimida realizada com argamassa de elevada ductilidade (*deflection hardening cement composite* - DHCC), almas em GFRP para transmitir esforços de corte entre as duas camadas extremas de GFRP e DHCC e uma camada de espuma de poliuretano, posicionada entre as duas camadas extremas, capaz de garantir um bom comportamento térmico e acústico do painel. A camada de argamassa de elevada ductilidade tem com função contribuir para a capacidade de carga e de deformação do painel, uma vez que é um material que apresenta elevada resistência à compressão e elevado módulo de elasticidade. A camada de argamassa oferece resistência à ocorrência de fenómenos de encurvadura nas almas de GFRP, melhora o desempenho do painel sob ações extremas, como cargas de impacto e fogo, e constitui um excelente meio para a aplicação de materiais de acabamento, tal como os elementos cerâmicos ou a madeira.

Para avaliar a eficência da solução desenvolvida, foram fabricados vários provetes, com diferentes vãos, e testados sob o efeito de várias condições de carregamento, onde se incluem situações onde os esforços principais são de flexão, de corte ou resultantes de carregamentos de longa duração. Os parâmetros medidos durante os ensaios experimentais são avaliados e analisados de forma pormenorizada.

São também desenvolvidos modelos numéricos baseados no Método dos elementos finitos (FEM), com base na geometria e nas propriedades dos provetes testados experimentalmente. Os modelos desenvolvidos são calibrados com base nos resultados obtidos durante esses ensaios. É avaliada a influência de considerar o comportamento isotrópico ou ortotrópico dos componentes de GFRP e o comportamento linear ou não linear da argamassa de elevada ductilidade (DHCC).

Na avaliação do comportamento dos painéis, são considerados requisitos que resultam da verificação de estados limite de serviço e estados limites últimos. Além disso, os resultados obtidos durante os ensaios experimentais são utilizados para avaliar o desempenho dos modelos constitutivos adoptados nas simulações numéricas e a qualidade das malhas adotadas. Complementarmente, são propostos alguns modelos analíticos que consideram a relação entre força e deformação com o objetivo de avaliar a resposta deste sistema estrutural sob efeito de carregamentos estáticos e de longa duração.

Contents

Page

Chapter 4- Numerical simulations and analytical studies of the flexural behavior of hybrid slabs

List of Tables

List of Figures

Page

Notations and symbols

Chapter 2

D_U	The ultimate deflection when the failure crack is formed, and the applied load starts decreasing	mm
D_Y	The maximum deflection in linear behavior	mm
μ	Ductility	---
$\sigma_{f,\max}^{S}$	The maximum flexural stress at sagging region	MPa
$\sigma_{f,\max}^{H}$	The maximum flexural stress at sagging region	MPa

Chapter 3

δ	Mid-span deflection of slabs	mm
P	The applied load	N
L	The slab's span	mm
EI	The flexural stiffness	mm^2.N
A	The cross section of the ribs	mm^2
G_{rib}	The shear modulus of the GFRP ribs	GPa

Chapter 4

$\Delta\underline{\sigma}_{mf}$	The vectors corresponding to the in-plane stress increment	---
$\Delta\underline{\varepsilon}_{mf}$	The vectors corresponding to the in-plane strain increment	---
$\underline{\sigma}_s$	The vectors corresponding to the out-plane stress increment	---
$\underline{\varepsilon}_s$	The vectors corresponding to the out-plane strain increment	---
$\varepsilon_{n,u}^{cr}$	The ultimate crack normal strain	---
(G_f^I),	Fracture energy	N/mm
l_b	Crack bandwidth	mm
$\sigma_{n,1}^{cr}$	Tensile strength	MPa
ε_n^{cr}	The crack normal strain component	---
E_C	Young Modulus	MPa
υ	Poisson's ratios	---
LL	Live load	kN/m^2
PL	Permanent load	kN/m^2
E_{R1}	Young's modulus of the GFRP rib in 1 material axis	MPa
E_{R2}	Young's modulus of the GFRP rib in 2 material axis	MPa
d_R	The rib height	mm
G_{R12}	The shear modulus of the rib	GPa
t_R	The rib thickness	mm
γ_m	Safety factor	---
γ_{m1}	The material property data	---
γ_{m2}	The material manufacturing process	---
γ_{m3}	the effects of environmental variables and the duration of the loading period	---

$\tau_{Critical}$	The critical in-plane shear stress	MPa
G_{cr}	Cohesive fracture energy	N/mm
τ_{max}	The maximum traction	MPa
δ_f	The ultimate separation	mm
σ_n	The cohesive tensile stress	MPa
τ_1	The shear stress in direction 1	MPa
τ_2	The shear stress in direction 2	MPa
σ^0_n	The cohesive tensile strength	MPa
τ^0_1	The shear strength in direction 1	MPa
τ^0_2	The shear strength in direction 2	MPa
G_{IC}	The critical fracture energies for mode I	N/mm
G_{IIC}	The critical fracture energies for mode II	N/mm
G_I	The fracture toughnesses derived from the opening mode	N/mm
G_{II}	The fracture toughnesses derived from the sliding mode	N/mm
G_{III}	The fracture toughnesses derived from the tearing mode	N/mm
K_0	The stiffness	N/mm^3
A_N	The values obtained from numerical results	---
A_E	The values obtained from experimental results	---
δ	Mid-span deflection of slabs	mm
P	The applied load	N
L	The slab's span	mm
EI	The flexural stiffness	$mm^2.N$
A	The cross section of the ribs	mm^2
G_{rib}	The shear modulus of the GFRP ribs	GPa

Chapter 5

I_{exp}	The experimental moment of the inertia of specimens	mm^4
I_{fc}	The numerical moment of the inertia of specimens corresponding to numerical full-composite action	mm^4
I_{nc}	The numerical moment of the inertia of specimens corresponding to numerical non-composite action	mm^4
κ	Degree of composite action associated to the initial phase of loading	---

Chapter 7

$\Delta(t)$	The time-dependent general deformation (strain or deflection)	Sec.
Δ_0	The instantaneous general deformation	mm
t	Indicates time	Hour
m	Stress-dependent coefficient	---
n	Stress independent coefficient	---
$E(t)$	The time-dependent elasticity modulus	GPa
$G(t)$	The time-dependent shear modulus	GPa
E_0	The instantaneous elasticity modulus	GPa
G_0	The instantaneous shear modulus	GPa

n_E	Findley's law stress-independent parameters for bending	---
n_G	Findley's law stress-independent parameters for shear	---
h_0	Equivalent thickness of the element	mm
f_{cm}	Compressive strength of the concrete at 28 days of age	MPa
t_0	Age of the concrete during loading	Days
T	Temperature	^{0}C
RH	Relative humidity	%
$\varphi(t,t_0)$	Creep coefficient over the time	---
$\chi(\mathrm{t},\mathrm{t}_0)$	Trevino's ageing coefficient	---
φ_0	Constant creep coefficient	---
$\beta_c(t,t_0)$	The creep behavior over the time	---
Ac	Section area of the concrete	mm^2
u	Perimeter of the section edge exposed to the environmental conditions	mm
β_{H}	The environmental conditions	---
q	Distributed load	kN/m^2

Chapter 1

Introduction

1.1. Introduction

Many old masonry buildings exhibit timber-joisted floors that often need to be replaced. Rehabilitation with traditional materials introduces significant dead loads in construction, increasing their seismic vulnerability, and poses constructive problems associated to transport, elevation and placement operations in narrow accesses. The resolution of these problems based on current steel/concrete solutions usually involves high costs and practical constraints, associated to the dead load introduced on the existing construction and the need for heavy weight elevation devices.

Fiber Reinforced Polymer (FRP)'s in general and Glass Fiber Reinforced Polymer (GFRP) sandwich panels in particular are a potentially good solution to be used in the rehabilitation of degraded building floors, as they make it possible to overcome the above mentioned technical and practical constraints. Fiber reinforced polymer materials (FRPs), including GFRP sandwich panels, present several advantages over traditional materials, namely high mechanical performance, lightness, insulation properties, low maintenance, durability and increasingly competitive costs. These characteristics are particularly relevant for building rehabilitation, since the use of FRPs may avoid the need for elevation devices and introduces much lower dead loads.

However, the mechanical properties of standard cost-competitive GFRP sandwich panels may not be sufficient to enable their use in building floors, with optimized/enhanced architectures being needed. Standard GFRP sandwich panels with different foam cores such as rigid polyurethane (PU) are cost competitive, but their mechanical properties, in particular the shear strength of the core and the top skin susceptibility to buckling, may be a difficulty in the envisaged application (building floors with spans of 4-5 m).

Therefore, in this thesis, the sandwich panels are developed based on an innovative GFRP-DHCC hybrid solution that will use PU foam as core material, but featuring an innovative type of reinforcement composed by a grid of GFRP ribs connected to the GFRP bottom skin and the DHCC top layer. This solution is expected to increase the shear stiffness and the strength of the panel. The GFRP skins and ribs are produced using the vacuum assisted resin transfer molding

(VARTM) process, which guarantees a good material homogeneity and lower fabrication costs when compared to other techniques such as reaction injection molding (RIM) and same qualified resin transfer molding (SQRTM). A GFRP laminate is placed on the bottom tension skin, where it performs better, and a Deflection Hardening Cementitious Composite (DHCC) layer is used on the top compression skin, preventing the occurrence of buckling phenomena, providing a ductile behavior and allowing for an easy application of floor cover materials. Using DHCC material as compressive layer in the hybrid sandwich panel will increase the flexural stiffness of the panel, its acoustic, thermal and impact resistance, will provide extra fire protection to the core of the panel. Moreover, using DHCC material will provide increasing load carrying capacity and ultimate deflection of the proposed hybrid slabs. It is worth stating that using DHCC material as top skin introduces higher self-weight and more difficulties in installation.

1.2. Objectives

The aim of this work is to design and test full-scale prototypes of the proposed innovative hybrid GFRP-DHCC sandwich panels, so that their adequacy to be used in the replacement of degraded building floors is proven. As mentioned before, this innovative hybrid GFRP-DHCC sandwich panel will be developed with a GFRP laminate on the bottom tension skin and a DHCC layer on the top compression skin, in order to increase strength, ductility, and to allow an easy application of floor covering materials.

The proposed hybrid slabs were developed considering:

1. High load carrying capacity,
2. High shear strength,
3. High stiffness,
4. Ductile behavior,
5. High resistance against buckling phenomenon in the GFRP ribs,
6. Good material homogeneity,
7. Lightness, in order to allow an easy transport and assemblage,

8. Safety, considering the loadings, spans and support conditions usually found in this type of applications and the SLS and ULS limit states proposed in the structural Eurocodes.

1.3. Methodology

The experimental and numerical studies were implemented in three different phases, as indicated in Fig. 1.1. The results obtained in these three different stages are described in eight chapters, including:

Chapter 1: Introduction

This chapter presents an introduction on the subject of sandwich panels. An explanation is given on the concept of the hybrid sandwich panel solution proposed, why it is chosen for the rehabilitation of degraded floors in old buildings and how it will be able to solve the problems that commonly arise in this application. Finally, the main objectives of this work and the methodology chosen to approach them are described.

Chapter 2: Characterization and development of hybrid slab's materials and manufacture processing

In this chapter, a lightweight deflection hardening fiber reinforced mortar is developed by using 4% hybrid Polyacrylonitrile (PAN) fibers (1% short fibers with 6 mm length and 3% long fibers with 12 mm length). This material is specifically designed for this application and the following characteristics are sought: an hardening deflection behaviour under four point bending test with flexural strength higher than 7 MPa and also an average compressive strength higher than 24 MPa.

To develop this material, various tests are carried out, such as compressive test, flexural test, and tensile test. SEM images are used to identify and analyse the micro-structure of the DHCC material and the failure modes of the PAN fibers. GFRP coupons are used to evaluate the

material properties of GFRP sheets under direct tensile loading. Moreover, the behavior of the polyurethane foam cores under compressive loading condition is analyzed.

In the second phase of this chapter, the manufacture process of hybrid slabs is described, with focus on the technique used, the vacuum assisted resin transfer molding (VARTM) process.

Chapter 3: Preliminary flexural tests on hybrid panels

Full-scale preliminary tests are performed to determine the mechanical behavior of GFRP-DHCC sandwich panels in both service and ultimate conditions. The most relevant failure modes are identified, such as tensile and compressive damage of the GFRP skin and the DHCC layer, respectively, compressive damage of GFRP ribs due to excessive compressive stress, damage of the connection between foam core and DHCC layer and between GFRP ribs and DHCC layer. The following mechanical properties are evaluated: flexural stiffness and strength.

Of particular interest is to understand and quantify the effect, on those properties, of (i) the different thicknesses of GFRP ribs and GFRP skins tested; (ii) the different heights of the hybrid slabs; and iii) the connection between the GFRP ribs and the DHCC layer.

The experimental tests to evaluate the flexural performance and the ultimate load carrying capacity of the hybrid GFRP-DHCC panels were carried out at the Structural Laboratory of University of Minho.

Chapter 4: Numerical and analytical simulations of hybrid slabs

This chapter consists of an analytical and numerical parametric study that aims to determine the effects of thickness, height, strength and elastic modulus variations of each slab's component on its global behavior. The study is developed taking into account the standard criteria applicable to building floor solutions.

Therefore, parametric studies were carried out in three different phases, by increasing successively the complexity of the adopted approach: 1st) FEM analyses were executed assuming a linear-elastic-isotropic behavior for the constituent materials used; 2nd) a linear

orthotropic behavior was adopted for GFRP skin and ribs, while a linear-elastic-isotropic behavior was considered for the DHCC layer; 3rd) an elasto-crack constitutive model was adopted to simulate the nonlinear behavior of DHCC layer due to crack initiation and propagation, while GFRP ribs and skin were assumed having a linear orthotropic behavior.

The second part of this chapter was mainly devoted to 3D FEM simulations of the hybrid slabs, with special focus on modeling the interfaces between slab's components. The parameters of the used constitutive law at the interfaces were obtained by validating the numerical models with experimental results in terms of the force-deflection response, force-strain response, and the observed damages.

Chapter 5: Flexural performance of hybrid sandwich panels with special focus on the shear connection behavior

An efficient and simple technology was adopted in Chapter 2 for connecting the DHCC layer and the GFRP ribs, by executing holes of small diameter in the top zone of the GFRP ribs that stays embedded in the DHCC layer. The results obtained in the preliminary flexural tests presented in Chapter 3 indicated that a high stress concentration is induced around the shear connectors perforated in the GFRP ribs, which reduced the panels´ ductility. Considering this problem, indented shear connectors were proposed to replace the perforated shear connectors in the GFRP ribs. New hybrid slab specimens, with indented shear connectors, were then assessed under flexural load conditions. Finally, a comparative study was executed to assess the flexural performance of hybrid slabs, with special focus on the behavior of indented and perforated shear connectors. This comparative study includes the evaluation of strength, stiffness, post-peak response, composite action, slip between GFRP ribs and DHCC layer and distribution of strain along the cross section.

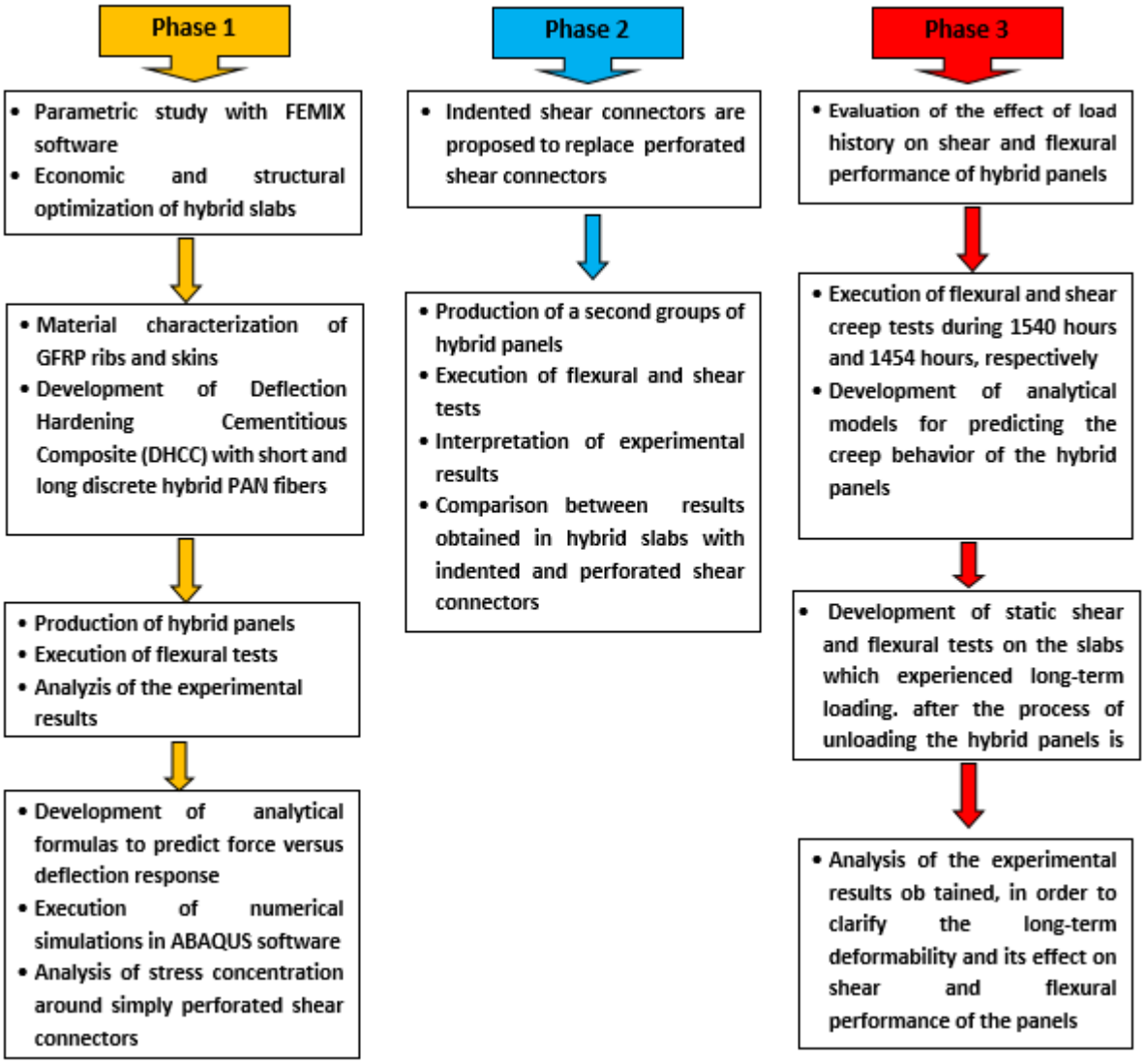

Fig 1.1. Experimental and numerical tasks developed within the present work and divided in three different phases

Chapter 6: Shear performance of hybrid sandwich slabs using indented shear connectors

Hybrid slabs with different lengths are built and experimentally tested under different shear load conditions. Considering the results previously obtained in Chapter 3 and Chapter 5, it was decided to build all the specimens tested in the present experimental campaign with indented shear connectors positioned in the top zone of the GFRP ribs, in order to guarantee an effective load transfer from DHCC layer to GFRP skin and also to provide a high load carrying capacity and an improved ductility. The shear performance of the hybrid slabs was assessed by

executing experimental monotonic shear tests in specimens with span to depth ratios in the range between 0.77 and 2. There is a special concern with the structural performance of the indented shear connectors used at the GFRP rib/DHCC layer connection. By imposing loadings with different shear spans, it is possible to determine the effect of shear on the strength, stiffness, post-peak response, composite action and slip between GFRP ribs and DHCC layer.

Chapter 7: The effects of load history on shear and flexural performance of hybrid sandwich panel slabs

The structural performance of hybrid sandwich panels under monotonic flexural and shear loadings was assessed in previous chapters. In literature, few studies have been dedicated to behavior of hybrid structures (of the types in consideration within this study) under long-term loading. And yet, no studies have been implemented to clarify the effects of long-term loading on the performance of hybrid sandwich panels under shear and flexural loads. Therefore, this chapter establishes an attempt to do so, in two stages. In the first stage, hybrid DHCC-GFRP sandwich panel specimens are submitted to shear and flexural creep tests. Then, an analytical model is developed to predict the hybrid GFRP-DHCC sandwich panel slab behavior under long-term loading. Finally, in the second stage of this chapter, the hybrid DHCC-GFRP sandwich panels which experienced long-term deformability are assessed under shear and flexural static loadings, in order to identify the influence of load history on the shear and flexural performance of the hybrid sandwich panels tested.

Chapter 8: Conclusions and future works

This chapter summarizes the results obtained in chapters 2, 3, 4, 5, 6 and 7 and establishes concluding remarks on the work developed. Some recommendations are also presented for future studies.

1.4. Expected Results

The main result arising from this work is the development of an innovative and optimized hybrid GFRP-DHCC sandwich panel system that is suitable for the rehabilitation of degraded building floors. This solution presents several advantages over other traditional ones, in terms of structural/seismic performance, lightness, durability, ease of application and maintenance, economy and it is expected that the present work is able to establish its main disadvantages, relevant modes of failure, behaviour under SLS (service limit state) and ULS (ultimate limit state) conditions, behaviour under long term loadings. The work to be developed should also provide information on dimensions and solutions that can improve and optimize the structural behaviour. These solutions include the materials tailored properties, the cross section configuration, the shear connection configuration, etc.

The numerical models to be developed (calibrated based on experimental results) will try to simulate the mechanical behaviour of the tested sandwich panels in order to allow further studies where other architectures are chosen. Thereby, the calibrated numerical models will constitute a robust tool for design.

Chapter 2

Characterization and development of hybrid slab's materials and manufacture processing

2.1. Structural concept of the proposed sandwich composite slab

The innovative hybrid GFRP-DHCC sandwich slabs proposed in the present study have a GFRP laminate on the bottom tension skin, and a Deflection Hardening Cement Composites (DHCC) layer on the top compression skin. The DHCC layer has the purpose of increasing the strength and ductility, and allowing easy application of floor cover materials. Utilizing DHCC materials in the compressive layer increases the flexural stiffness of the slab, its acoustic and thermal performance, and resistance against impact. Furthermore, it also provides extra fire protection for the core of the panel. Shear stresses in the proposed new hybrid sandwich panel are transferred by both GFRP ribs and foam core, but it is expected that most part of the stress is carried out by the GFRP ribs to prevent premature failure in foam core. In this case, the shear connection is obtained by executing openings in the upper part of the GFRP ribs (Fig. 2.1b). These openings are filled with DHCC during casting, forming DHCC dowels that are capable of transferring the mobilized shear forces. Another important aspect related to the sandwich slab is the adhesive bond between the foam and GFRP ribs and skins. This adhesive bond is introduced through VARTM process for enhancing the transference of shear forces between layers, by contributing in this way for the desired composite action [1].

According to the aforementioned reasons, these structural elements can also be used in other applications like walls or roofs, where a combination of relatively high flexural stiffness and low dead weight justifies the use of constituent materials of higher price than traditional ones. Fig. 2.1 presents the geometry of the sandwich slab developed in the scope of the present research project. Each component can be considered as relatively weak by itself, but together they provide a strong and lightweight structural system. Fig. 2.1b presents the holes pattern executed in the GFRP rib to promote an appropriate solution for connecting this rib to the DHCC layer. Furthermore, to ensure proper transfer of stress from the DHCC layer to the GFRP skin through GFRP rib, the connection zone between GFRP skin and rib was further improved with a rounded transition, as shown in Fig. 2.1c.

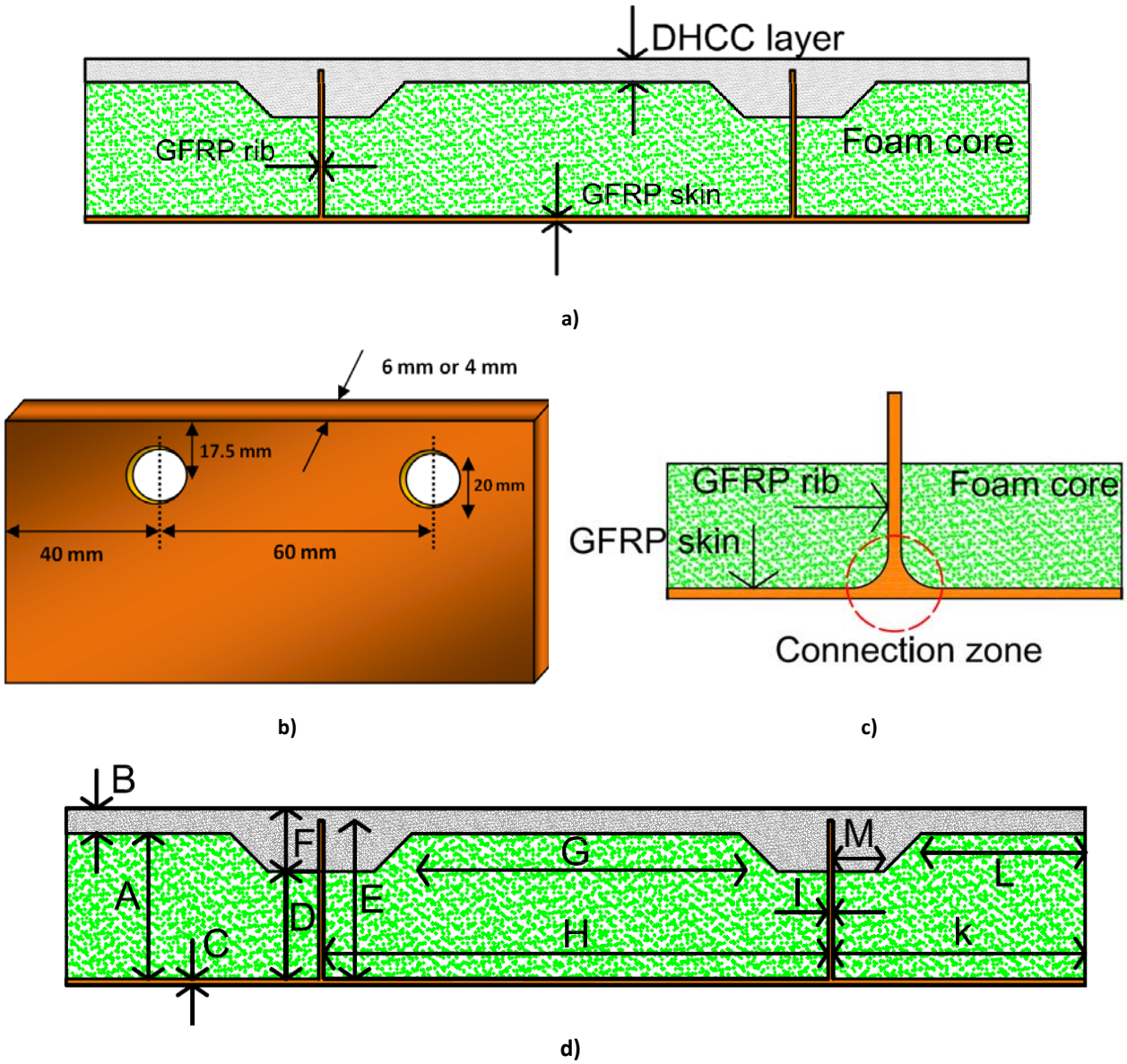

Fig 2.1. Schematic representation of the proposed hybrid sandwich panel: a) Components of the hybrid sandwich panel; b) Geometry and disposition of openings in the ribs; c) Transition between GFRP rib and GFRP skin; d) Geometry characterization of the proposed hybrid sandwich panels

Table 2.1 lists the geometry of the components forming the two types of sandwich panels developed, herein designated by Slab 1 and Slab 2. Each array of the properties corresponds to a column in Table 2.1, where the meaning of the parameters is represented in Fig. 2.1d. The thickness of slab's component and geometry of slabs were determined through execution of a parametric study, which will be discussed later, in chapter four.

Table 2.1. Geometrical properties of the proposed slabs

Name	Height (mm)		Width (mm)	
	Slab 1	Slab 2	Slab 1	Slab 2
A	149	115	---	---
B	20	20	---	---
C	3	5	---	---
D	119	85	---	---
E	160	130	---	---
F	50	50	---	---
G	---	---	260	260
H	---	---	400	400
I	---	---	6	4
K	---	---	200	200
L	---	---	130	130
M	---	---	40	40

2.2. Assessment of material properties by experimental tests

The developed hybrid sandwich panel is composed of different materials. An extensive experimental program was executed for characterization of the material properties of GFRP ribs, GFRP skin and Polyurethane foam core. Furthermore, a new fiber reinforced cement mortar for having a deflection hardening behavior (DHCC) and a high ductility was developed within this study.

2.2.1. GFRP rib and skin

For the GFRP ribs and skins various layers of GFRP fabrics with specific fiber orientations are used. Fibers of type UNIE640 [2] are adopted in the skin as bidirectional layer, oriented at 0 and 90 degree. For this type of fibers, the percentage of stitched fibers at 0 degrees was 15 times the percentage of stitched fibers at 90 degrees. Thus, the stitched fibers at 0 and 90 degrees are aligned with the longitudinal and transversal directions of the slabs, respectively. Two fiber layers of UNIE640 type provide one millimeter thickness for skin layers. Based on preliminary FEM-based numerical simulations, it was decided to adopt 6 and 10 layers of UNIE640 for Slab 1 and Slab 2, respectively (see Fig. 2.2a and Fig. 2.2c). For assuring an adequate shear stress capacity, the GFRP ribs were made by EBX400 [2] layers with fibers oriented at ±45 degree. For the slab 1, 15 layers were adopted, assuring a thickness of 5 mm (Fig. 2.2b), while in the slab 2, 9 layers were applied, resulting a thickness of 3 mm (Fig. 2.2d). The layered organization of these ribs was complemented with outer bidirectional UNIE640 layers with fibers oriented at 0 and 90 degree for supporting the

membrane stress components that are developed in consequence of the stress transfer process between the bottom GFRP skin and the top DHCC layer. The total thickness of the ribs of slab 1 and 2 was 6 mm and 4 mm, respectively (Fig. 2.2b and Fig. 2.2d).

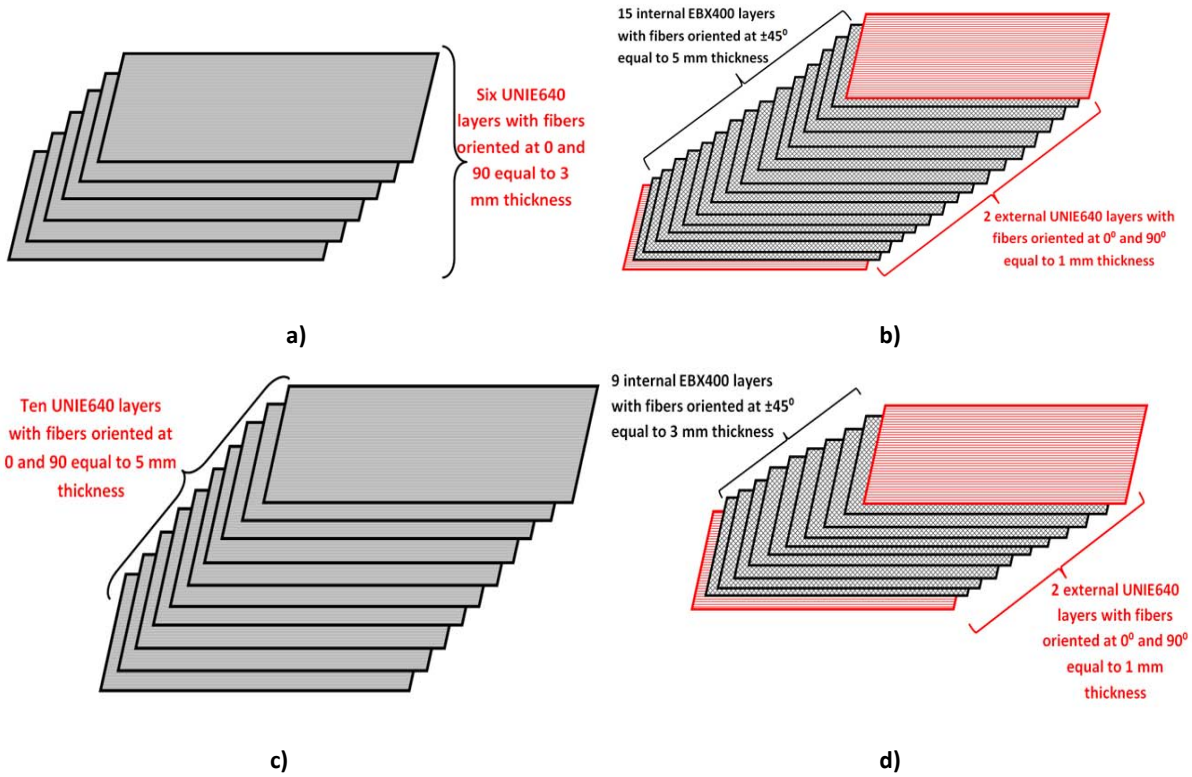

Fig 2.2. Sort of GFRP layers for: a) skin in Slab 1 with the laminate thickness of 3 mm; b) rib in Slab 1 with the laminate thickness of 6 mm; c) skin in Slab 2 with the laminate thickness of 5 mm; b) rib in Slab 2 with the laminate thickness of 4 mm

Resin Distitron 3501S1 (Orthophthalic type) [3] was used to impregnate the fibers of the ribs and skins, whose properties, according to the supplier, are listed in Table 2.2. The flexural modulus of elasticity indicated in this Table 2.2 is the ratio between the flexural stress and the flexural strain recorded in the tensile surface of the initial linear-elastic branch obtained in a three point bending test executed according to the ISO 178-2001 recommendations [4].

Table 2.2. Properties of resin Distitron 3501S1 in hardened state

Tensile strength (MPa)	Tensile modulus of elasticity (MPa)	Flexural strength (MPa)	Flexural modulus of elasticity (MPa)	Elongation at break (%)
65	4100	120	4200	2

The ribs and skins are composed, in volume, by 60% of fibers and 40% of resin. All details about properties of the GFRP layers applied in the ribs and skins of the developed slabs are indicated in Table 2.3. Five coupons were cut in the longitudinal direction (C11, C12, C23,

C24 and C25) and other six were cut in the transversal direction of GFRP skin (C8, C9, C10, C20, C21 and C22), and other fourteen coupons, including four coupons in longitudinal direction (C1, C2, C13 and C14), five coupons in transverse direction (C3, C4, C15, C16, and C17) and five specimens at ±45 degrees (C5, C6, C7, C17, and C18) were cut and prepared based on ASTM D3039/D 3039M-00 [5] recommendations (see details in Fig. 2.3 and Table 2.3).

Table 2.3. Properties of used materials for GFRP ribs and skins (see Fig. 2.3 and Fig. 2.4)

Specimen's designation	Slab number	Slab's component	UNIE640 (stitched unidirectional fabric)	EBX400 (biaxial fabrics)	Number of UNIE640 layers	Number of EBX400 layers	Thickness of slab's component	Specimens with fibers oriented at
C1 , C2	2	Rib	600 gr/m^2 at 0º + 40 gr/m^2 at 90º	400 gr/m^2 at ±45º	2	9	4 mm	0^0
C3 , C4								90^0
C5 , C6 , C7								45^0
C8 , C9 , C10		Skin		---	10	---	5 mm	90^0
C11 , C12								0^0
C13, C14	1	Rib		400 gr/m^2 at ±45º	2	15	6 mm	0^0
C15 , C16,C17								90^0
C18 , C19								45^0
C20 , C21,C22		Skin		---	6	---	3 mm	90^0
C23 , C24,C25								0^0

The longitudinal and transversal directions in Fig. 2.3 indicate the orientation of the fibers at 0 and 90 degree, respectively. Since in the ribs the highest fiber reinforcement and predominant axial stress fields are orientated at ±45 degrees, coupons were also extracted in these directions for assessing their tensile behavior. Tensile specimens with dimensions of 250×25 mm^2 were prepared and tested at a displacement rate of 2 mm/min. Fig. 2.4a, 2.4b, and 2.4c show details of the prepared type of specimen, test setup, and monitoring devices to evaluate the longitudinal tensile strains, while Fig. 2.4d presents representative failure modes in the tested GFRP coupons. The failure has occurred in the gage area for all the coupons, but in different zones and of distinct types. Amongst the failure modes proposed by ASTM D3039/D 3039M-00, in the present tests the following ones were observed (Fig. 2.4): Angled failure in the bottom (AGB) and in the middle (AGM) zone of the gage; Lateral failure in the middle zone of the gage (LGM); Explosive failure in the middle zone of the gage (EGM).

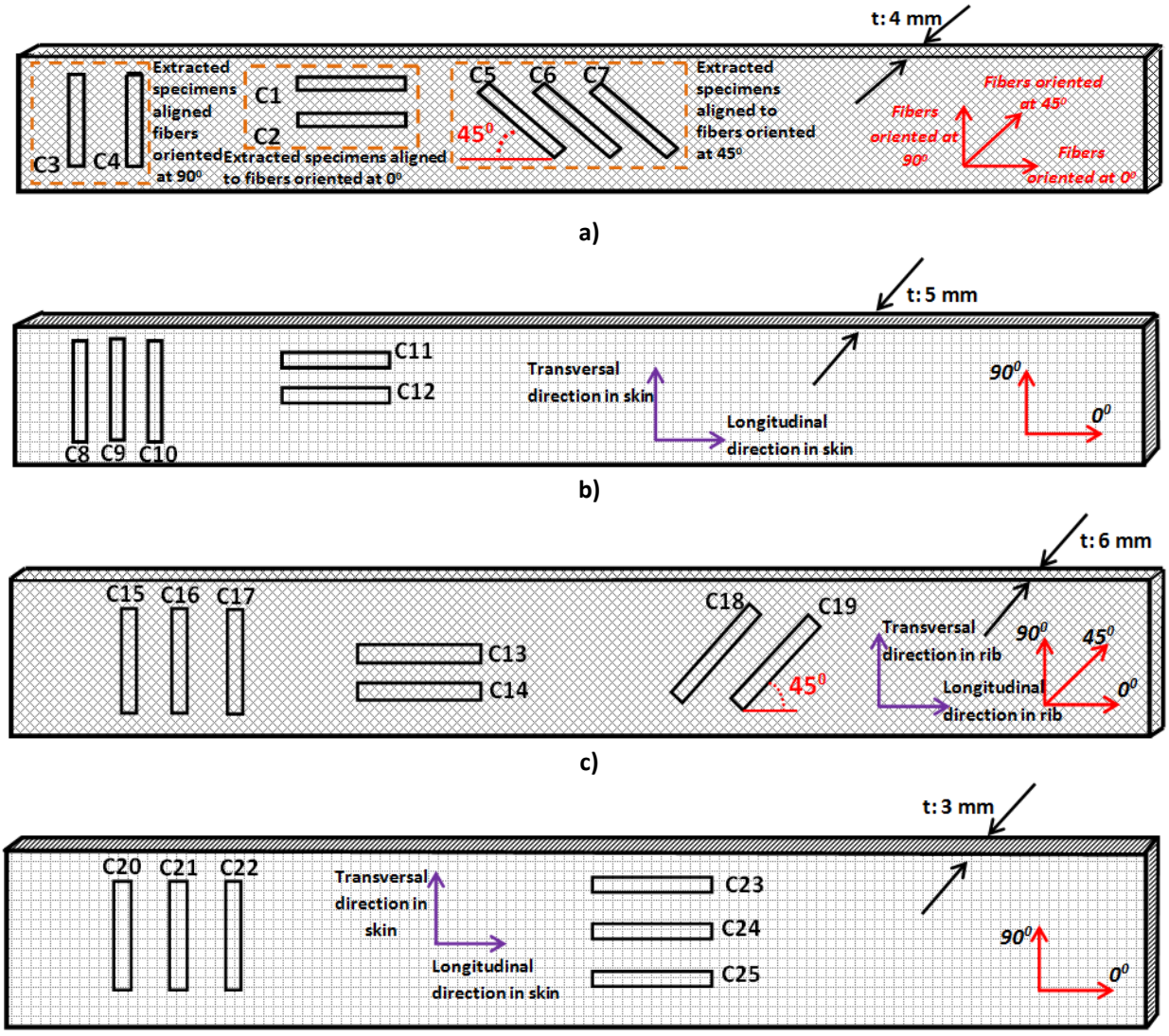

Fig 2.3. Nomenclature of GFRP specimens extracted from: a) rib of 4 mm thickness; b) skin of 5 mm thickness; c) rib of 6 mm thickness; d) skin of 3 mm thickness

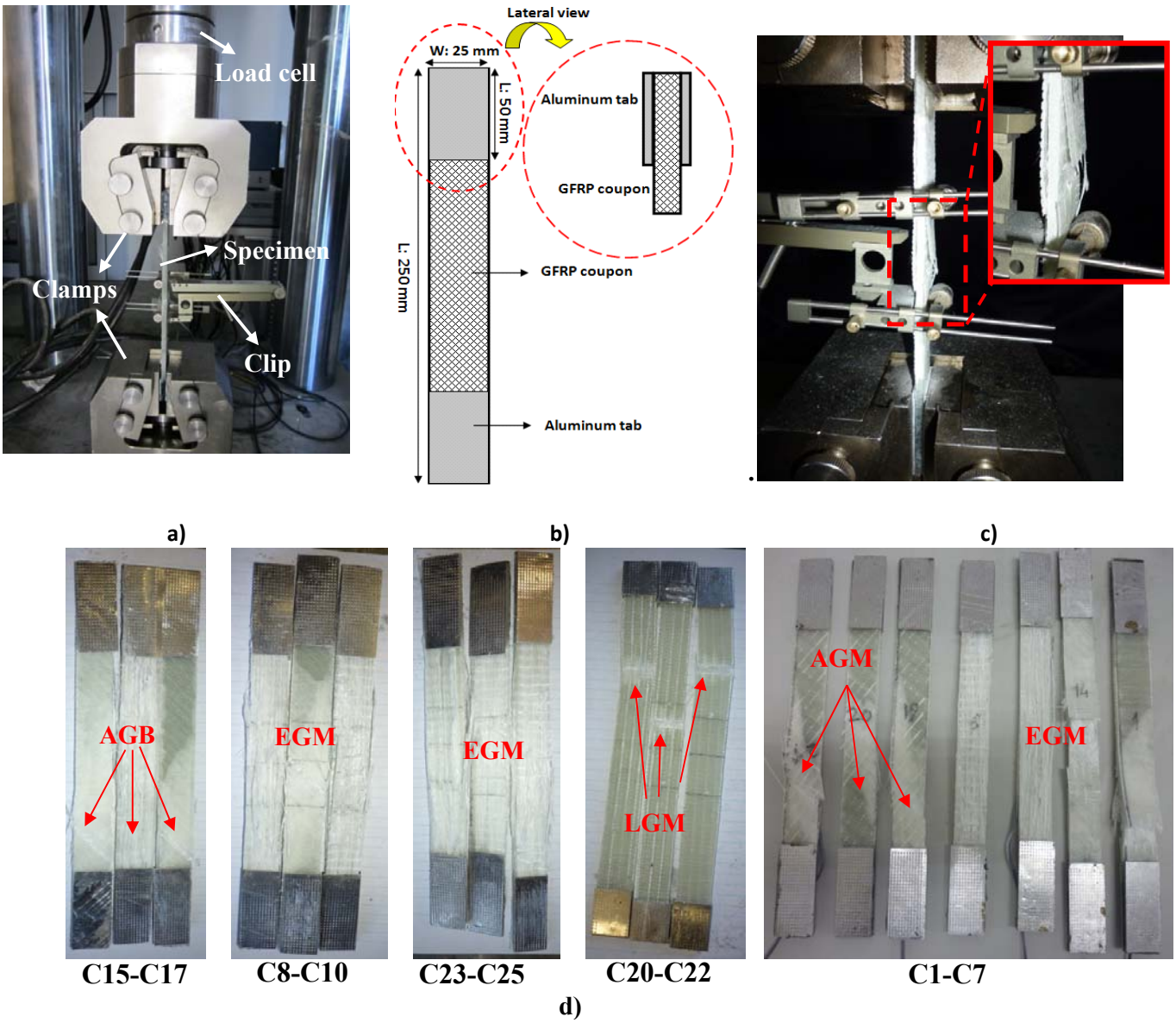

Fig 2.4. Assessment of the tensile properties of GFRP used in the ribs and skins: a) Test setup; b) details of the coupon; c) monitoring system for measuring the longitudinal strains; d) typical failure modes based on ASTM D3039 definition

From the tensile stress-strain responses obtained in the GFRP coupons, which are represented in Fig. 2.5, the tensile strength, modulus of elasticity and ultimate strain at failure of GFRP coupons were determined, whose average values are included in Table 2.4.

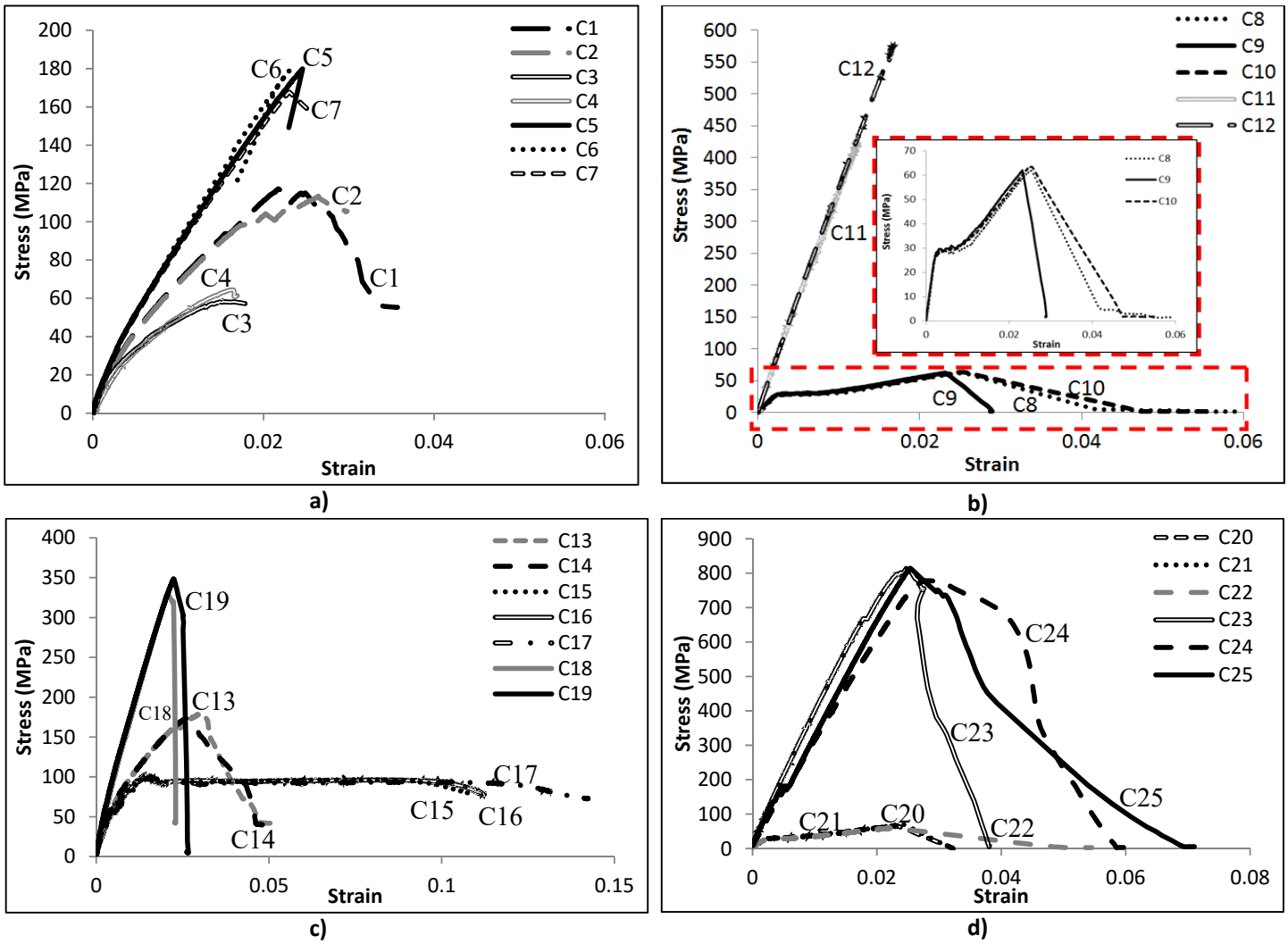

Fig 2.5. Stress-strain diagrams obtained in the GFRP specimens extracted from: a) Rib (Slab 2); b) Skin (Slab 2); c) Rib (Slab 1); d) Skin (Slab 1)

Table 2.4. Tensile properties of GFRP coupons representative of ribs and skins of the developed slabs (see Fig. 2.4)

Specimen's designation	Slab number	Slab's component	Specimens with fibers oriented at	Tensile strength (MPa)	Modulus of elasticity (GPa)	Ultimate strain (%)
C1 , C2	2	Rib	0^0	112.5	13.03	2.40
C3 , C4			90^0	61.08	8.62	1.51
C5 , C6 , C7			45^0	174.02	13.63	2.35
C8 , C9 , C10		Skin	90^0	63.03	12.10	2.40
C11 , C12			0^0	573.01	36.06	1.66
C13 , C14	1	Rib	0^0	170.80	13.18	2.59
C15 , C16 , C17			90^0	98.35	13.01	11.7
C18 , C19			45^0	332.21	15.96	2.20
C20 , C21 , C22		Skin	90^0	65.98	13.30	2.22
C23 , C24 , C25			0^0	785.68	31.41	2.50

In general the stress-strain response is composed of an initial linear stage followed by a phase of a degree of nonlinearity that depends on the arrangement and percentage of fiber reinforcement with respect to the direction of the applied load. In fact, when the highest percentage of fibers are aligned with the load direction, such is the case of C11 and C12 specimens, an almost linear elastic response was obtained with the highest tensile strength and stiffness. The results in the specimens extracted from the ribs (Figs. 2.5a and 2.5c) clearly show that, by decreasing the effective fiber reinforcement ratio (percentage evaluated in the loading direction), the aforementioned nonlinear stage is more pronounced and the tensile strength is decreased. The specimens extracted in transversal direction of the skin presented a stress vs. strain response that can be approximated by a trilinear diagram (inset of Fig. 2.5b). Up to a stress level of about 30 MPa these coupons presented a linear behavior due to the composite action or polymer reinforced with fibers. At this stress level, the polymer attained its tensile strength and the consequent stress release was transferred to the surrounding fibers. This process is followed by some fiber slippage that justifies the small stress plateau observed in these tests, followed by the main contribution of the fibers up to the peak tensile stress.

2.2.2. Foam core

The foam core of the proposed slab can offer some resistance to the lateral buckling of the ribs, as well as to provide some support to the DHCC layer. Additionally, it also helps to improve thermal insulation of the proposed hybrid sandwich panels. In the design of the proposed hybrid sandwich slabs, the contribution of the foam core on the load carrying capacity of the panel was not considered due to its premature failure. Due to the type of stress field expected to occur in the foam as a constituent element of the developed sandwich slab, its compressive behavior was the selected one since it can provide the relevant information for modelling the contribution of the foam for this structural system. In this regard, three prism-shape coupons of Polyurethane foam (PUR D/40) [6] with density of 42.5 kg/m^3 were prepared based on ASTM C365-03 recommendations [7]. As recommended by ASTM C 365-03, the minimum and the maximum square cross section of the prism should be 25×25 mm^2 and 100×100 mm^2, respectively [7]. Therefore, the square cross section of 70×70 mm^2 and a length of 50 mm were adopted for the dimensions of the specimens of this experimental program [8]. These specimens were tested by adopting a compressive loading

controlled by imposing an axial displacement rate of 0.5 mm/min. The test setup and obtained compressive stress-strain curves are shown in Fig. 2.6. The strain was the displacement between the two steel loading platens divided by the initial axial length of the specimen (50 mm). The results demonstrate that this foam presents an almost linear behavior up to an average compressive stress of 0.18 MPa, of an elasticity modulus of 5.83 MPa, followed by an almost perfectly plastic behavior up to an axial strain of about 0.3, followed by a strain hardening phase due to the internal re-organization of its material structure in consequence of the large deformation and restriction to its lateral expansibility caused by the direct contact of the steel machine platens and surfaces of the foam specimen.

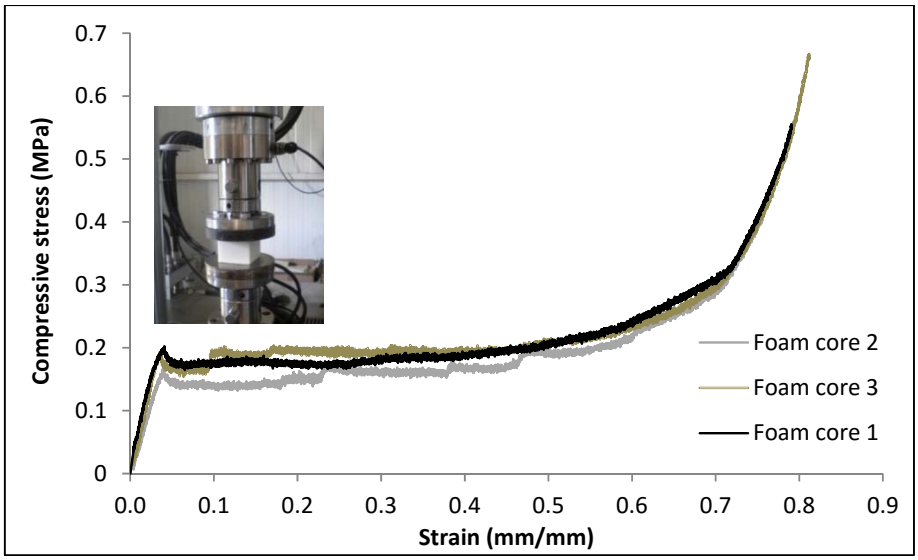

Fig 2.6. Foam cores specimens tested under compression loading

2.2.3. Properties of the Deflection Hardening Cement Composites (DHCC)

Fiber reinforced cement composites (FRCC) can be classified into two main categories (Naaman and Reinhard, 2005): strain softening cement composites (SSCC); strain hardening cement composites (SHCC) [9]. The strain character of a FRCC is evaluated by executing direct tensile tests with un-notched dog-bone type specimens. If after crack initiation the tensile strength is increased with the tensile strain, the FRCC is assumed pertaining to the SHCC category, otherwise is considered a SSCC. During the strain hardening phase of a SHCC a diffuse crack pattern is formed up to the coalescence of several micro-cracks in the macro-failure crack. The formation of multiple cracks means that fiber-bridging action is capable of

arresting the further opening of cracks, and as a result, new cracks tend to form in the close vicinity. The macro crack, in general, occurs for a tensile strain higher than 1.5%.

In bending (un-notched specimens), SSCC can present a deflection softening (DSCC) or a deflection hardening (DHCC) nature. During the deflection hardening phase of a DHCC several cracks are formed in the tensile face of the specimen, up to the formation of the failure macro-crack. It should be noted that the deflection hardening level is not only influenced by the fiber reinforcement mechanisms and matrix properties, but also by the dimension and cross-section geometry of the sample, since these aspects influence the fiber orientation and distribution [10]. The fiber-reinforced mortar developed in the scope of the present research project has a deflection hardening character. Due to the formation of several cracks, the SHCC and DHCC are also connoted as high to ultra-high ductile materials since during the process of formation of several cracks, high energy is absorbed, and the ultimate tensile strain (in the case of SHCC) and the ultimate deflection (in the case of DHCC) are much higher than the corresponding values at crack initiation.

The parameters that have higher influence on the mechanical performance of a FRCC are the material type, geometry, orientation, distribution and volume content of fibers, matrix properties, fiber-matrix bond, casting technology to apply the FRCC, and the geometry of the element to be cast [10]. Fiber-matrix bond is a governing requisite for the performance of a FRCC [11-13]. Based on the results obtained in [11] a comparative assessment of the effectiveness of polypropylene (PP), PAN (polyacrylonitrile) and nylon fibers for the increase of flexural strength and ductility performance of cement based materials, it was verified that PAN fibers were the most effective for both strength and ductility purposes. PAN fibers were also the most effective in terms of controlling crack width. Taking into account this information, as well as the availability of FISIPE (company that produces PAN fibers in Portugal), and CiviTest (company with expertise on the development of FRCC) to collaborate in this project, the PAN fibers were those selected for the development of the DHCC. This decision was also supported on the results obtained in a preliminary experimental program for the selection of the most appropriate fiber reinforcement system, where considerations like reinforcement effectiveness, cost competitiveness and technological aspects for the production and application of a thin layer of DHCC in the sandwich slab to be developed were taken into account. Based on the results of this preliminary experimental program, and considering the synergetic benefits of fibers of different properties in terms of assuring

effective crack control at different stage of the crack propagation [11-14], the two types of PAN fibers, whose relevant properties are listed in Table 2.5, were used for the development of the DHCC. From SEM images of the hydrophilic PAN6 and PAN12 fibers adopted in the present study, it was verified they have the cross section shape schematically represented in Fig. 2.7. In result of an optimization process for the hybrid fiber reinforcement system, a total fiber volume content of 4% was obtained, composed of 3% of PAN12 and 1% of PAN6.

Table 2.5. Properties of used PAN fibers

Fiber	Length (mm)	Diameter (μm)	Elasticity modulus (MPa)	Tensile strength (MPa)	Density (gr/cm3)	Elongation %
PAN6	6	58	9910	564	1.17	13-17
PAN12	12	26	6856	264.4	1.17	14-18

a) **b)**

Fig 2.7. Geometry of the cross section of the fiber type: a) PAN6 (bean shape); b) PAN12 (circles in a trihedral configuration)

The constituent materials for the DHCC were: Portland cement type 42.5R, fly ash, limestone filler (of average diameter of 3.7 μm), sand, water, viscosity modification agent (VMA) and superplasticizer. The optimized composition is presented in Table 2.6.

Table 6. Mixture proportions

Cement/ Powder*	Fly ash/ Powder	Limestone filler/ Powder	Sand/ Powder	Admixture**/ Powder	Water/ Powder
0.5	0.5	0.09	0.2	0.033	0.388

* **Powder**: Cement + Fly ash

** **Admixture**: viscosity modification agent + superplasticizer

To characterize the flexural behavior of the developed DHCC, the type of specimen and test setup schematically represented in Fig. 2.8b were adopted. These specimens, of 250 mm × 80 mm × 18 mm dimensions, were cut from panels with dimensions of 500 mm × 500 mm × 18 mm (Fig. 2.8a) after have been cured during 28 days in a controlled environmental chamber at 23°C temperature and 70% relative humidity. From the four point bending tests carried out under displacement control at a displacement rate of 0.6 mm/min

it was obtained the force versus mid-span relationship, from which the flexural stress at crack initiation, the flexural strength and its corresponding deflection, and the energy absorption from crack initiation up to this deflection were determined, and the crack pattern registered (Fig. 2.9). The load was measured with a load cell of 10 kN capacity, while the deflection was recorded by a Linear Variable Differential Transformer (LVDT) of 10 mm stroke. According to the results presented in Table 2.7 and Fig. 2.9, the developed DHCC shows a pronounced hardening behavior and high energy absorption capacity in bending. To calculate ductility for DHCC material, the following equation was used:

$$\mu = \frac{D_U}{D_Y} \qquad (2.1)$$

where D_U is the deflection at point B (deflection measured when the failure crack is formed, and the applied load starts decreasing) and D_Y is the maximum deflection in linear behavior (the deflection when the first crack is formed) (Point A in Fig. 2.9c).

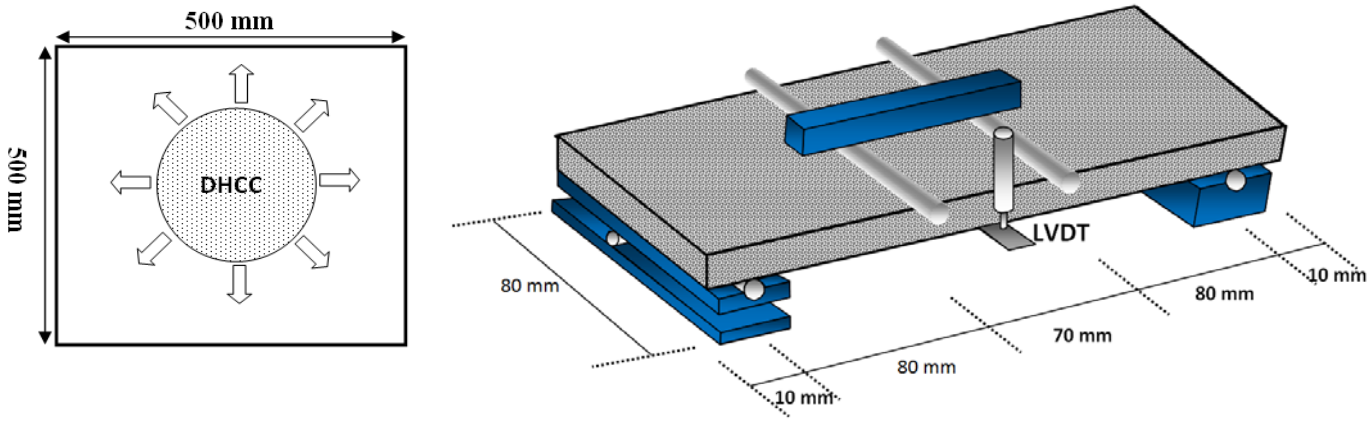

a) **b)**

Fig 2.8. Casting DHCC panels; b) Flexural test setup (width of the specimen's cross section = 80 mm)

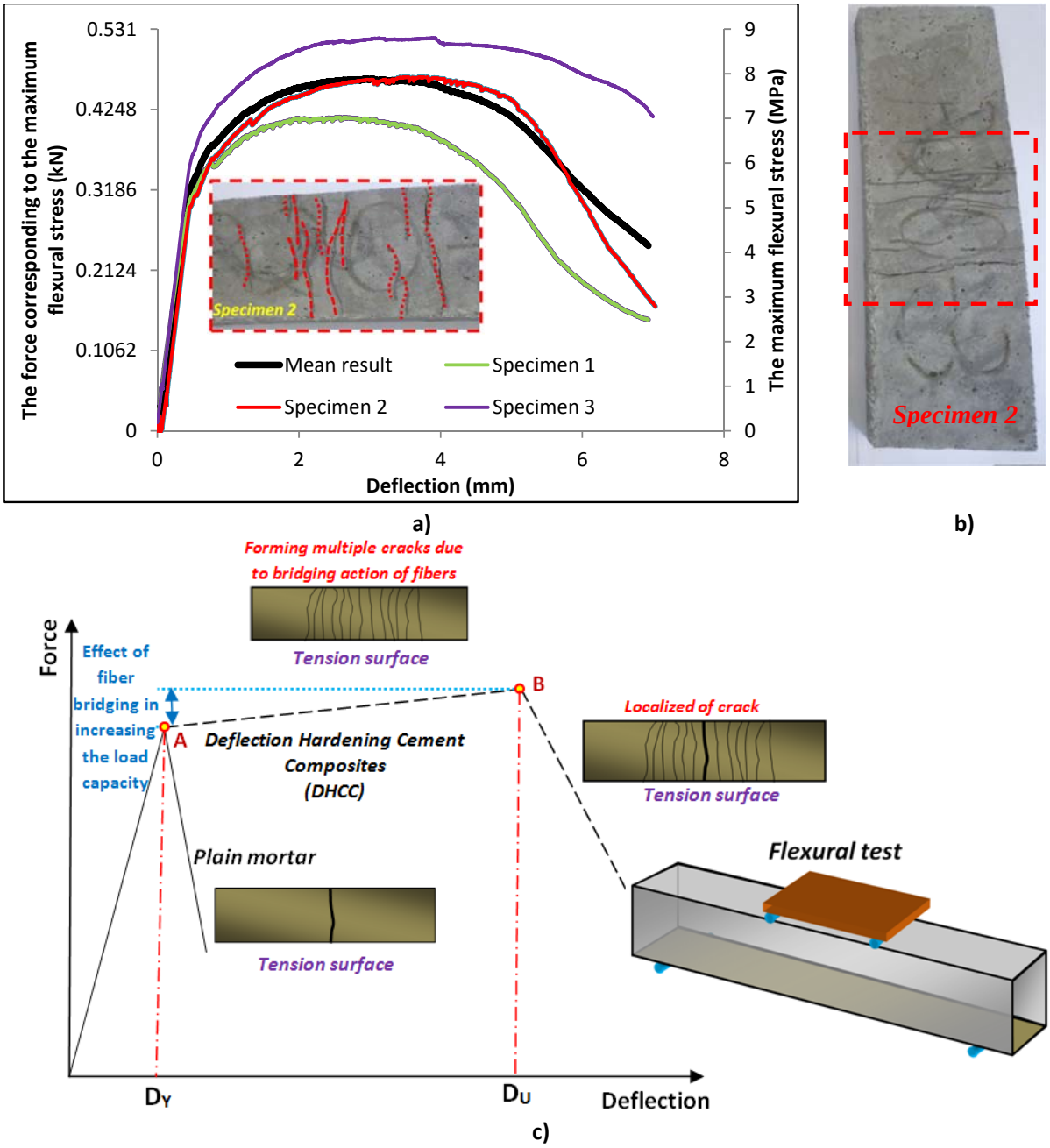

Fig 2.9. a) Flexural stress vs. mid span displacement; b) representative crack patterns; c) Symbols used for the evaluation of ductility

Table 2.7. Absorbed energy, ductility, flexural strength and its deflection

Flexural strength (MPa)	Maximum hardening deflection (mm)	Energy absorption (N/mm)	Ductility
7.85	3.48	24.68	8.76

SEM images were used to better understand the fiber reinforcement mechanisms provided by the used PAN fibers. Due to the excellent bond of PAN fibers to cement based materials, as shown in Fig. 2.10a where the surface of the fibers is covered by cement hydrated

particles, the SEM images obtained in the fracture surface of tested specimens show a tendency for the rupture of the longer fibers (PAN12), while the smaller fibers (PAN6) have preponderantly failed by debonding (Fig. 2.10b). The rupture of PAN12 fibers justifies the abrupt decay of the flexural capacity for a deflection in the interval of 5 to 7 mm (Fig. 2.9a) in this type of specimens.

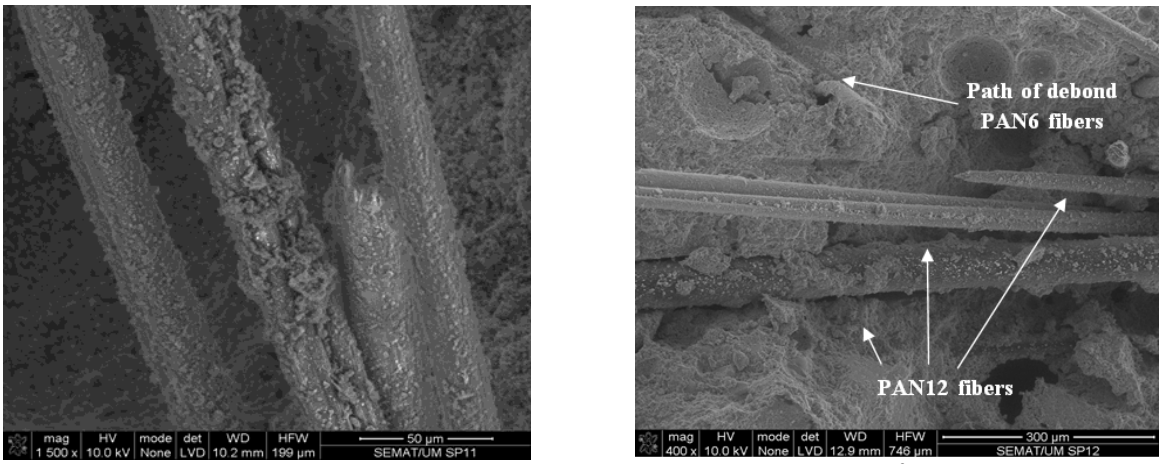

a) b)

Fig 2.10. a) PAN fiber surface covered by cement hydrated products; b) predominant failure modes for the fibers: rupture for PAN12 and debond for PAN6

To calculate the energy absorption in the fracture process of the developed DHCC, three and four point bending tests (TBT and FPB, respectively) were carried out with three notched prismatic specimens of 60 mm × 40 mm × 250 mm (Fig. 2.11). The notch was executed in the mid-span of the specimen, and has a depth of 10 mm and an average width of 2 mm (Fig. 2.11c). Furthermore, three un-notched prismatic specimens of this type were tested in FPB configuration in order to assess the flexural behavior and crack pattern when a stress concentration induced by the notch is not present (Fig. 2.11d). Both FPB and TPB tests were carried out with a deflection rate of 0.6 mm/min under displacement control. In the tests with notched specimens the deflection and the crack mouth opening displacement (CMOD) were measured, while in the un-notched specimens only the deflection was registered. According to the obtained results presented in Fig. 2.11a (each curve represent the average response of three specimens), the energy absorption in the fracture process up to a CMOD=2.5 mm was 18.56 N/mm and 14.27 N/mm in the TPB and FPB tests, respectively, while the flexural strength was 7.77 MPa and 8.66 MPa, respectively (Fig. 2.11a). In the FPB tests with un-notched DHCC specimens (Fig. 2.11b), an average flexural strength of 7.82 MPa was obtained at mid-span deflection of 3 mm, and multiple cracks were formed due to the

deflection hardening character of this composite. By executing four compression tests with cubic specimens of 50 mm edge of 28 days age, an average compressive strength of 24 MPa was obtained. Additionally, to evaluate the Young's modulus of DHCC material, four cylinders of 50 mm diameter and 100 mm height were casted, and after 28 days curing they were tested according to the ASTM C469 recommendations, and an average value of 10 GPa was obtained for the Young's modulus [15]. Furthermore, the specific weight of the developed DHCC material was 17.98 kN/m^3, which is about 75% of the one of the plain concrete. Therefore, developing a lightweight mortar with high flexural capacity and suitable compressive strength and stiffness can improve the structural performance of the hybrid sandwich panels. The properties of this DHCC will be also relevant for serving as a shear connectors for the GFRP ribs, as will be later discussed.

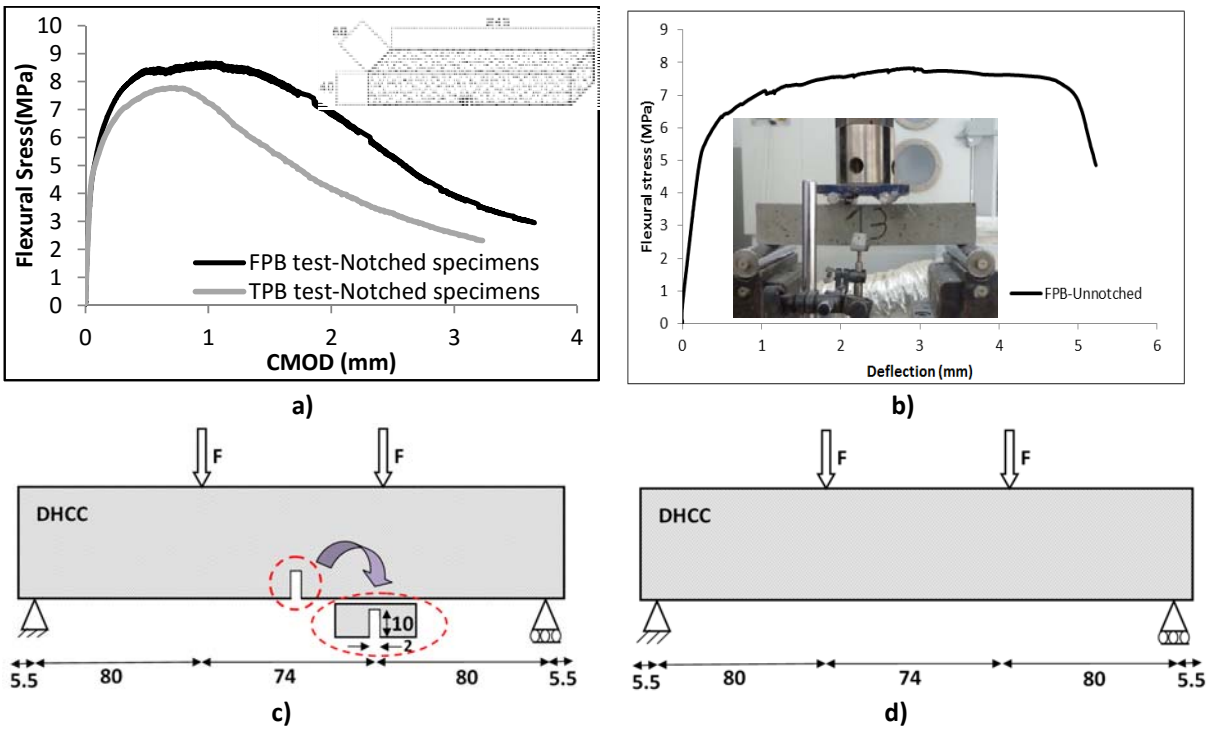

Fig 2.11. a) Average response in terms of flexural stress vs. CMOD in three and four point bending tests with notched specimens; b) Average response in terms of flexural stress vs. deflection in four point bending tests with un-notched specimens; c) Distance between the applied point loads in four point bending tests with notched beams; d) Distance between the applied point load in four point bending tests with un-notched beams (all dimensions are in mm)

Additionally, the developed DHCC material was also assessed under direct tensile loading. Fig. 2.12a indicates the tensile test setup used for assessing the DHCC material. The dimensions of the prismatic specimens, which were used was 250×80×18 mm^3. The

prismatic specimens were extracted from a panel with global dimensions of 500×500×20 mm^3. The tensile test was executed on the specimens by applying a displacement rate of 0.18 mm/min. The results presented in Fig. 2.12a and Fig. 2.12b indicate hardening behavior after initiation of the first crack. Subsequently, multiple cracks are formed. The initial crack is formed at a tensile stress of 2.06 MPa (see Fig. 2.12b). The bridging action of fibers across cracks through transfer stress from PAN fibers to matrix, provides ductility to the composite. Therefore, based on this mechanism, the tensile stress increased from 2.06 MPa to 2.42 MPa. It is further remarked that the representative curve fairly matches the average behaviour of these three specimens.

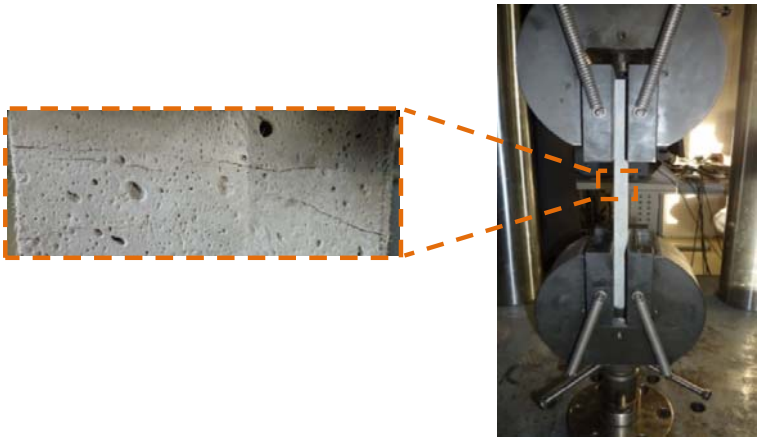

a)

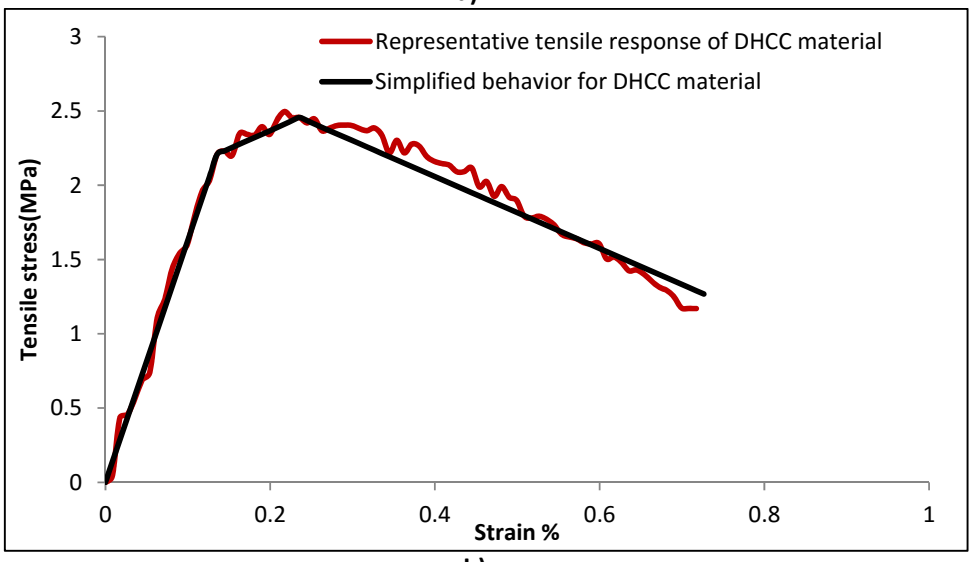

b)

Fig 2.12. Tests performed to define the mechanical properties of DHCC: a) Tensile test setup; b) Tensile response

2.2.3.1. Assessment of the performance of DHCC for statically indeterminate support conditions

By analyzing the support conditions of the DHCC layer in the sandwich slab represented in Fig. 2.1, the statically indeterminate character provided by the supports of the GFRP ribs can estimate a favorable effect in terms of maximum flexural capacity of the DHCC layer, due to the high stress redistribution capacity derived from the high post cracking tensile resistance of the DHCC. To assess these potentialities, an experimental program was executed with two continuous span specimens, whose geometry and test setup is represented in Fig. 2.13b. These specimens were extracted from two panels with dimensions of $620 \times 530 \times 16$ mm^3 (Fig. 2.13a) that were cured during 28 days in a controlled environmental chamber at a temperature of 23°C and 70% of relative humidity. Three specimens were cut in the longitudinal direction of one panel (L1 to L3), and three other specimens were extracted in the transversal direction (W1 to W3), in an attempt of also assessing the influence of fiber orientation on the flexural behavior of these specimens. The test setup is shown in Fig. 2.13b, where it is visible that each span of the specimen was submitted to two line loads (load distributed in the width of the specimen). The test was controlled with a deflection rate of 0.6 mm/min by using an LVDT of 10 mm stroke for this purpose. One LVDT was installed in the center of each span for measuring the deflection of each specimen.

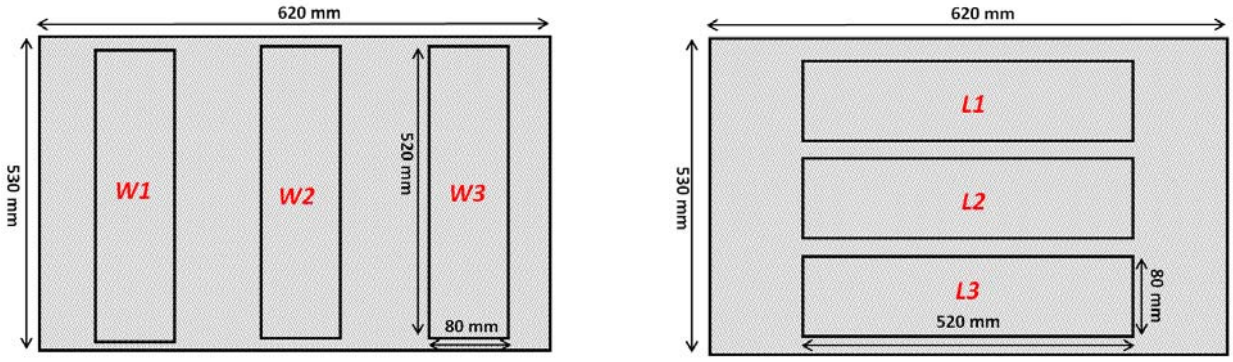

a)

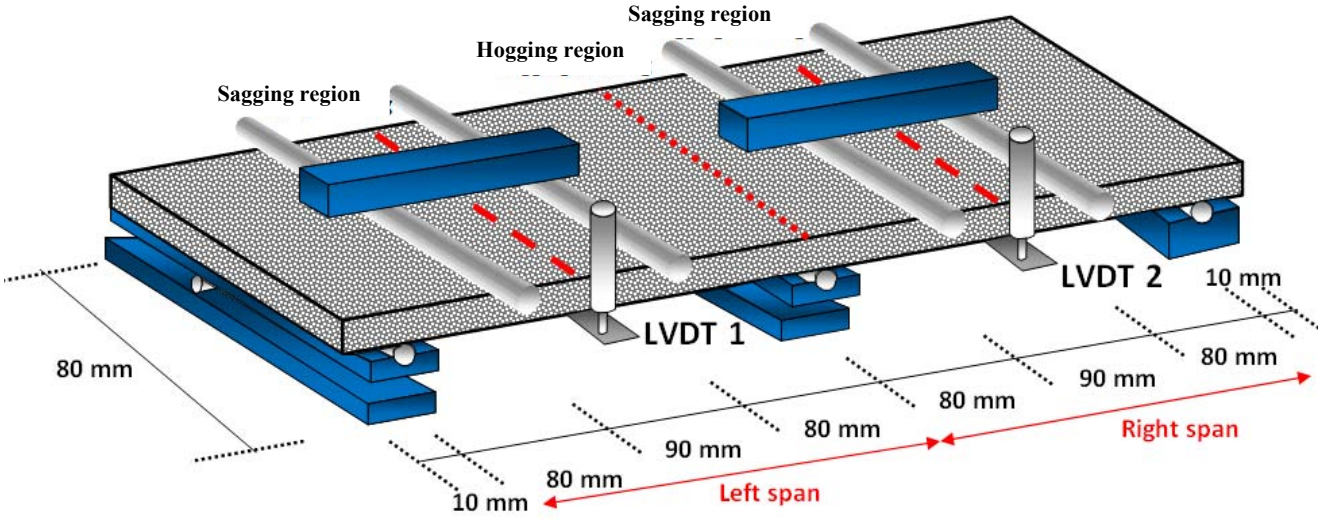

b)

Fig 2.13. Specimens cut from DHCC panels: a) Extraction configuration; b) Test setup, load and support conditions

The relationship between deflection (in each span) and both the total applied load, and the flexural stress (at the section of the sagging region of maximum flexural stress, $\sigma_{f,\max}^{S}$, Fig. 2.14a; at the hogging region, σ_{f}^{H} ,Fig. 2.14b) is represented in Fig. 2.14. In the legends of this figure the "Li-left/right span" means the relationship between the load (or flexural stress) versus deflection in the left or right span of the specimen "I (1 to 3)" extracted in longitudinal direction "L". Similar meaning has "Wi-left/right span" with the unique difference that now the specimen was extracted in the transversal direction. Due to deficient functioning of the LVDT placed at the right span of the L1 specimen it was not possible to register the corresponding deflection. It is visible that the orientation and distribution of the fibers did not have a significant influence in terms of load and flexural capacity, indicating an almost homogenous distribution and orientation of the fibers. The average value of the maximum flexural capacity at the sagging regions of specimens extracted in the longitudinal (Fig. 2.14a) and in the transversal (Fig. 2.14b) was 10.63 MPa and 9.87 MPa, respectively,

which are higher than the flexural strength registered in the statically determinate specimens (Fig. 2.9a, 7.85 MPa). The favourable effect of the statically indeterminate character when using DHCC is more visible in Fig. 2.14c where a maximum flexural stress in the hogging region has attained a value of 15.78 MPa, which is much higher than the value registered in simply supported beams. However, this evaluation did not consider any moment redistribution [16] that may have occurred, but was not possible to estimate since the reaction forces were not measured. If a moment redistribution has occurred in an interval acceptable for ductile materials [17], the maximum flexural stress in the sagging region will have increased, while the maximum flexural stress in the hogging region will have decreased, for a level that will be, in any case, much higher than the flexural strength registered in the statically determinate beams. Fig. 2.14d represents the crack patterns in the top surface of the hogging (intermediate support) region and in the bottom surface of the sagging (mid-span) regions of the longitudinal specimens. In general, several cracks were formed in these regions, which support the occurrence of moment redistribution.

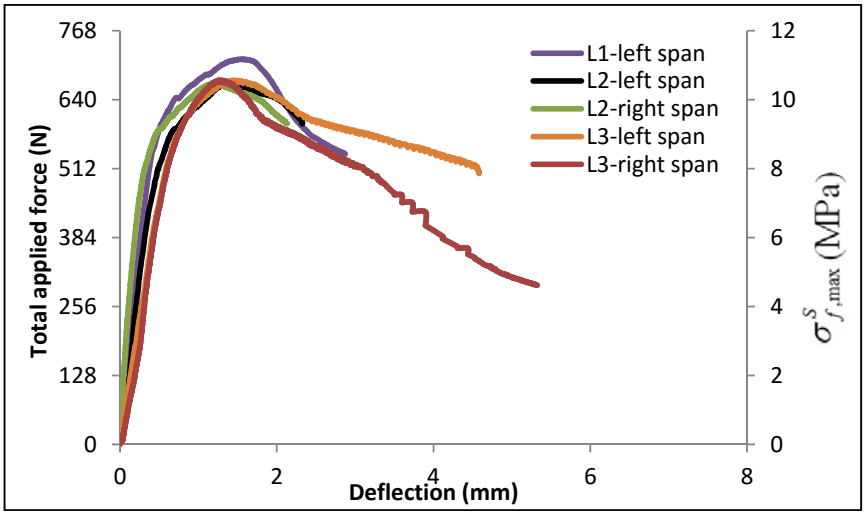

a)

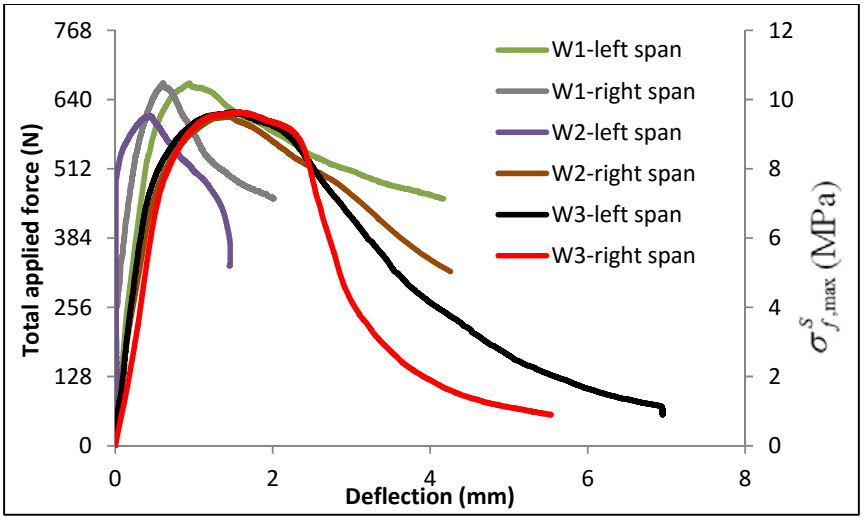

b)

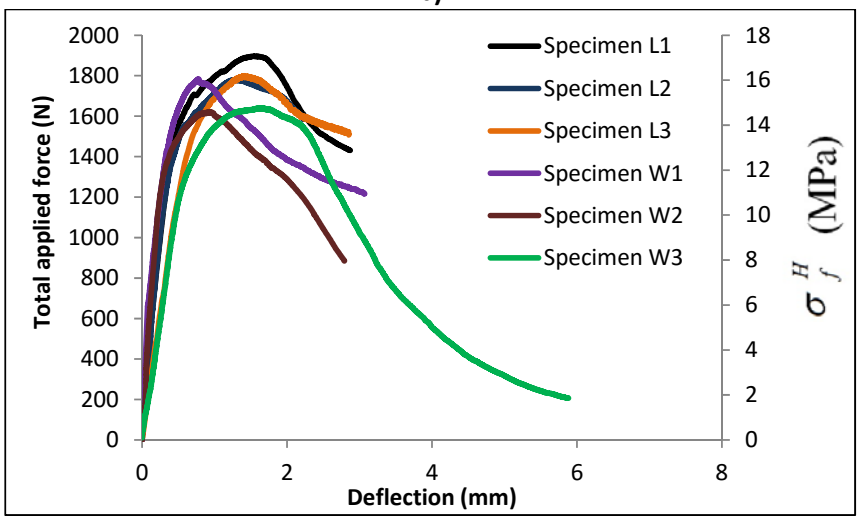

c)

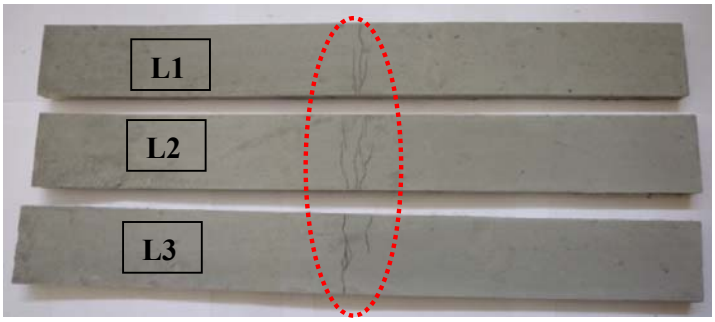

Formed cracks in the hogging region (see Fig. 2.13b)

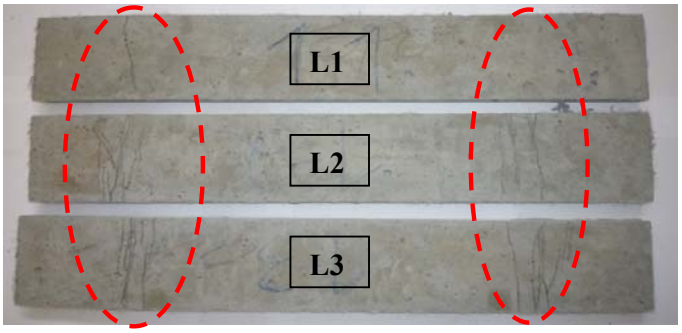

Formed cracks in the sagging regions (see Fig. 2.13b)

d)

Fig 2.14. Deflection in the middle right and left spans versus total load and maximum flexural stress in the sagging regions of specimens extracted in a) longitudinal (L), b) transversal (W) direction; c) average deflection versus total load and flexural stress in the hogging region; d) Crack patterns in the longitudinal specimens tested in statically indeterminate support conditions

The author is aware that the results obtained with the standard beam specimens for thin elements are questionable, because the fiber dispersion and orientation is strongly affected by the elements geometry. Moreover, due to the geometry of the DHCC layer, the fiber distribution tends to be predominantly parallel to the slab's plane (between GFRP ribs), while in the standard beams, the fibers have a 3D random distribution character. Even so, the results obtained provide a general idea of the DHCC material behavior.

Considering the cross section adopted for the DHCC layer in the proposed hybrid slab, which was presented in Fig. 2.1, it is considered important to look for a deeper understanding on the flexural performance of the cross section chosen for DHCC layer. As shown in Fig. 2. 15a, three prismatic beams were cut from the DHCC layer of the hybrid slab along the longitudinal and transversal orientations. The specimens have rectangular and trapezoidal cross sections, as presented in Fig. 2.15, and were tested experimentally under flexural loading.

Width of the prismatic beams was defined by 80 mm, while length of longitudinal and transversal extracted beams was equal to 400 mm and 250 mm, respectively. The thickness of longitudinal and transversal beams was 20 mm, which is the original thickness of the flat surface of the DHCC layer. The cross section of the trapezoidal beams is indicated in Fig. 2.15a and Fig. 2.15d. The test setup adopted for the execution of FPB test is presented in Fig. 2.15b and Fig. 2.15c. The beams were loaded with a displacement rate of 0.6 mm/min. The load was recorded using a load cell with 10 kN maximum capacity, and the deflection was measured with a Linear Variable Differential Transformer (LVDT) of 10 mm stroke. Displacements were registered at the mid-span of the beams.

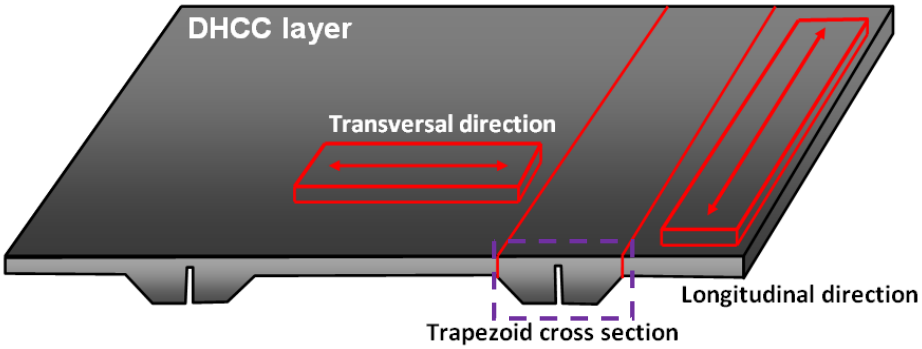

a) DHCC layer and schematic figure of extracted beams

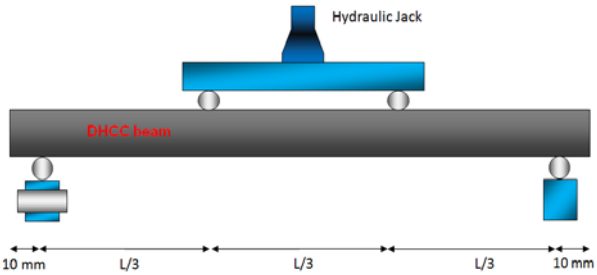

b) Test setup for FPB test on DHCC beams

c) Bending test on longitudinal beam

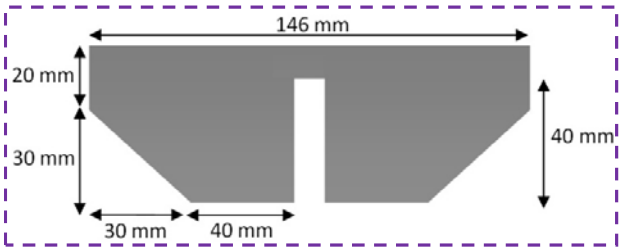

d) Bending test on trapezoidal beam

Fig 2.15. Beams extracted from DHCC layer and corresponding bending tests

The results obtained in the experimental assessment are depicted in Fig. 2.16 and listed in Table 2.8. Considering the results obtained, different ductility index values and flexural strength values were registered in the extracted beams. A maximum flexural strength of 8.54 MPa and a minimum ductility index of 2.3 were registered for beams extracted in the transversal direction. Differences in the recorded results could be justified by differences in the geometry and length of beams, which affect the stiffness and flexural performance of beams made with DHCC material.

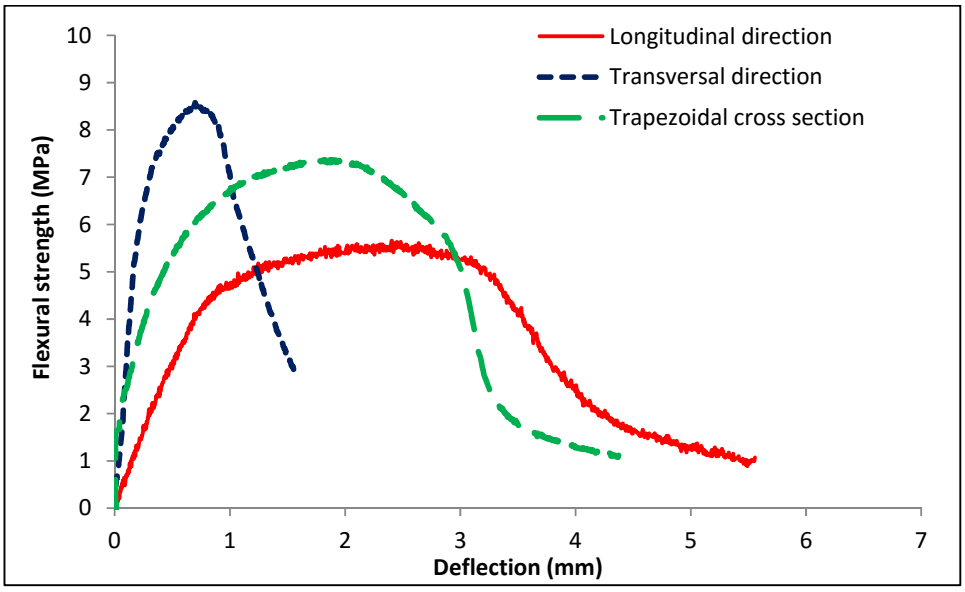

Fig 2.16. Obtained flexural stress vs. deflection responses of extracted beams

Table 2.8. Recorded results of flexural response from extracted beams

Specimens	Flexural stress at crack initiation (MPa)	Ultimate hardening deflection (mm)	Ultimate flexural stress (MPa)	Ductility index (μ)
Transversal direction	6.98	0.69	8.54	2.30
Longitudinal direction	4.26	2.70	5.52	3.55
Trapezoidal cross section	2.47	2.06	7.30	25.75

2.3. Manufacture process of the proposed sandwich slab system

The process of manufacturing the slabs was developed in two phases that include (Fig. 2.17): 1) Fabrication of GFRP body (GFRP ribs and skin) with pre-installed foam cores, by using vacuum assisted resin transfer molding (VARTM) process; and 2) Casting the DHCC material in order to form a top compressive layer of the sandwich panel. VARTM is an advanced fabrication process for polymer-matrix composite structures. The process has been developed over the last decade and has several advantages over the traditional Resin Transfer Molding (RTM) process; since VARTM process eliminates the costs associated with matched-metal tooling, it reduces volatiles emission and allows the use of lower resin injection pressures [18]. The matched-metal tool commonly found in RTM process is replaced in the VARTM process by a formable vacuum plastic bag. In VARTM process, the resin is injected through single or multiple inlet ports depending upon parts size and shape.

RTM process is commonly used to form moulds with liquid composites. This method is primarily used to mould components with large surface areas, complex shapes and smooth finishes. The VARTM process commonly involves three steps: (a) preforming lay-up of the fiber reinforcing system on a rigid plate surface, which is surrounded by a formable vacuum bag; (b) impregnation of the fiber-reinforced system with resin and then resin transferred into the element by a pressure gradient (induced by the vacuum pressure), gravity and capillary effects; and (c) curing of the impregnated resin for at least 24 hours. In the first step of manufacture process, the layers of the GFRP skin were laid out on a steel table. Then, the layers of GFRP ribs and the pieces of foam cores were put on the layers of the GFRP skin (see Fig. 2.17a and Fig. 2.17b). To perform vacuum process, the GFRP layers and foam were carefully wrapped using a plastic cover and subsequently tubes were used to suck the air content in the sandwich panel for 24 hours. After ensuring total air evacuation, the resin was injected inside the sandwich panel through multiple inlet ports (see Fig. 2.17c). Afterwards, the vacuumed GFRP layers were cured for 24 hours. After the cure procedure was

concluded, demoulding of specimens was performed by removing the wrapped formable plastic bag, which was used for vacuuming of specimens in the VARTM process. As shown in Fig. 2.17d, the shear connection between GFRP ribs and DHCC layer was later assured by drilling holes into the GFRP ribs.

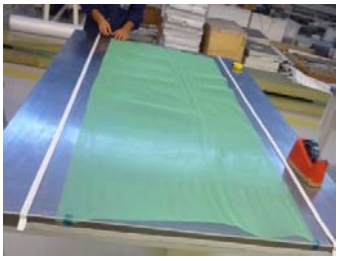
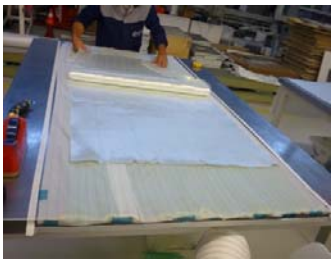


a) Preparing fiber layers and putting the fibers beside the foam cores


b) Installing tubes in different parts the slabs for vacuuming the hybrid sandwich panel

c) Vacuuming the hybrid sandwich panel and resing inlet during infusion process


d) Execution of holes in ribs to assure shear connections

Fig 2.17. Steps of the manufacture process of the sandwich slabs by using VARTM technology

As illustrated in Fig. 2.18, the rheology of the DHCC was designed in order to flow properly through the holes created in the GFRP ribs for assuring shear connection between these two components of the sandwich slab system. For the execution of the DHCC layer for each slab, approximately 50 liters of DHCC was prepared. After casting the DHCC layer, the specimens were cured for 28 days.

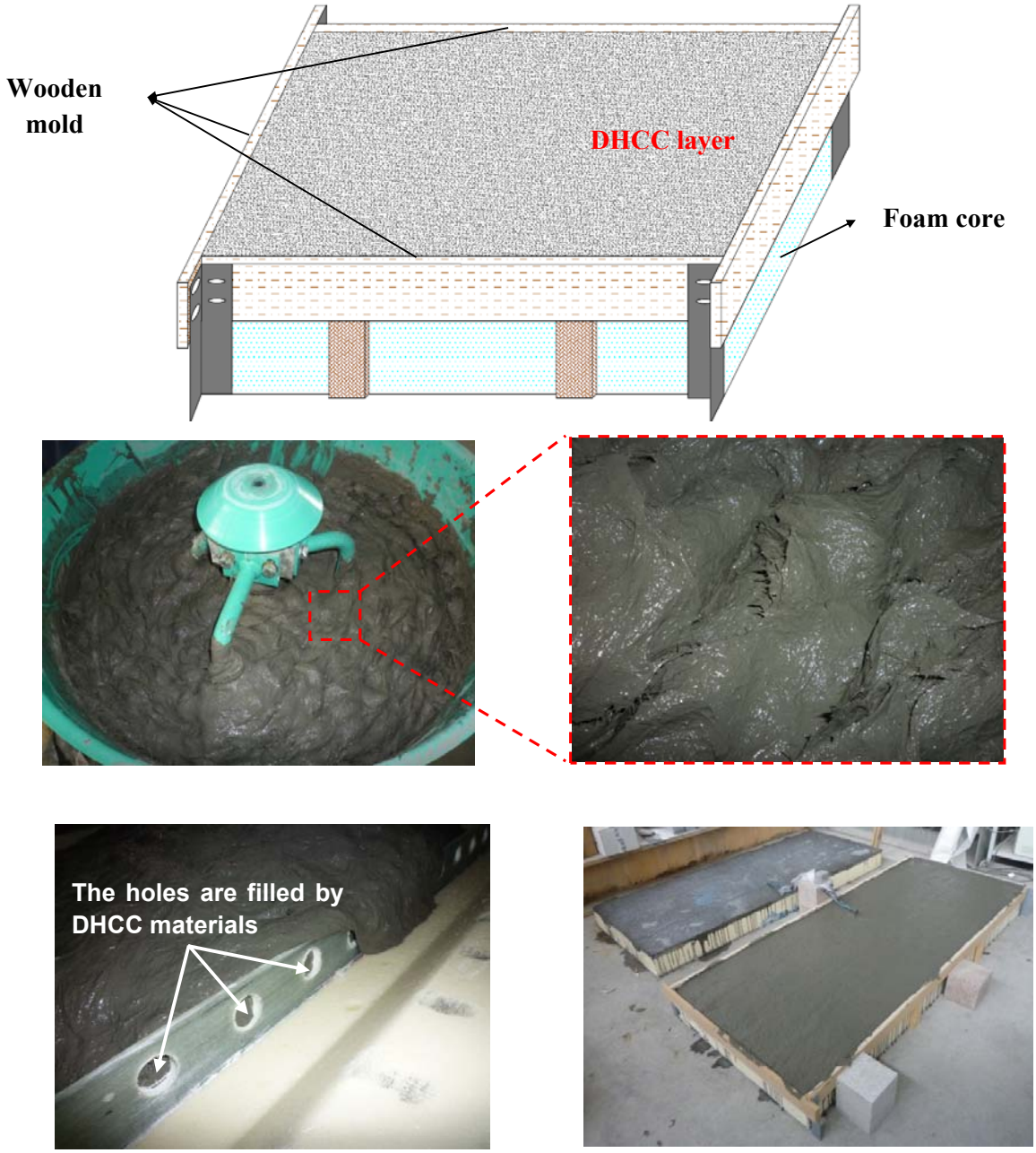

Fig 2.18. Casting the DHCC layer of the sandwich slabs

2.4. Conclusions

For assuring a lightweight slab with a convenient compromise of strength and ductility, this hybrid sandwich panel is formed by a top compressive layer of deflection hardening cement composite (DHCC), ribs and bottom skin in glass fiber reinforced polymer (GFRP) laminate, and a core foam with insulation requisites. The developed DHCC was reinforced with different PAN fibers, and presented a very ductile flexural behavior. For assuring an effective connection between DHCC and GFRP ribs, a simple, but efficient technology was adopted by executing holes of small diameter the top zone of the GFRP embedded in the DHCC layer. In the development of the GFRP ribs and skins, the number and organization of layers, and the orientation of fibers were selected for assuring level of stiffness and strength suitable for this type of applications.

References

[1]. Tassinari L., Monleon S., Gentilinib C., "Unified formulation for Reissner-Mindlin plates: a comparison with numerical results", Proceedings of the International Association for Shell and Spatial Structures (IASS) Symposium, 2009, Valencia, Spain.

[2]. Selcom multiaxial technology company, Biaxial products. http://www.multiaxialfabricselcom.com/en/Products/

[3]. Brands Composite factory, Resin and additive materials link: http://www.brandscomposiet.nl/en/products

[4]. UNE-EN ISO 178:2003. Plastics. Determination of flexural properties. (ISO 178:2001).

[5]. American Society for Testing and Materials (ASTM) D3039: Standard method for tensile properties of polymer matrix composite materials, 2000.

[6]. Poliuretanos foam factory link: http://www.poliuretanos.com/en/productos/planchas/pur-d40.html

[7]. American Society for Testing and Materials (ASTM) C365-03. Standard test method for flatwise compressive strength of sandwich cores, 2004.

[8]. Sharaf T., Fam A., 2010, "Flexural performance of sandwich panels comprising polyurethane core and GFRP skins and ribs of various configurations", Composite Structures, Vol. 92, pp. 2927-2935.

[9]. Naaman A. E., Reinhard, H. W., 2005, “Proposed classification of HPFRC composites based on their tensile response”, Proceedings 3rd international Conference on Construction materials: Performance, Innovations and Structural Implications (ConMat'05) and Mindess Symposium, p. 458, Eds: N. Banthia, A. B., T. Uomoto & Shah, S., University of British Columbia, Vancouver, Canada.

[10]. Zollo RF., 1997, “Fibre-reinforced concrete: An overview after 30 years of development”, Cement and Concrete Composites, Vol. 19, pp: 107–122.

[11]. Pakravan H.R., Jamshidi M., Latifi M., 2012, “Investigation on polymeric fibers as reinforcement in cementitious composites: Flexural performance”, Industrial textiles, Vol. 42, pp: 3-18.

[12]. Pakravan H.R., Jamshidi M., Latifi M., 2012, “Adhesion polypropylene fiber to cement matrix”, Adhesion science and technology, Vol. 26, pp: 1383- 1393.

[13]. Pakravan H.R., Jamshidi M., Latifi M., F. Pachaco-Torgal, 2012, “Evaluation of adhesion of polymeric fiber reinforced cementitious composites”, Adhesion and adhesives, Vol. 32, pp: 53-60.

[14]. Pereira E.N.B., Fischer G., Barros A.O. Joaquim, 2012, “Direct assessment of tensile stress-crack opening behavior of Strain Hardening Cementitious Composites (SHCC)”, Cement and concrete Research, Vol. 42, 834-846.

[15]. American Society for Testing and Materials (ASTM) C469, “Standard Test Method for Static Modulus of Elasticity and Poisson’s Ratio of Concrete in Compression”, 1994.

[16]. Dalfré G.M., Barros A.O. Joaquim, 2011, “Flexural strengthening of RC continuous slab strips using NSM CFRP laminates”, Advances in Structural Engineering, Vol. 14, pp: 1223-1245.

[17]. Breveglieri M., Barros Joaquim A.O., Dalfré G.M., Aprile A., 2012, “A parametric study on the effectiveness of the NSM technique for the flexural strengthening of continuous RC slabs”, Journal of Composites – part B: Engineering, Vol. 43, pp: 1970-1987.

[18]. Sayre J.R., 2000, “RFI and SCRIMP Model Development and Verification’’, Ph.D. Dissertation, Department of Engineering Science and Mechanics, Virginia Polytechnic Institute and State University, Blacksburg, VA, USA.

Chapter 3

Preliminary experimental tests on the hybrid slabs

3.1. Introduction

Flexural tests were used to assess the proposed hybrid slabs, including Three Point Bending (TPB) test and Four Point Bending (FPB) test. The major difference between FPB and TPB tests is that FPB test brings a much larger portion of the slab to the maximum stress, as opposed to only the material right under the central bearing.. Therefore, a total of four hybrid slabs were assessed under flexural load conditions, including two specimens (Slab 1 and Slab 2) with lengths of 2 meters were employed under FPB test (phase 1). Moreover, two hybrid slabs (Slab 1 and Slab 2)with 1 meter length were used to evaluate the flexural performance of slabs under TPB test (phase 2).

3.2. FPB tests on DHCC-GFRP sandwich panels – Phase 1

3.2.1. Test setup and loading sequence

The behavior of the developed hybrid sandwich slabs was assessed by adopting two different flexural loading configurations: Three Point Bending (TPB), and Four Point Bending (FPB). Slab 1 was subjected to both TPB and FPB loading configurations, while Slab 2 was only submitted to FPB loading configuration.

According to Table 3.1 and Fig. 3.1, the tests were carried out based on displacement control, and two cycles were applied in each sequence of loading, followed by a last monotonic loading up to a mid-span deflection of 100 mm (=L/18). In each cyclic loading sequence, the applied load was increased up to a certain deflection corresponding to the mentioned mid-span deflections in Table 3.1 and then, after reaching the target deflection at the mid-span, it was maintained constant for one minute. Both Slab 1 and Slab 2 were experimentally assessed under cyclic flexural loading by applying a displacement rate of 30 μm/sec. The first step of loading for Slab 1 was composed of the FPB test configuration represented in Fig. 3.2a by applying two cycles with a maximum mid-span deflection of 14.4 mm. After has been unloaded, this slab was subjected to a TPB cyclic loading configuration with the same mid-span deflection. The third and the fourth loading steps were performed under FPB and TPB tests, respectively, by applying 21.6 mm deflection at mid-span. Then, in the last loading sequence to Slab 1, the mid-span deflection was increased up to 60 mm under

TPB test up to failure. The loading sequences applied to Slab 2 are shown in Fig. 3.1b, and listed in Table 3.1. As shown in Table 3.1, the mid-span deflections for Slab 1 and Slab 2 are different. Before implementing the flexural tests, it was decided to increase the mid-span deflection up to 2δ ($\delta = L/250$, with *L*=1800mm) for the first load sequence. Based on preliminary numerical simulations, significant damages were not expected to occur on the slabs up to a load level corresponding to the mid-span deflection of 2δ ($\delta = L/250$, with *L*=1800mm) when a four point loading configuration is adopted. Therefore, this deflection limit was assumed for the first load sequence in Slab 1, followed by load sequences of an increase of δ in terms of mid-span deflection (Table 3.1). However, the experimental response of this slab during the first load sequence has presented signs of damage, as will be later discussed. Therefore, in order to have a first load sequence with a linear response, the increment of deflection adopted in the load sequences of the Slab 2 was limited to δ/2 (Table 3.1).

Table 3.1. Flexural loading sequence of Slab 1 and Slab 2 (see Fig. 3.1)

	Sequences of applied loading	**Type of applied cyclic loading**	**Numbers of applied cyclic loading in each sequence**	**Mid-span deflection in each cyclic loading sequence (mm)**
Slab 1	1	FPB	2	14.4
	2	TPB		14.4
	3	FPB		21.6
	4	TPB		21.6
	5	FPB	1	28.8
	6	FPB	Increasing up to failure	100
Slab 2	1	FPB	2	3.6
	2			7.2
	3			10.5
	4			14.4
	5		Increasing up to failure	80

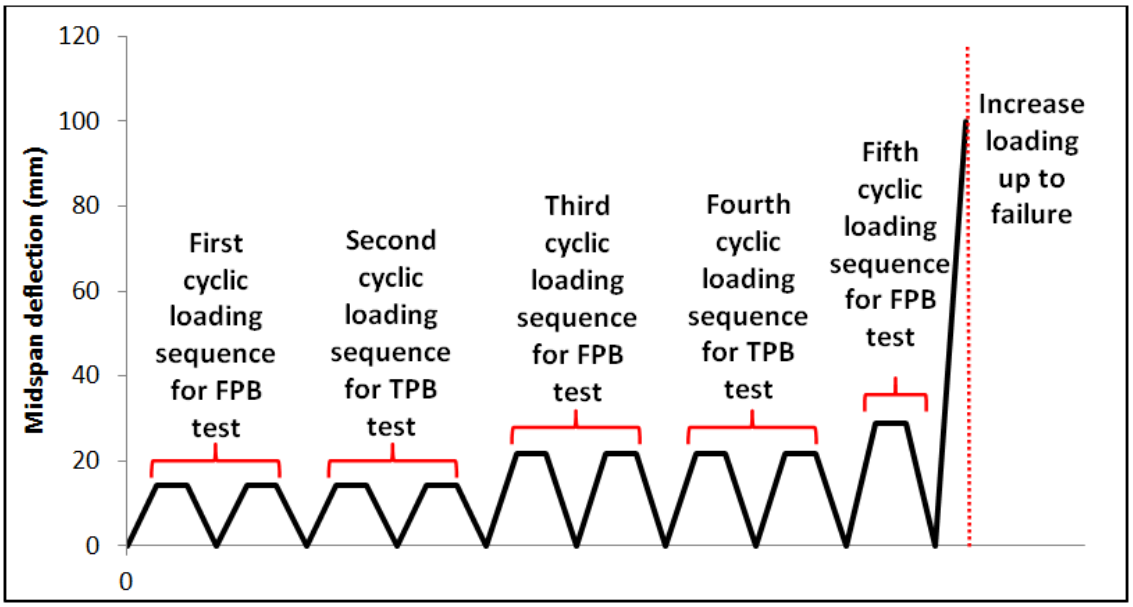

a)

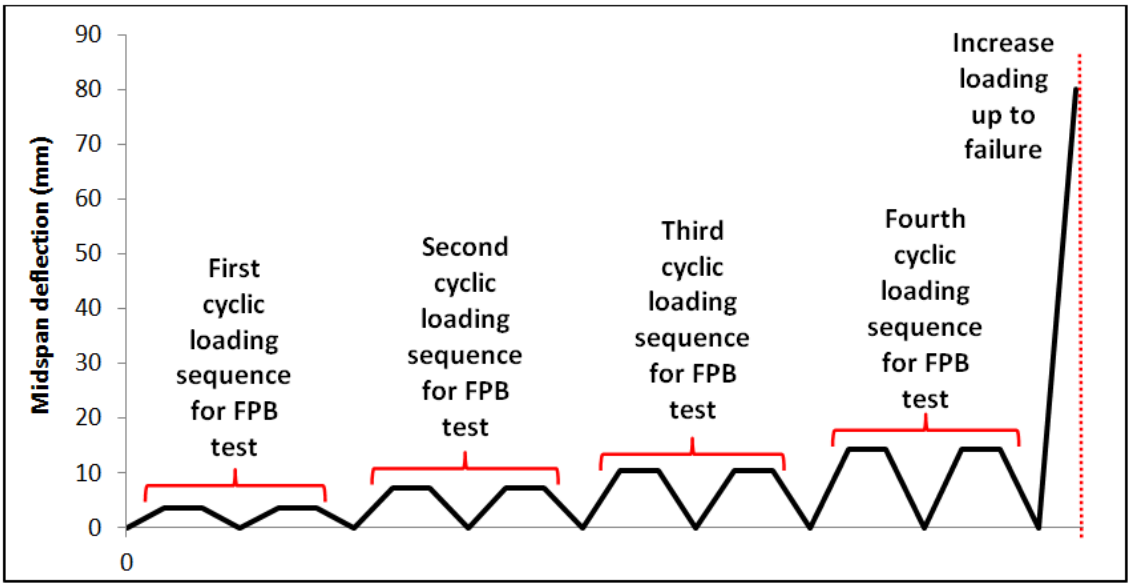

b)

Fig 3.1. Cyclic tests loading sequences: a) Slab 1; b) Slab 2

According to Fig. 3.2a, seven LVDTs were used to measure deflection and slip on different locations of the slabs. In Slab 1, the LVDTs 3, 4 and 5 were used to measure deflections, the LVDTs 2 and 6 for measuring vertical displacements on the top surface in the alignment of the slab's supports, and LVDTs 1 and 7 were used to measure slip between DHCC layer and GFRP ribs. Slip between GFRP ribs and DHCC layer was measured, mainly, to assess the performance of the designed shear connectors. In Slab 2 the LDVTs 3, 4 and 5 were adopted to measure deflections, LVDT 2 for measuring the vertical displacement on one side support, LVDTs 1 and 7 to measure slip between DHCC layer and GFRP ribs on both end sides, and LVDT 6 for measuring slip between

foam core and DHCC layer. After assessing the flexural performance of Slab 1 under different flexural load sequences, it was found that recording the provided bond between DHCC layer and foam core can be more interesting, compared the results obtained from uplift of DHCC layer. Thus, for Slab 2, it was decided to measure the horizontal slip between DHCC layer and foam cores instead of measuring uplift of DHCC layer at end of one side of slab.

For slab 2, LVDT 6 used to measure slide between DHCC layer and foam core (see Fig. 3.2c)

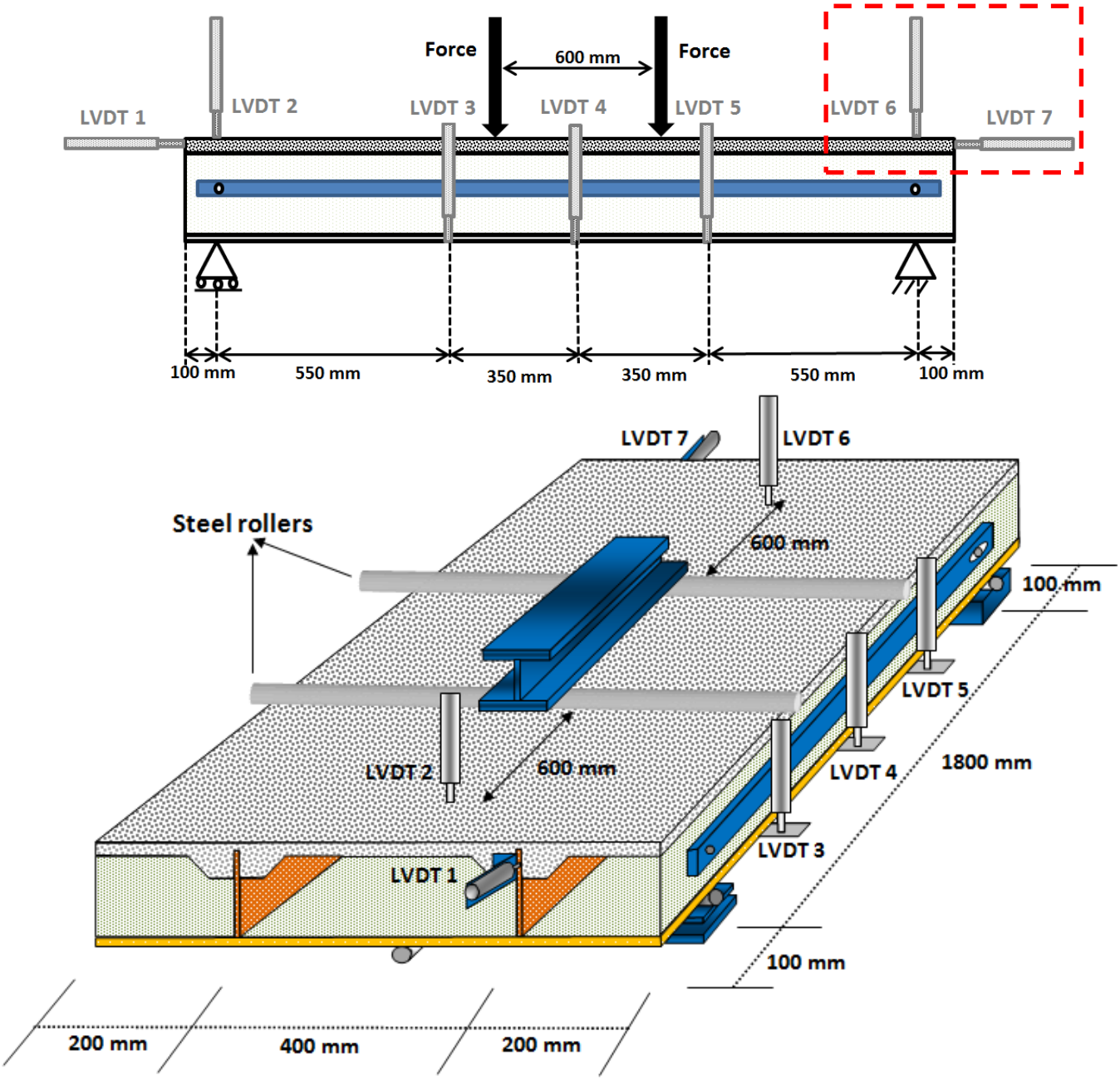

a)

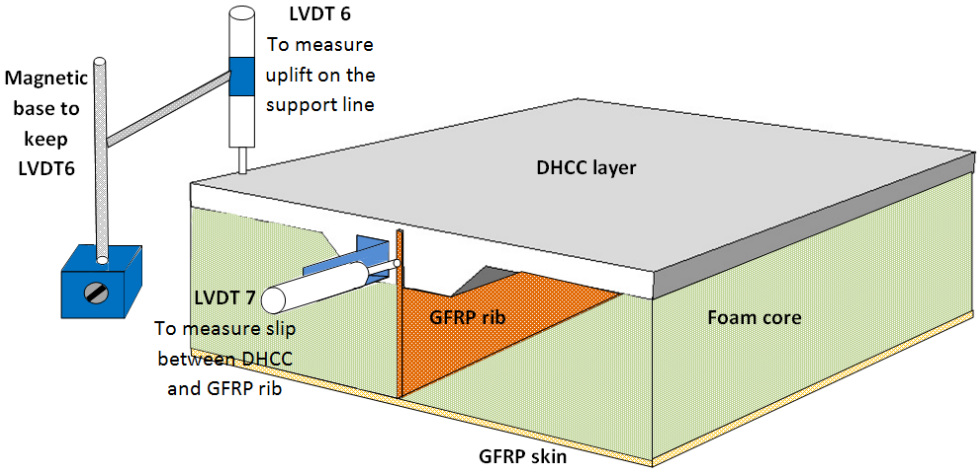

b)

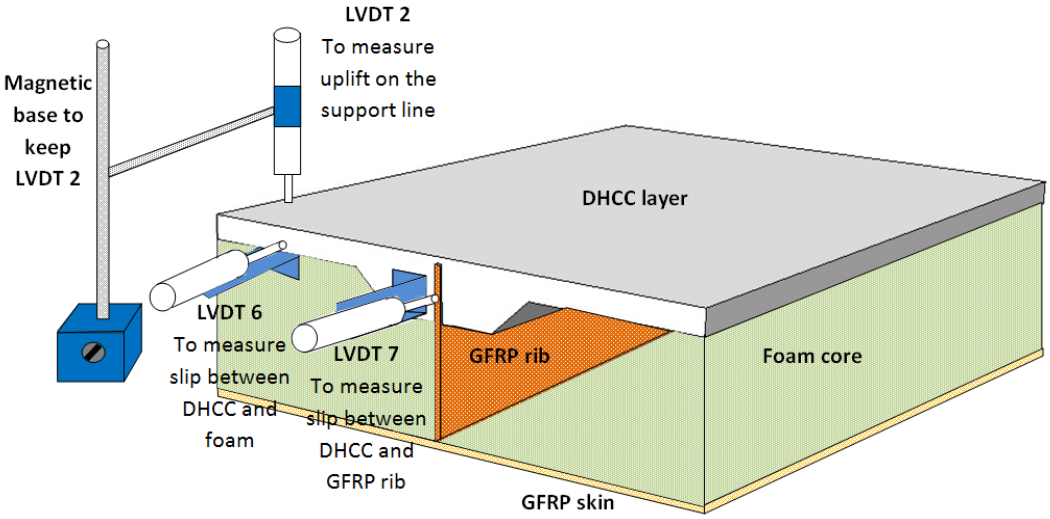

c)

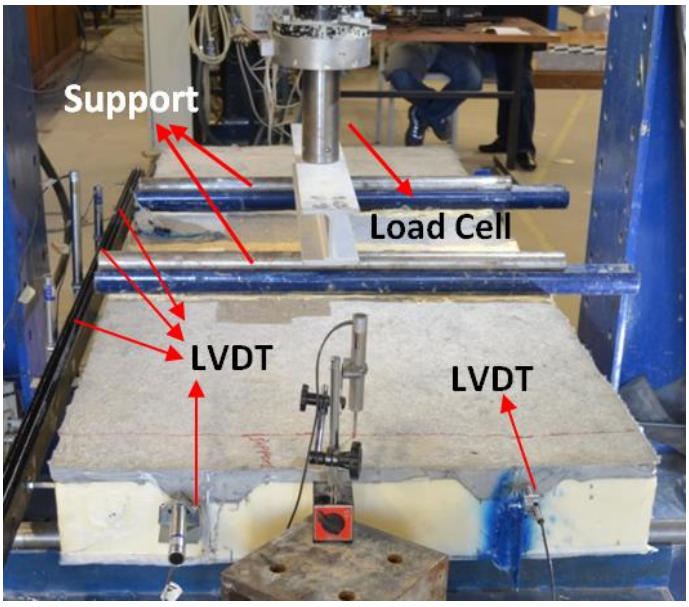

d)

Fig 3.2. a) LVDT's positions on the slab 1; b) 3D view of LVDTs 6 and 7 positions in Slab 1; c) 3D view of LVDTs 2, 6, and 7 positions in Slab 2; d) Test setup

As shown in Fig. 3.3, eight strain gauges (SG) were used in different positions of the slabs to measure strain values. Two SGs were installed in one side of the GFRP rib (SG1 and SG2) and two other SGs were installed on top of the GFRP skin layer (SG3 and SG4). The rest of the gauges were installed at the bottom of the GFRP skin: three of them for measuring strains in longitudinal direction of the slabs (SG5, SG6 and SG7) and the other one for measuring strain in transversal direction (SG8).

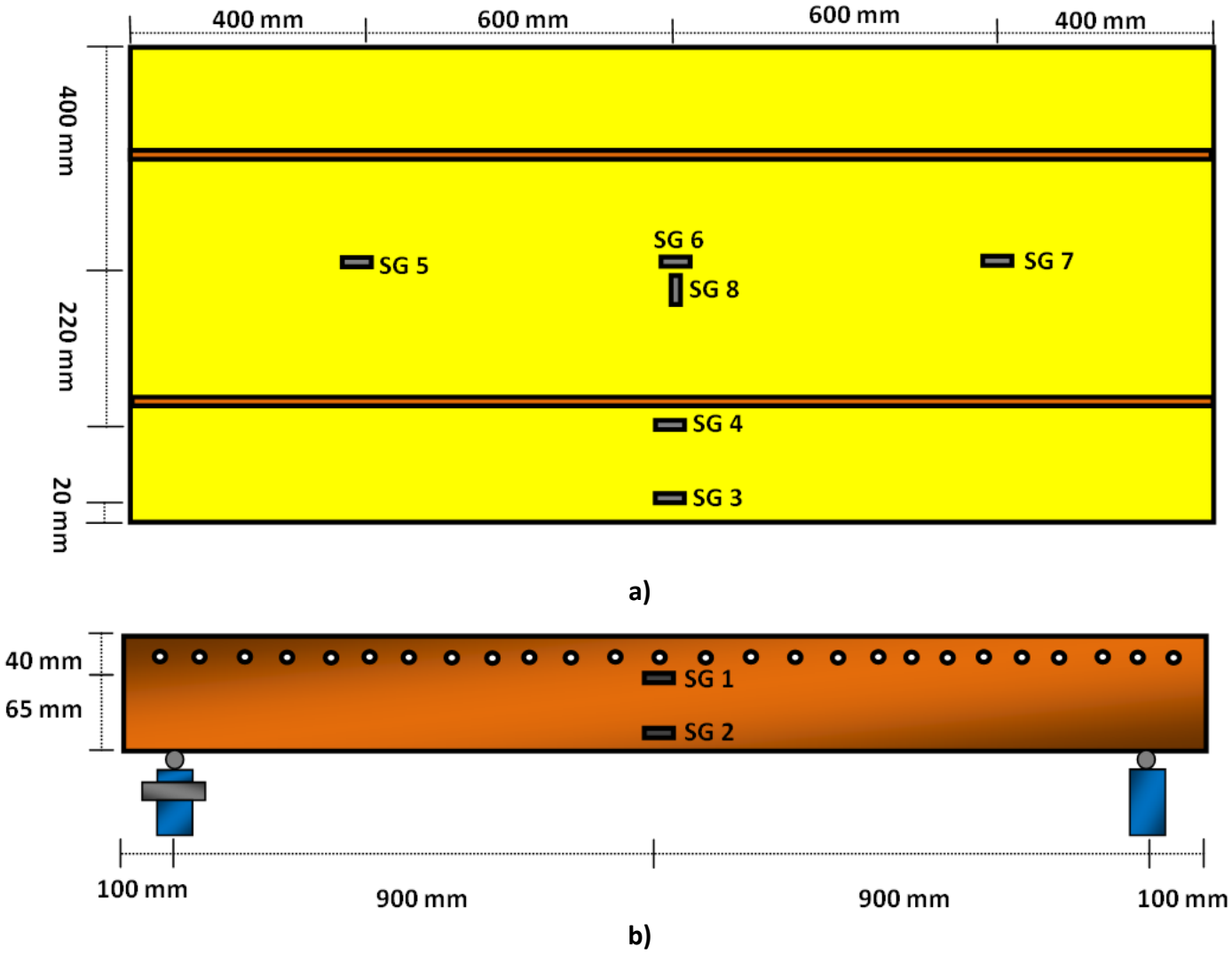

Fig 3.3. Positions of strain gauges (SG): a) on the GFRP skin from top view; b) GFRP rib (Slab 2) from lateral view

3.2.2. Results and discussion

The damages observed in the slabs due to the applied loadings are shown in Fig. 3.4. The failure of slabs involved the following sequence of damages:

1) Loss of contact between foam and DHCC layer with visible slip (Fig. 3.4a);

2) Damage in the GFRP ribs (Fig. 3.4b);

3) Loss of bond between the designed shear connectors in the GFRP ribs and the DHCC layer (Fig. 3.4c);

4) Splitting cracks formed on the surface of DHCC layer in the alignment of the GFRP ribs (Fig. 3.4d);

5) Crushing of foam cores around the applied load lines (Fig. 3.4e)..

a) Loss of connection between foam and DHCC layer with visible slip

b) Compressive failure in the GFRP rib

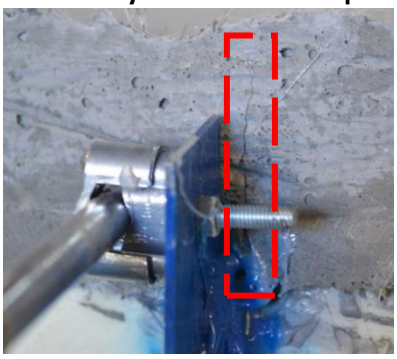

c) Crack formation in the connection zone between DHCC layer and GFRP rib

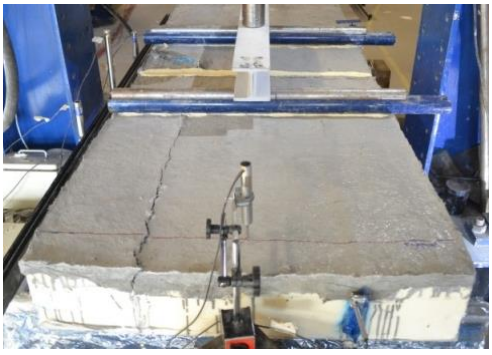

d) Splitting cracks formed on the surface of DHCC layer

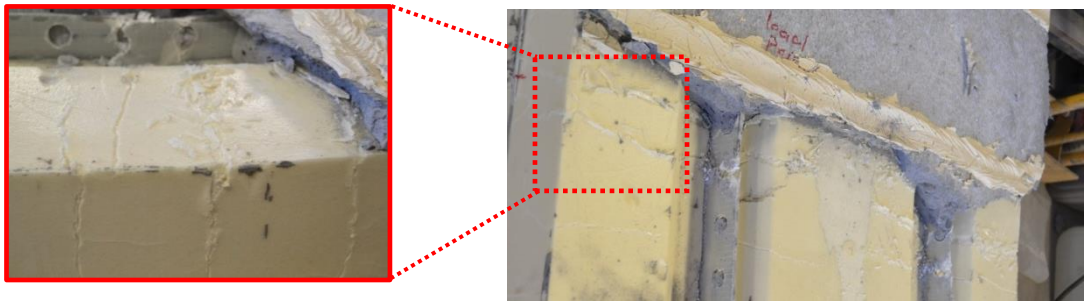

e) Crushing of foam core around load line

Fig 3.4. Sequences of damages observed in the proposed hybrid sandwich panels

The numerical results, which will be later discussed in Chapter 4, justify the sequences of the occurred damages in different positions of slabs.

According to Fig. 3.5, the GFRP skin layer did not experience severe damage, without signs of tensile rupture or loss of connection with the GFRP ribs. The present study

indicates that VARTM process is a very efficient method to produce the sandwich panel slabs, since it has assured the occurrence of several localized damages at different stages of the loading process, which has avoided an abrupt rupture to the developed slabs, assuring a pseudo hardening behavior for the slabs. For this functioning of the slabs, it has contributed the proper bond conditions between the constituent parts of the slab assured by this method.

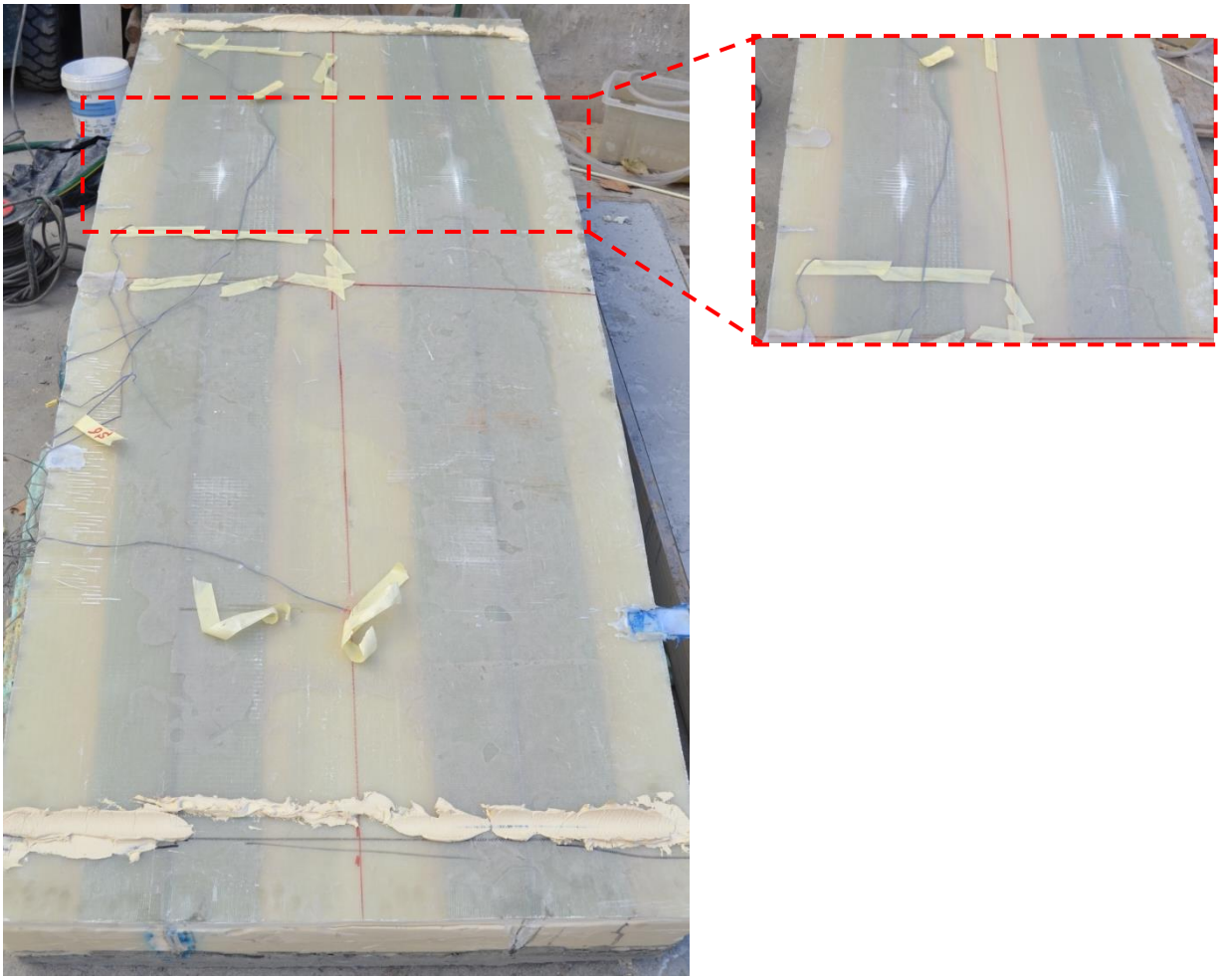

Fig 3.5. No signs of tensile rupture or loss of connection between GFRP skin the GFRP ribs

Fig. 3.6 shows the relation between the applied load and the deflection measured at the slabs' mid span through the various applied loading steps. In the first loading branch the Slab 1 has presented an almost linear force-deflection response up to 91.8 kN, when a deflection of 5.7 mm was registered (Point B in Fig. 3.6a). In spite of the first register of damage has been detected for a load level of about 70 kN (Point A in Fig. 3.6a), due to the loss of contact between foam and DHCC (Fig. 3.4b), the decrease of stiffness up to point B was almost imperceptible. At point B, the damage

level has progressed significantly, mainly due to excessive compressive strain in the GFRP ribs, the shear connection between these ribs and the DHCC layer has assured an increase of load with a larger increment of deflection (branch BC in Fig. 3.6a), and a load of 98.5 kN and a deflection of 11.1 mm were registered at Point C. By further increasing the deflection, the deterioration of the connection between the ribs and the DHCC layer has intensified, and a splitting crack started to be visible in the top surface of the DHCC layer along the alignment of the GFRP ribs (Fig. 3.4d). When the target deflection of 14.4 mm was attained in the first loading step, unloading followed by another loading cycle was applied up to this deflection limit with the same setup. As Slab 1 was damaged during the first cycle, in the second cycle the stiffness of the reloading branch was decreased, but the applied load value reached 84.3 kN, which corresponds to a decrease of 11.2% in comparison with the peak load (Point C in Fig. 3.6a). After performing the first loading step, the test setup was changed and configured for TPB test. In this load step, the damaged Slab 1 has supported 60 kN at 14.4 mm mid-span deflection.

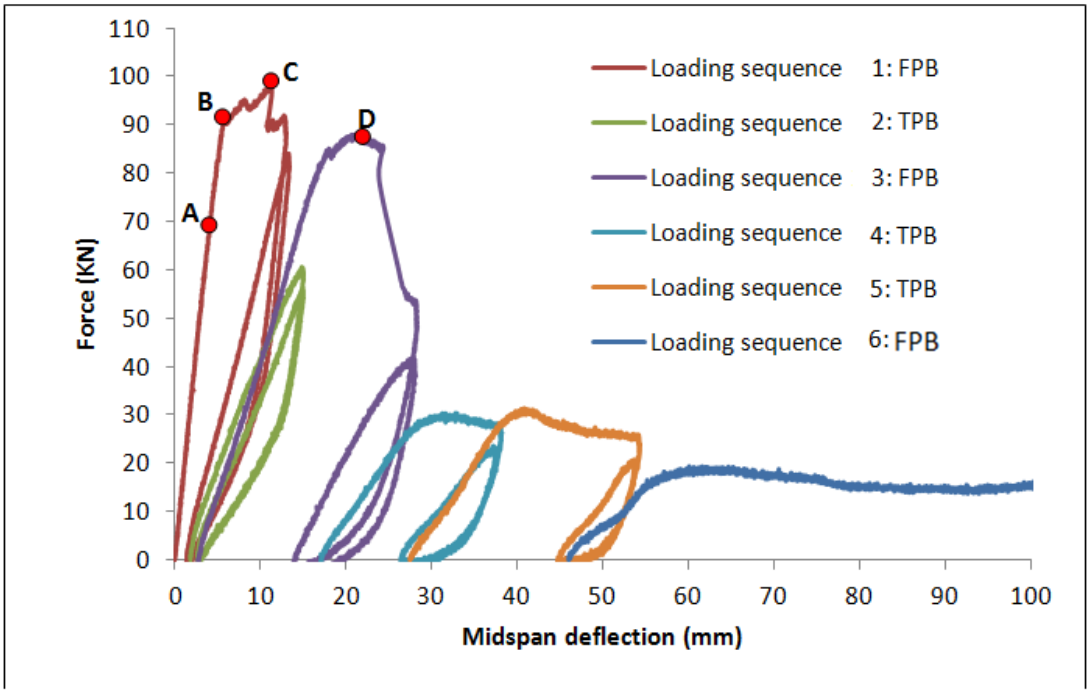

a)

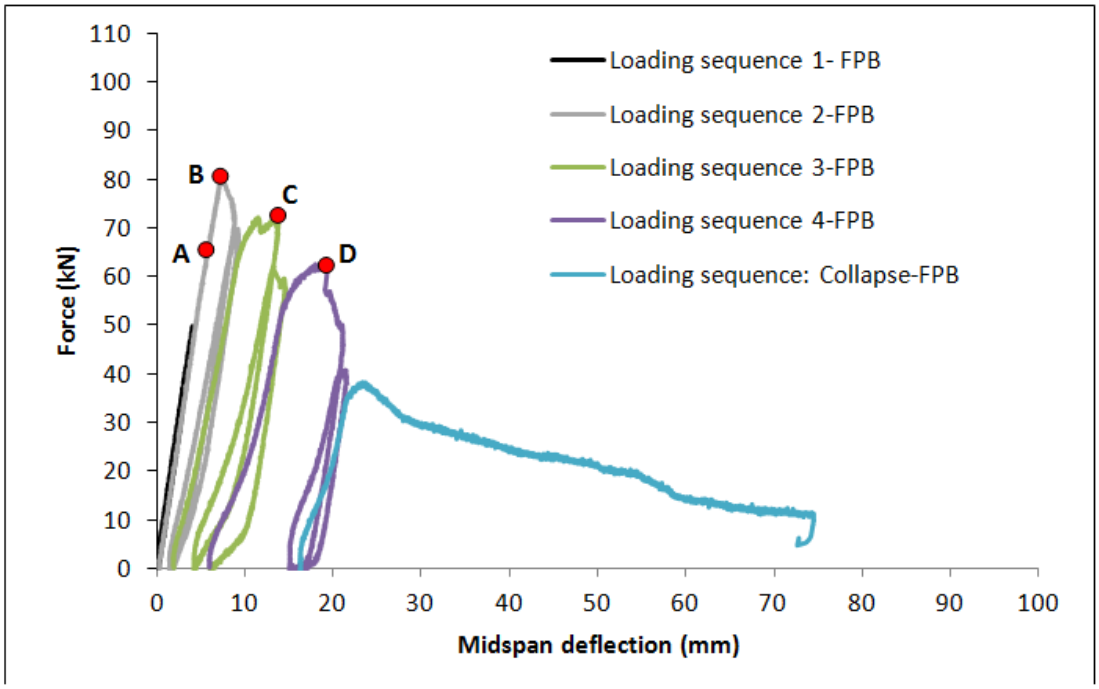

b)

Fig 3.6. Obtained results from the applied cyclic flexural loading in the: a) Slab 1; b) Slab 2

The third load step was carried out by conducting a FPB test. During this step, Slab 1 showed linear behavior for up to 17.8 mm mid-span deflection and 84.5 kN of applied force. The stiffness in this reloading phase was almost equal to the one registered in the previous load step. In the first cycle of the third load step, a hardening stage was observed above 17.8 mm of deflection, and a peak load of 87.4 kN for a deflection of 21.3 mm were recorded in the Point D (Fig. 3.6a). Above this deflection, the Slab 1 entered in a structural softening stage, and at the target deflection of this loading cycle (21.6 mm), this slab presented a load carrying capacity of 53.8 kN, which is 55% of the peak load. In the second cycle of this third loading sequence, the peak load has decreased 50% in comparison to the peak load of the first cycle of this loading sequence. Fig. 3.7a shows the measured slip between the DHCC layer and the GFRP ribs registered in the first cycle of the first loading sequence. It is observed that an abrupt increment of slip has occurred at a force/deflection corresponding to the end of the linear branch of the first loading cycle applied to the Slab 1. This indicates the stiffness and load carrying capacity of this slab is mainly governed by the GFRP ribs-DHCC layer connection. As already indicated, the sequence of local failures occurred during the loading process of the Slab 1 assured a gradual decrease of load carrying capacity after peak load, and an almost constant residual load carrying capacity of

about 14.5 kN was registered in the final stage of the last load sequence (between 90 and 100 mm, ≈L/20), which is 15% of the peak load.

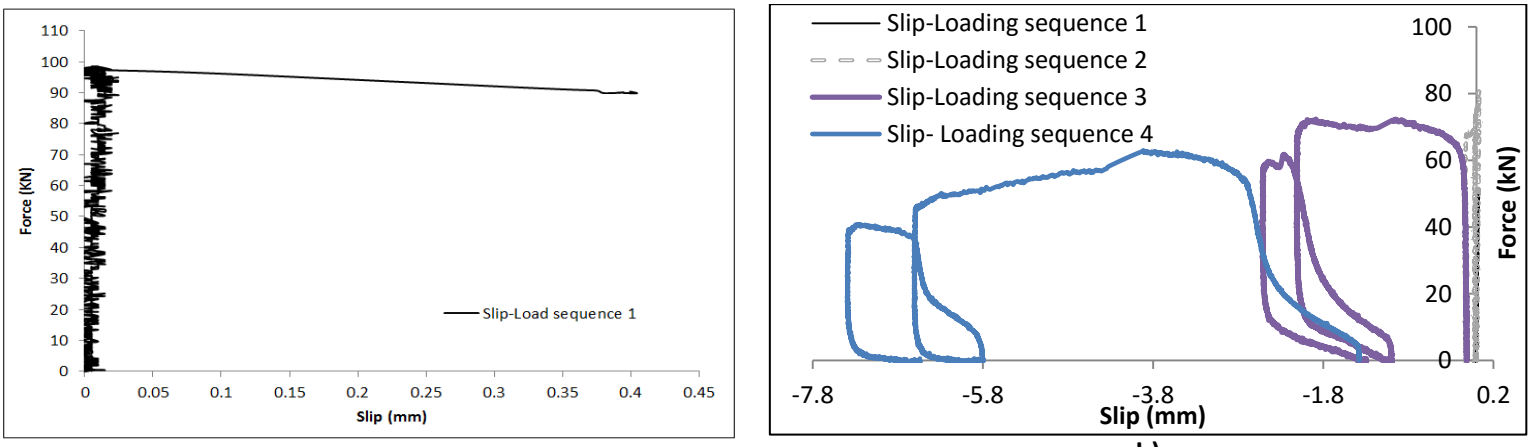

a) b)

Fig 3.7. Measured slip between GFRP rib and DHCC layer in: a) Slab 1 (LVDT 7 in Fig. 2b); b) Slab 2 (LVDT 7 in Fig. 3.2c)

As stated in the section 3.2.1., eight strain gauges were installed in the slabs to measure the variation of strains in relevant zones of the slabs. Fig. 3.8 illustrates the variation of strains during the loading process of the first and the sixth loading steps for Slab 1. According to the results, a maximum compressive strain of 0.0027 (see Fig. 3.8a) was recorded in the GFRP rib (SG1), while a maximum tensile strain of 0.0013 (see Fig. 3.8b) was registered in the GFRP skin (SG3). The tensile strains measured in the GFRP ribs and skins of Slab 1 were much lower than the ultimate strains recorded in the direct tensile tests carried out with specimens extracted from these components of the slab (see Table 2.4). In Slab 1, a compressive strain of 0.00023 (Point A in Fig. 3.8a) was registered in the GFRP rib (SG1) at load of 91.8 kN (Point B in Fig. 3.6a). During the deflection hardening stage of the slab 1 (BC in Fig. 3.6a) the compressive strain in the SG1 has increased significantly due to the deterioration of the shear connection between the ribs and the DHCC layer. The evolution of the strains in the other SGs was almost linear with the applied load, indicating that the damage is almost concentrated in the connection between ribs and DHCC layer.

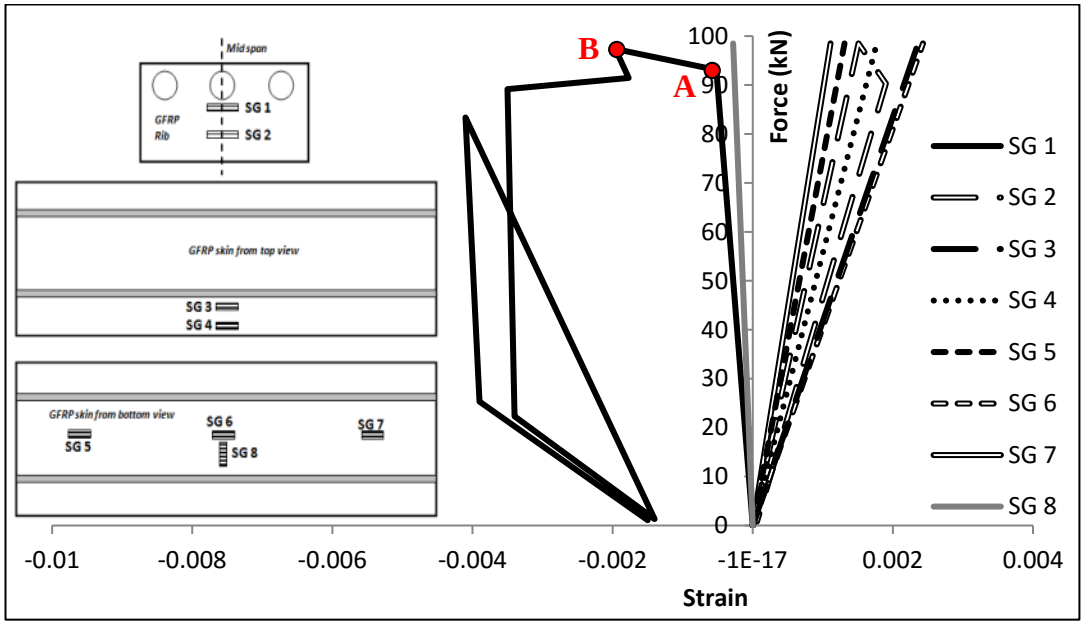
Mid span
GFRP Rib
SG 1
SG 2
GFRP skin from top view
SG 3
SG 4
GFRP skin from bottom view
SG 5
SG 6
SG 7
SG 8
B
A
Force (kN)
100
90
80
70
60
50
40
30
20
10
0
-0.01
-0.008
-0.006
-0.004
-0.002
-1E-17
0.002
0.004
Strain
SG 1
SG 2
SG 3
SG 4
SG 5
SG 6
SG 7
SG 8

a)

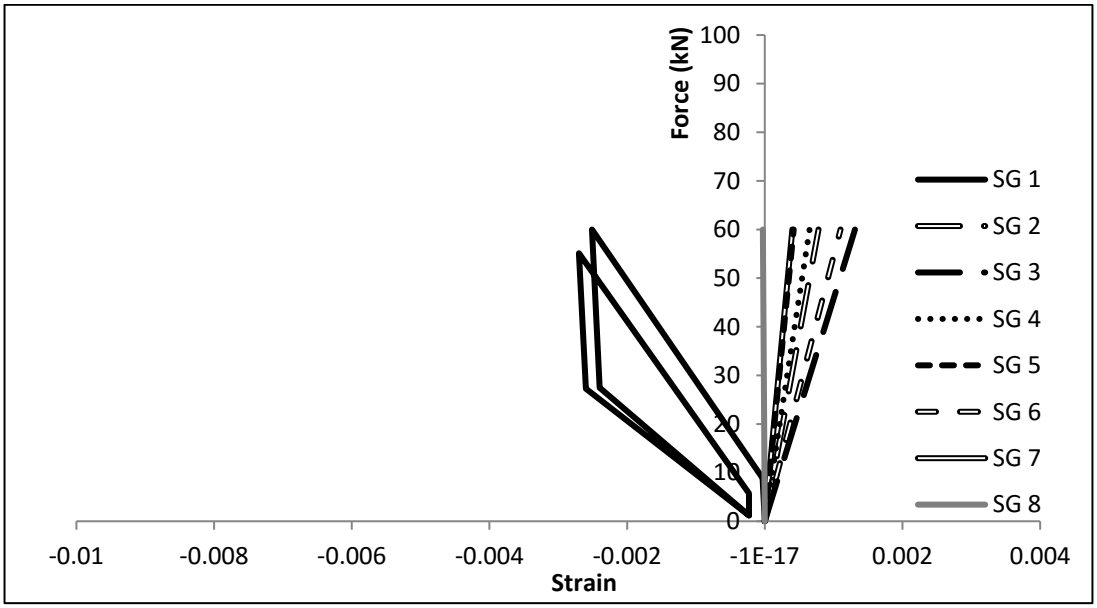
Force (kN)
100
90
80
70
60
50
40
30
20
10
0
-0.01
-0.008
-0.006
-0.004
-0.002
-1E-17
0.002
0.004
Strain
SG 1
SG 2
SG 3
SG 4
SG 5
SG 6
SG 7
SG 8

b)

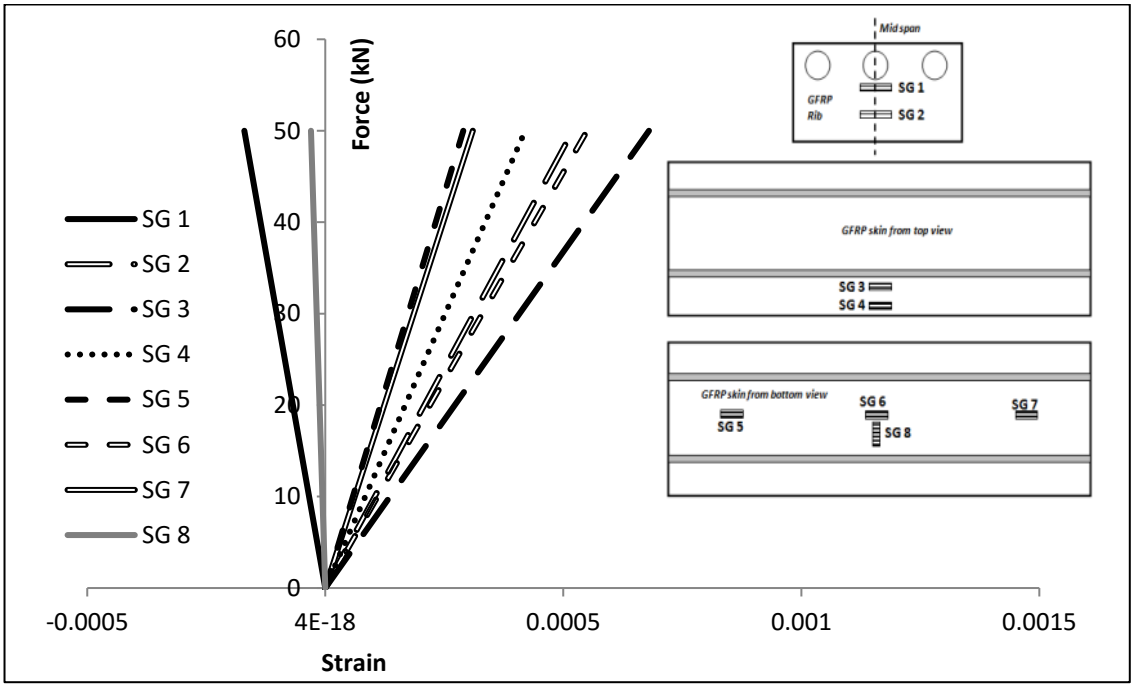
Force (kN)
60
50
40
30
20
10
0
-0.0005
4E-18
0.0005
0.001
0.0015
Strain
SG 1
SG 2
SG 3
SG 4
SG 5
SG 6
SG 7
SG 8
Mid span
GFRP Rib
SG 1
SG 2
GFRP skin from top view
SG 3
SG 4
GFRP skin from bottom view
SG 5
SG 6
SG 8
SG 7

c)

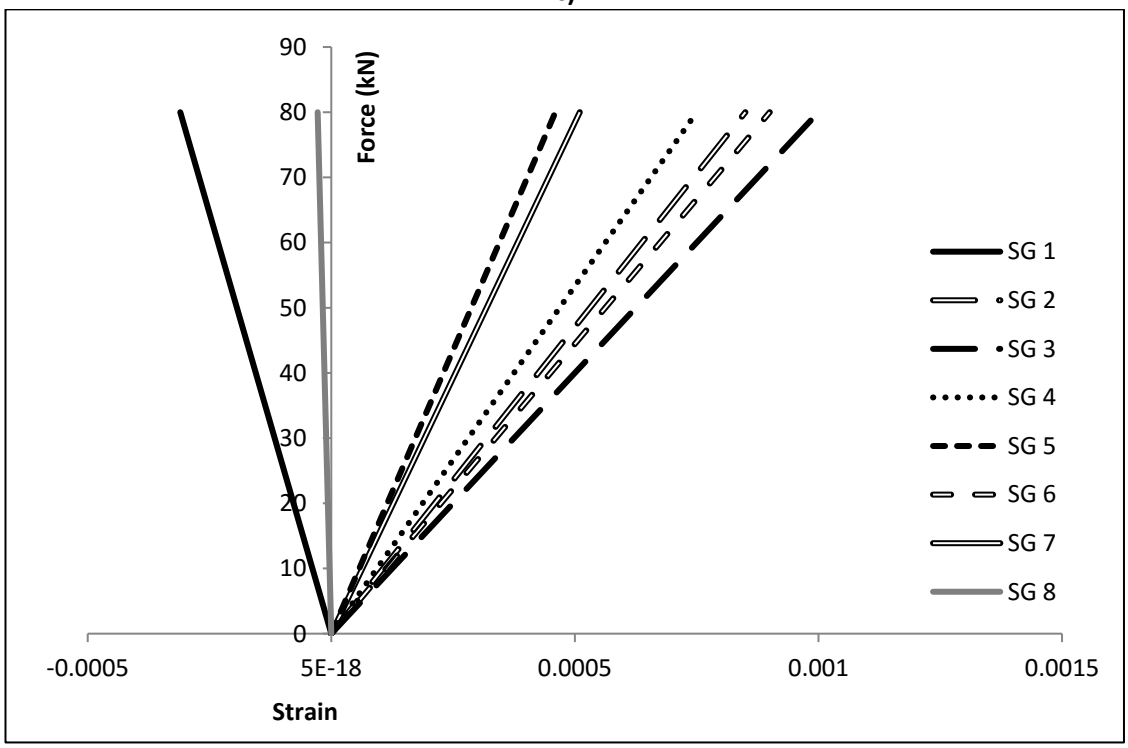
Force (kN)
90
80
70
60
50
40
30
20
10
0
-0.0005
5E-18
0.0005
0.001
0.0015
Strain
SG 1
SG 2
SG 3
SG 4
SG 5
SG 6
SG 7
SG 8

d)

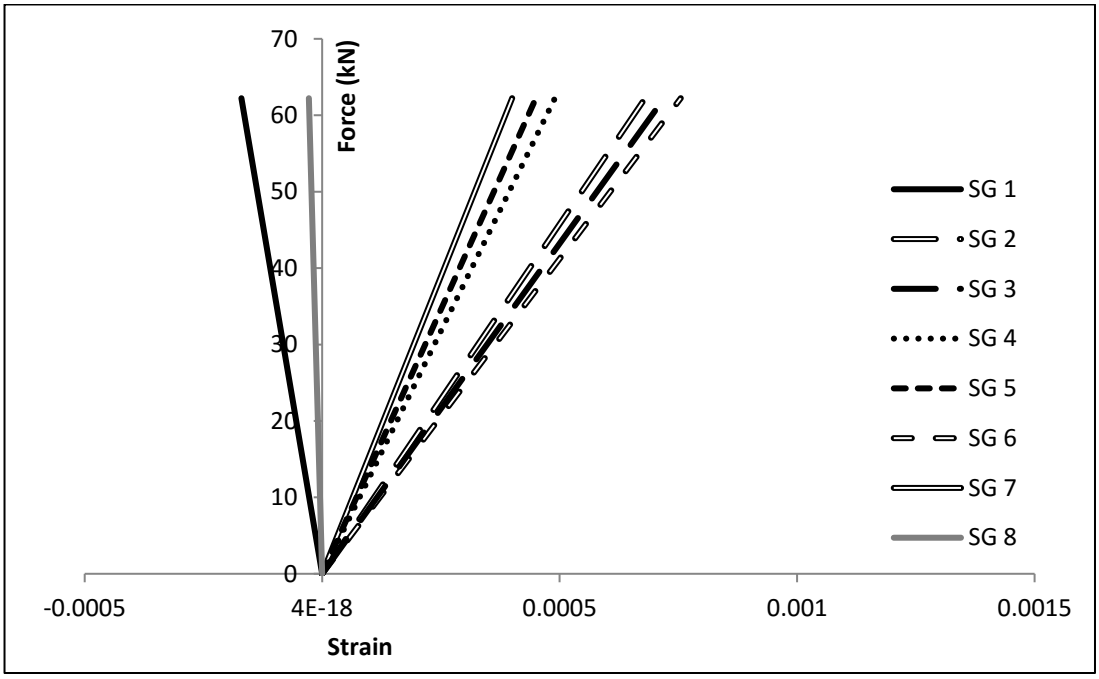

e)

Fig 3.8. Measured strains in: a) The first cycle of FPB test in the slab 1; b) The first cycle of TPB test in the slab 1; c) The first cycle of FPB test in the slab 2; d) The second cycle of FPB test in the slab 2; e) The fourth cycle of FPB test in the slab 2

The test setup of Slab 2 was prepared for a FPB test based on the loading sequence described in Table 3.1. The tests were displacement controlled by using the LVDT included in the servo-actuator for this purpose, and following the loading steps specified in Table 3.1. The relationship between the load versus slip between the DHCC layer and the GFRP ribs is depicted in Fig. 3.7b.

According to the results presented in Fig. 3.6b, the Slab 2 presented a linear-elastic behavior during the first loading step, and no slip between GFRP ribs and DHCC layer was registered (Fig. 3.7b). The results shown in Fig. 3.6b are based on external LVDTs. According to the loading sequence defined for Slab 2, mid-span deflection was set to 7.2 mm during the first loading step using internal LDVT of the servo-actuator, but the results illustrated in Fig. 3.6b shows 4.3 mm measured with the external LDVT. Furthermore, in the second loading step 10.5 mm was applied to Slab 2 using internal LVDT, while the corresponding external LDVT measured 7.2 mm deflection at mid-span.

In the first load sequence, Slab 2 presented a linear behavior up to the target deflection of 3.6 mm ($\delta/2$, where $\delta=L/250$, with L=1800mm) without observing any damage. The maximum force registered at mid-span deflection of 3.6 mm was 49 kN.

As Slab 2 did not experience any damage during this first load sequence, in the second sequence the stiffness of the slab's response was almost unaltered up to 80.5 kN (Point B in Fig. 3.6b), at which compressive damage has occurred in the GFRP ribs (Fig 3.4b). It is worth mentioning that the compressive damage in GFRP ribs did not occur under the loaded section. Like in the Slab 1 the loss of contact between DHCC layer and foam was also observed in Slab 1 before peak load (Point A in Fig. 3.6b, at a load of 65 kN), but this had no significant impact in terms of loss of stiffness for the slab. Due to the damage at the ribs/DHCC connection, the slab entered in a structural softening stage immediately before the second cycle of this second load sequence, and the stiffness of this load cycle was not too different from the previous one, with a maximum load of 72.2 kN. The stiffness in the first loading branch of the third load sequence was almost equal to the one registered in the previous load step. At a load level corresponding to the maximum load registered in the previous load cycle, a pronounced nonlinear behavior has occurred due to the propagation of damage in that region up to the load level of 72.2 kN (point C), which corresponds to a decrease of about 9% in terms of load carrying capacity in comparison to point B. This was well captured in Fig. 3.7b where an abrupt slip was recorded at this loading stage (from 0.15 mm at 60.5 kN to 1.98 mm at 72.2 kN). In the second cycle of this load sequence, for the target deflection, the maximum load was limited to 60.8 kN. In the first loading branch of the fourth load sequence the stiffness evolution was similar to the one occurred in the previous cycle up to the peak load in this cycle, followed by a pronounced nonlinear response up to the peak load (point D). Like at the end of the first load cycle of the previous load sequence, an abrupt increase of slip (Fig. 3.7b) has occurred during the nonlinear stage of the first load cycle of the fourth load sequence (from 2.7 mm at 49.4 kN to 3.9 mm at 62.3 kN). In the second cycle of this load sequence, for the target deflection, the maximum load was limited to 40.7 kN. In the last load sequence, composed of a monotonically increasing deflection, the load carrying capacity of the slab was decreased smoothly. From the first to the second cycle the ultimate load has decreased 14.2%, 15.8%, and 17.9% in the 2nd, 3rd and 4th load sequence, respectively.

The slab's load carrying capacity at the ultimate deflection (about 75 mm, ≈L/24) was approximately 11.4 kN, which is about 14% of the peak load. The stiffness of the

unloading/reloading for the loading sequences have smoothly decreased during the loading process of the slab, indicating that the linear-elastic nature of the GFRP components of the slab has a mandatory influence on the global behavior of the slab. Additionally, the relatively high permanent residual deflection at completed unloading stage of the slab is mainly caused by the damage propagation in the connection between GFRP ribs and DHCC layer.

The strains recorded in the SG installed in the Slab 2 are shown Fig. 3.8 for the first, second and the fourth loading sequences. According to the results, a maximum compressive strain of 0.00088 was recorded in the GFRP ribs (SG1) (see Fig. 3.8c), and a maximum tensile strain of 0.001 was measured in the GFRP skin (SG3) (see Fig. 3.8d). At peak load (80.5 kN, Point B in Fig. 3.6b), a maximum compressive strain of 0.0003 was registered in the SG1, while the maximum tensile strain was 0.001 in the SG3. Therefore, it can be concluded that the maximum tensile strains measured in the GFRP ribs and skins of Slab 2 were much lower than the ultimate strains recorded in the direct tensile tests executed in specimens extracted from these GFRP elements (see Table 2.4). The differences in the flexural performances of Slab 1 and Slab 2 may be justified by differences in the height and thickness of slab's components.

By evaluating the flexural stiffness, EI, of slab 1 and 2 in their elastic stage (1790 kN.m^2 in Slab 1 and 1160 kN.m^2 in Slab 2), and assuming for mid-span deflection the values corresponding to the initiation of damaged in the tested slabs (5.5 mm in Slab 1 and 7.2 mm in Slab 2), the developed slab system can be used for a simply supported slab of span length of about 5 m and supporting a live load of 1.5 kN/m^2 (the one recommended by EuroCode1 for residential buildings [5]) by applying the following equation under FPB test:

$$\Delta = \frac{(23PL^3)}{(648EI)_{Total}} + (\frac{PL}{3KGA})_{Rib} \qquad (3.1)$$

where, P is the applied load, L is the slab's span, EI is the flexural stiffness, G_{rib} is the shear modulus of the GFRP ribs, and A is the cross section of the ribs. In this study, the shear modulus value (of the GFRP ribs) adopted was 8 GPa [6]. In Table 3.2., the experimental results are summarized and listed.

Table 3.2. Summarized experimental results for Slab 1 and Slab 2

	$(EI)_{Exp}$ (kN.m^2)	F_{max} (kN)	δ_{max} (mm)
Slab 1	1790	98.50	11.11
Slab 2	1160	80.58	7.34

3.3. TPB tests on DHCC-GFRP sandwich panels – Phase 2

To reveal the flexural performance of hybrid sandwich panels under concentrated load, two hybrid sandwich panels with length of 1 meter were manufactured and tested under Three Point Bending test (TPB). The main aim in this section was to assess the structural performance of shear connectors under flexural loading by reducing the shear span to height ratio of the slab. Therefore, the slabs' span was reduced from 1.8 m to 0.8 m. The experimental results were interpreted in terms of force-deflection response, force-slip response between DHCC layer and GFRP ribs and observed damages. Details about test setup, used instrumentations for measuring horizontal and vertical displacements in different parts of slabs, and results recorded are presented in the following.

3.3.1. Test setup and instrumentation

Two tested slabs loaded under flexural TPB loading in order to assess their flexural performance. Seven Linear Variable Differential Transformers (LVDTs) used to measure deflections in various positions of the two slabs that are indicated in Fig. 3.9. Three LVDTs used to record vertical deflections (LVDT 2, LVDT 3, and LVDT 4), one LVDT employed to measure vertical displacements at one side support (LVDT 5), and three LVDTs used to register sliding between foam, GFRP rib and DHCC layer. LVDT 1 and LVDT 7 applied to measure sliding between DHCC layer and GFRP rib and also LVDT 6 used to record sliding between foam core and DHCC layer. Additionally, four strain gauges installed in each slab where three strain gauges were positioned in the bottom skin and one was positioned in the rib. The GFRP ribs and skin were instrumented with strain gauges, type BFLA-5-5, from TML with a 5 mm measuring length. The strain gauge were installed in GFRP ribs (SG 4), where shear stress has its maximum value. The details of strain gauge positions are illustrated in Fig. 3.10. Both Slab 1 and Slab 2

were assessed under monotonic flexural loading with a displacement rate of 30 µm/sec.

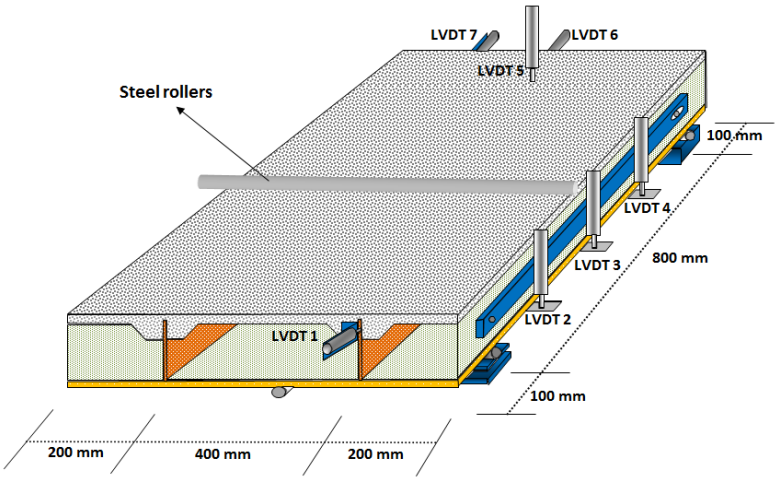

Fig 3.9. Instrumentations for measuring displacements and test setup

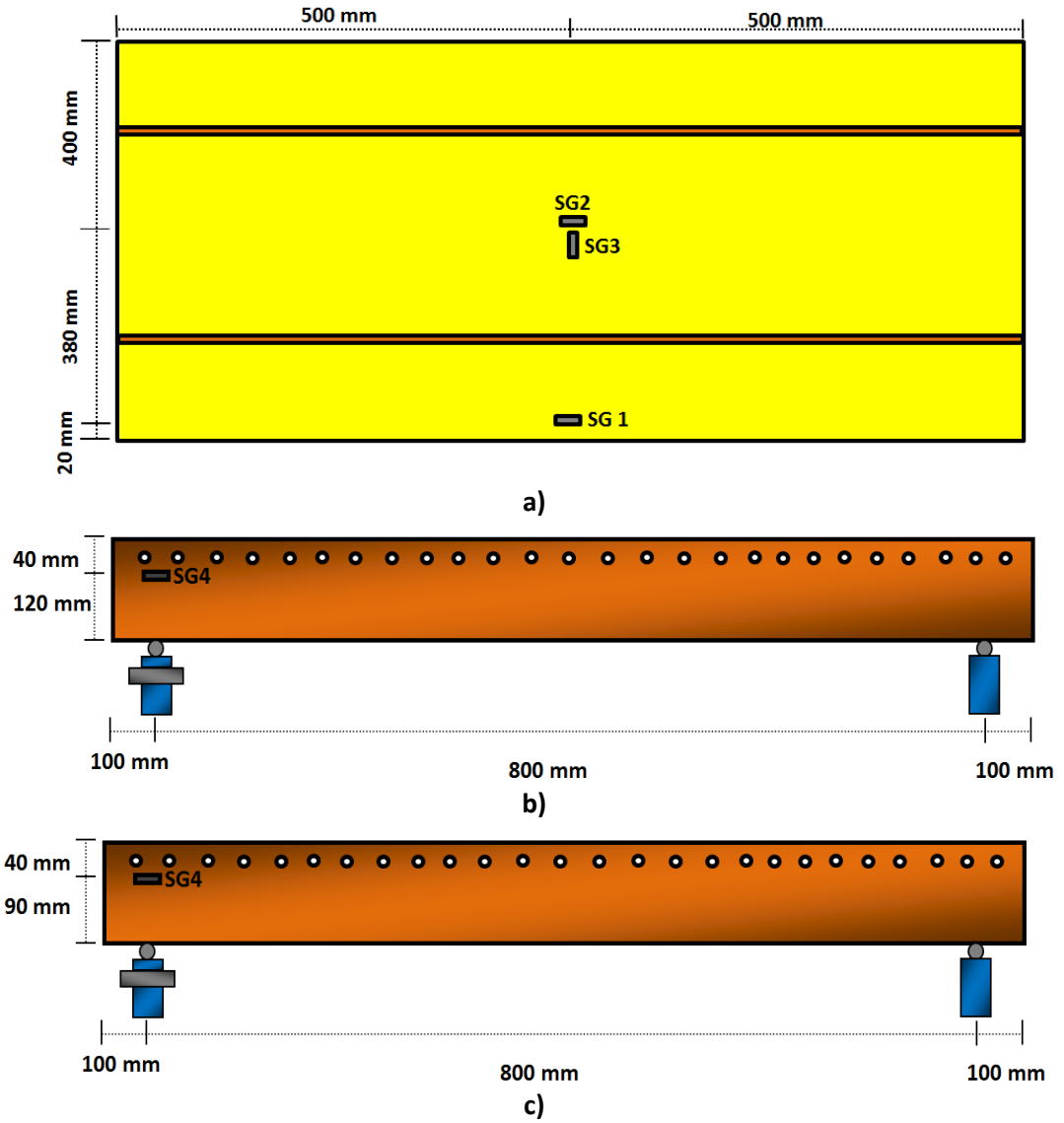

Fig 3.1. Placement of strain gauges in the hybrid sandwich panels: a) GFRP skin; b) GFRP rib in Slab 1; c) GFRP rib in Slab 2

3.3.2. Results and discussion

The flexural assessment was implemented on the proposed hybrid sandwich panels by utilizing TPB test and the recorded force-deflection responses are indicated in Fig. 3.11.

In Slab 1, the load is linearly increased up to 62.87 kN at 0.601 mm mid-span deflection. In this point, damage has occurred in the GFRP ribs (Point A in Fig. 3.11 and damage in Fig. 3.14a). Despite occurring compressive damage in GFRP ribs, load carrying capacity increased due to imposed larger increment of deflections. It is postulated that the flexural hardening behavior of Slab 1 is governed by two main reasons: 1) Using ultra-high ductility mortar as top skin, which have high potential to increase ductility of slabs under flexural loading; 2) Good performance of designed shear connectors. After occurring damage in GFRP ribs, the transfer of shear stresses continued through shear connectors while the occurrence of damage did not interrupt shear stress transferring. Due to deflection hardening behavior in Slab 1, the load carrying capacity increased about 40% and recorded 86.39 kN at 2.29 mm mid-span deflection. With respect to the criterion defined for ductility in equation 2.1, combination of the proposed GFRP shear connectors in the ribs and utilizing high ductile mortar results in measuring the ductility about 4 in Slab 1. It is worth stating that before reaching the load of 62.87 kN, foam cores and DHCC layer detached (Point C in Fig. 3.11 and damage in Fig. 3.14a). Concerning the results obtained, detachment between foam and DHCC layer has no significant effects on shear stress transferring because load was linearly increased and no damage effects observed on the recorded results.

In Slab 2, the applied load was linearly increased up to 62.08 kN at mid-span deflection 1.04 mm. At this deflection, GFRP ribs damaged due to exceed compression stress from compression strength (Point B in Fig. 3.11 and see Fig. 3.14a). Despite forming damages to GFRP ribs, in Slab 2 a similar flexural behavior like Slab 1 observed due to applied above deflection. The load carrying capacity of Slab 2 increased about 25% and recorded 78.07 kN at 3.41 mm mid-span deflection. Furthermore, the ductility in Slab 2 obtained about 3.5. One the main advantages of the proposed hybrid sandwich panels

is unlike typical sandwich panels, forming one damage does not lead to stop increasing trend of load.

The measured slip between DHCC layer and GFRP ribs is indicated in Fig. 3.12. The efficiency of the designed shear connectors in GFRP ribs can be obviously observed in Fig. 3.12. The shear stresses transferred from top DHCC layer to bottom GFRP skin up to force of 86.39 kN and 78.07 kN for Slab 1 and Slab 2, respectively. Providing high stiffness between DHCC layer and GFRP ribs by using the designed simply perforated shear connectors beside the flexural properties of DHCC material resulted in observing deflection flexural hardening behavior in both hybrid slabs.

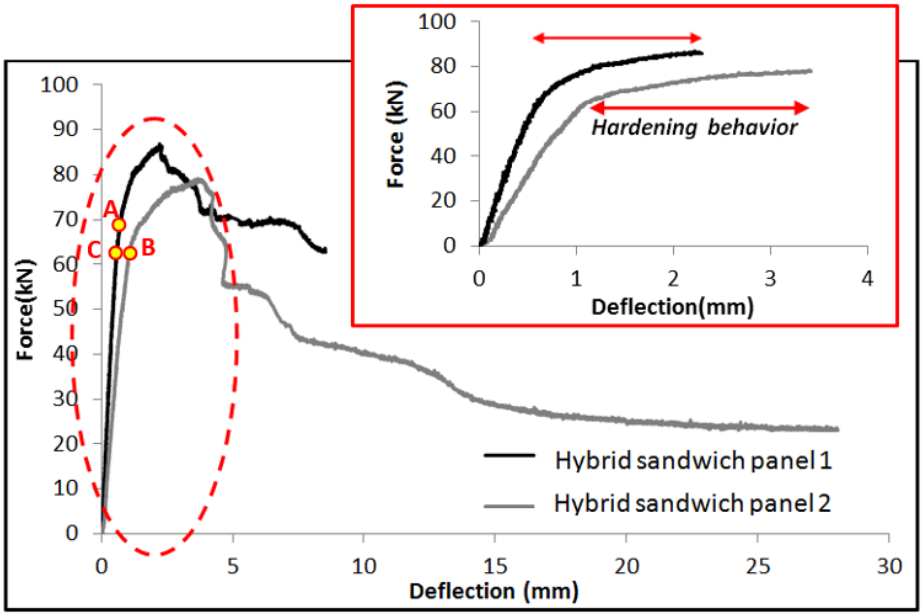

Fig 3.2. Force-deflection responses of hybrid sandwich panels

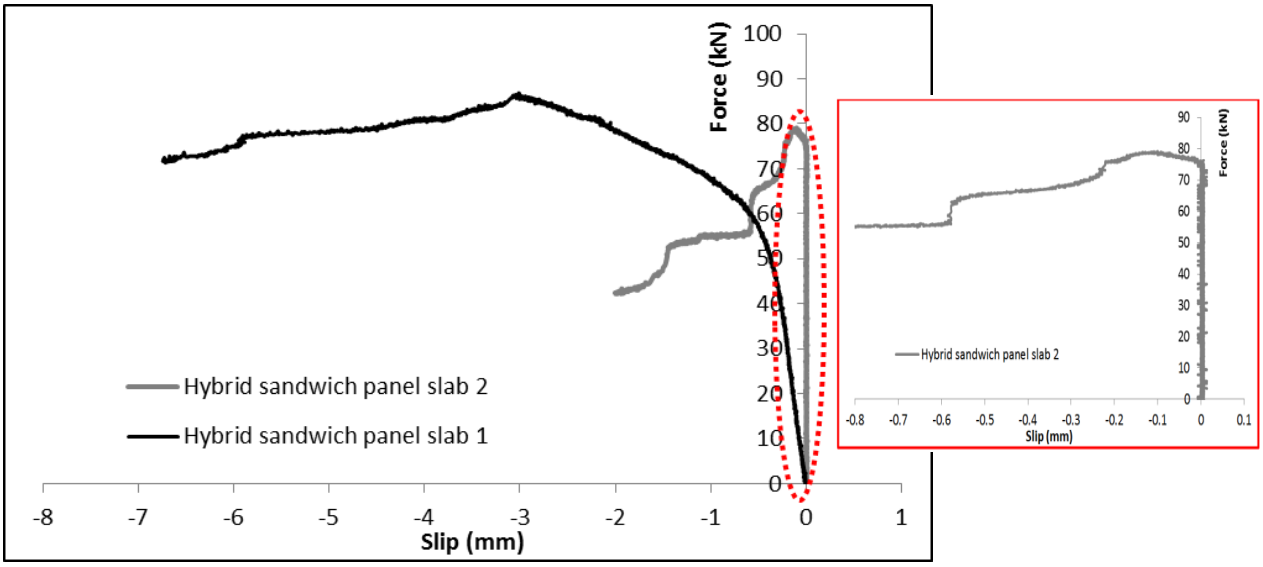

Fig 3.3. Force-slip between GFRP rib and DHCC layer

Fig. 3.13 shows the recorded strains for both Slab 1 and Slab 2. The maximum and minimum measured tensile strains in Slab 1 are assigned to SG 2 and SG 1 with strains 0.00098 and 0.0001, respectively. The recorded strain values in SG 1 indicated compressive strains when Slab 2 had linear behavior, while forming compressive damage in GFRP ribs resulted in changing strains of SG 1 from compression to tension. In this regard, the maximum and minimum tensile strains are assigned to SG 1 and SG 4 with strains 0.001317 and 0.000486, respectively. The measured strains in both slabs are much lower than achieved ultimate strains in Table 2.4.

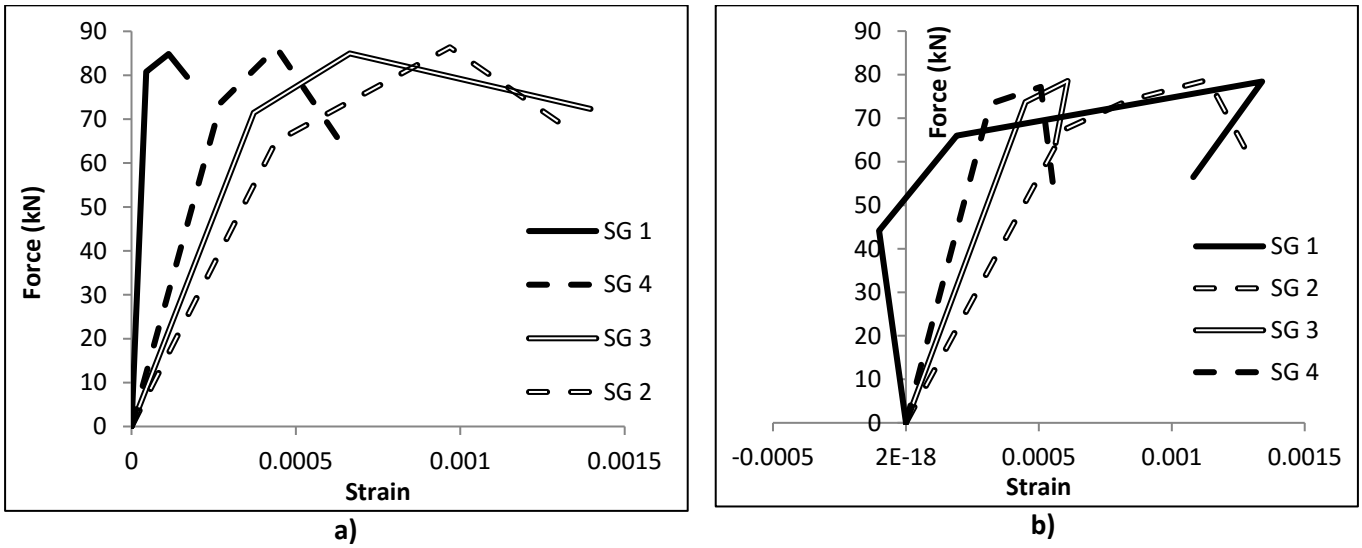

Fig 3.13. Measured strain values in: a) Slab 1; b) Slab 2

Slab 1 and Slab 2 were assessed under flexural loading by implementing TPB test and five damages occurred in the slabs, which are included:

1) Loss connection between DHCC layer and foam cores (see Fig. 3.14a);

2) Damage in the GFRP ribs due to compressive stress (see Fig. 3.14b);

3) Sliding between DHCC layer and GFRP ribs due to lose bond (see Fig. 3.14c);

4) Splitting cracks formed on the surface of DHCC layer in the alignment of the GFRP ribs (see Fig. 3.14d);

5) Crushing of foam cores around the applied load lines (see Fig. 3.14e).

a) Loss connection between DHCC layer and foam cores

b) Compressive damage in the GFRP ribs

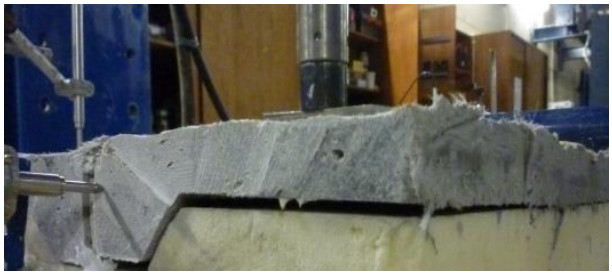

c) Slip between DHCC layer and GFRP ribs

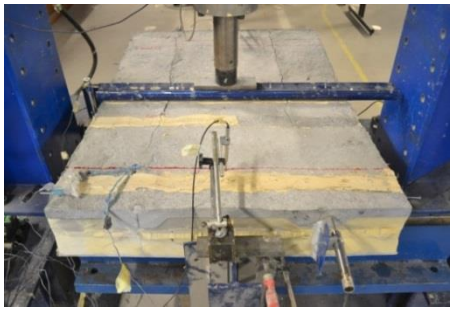

d) Splitting cracks alignment of the GFRP ribs

e) Crushing of foam cores

Fig 3.14. Recorded subsequences of observed damages during implementation of TPB test on hybrid slabs

3.4. Connection of hybrid slabs to the masonry walls

Frequently, in building rehabilitation, the vertical supporting elements correspond to relatively thick masonry walls. In such cases, the general solution for the slab-to-wall connections is based on steel angles anchor bolted to the masonry walls. These supports must be capable of mobilizing enough strength in the masonry walls to withstand the necessary vertical support reactions. The supporting solution should also guarantee an effective load transfer and capable of being easily installed. The proposed solution is represented in Fig. 3.15. The steel angle is previously connected to the masonry wall using anchoring systems that are commercially available. Afterwards, a steel plate and an elastomeric layer are installed on the top part of the

steel profile in order to minimize the bending moment transferred from the sandwich slab to the masonry wall. Steel bolts are inserted in the top part of the steel profile, in order to assure proper medium for the transference of the resultant stresses from the sandwich slab to the steel profile. These bolts are fixed to the bottom GFRP skin of the panel by interposing a steel plate for avoiding the occurrence of local damages in the GFRP skin. To avoid any type of local failure around this steel bolt, a foam strip at the extremities of the sandwich panel is replaced by DHCC.

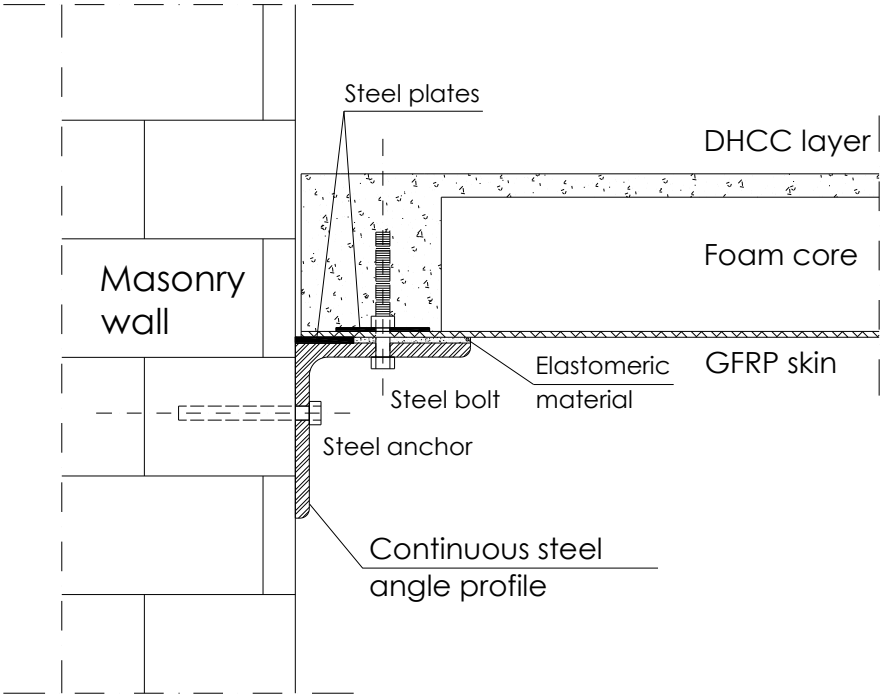

Fig 3.15. Hybrid slab-to-wall connection

3.5. Conclusions

Two slabs based on a new hybrid sandwich concept were built and experimentally tested. The type of materials and their disposition were conveniently developed and arranged for obtaining a slab system suitable for rehabilitation of the old buildings. For assuring a lightweight slab with a convenient compromise of strength and ductility, this hybrid sandwich panel is formed by a top compressive layer of deflection hardening cement composite (DHCC), ribs and bottom skin in glass fiber reinforced polymer (GFRP) laminate, and a core foam with insulation requisites. The flexural performance of the proposed hybrid sandwich slabs was assessed by executing

experimental cyclic tests, and from the results the following relevant observations can be pointed out:

1) Both slabs have presented an almost linear force versus mid-span response up to pick load, followed by a smooth load carrying degradation in the structural softening, which is justified by the predominance of the linear behavior of the GFRP systems;

2) Up to the deflection corresponding to serviceability limit state (L/250), no relevant damages were observed;

3) The nonlinearities observed in the response of the tested slabs are mainly caused by the damage occurred in the GFRP ribs-DHCC connection, and the splitting cracks formed in the DHCC in the alignment of the GFRP ribs;

4) The stiffness degradation in load cycles of a loading sequence, as well as between consecutive loading sequences was relatively small, resulting instantaneous permanent deflections at unloading stages that are relatively high, which is caused by the continuous damage at the GFRP ribs-DHCC connection;

5) The maximum strain levels in the GFRP components were much lower than the ultimate strain determined on the tensile tests carried out with coupons of these composites;

References

[1]. Sharaf T., Fam A., 2010, “Flexural performance of sandwich panels comprising polyurethane core and GFRP skins and ribs of various configurations”, Composite Structures, Vol. 92, pp. 2927-2935.

[2]. Mastali M., Valente I.B., Barros A.O. Joaquim, “New composite slab system for structural rehabilitation of traditional buildings”, 11th International symposium on fiber reinforced polymers for reinforced concrete structures (FRPRCS-11), 2013, Guimaraes, Portugal.

[3]. Lameiras R., Barros A.O. Joaquim, Valente I.B., Azenha M., 2013, “Development of sandwich panels combining fiber reinforced concrete layers and fiber reinforced polymer connectors. Part I: Conception and pull-out tests”, Composite Structures, Vol. 105, pp: 446-459.

[4]. Link address: http://www.rdpe.com/ex/index.htm

[5]. Eurocode 1: Actions on structures – Part 1-1: General actions - Densities, self-weight, imposed loads for buildings, [Authority: The European Union Per Regulation 305/2011, Directive 98/34/EC, Directive 2004/18/EC].

[6]. Selcom multiaxial technology company, Biaxial products. http://www.multiaxialfabricselcom.com/en/Products/

Chapter 4

Numerical simulations and analytical studies of the flexural behavior of hybrid slabs

4.1. Introduction

Sandwich panels are lightweight construction systems of high strength-to-weight ratio. A typical sandwich panel consists of a low-density core material with two thin outer faces. The skins have a relatively high stiffness and tensile strength for assuring the flexural load carrying capacity, while the low-density core material provides appropriate thermal insulating properties and might offer some shear resistance. The structural behavior of a sandwich panel strongly depends on the geometry, arrangement and properties of its components. Numerous experimental and numerical studies have been developed during the last decade for assessing and enhancing the structural behavior of sandwich panel systems.

Ziad *et al.* worked on the experimental and numerical analysis of an innovative Glass Fiber Reinforced Polymer (GFRP) sandwich floor panel submitted to a concentrated load [1]. The proposed sandwich panel was developed to be used as a slab system, comprising a modified phenolic core in-between top and bottom skins made by bi-axial E-CR glass fibers at $0^0/90^0$orientation angles. This study presented the results of the experimental behavior and the nonlinear finite element analysis of the GFRP sandwich panel. The behavior of the GFRP sandwich panel, skin–core interaction and core of GFRP sandwich panel were investigated experimentally [1]. From the obtained results, it was verified that the failure of the modified phenolic core has occurred without the detachment of the skin-core interface, which means that the skin–core interaction did not have significant effect on the failure behavior. Moreover, material nonlinear analysis using Finite Element Method (FEM) was carried out to simulate the experimental test on a GFRP sandwich panel slab. From the experimental results it was verified the adequacy of assuming a linear behavior for the GFRP with a stress field limit governed by the Hashin failure criterion, while for the phenolic core, the crushable foam model available in ABAQUS was used [1].

In 2015, Raj *et al.* developed a basalt fiber reinforced composite (BFRC) sandwich panel consisting of a prefabricated corrugated plate with basalt fibers reinforced polymer (BFRP) working like a permanent mold in the bottom face of a cast in place concrete slab, and providing to this system the required tensile capacity [2]. The panel was tested experimentally under four point bending load conditions. The deflection at peak load was almost 1.7 times higher than the deflection at service limit states (L/250=6mm, where L=1500 mm is the slab's span length), and after peak load a smooth structural softening stage was observed with a decrease of less than 10% of load capacity up to a deflection two times higher than the deflection at peak load, reviling a certain ductile behavior for this construction system. This system has failed by a combination of delamination between the two constituent materials and concrete crushing. By using ABAQUS with a concrete damage plasticity (CDP) model to simulate the nonlinear behavior of concrete, cohesive-zone model for the concrete-BFRP

plate interface, and assuming linear-elastic behavior for the BRFP, a deviation of about 4% on the maximum load of the experimentally tested slab was obtained. Moreover, the numerical simulations have indicated that, by assuring anchorage mechanism that avoid premature concrete-BFRP debond, the stiffness and the maximum load carrying capacity of this slab system are increased [2]. Mostafa *et al.* presented a sandwich panel designed for having an improved behavior in terms of shear performance, by using shear keys with semi-circular shape [3]. The shear keys, of chopped strand (CS) glass fibers impregnated by epoxy resin, were installed between the GFRP skins and foam (Polyvinylchloride, PVC, and polyurethane, PU, were investigated) in an attempt to increase the in-plane shear resistance of this interface zone [3]. By using ABAQUS computer program, assuming linear elastic behavior for all the intervening materials, and adopting contact elements for modeling the interface between shear keys and surrounding materials, a parametric study was executed for assessing the influence of the diameter and spacing of these shear keys on the in-plane shear performance of this type of sandwich panel, and an optimized configuration was determined [3].

By considering the nonlinear behavior of the materials and the geometric nonlinear response of the structural system, through a 3D FEM model, Sharaf and Fam analyzed large-scale sandwich panels with internal ribs, tested under transverse loading [4]. These simulations were capable of capturing the global structural behavior and the local failure modes registered experimentally, which were essentially skin wrinkling and crushing in compression [4]. In 2015, Mastali *et al.* [5] (the first part of this two companion papers) proposed an innovative hybrid sandwich panel formed by a GFRP bottom tension, a Deflection Hardening Cement Composite (DHCC) top compression layer, GFRP shear ribs and foam core material. The DHCC layer has the purpose of increasing the stiffness, ductility, impact resistance and acoustic performance of the panel, as well as to constitute a proper substrate for the application of floor cover materials. This layer also provides an extra fire protection to the panel (see Fig. 4.1a).

An extensive experimental program was executed at Minho University to investigate the flexural performance of this hybrid slab system. Within the scope of the second part of this investigation, a parametric study was performed on one-way bending slabs to assess the influence of the geometric and material properties of the constituents of this slab system in its global behavior. To validate the applicability of the FEM 3D Model adopted in this parametric study, the experimental tests were simulated, having been demonstrated capable of capturing the observed damages, and the force-deflection and force-strain responses registered experimentally.

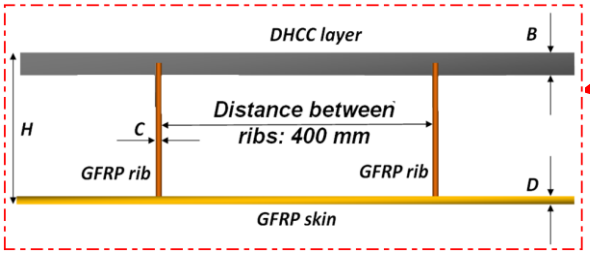

a) Cross section of the proposed sandwich panel

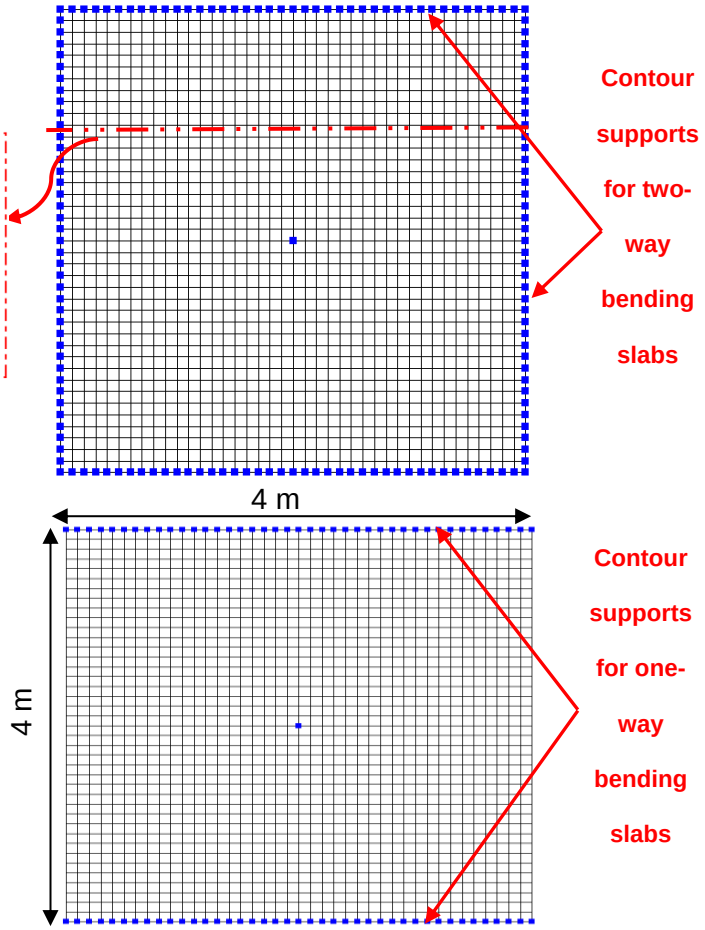

b) Slab plan and support conditions

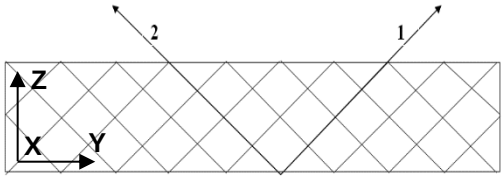

c) Ribs: fibers oriented at ± 45º

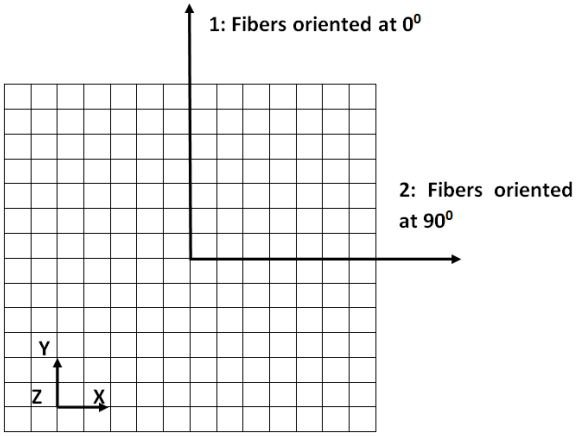

d) Skins: fibers oriented at 0º and 90º

Fig 4.1. Schematic representations of the slab

4.2. FEM model approaches

The constitutive models adopted in FEMIX and ABAQUS computer programs for modeling the behavior of the hybrid slab constituent materials are briefly presented in this section.

4.2.1. Introduction

FEMIX 4.0 is a computer code whose purpose is the analysis of structures by the Finite Element Method (FEM). This code is based on the displacement method, and offers a large library of finite element types, namely 3D frames and trusses, plane stress elements, flat or curved elements for shells, and 3D solid elements. Linear elements may have two or three nodes, plane stress and shell elements may be 4, 8 or 9-noded and 8 or 20 noded hexahedra may be used in 3D solid analyses. This element library is complemented with a set of point, line and surface springs that model elastic contact with the supports, and also several types of interface elements to model inter-element contact. Embedded line elements can be added to other types of elements to model reinforcement bars. All these types of elements can be simultaneously included in the same analysis, with the exception of some incompatible combinations. The analysis may be static or dynamic and the material behavior may be linear or nonlinear. Data input is facilitated by the possibility of importing CAD models. Post processing is performed with a general-purpose scientific visualization program named *draw mesh,* or more recently by associating FEMIX 4.0 with GID software.

Several nonlinear models may be simultaneously considered. In the same nonlinear analysis, allowing, for instance, the combination of reinforced concrete with strengthening components, which exhibit distinct nonlinear constitutive laws. Interface elements with appropriate friction laws and nonlinear springs may also be simultaneously considered. The global response history is recorded in all the sampling points for selected post-processing.

Advanced numerical techniques are available, like the Newton-Raphson method combined with path dependent or independent algorithms and arc-length techniques. When the size of the systems of linear equations is very large, a preconditioned conjugate gradient method can be advantageously used.

ABAQUS is a commercial software with several FEM-based potentialities for a multi-physics modeling in structural analysis [6].

4.2.2. Constitutive models adopted in FEMIX simulations

The Reissner-Mindlin shell theory was selected to simulate the behavior of the slab system. GFRP materials were modeled assuming linear-elastic behavior, with two alternatives: isotropic and orthotropic. Since experimental tests have demonstrated that foam cores had no significant contribution for the load carrying capacity and flexural performance of the hybrid slabs, this material was not considered in the simulations with FEMIX. The DHCC is the material of the slab system more prone to develop nonlinear behavior due to cracking. Therefore, the influence of considering the linear or the nonlinear behavior of DHCC on the performance of the slab system was investigated in the parametric studies. The damage due

to crack formation and propagation was simulated by discretizing the thickness of the DHCC in ten layers. Fibers bridging micro-cracks contribute to the formation of diffuse crack patterns, since they offer resistance to the coalescence of those micro-cracks into macro-cracks. Therefore, smeared crack constitutive models are, conceptually, more appropriate than discrete crack models in the simulation of crack propagation in fiber reinforced cement composites (FRCC) structures, mainly, in those with a high number of redundant supports, such as the present case (the DHCC layer is supported on the GFRP ribs) [7]. In the present section only the relevant aspects of the adopted multidirectional fixed smeared crack model available in the FEMIX 4.0 software are pointed out, since its full description can be found elsewhere [7]. For the case of cracked concrete, the constitutive law is defined by Equation (4.1),

$$\begin{bmatrix} \Delta\underline{\sigma}_{mf} \\ \underline{\sigma}_{s} \end{bmatrix} = \begin{bmatrix} \underline{D}_{mf}^{crco} & \underline{0} \\ \underline{0} & \underline{D}_{s}^{crco} \end{bmatrix} \begin{bmatrix} \Delta\underline{\varepsilon}_{mf} \\ \underline{\varepsilon}_{s} \end{bmatrix} \tag{4.1}$$

where $\Delta\underline{\sigma}_{mf}$ and $\Delta\underline{\varepsilon}_{mf}$ are the vectors corresponding to the in-plane stress and strain increment components, respectively (membrane and bending components); $\underline{\sigma}_{s}$ and $\underline{\varepsilon}_{s}$ are the vectors corresponding to the out-of-plane shear stress and shear strain components, respectively, and $\underline{D}_{mf}^{crco}$ is the in-plane cracked concrete constitutive matrix [8].

Fig. 4.2 defines the fracture mode I modulus, D_I^{cr}, where α_i and ξ_i are the parameters that define the shape of the crack's normal stress vs. normal strain diagram. The ultimate crack normal strain ($\varepsilon_{n,u}^{cr}$) is defined as a function of α_i and ξ_i parameters, fracture energy (G_f^I), tensile strength ($f_{ct} = \sigma_{n,1}^{cr}$) and crack bandwidth ($l_b$) [7].

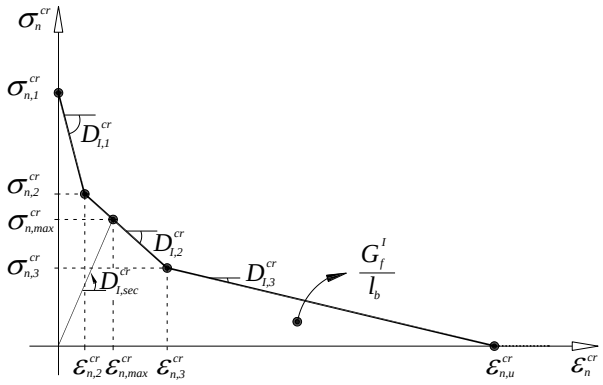

Fig. 4.2 Trilinear stress-strain diagram to simulate the fracture mode I crack propagation

$$(\sigma_{n,1}^{cr} = f_{ct}, \sigma_{n,2}^{cr} = \alpha_1 \sigma_{n,1}^{cr}, \ \sigma_{n,3}^{cr} = \alpha_2 \sigma_{n,1}^{cr}, \ \varepsilon_{n,2}^{cr} = \xi_1 \varepsilon_{n,u}^{cr}, \ \varepsilon_{n,3}^{cr} = \xi_2 \varepsilon_{n,u}^{cr}; \ D_{I,i}{}^{cr} = -k_i \frac{l_{cr} f^{2}{}_{ct}}{G_f},$$

$$k_1 = \frac{(1-\alpha_1)(\xi_1 + \alpha_1\xi_2 - \alpha_2\xi_1 + \alpha_2)}{2\xi_1}, \ k_2 = \frac{(\alpha_1 - \alpha_2)(\xi_1 + \alpha_1\xi_2 - \alpha_2\xi_1 + \alpha_2)}{2(\xi_2 - \xi_1)},$$

$$k_3 = \frac{\alpha_2(\xi_1 + \alpha_1\xi_2 - \alpha_2\xi_1 + \alpha_2)}{2(1-\xi_1)}).$$

Regarding fracture mode II, the total and the incremental approaches, schematically represented in Fig. 4.3, and described in detailed elsewhere [9], are available in FEMIX, but in the simulations carried out the total approach was adopted due to its better performance. Both approaches mobilize the concept of shear retention factor, β [9, 10]. The shear retention factor is defined in Eq. (4.2),

$$\beta = \left(1 - \frac{\varepsilon_n^{cr}}{\varepsilon_{n,u}^{cr}}\right)^{p_1} \tag{4.2}$$

where, p_1 is a parameter to define the decrease rate of β with the increase of the crack normal strain component, ε_n^{cr}. The values of the model parameters for simulating the behaviour of DHCC are listed in Table 4.1.

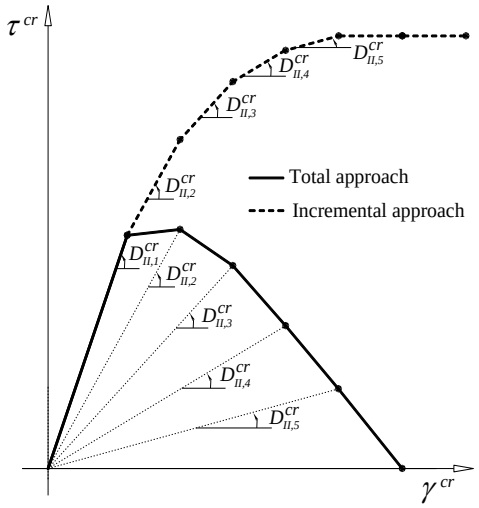

Fig. 4.3. Relation between crack shear stress and crack shear strain for the incremental and total approaches

Table 4.1. Properties adopted to simulate the nonlinear behavior of DHCC

Parameters of DHCC	
Poisson's ratio	v_c= 0.15
Initial Young's modulus	E_c = 18420 MPa
Compressive strength	f_c= 24 MPa
Maximum number of cracks per integration point	*2*
Tri-linear softening diagram parameters	f_{ct} = 2.57 MPa ; G^I_f = 4.18 N/mm ξ_1 = 0.24; α_1 = 1.43; ξ_2 = 0.6; α_2 = 0.58
Parameter defining the mode I fracture energy available to the new crack [10]	*2*
Parameter defining the shear retention evolution (p_1)	*2*
Crack band-width, l_{cr}	*Square root of the area of the integration point ($\sqrt{Ai}$)*
The adopted values for the CDP model parameters	
Dilation angle (ψ)	38^0
Plastic potential eccentricity (e)	*0.1*
Stress ratio (f_{b0}/f_{C0})	*1.16*
Shape of the loading surface (Kc)	*2/3*
Viscosity parameter (VP)	0

4.2.3. Constitutive models adopted in ABAQUS simulations

A plastic damage model was used to simulate the DHCC, while foam core was simulated by a crushable foam model. Additionally, GFRP materials were assumed as having orthotropic behavior.

4.2.3.1. DHCC

The concrete damage plasticity (CDP) model was used to simulate the damage due to crack initiation and propagation, as well as the inelastic deformation of cement-based materials in compression. The typical stress–strain response obtained in uniaxial tensile tests is schematically represented in Fig. 4.4a and Fig. 4.4b. After a linear response up to the crack initiation, a tensile strain hardening stage, of relative small amplitude, occurs due to the formation of several micro-cracks. This cracking phase is followed by a softening stage up to a relatively high tensile strain in consequence of the widening localization in the tensile failure crack. The values adopted for the model parameters are included in Table 4.1.

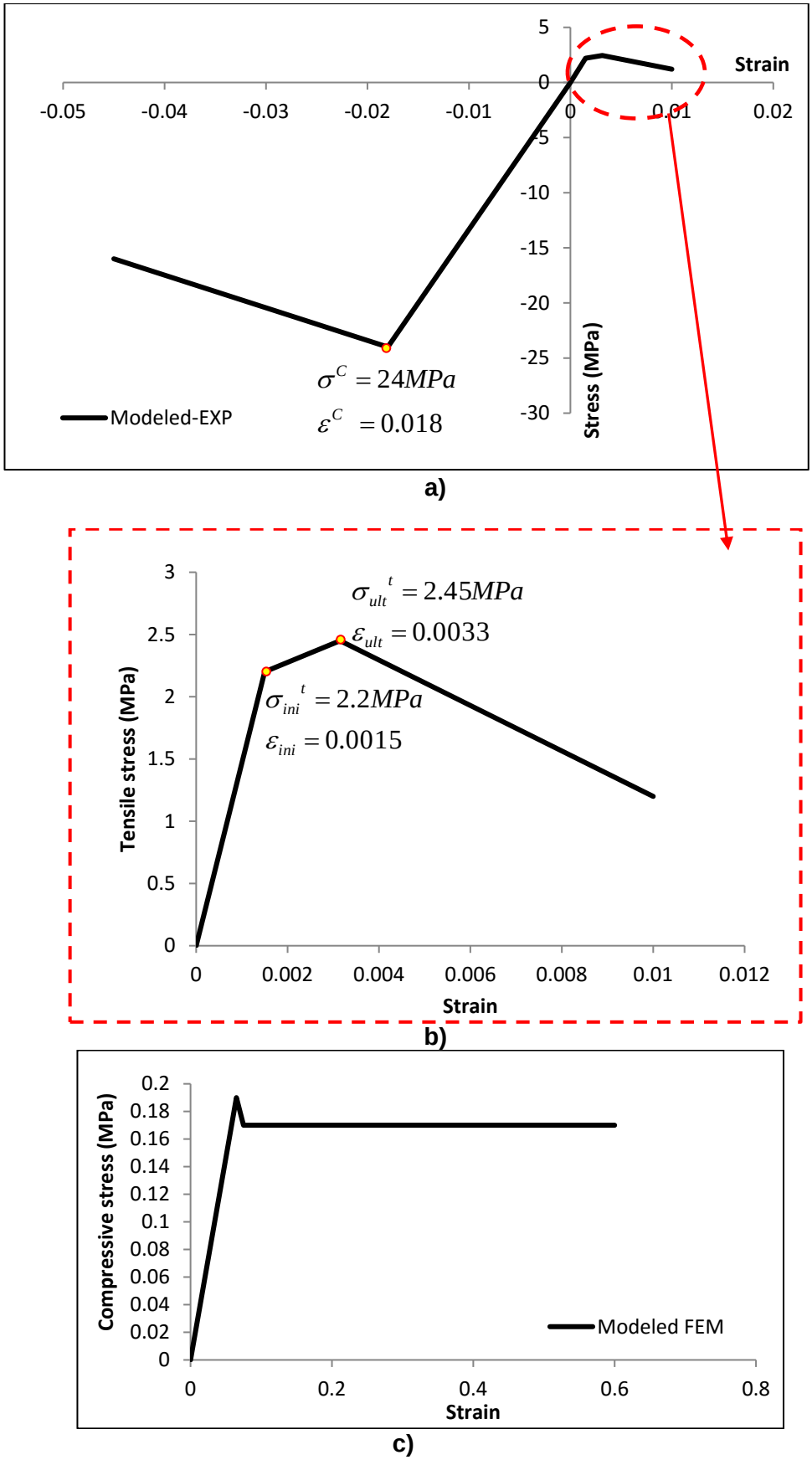

Fig 4.4. Stress-strain curves for FEM modeling: a) DHCC layer in both compression and tension; b) DHCC layer in compression; c) Foam core in compression

4.2.3.2. Foam core

The crushable model for simulating foam type materials was used, by considering null tensile capacity and a compressive stress-strain response represented by the diagram depicted in Fig. 4.4c.The values adopted for the model parameters are included in Fig. 4.4c.

4.2.3.3. GFRP ribs and skin

The GFRP materials were considered orthotropic, with linear elasticity. Their compliance matrix is indicated in Equation (4.3), defined by engineering constants in the three principal material directions, namely: E_1, E_2, E_3 (elasticity moduli); v_{12}, v_{13}, v_{23} (Poisson's ratios); and G_{12}, G_{13}, and G_{23} (shear modules).

$$\begin{bmatrix} \varepsilon_1 \\ \varepsilon_2 \\ \varepsilon_3 \\ \gamma_4 \\ \gamma_5 \\ \gamma_6 \end{bmatrix} = \begin{bmatrix} \frac{1}{E_1} & \frac{-\upsilon_{21}}{E_2} & \frac{-\upsilon_{31}}{E_3} & 0 & 0 & 0 \\ \frac{-\upsilon_{12}}{E_1} & \frac{1}{E_2} & \frac{-\upsilon_{32}}{E_3} & 0 & 0 & 0 \\ \frac{-\upsilon_{13}}{E_1} & \frac{-\upsilon_{23}}{E_2} & \frac{1}{E_3} & 0 & 0 & 0 \\ 0 & 0 & 0 & \frac{1}{G_{12}} & 0 & 0 \\ 0 & 0 & 0 & 0 & \frac{1}{G_{13}} & 0 \\ 0 & 0 & 0 & 0 & 0 & \frac{1}{G_{23}} \end{bmatrix} \begin{bmatrix} \sigma_{11} \\ \sigma_{22} \\ \sigma_{33} \\ \sigma_{12} \\ \sigma_{13} \\ \sigma_{23} \end{bmatrix} \quad (4.3)$$

The values adopted for some of these parameters were determined from experimental tests, while the remaining ones were obtained from [10]. All these values are indicated in Tables 2.4 and 4.2.

Table 4.2. Properties considered for GFRP materials [11]

GFRP *material*	***E₁***	***E₂***	ν_{12}	***In-plane shear modulus***	***Tensile strength at 0^0 (1)***	***Tensile strength at 90^0 (2)***	***In-plane shear strength***	***Compressive strength at $\pm45^0$ (1)&(2)***
	[GPa]	[GPa]		[GPa]	[MPa]	[MPa]	[MPa]	[MPa]
Ribs	12.2	12.2	0.53	8	-----	-----	100	90
Skin	40.0	8.0	0.25	4	1000	30	-----	-----

4.3. Parametric studies and complementary analysis for the optimization of the hybrid slab system

4.3.1. Introduction

Parametric studies were executed in three phases to approach the optimized slab's dimensions and to indicate the effects of material and geometric attributes (slab's height and thickness of each slab's component) on the global behavior of this type of slabs.

In the first stage of the parametric studies, FEM analyses were executed assuming a linear-elastic-isotropic behavior for the constituent materials used. The second stage differs from the previous one only on the behavior adopted for the GFRP that was considered orthotropic. The third stage differs from the previous one only on the behavior adopted for the DHCC that was now considered nonlinear due to crack initiation and propagation. FEMIX computer program was used in these three phases.

4.3.2. Parametric studies

4.3.2.1. Assumptions, loading and support conditions

The parametric studies were executed by adopting the following two assumptions:

1. Perfect bond between GFRP ribs and DHCC layer since signs of debond were only observed at the stage of slab's maximum load carrying capacity, caused by the formation of splitting cracks in the alignment of the GFRP ribs [5];
2. The stiffness and strength contribution of the foam core were neglected due to their relatively low values.

The generic cross section geometry of the slab is represented in Fig. 4.1a. Mindlin shell isoparametric finite elements of 8 nodes, with 2×2 Gauss Legendre integration scheme are used in the numerical simulations [12]. Fig. 4.1b illustrates the support conditions, where markers indicate the points with null displacement in the vertical direction (Z), while the nodes in the middle span have null displacement and rotation in Y and X direction, respectively, in order to simulate symmetry conditions. As already indicated, this type of hybrid slab system is aimed to be used in the rehabilitation of masonry buildings. In this type of buildings the existing resisting masonry walls can, in general, provide support conditions for a slab's span ranging between 3.5 and 5 m. Therefore, a slab's span of 4 m was adopted in these parametric studies. Furthermore, the main occupation expected for these buildings is of residential character, and therefore a live load of 1.5 kN/m^2 was considered. By adopting the specific mass of the intervening materials and taking into account the results obtained in chapter three, an average value of 1.0 kN/m^2 was assumed for the dead weight of the slabs, which already includes a uniform distributed load of about 0.3 kN/m^2 for the covering materials (ceramic or timber).

4.3.2.2. Assuming linear-elastic-isotropic behavior for the constituent materials

In the first phase of the parametric study, linear-elastic-isotropic behavior was assumed for the materials used in the hybrid slabs. The main objective of this preliminary parametric study is to have a first estimative of adequate thicknesses for all the slab's components, and a first assessment on the effects of the material properties on the hybrid slab behavior. Therefore, thickness variations were considered for the ribs (2, 4, 6, 8 and 10 mm), skin (2, 5 and 8 mm) and DHCC layer (10, 15, 20, 25 and 30 mm). Moreover, the values considered for the modulus of elasticity of the constituent materials (10, 20, 30, 40 and 50 GPa for DHCC; 5, 20 and 35 GPa for GFRP ribs and 10, 30 and 50 GPa for GFRP skin). Values of 0.15 and 0.2 were adopted for the Poisson coefficient of the, respectively, DHCC layer, and the GFRP ribs and skin.

The analysis considered a slab supported on its four sides (two-way bending behavior). Three possible heights (H) for the slab's cross section were considered (see Fig. 4.1a): 162.5 mm, 130 mm and 100 mm. The value of H extends from the middle surface of the DHCC layer up to the middle surface of the GFRP skin layer.

The analysis was executed based on the following design criteria: the maximum slab's deflection at serviceability limit state (SLS) conditions was limited to *L*/250, as defined in EN1992-1-1:2004 [13]; and the maximum values in the stress fields installed in the constituent materials are limited to the governing strength capacity of these materials (compressive, tensile and shear strength for the DHCC, GFRP skin and GFRP rib, respectively).

According to the experimental tests performed in DHCC specimens, a compressive strength of 24 MPa was adopted, while a tensile strength of 100 MPa for the GFRP skin and an in-plane shear strength of 50 MPa for the GFRP rib were taken by considering the data from the supplier.

The loading combinations were obtained by multiplying the characteristic loads by appropriate partial safety factors, according to the recommendations of the Model Code [13]. Since slabs were considered subjected to dead load (DL) and live load (LL), only strain and stress values were exclusively verified for the following loading combination: 1.35 DL + 1.5 LL [13]. The following main conclusions can be pointed out considering the results obtained in this linear analysis:

1. By increasing the thickness of DHCC layer, the maximum compressive stress in DHCC layer has decreased, while the maximum in-plane shear stress in GFRP ribs and the maximum tensile stress in GFRP skin have increased. An opposite trend was observed by increasing the elastic modulus of DHCC material. The variation on both parameters has minor influence on the slab's deflection.

2. Increasing the thickness of GFRP ribs and skin resulted in a decrease of deflection, maximum compressive stress in DHCC layer, in-plane maximum shear stress in GFRP ribs, and maximum tensile stress in GFRP skin.
3. Increasing the elastic modulus of GFRP ribs and skin conducted to a decrease in: slab's deflection, tensile stress in GFRP skin and compressive stress in DHCC layer, while in-plane shear stress on GFRP ribs has increased.

4.3.2.3. Assuming linear-elastic-orthotropic behavior for the GFRP

From the linear analysis of the proposed slabs with two-way bending behavior, very small stresses and deflections were obtained. By considering also that the GFRP ribs are disposed in only one direction, the configuration of the slab is changed to one-way bending behavior, as represented in Fig. 4.1b. Additionally, the behavior of GFRP materials used for ribs and skin was assumed orthotropic, reflecting the mechanical behavior of the GFRP materials used and taking advantage of the optimization process that is developed on the materials' properties. GFRP sheets with oriented fibers at 0º and 90º were adopted in skins, while GFRP sheets with oriented fibers at ±45º were chosen for ribs, in order to take into account that in these components the predominant stress field is longitudinal tension and shear, respectively. The mechanical properties considered for GFRP ribs and skins are listed in Table 4.2.

Like in the previous phase of the parametric studies, in this second phase the DHCC was considered with a linear-elastic behavior with the properties already indicated. From this analysis, the following main conclusions can be pointed out:

1. By changing the support conditions from two-way to one-way bending, and adopting orthotropic behaviour instead of isotropic for the GFRP materials, both the maximum normal stresses (σ_1 and σ_2 in the directions 1 and 2, respectively, in Figs 4.1c and 4.1d) in the GFRP ribs and skin, as well as the slab's deflection, have increased more than 2 times.
2. To accomplish the deflection limit imposed by SLS conditions, $L/250 = 16$ mm, the thickness of the slab must be higher than 100 mm.
3. By increasing the DHCC thickness, the maximum slab's deflection and maximum compressive stress in DHCC layer have decreased, while the maximum in-plane shear and the maximum normal tensile stresses have increased in both GFRP ribs and skin.
4. By increasing the thickness of GFRP ribs, the maximum compressive and tensile stresses in the DHCC layer and GFRP skin, respectively, have decreased.
5. By increasing the GFRP skin thickness, the neutral surface has moved downward, and the in-plane shear stresses in the GFRP ribs have slightly decreased.

Since GFRP materials used in the skin and ribs have linear behavior up to failure, the DHCC material is the unique component of the proposed hybrid sandwich slab that can develop nonlinear behavior, mainly due to its susceptibility to crack formation and propagation. Therefore, in the third phase of the parametric analysis, the material nonlinear behaviour of the DHCC layer was simulated.

4.3.2.4. Assuming material nonlinear behavior for the DHCC

A new parametric study was carried out by varying the slab's cross section height and the thickness of the slab's components, according to the intervals indicated in Table 4.2. The range of values assumed for the thickness of the slab's components investigated (H, B, C and D) are indicated in this table. The meaning of the parameters defined in Table 4.3 is represented in Fig. 4.1a.

Table 4.3. Variables and corresponding values assumed in the parametric study

Name	*H*	*Thickness*			*Name*	*H*	*Thickness*			*Name*	*H*	*Thickness*		
		B	*C*	*D*			*B*	*C*	*D*			*B*	*C*	*D*
	[mm]	[mm]				[mm]	[mm]				[mm]	[mm]		
SGH 1		10	2	5	SMH 1		10	2	5	SZH 1		10	2	5
SGH 2		15	2	5	SMH 2		15	2	5	SZH 2		15	2	5
SGH 3		20	2	5	SMH 3		20	2	5	SZH 3		20	2	5
SGH 4		25	2	5	SMH 4		25	2	5	SZH 4		25	2	5
SGH 5		30	2	5	SMH 5		30	2	5	SZH 5		30	2	5
SGR 2	162.5	30	4	5	SMR 2	130	30	4	5	SZR 2	100	30	4	5
SGR 3		30	6	5	SMR 3		30	6	5	SZR 3		30	6	5
SGR 4		30	8	5	SMR 4		30	8	5	SZR 4		30	8	5
SGR 5		30	10	5	SMR 5		30	10	5	SZR 5		30	10	5
SGS 1		30	2	2	SMS 1		30	2	2	SZS 1		30	2	2
SGS 3		30	2	8	SMS 3		30	2	8	SZS 3		30	2	8

In a first step of the analysis, the load combination corresponds to a service load level. It considers the addition of the permanent load, PL, (slab's dead load plus a load corresponding to the covering materials, 1 kN/m^2) with the live load, LL, resulting in PL+LL. Relevant results related to the FEM material nonlinear analysis can be pointed out:

1. Increasing the thickness of each slab's component results in reducing the maximum stress in slab's component that the thickness increased, while the maximum stresses increased in other slab's components which thickness kept constant. For instance, increasing the thickness of DHCC layer led to an increase of the maximum in-plane shear stress on GFRP ribs and tensile stress in GFRP skin, while the maximum compressive stress in DHCC layer decreased (see Figs 4.5b to 4.5d).
2. A maximum reduction of stress was found when the thickness of the GFRP ribs was increased.

3. Increasing the slab's height conducted to an increase of the applied distributed load and reduced all types of stress fields, including in-plane shear, compression, and tension.

To assess the effects of thickness variation on the maximum values of the stress fields installed in the constituent materials and on the obtained ultimate load carrying capacity of hybrid slabs, the slabs were also loaded under a load combination that included the permanent load and the live load. The permanent load, PL (slab's dead load plus a load corresponding to the covering materials, 1 kN/m^2) was applied to the slabs, and then the live load was imposed and increased up to a predefined limit, where the total load is defined by PL+αLL, with alpha (α) being higher than 1 and LL=1.5 kN/m^2.

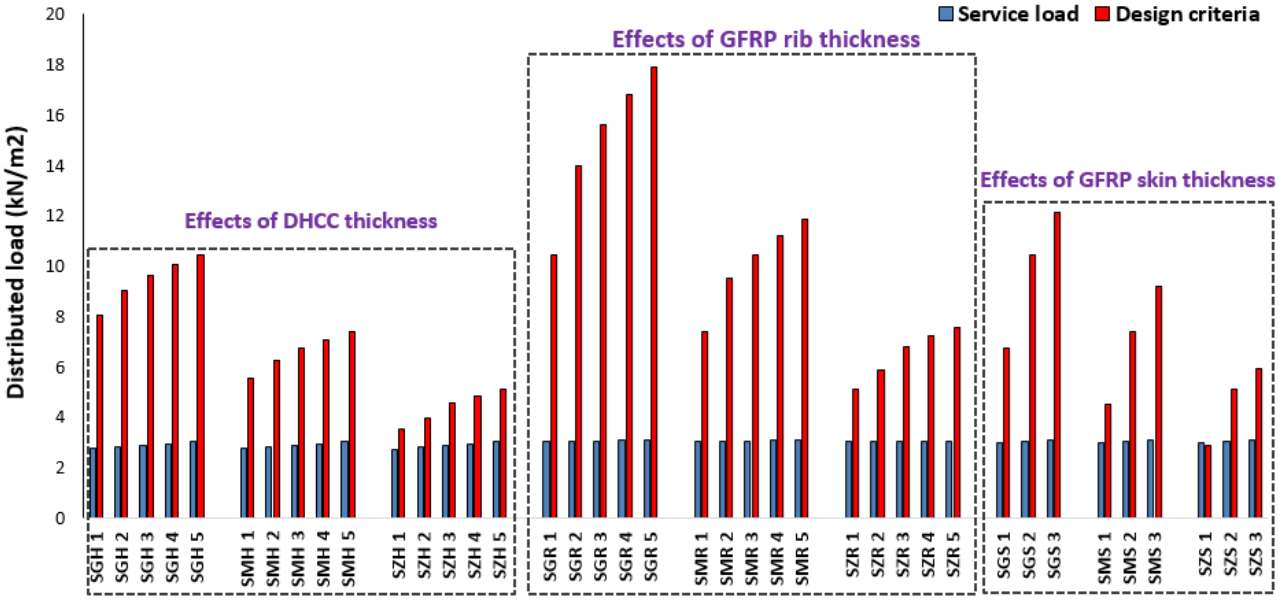

a)

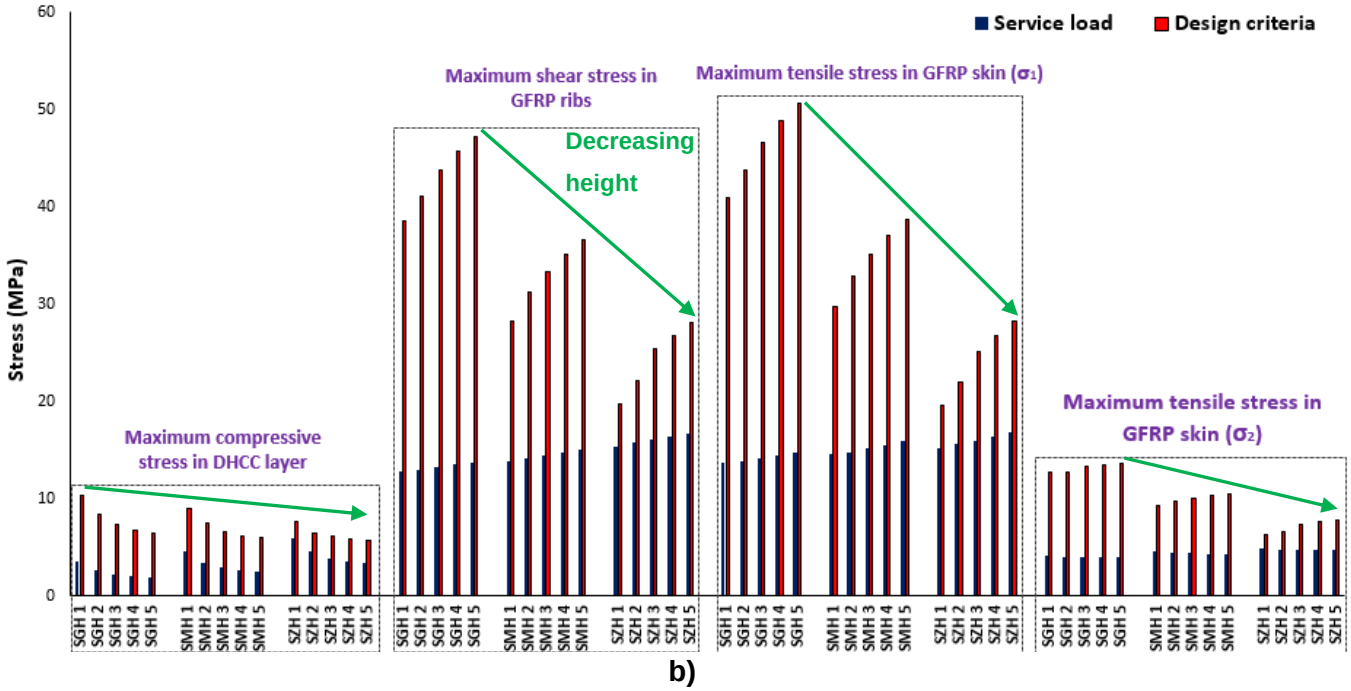

b)

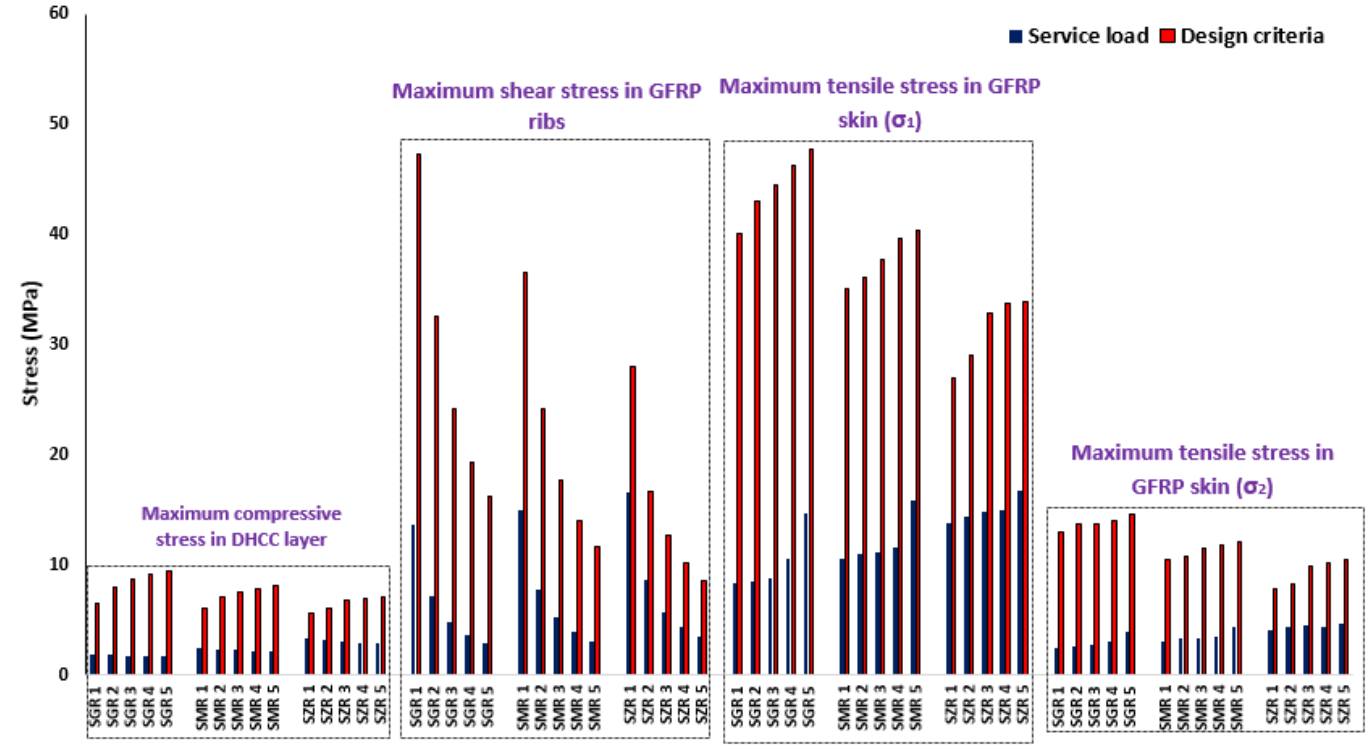
Service load
Design criteria
Stress (MPa)
Maximum compressive stress in DHCC layer
Maximum shear stress in GFRP ribs
Maximum tensile stress in GFRP skin (σ1)
Maximum tensile stress in GFRP skin (σ2)
SGR 1 SGR 2 SGR 3 SGR 4 SGR 5 SMR 1 SMR 2 SMR 3 SMR 4 SMR 5 SZR 1 SZR 2 SZR 3 SZR 4 SZR 5

c)

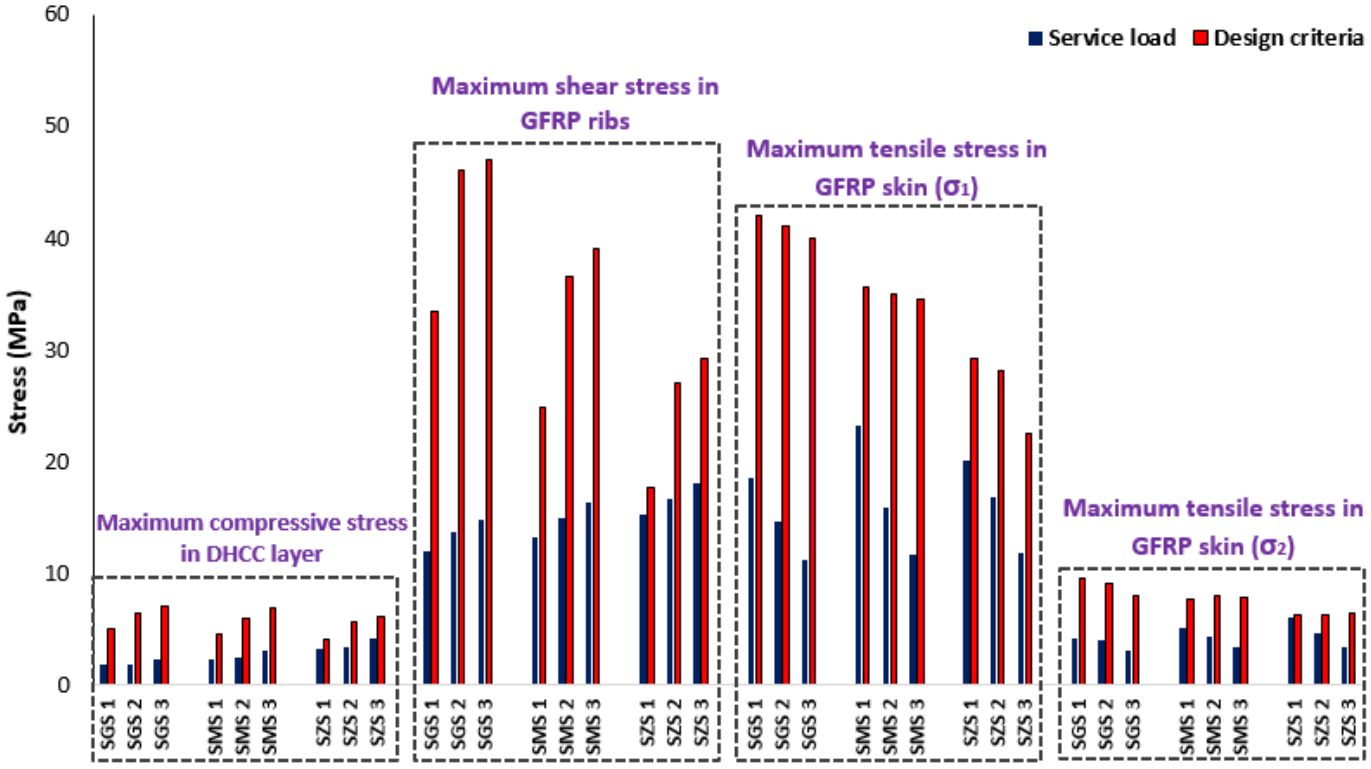
Service load
Design criteria
Stress (MPa)
Maximum compressive stress in DHCC layer
Maximum shear stress in GFRP ribs
Maximum tensile stress in GFRP skin (σ1)
Maximum tensile stress in GFRP skin (σ2)
SGS 1 SGS 2 SGS 3 SMS 1 SMS 2 SMS 3 SZS 1 SZS 2 SZS 3

d)

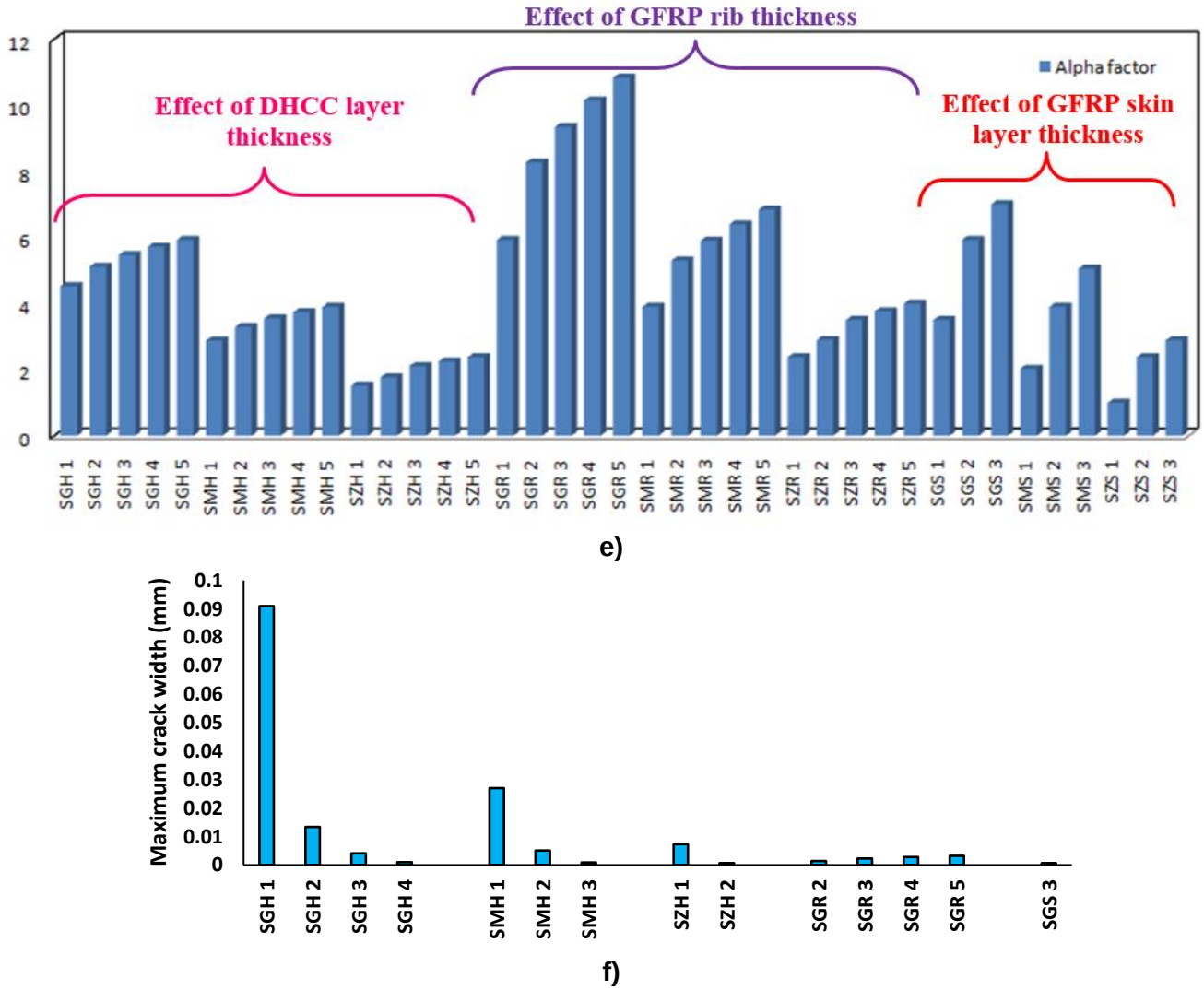

Fig 4.5. a) Effects of increasing slab's components on distributed load; b) Effects of increasing DHCC layer on stress fields; c) Effects of increasing GFRP ribs on the stress fields; d) Effects of increasing GFRP skin on the stress fields; e) Effects of increasing slab's components on α factor; f) The recorded maximum crack width

This limit resulted from one of the following design criteria [13]: a maximum crack width of 0.3 mm in the DHCC layer; the material strength limit is reached in one of the slab's components (compressive strength of 24 MPa for the DHCC; tensile strength of 1000 and 30 MPa in 1 and 2 material directions, respectively, for the GFRP skin; in-plane shear strength of 100 MPa for the GFRP rib); a slab's mid-span deflection of $L/250$ = 16 mm.

The maximum crack width was numerically computed by multiplying the crack bandwidth, l_{cr}, (Table 4.1), by the maximum normal crack strain determined in the integration points (Ips) [12]. According to EN 1992-1-1:2004, the maximum crack width should be limited to 0.3 mm under service load conditions [13].

The numerical results obtained are related to the maximum load level attained, which is limited by the design criteria previously listed and pointed out in Fig. 4.5. The following aspects can be highlighted:

1. Increasing the thicknesses of slab's components resulted in increasing the distributed load that is applied to the slabs (see Fig. 4.5a).
2. Increasing the thickness of each slab's component results in reducing the maximum stress in slab's component that the thickness increased, while the maximum stresses increased in other slab components that kept constant.
3. Increasing the thickness of GFRP ribs has a significant impact on increasing the alpha (α) factor in comparison to increasing the thickness of the GFRP skin or the thickness of the DHCC layer.
4. The minimum hybrid slab's height that meets the design requirements is limited to 100 mm height.
5. Increasing the thickness of DHCC layer leads to a reduction of the crack width (see Fig. 5e) and the number of formed cracks (see Fig. 4.6).

4.3.3. Buckling verifications

Using relatively thin GFRP ribs to transfer shear stresses from top DHCC layer to bottom GFRP skin increased the possibility of localized buckling in the webs due to in-plane shear and compressive stresses. The possibility of local buckling in the GFRP ribs was investigated through equations that consider the contribution of the compressive and in-plane shear stresses [14]. Since a direct simulation of buckling phenomenon in FEMIX software was not possible, equations (4.4) to (4.10) were used to consider the contribution of compressive stresses in the buckling of GFRP ribs [15],

$$\sigma = \frac{\pi^2}{t_R {d_R}^2}(13.9\sqrt{D_{R1}D_{R2}} + 11.1D_{R12} + 22.2D_{RS}) \tag{4.4}$$

$$D_{R1} = \frac{E_{R1}{t_R}^3}{12(1-\upsilon_{R1}\upsilon_{R2})} \tag{4.5}$$

$$D_{R2} = \frac{E_{R2}{t_R}^3}{12(1-\upsilon_{R1}\upsilon_{R2})} \tag{4.6}$$

$$D_{R12} = \upsilon_{R1}D_{R2} = \upsilon_{R2}D_{R1} \quad , \quad \upsilon_{R2} = \frac{E_1}{E_2}\upsilon_{R1} \tag{4.7}$$

$$D_{RS} = \frac{G_{R_{12}}t_R^3}{12} \tag{4.8}$$

$$\sigma_{critical} = \frac{\sigma}{\gamma_m} \tag{4.9}$$

$$\gamma_m = \gamma_{m1} * \gamma_{m2} * \gamma_{m3} \tag{4.10}$$

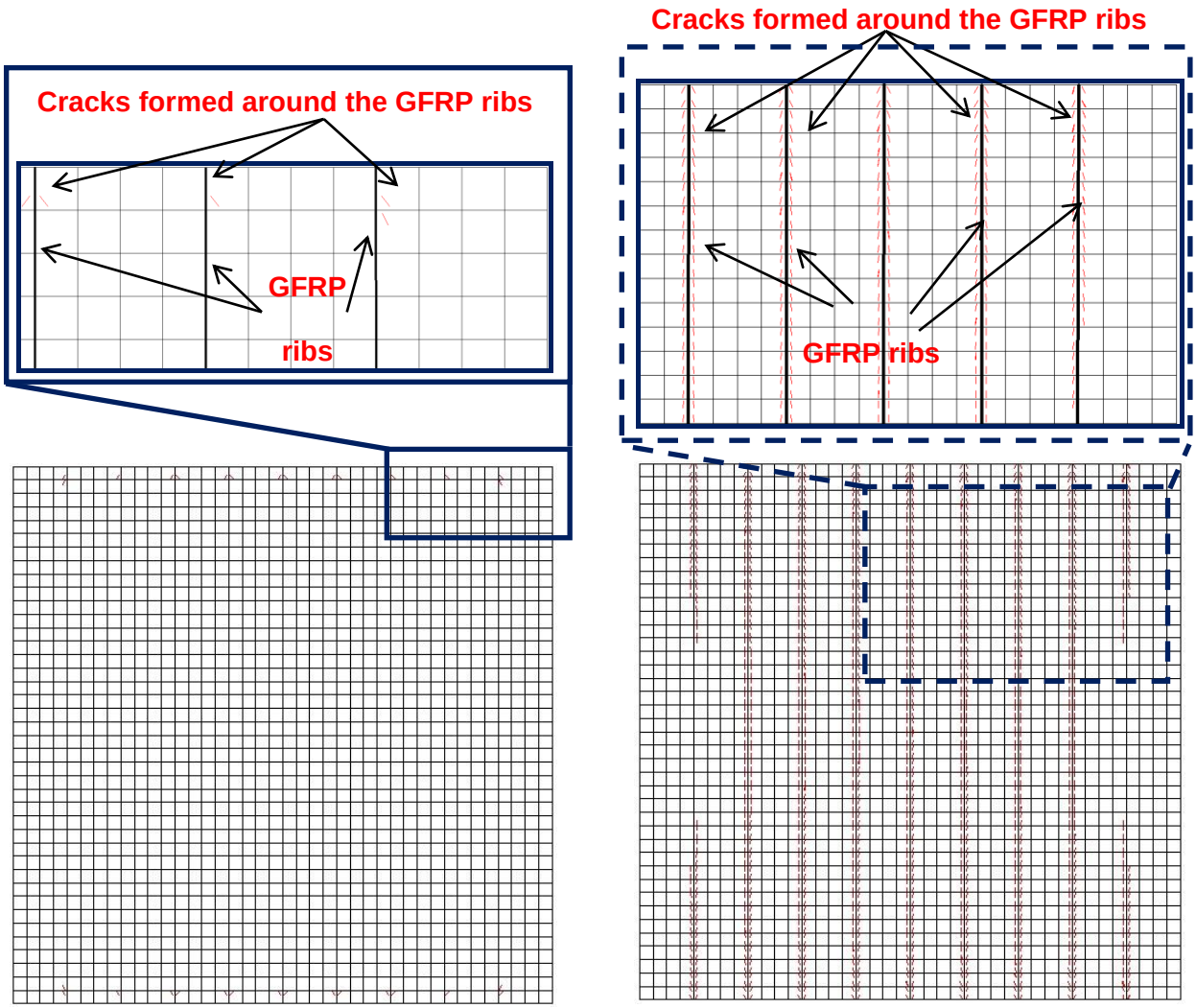

a) **b)**

Fig 4.6. Crack patterns in DHCC layer: a) with 25 mm thickness (SGH4); b) with 10 mm thickness (SGH1)

where, E_{R1}, E_{R2} are the Young's modulus of the GFRP rib in 1 and 2 material axis, as shown in Fig. 4.1c, d_R is the rib height, G_{R12} is the shear modulus of the rib (based on Table 4.2, this value was considered equal to 8 GPa), t_R is the rib thickness, and γ_m is a safety factor. The material partial safety factor, γ_m, was computed based on the EUROCOMP design guide [16]. The values of 1.15, 1.1, and 2.5, were considered to approach, respectively, the material property data (γ_{m1}), the material manufacturing process (γ_{m2}), and the effects of environmental variables and the duration of the loading period (γ_{m3}) [16]. By multiplying these three coefficients, a safety factor of 3.16 was obtained [14].

Moreover, the critical in-plane shear stress ($\tau_{Critical}$) in the ribs can be computed with equations (4.11) to (4.14) [14].

$$\tau = \frac{4K_{12}\sqrt[4]{D_{R1}D_{R2}{}^3}}{t_R d_R{}^2} \quad (4.11)$$

$$K_{12} = 8.125 + 5.045K, \ \ for\ K \le 1 \quad (4.12)$$

$$K = \frac{(2D_{RS} + D_{R_{12}})}{\sqrt{D_{R1}D_{R2}}} \quad (4.13)$$

$$\tau_{Critical} = \frac{\tau}{\gamma_m} \quad (4.14)$$

For the orthotropic materials in conventional GFRP profiles *K* is taken into account lower than 1, while for the isotropic materials *K* is considered equal to 1 [14]. More details can be found in [23] when *K* exceed 1. Since, isotropic and orthotropic materials were used in this study for GFRP profiles, K was considered lower and equal to 1 in equation (12).

4.3.4. Optimized slab's cross section

The effect of each parameter on the slab's global behavior was investigated during the parametric study. Based on the results obtained, seven slabs were selected among the large group evaluated and proposed for further analysis. The dimensions of the proposed seven slabs are listed in Table 4.4.

Table 4.4. The proposed optimized slabs and the corresponding results

Name	*H*	*B*	*C*	*D*	***Maximum crack width***	***Force***	$\sigma_{GFRP\ 90}$	$\sigma_{GFRP\ 0}$	τ_{GFRP}	σ_{DHCC}	***Deflection***	α
	[mm]	[mm]	[mm]	[mm]	[mm]	[kN]	[MPa]	[MPa]	[MPa]	[MPa]	[mm]	
SGO 1	162.5	30	6	5	0.0023	249.46	13.74	44.50	24.12	8.65	3.24	9.35
SGO 2		30	6	3	-----	181.34	11.06	46.88	17.67	6.98	4.27	6.54
SGO 3		20	6	3	0.0036	165.65	10.90	44.20	16.20	7.87	4.66	5.88
SMO 1	130.0	20	4	5	0.0038	149.05	10.71	35.15	15.73	8.50	4.87	5.34
SMO 2		20	6	3	-----	103.69	8.46	35.56	11.12	6.37	6.44	3.46
SMO 3		30	6	2	-----	167.23	11.50	37.74	17.61	7.55	4.74	7.38
SMO 4		30	6	3	-----	122.13	9.49	40.38	13.30	6.18	6.13	4.13

The seven hybrid slabs proposed were analyzed in order to select the ones that present the best structural performance and cost effectiveness. First, the permanent load was imposed to the slabs in order to determine the relevant deflection. Then, a live load equal to 1.5 kN/m^2 was applied and this load was increased up to the criteria already indicated in paragraph 4.3.2.4 were met, namely:

1. Attainment of a maximum crack width of 0.3 mm in DHCC layer;
2. Attainment of the strength limits of slab's components: compressive strength of 24 MPa for the DHCC; tensile strength of 1000 and 30 MPa in 1 and 2 material directions, respectively, for the GFRP skin; in-plane shear strength of 100 MPa for the GFRP rib;

3. Slab's mid-span deflection of L/250 = 16 mm.

The results attained during the numerical analysis of the proposed seven hybrid slabs are presented in Table 4.4. Moreover, the possibility of buckling phenomenon in GFRP ribs was also checked by calculating the compressive and the in-plane shear stresses. The results listed in Table 4.5 show that buckling of ribs does not occur in the proposed hybrid slabs.

Table 4.5. Buckling due to in-plane shear and compressive stress in optimized specimens

Name	***Critical buckling stress due to in-plane shear in ribs***	$\tau_{in-plane}$	***Critical buckling stress due compression in ribs***	$\sigma_{compressive}$	***Status***
	[MPa]	[MPa]	[MPa]	[MPa]	
SGO 1	32.10	24.12	181.78	16.20	Ok
SGO 2	32.10	17.67	181.78	38.38	Ok
SGO 3	32.10	16.20	181.78	35.11	Ok
SMO 1	50.16	15.73	284.04	17.67	Ok
SMO 2	50.16	11.12	284.04	22.65	Ok
SMO 3	50.16	17.61	284.04	10.20	Ok
SMO 4	50.16	13.30	284.04	26.64	Ok

The combination of cost effectiveness and structural safe behavior were considered the main criteria to select the optimized slabs. Therefore, a preliminary cost analysis was carried out on the proposed hybrid slabs to attain the cost of slabs. Then, following results obtained from execution of cost analysis and parametric studies, two hybrid slabs (SMO 1 and SGO 3) were chosen as the optimized hybrid slabs. Afterwards, the two optimized slabs indicated in Fig. 2.1 were manufactured and experimentally tested at University of Minho. The dimensions and the materials used in each slab's component are listed in Table 2.1.

4.4. Experimental tests performed on the proposed hybrid slabs

In chapter three, two hybrid slabs with span length of 1.8 m were loaded under cyclic four point bending load conditions by applying a displacement rate of 30 μm/s. Flexural loading was applied to the slabs through two load lines with 40 mm width and 800 mm length (corresponding to the slabs' total width). This load line was located at 600 mm distance from each support. A schematic figure of the tested hybrid slabs and the used monitoring devices is presented in Fig. 4.7. The experimental response of Slab 1 during the first load sequence presented signs of damage. Therefore, in order to have a first load sequence with a linear response, the increment of deflection adopted in the load sequences of Slab 2 was limited to δ/2 (δ=L/250, with L = 1800 mm).

Advanced numerical simulations of the experimental tests were carried out on the first cycle of the first load sequence for both Slab 1 and Slab 2. In the first cycle of the first load step in

Slab 1, damage occurred in GFRP ribs due to excessive compressive stress, leading to a hardening behavior for a deflection above 5.5 mm, where no sliding and uplift were registered. In Slab 2, compressive damage occurred in the GFRP ribs for a deflection of about 7.5 mm. Furthermore, splitting crack was formed on the surface of DHCC layer. Slab 2 entered in a structural softening stage immediately before the second cycle of the second load sequence and GFRP ribs slipped and uplifted from its embedded DHCC layer.

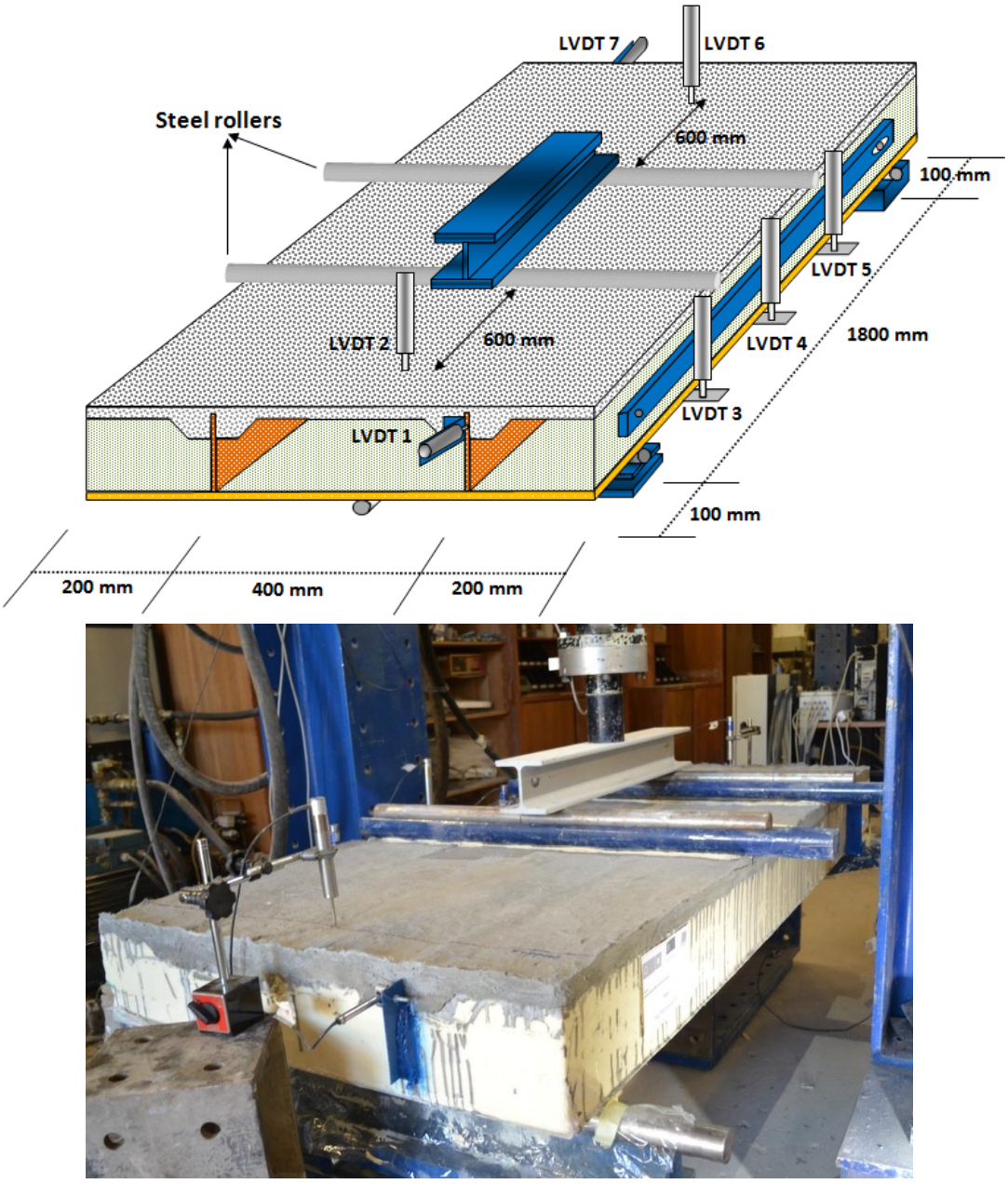

Fig 4.7. Schematic figure of the tested hybrid sandwich panels

During the experimental tests, damages occurred in different load levels. Therefore, using proper constitutive models and adequate interface surfaces for slab's components could well be the way to capture the damage observed and the flexural response of the tested hybrid sandwich panels.

4.4.1. Advanced numerical simulations of the proposed hybrid slabs

The three-dimensional FE model indicated in section 4.2.3 was used for simulating the experimental tests carrying out with the proposed hybrid slabs.

Contact surface properties are especially important on the numerical simulation of hybrid slabs because the structural performance of composite slabs is governed significantly to the contact surface properties between slab's components. There are three different contact surfaces that may be considered in the proposed hybrid slabs: between foam and GFRP ribs and skin, between foam and DHCC layer, and between GFRP ribs and DHCC layer.

During the experimental tests, foam cores detached from DHCC layer without any significant influence on the slab stiffness. Compressive damage in GFRP ribs and crack formation on the top surface of the DHCC layer were observed in the experimental tests and should be well captured in the numerical models. In these numerical simulations, a Cohesive Zone Model (CZM) was used to simulate the interface between slab's components. CZM has been increasingly used for simulate the form and progress of damages in structural analysis of composite materials. CZM is particularly well-suited for modeling delamination in laminar composites. The basis of CZM is a cohesive law consisting of an initial linear elastic zone until a cohesive strength is reached.

One contact surface was used for the GFRP ribs embedded within the DHCC material, and another contact surface was defined between DHCC material and foam core. The cohesive surfaces behave in a quasi-rigid way up to the initiation of damage. Failures at each interface were allowed to occur between the embedded GFRP ribs and the DHCC layer and also between the DHCC layer and the foam cores. No slip was detected between foam cores and GFRP skin or ribs during the experimental tests and, therefore, perfect bond was assumed adequate to model the contact between foam cores and GFRP skin or ribs.

To assess the adequacy and the accuracy of the interface models employed, two different approaches were used in the numerical simulations with the tested hybrid slabs. The first approach considers the different interfaces between slab's components, as already mentioned, and the second approach assumes perfect bond between the slab's components. These two approaches are considered because the computational demands when interface models between contact surfaces are adopted are much higher than when perfect bond is assumed.

Fig. 4.8a shows an interpretation of a simple bilinear traction–separation constitutive law that is governed the stiffness K_0, maximum traction τ_{max}, and cohesive fracture energy G_{cr}. The G_{cr} is the required energy to complete the debonding between contact surfaces, and it is equal to the area under the traction (τ) – separation (δ) curve up to the ultimate separation (δ_f).

Contact with cohesive behavior (traction-separation law) was used to model the interface

between DHCC layer, foam core, and GFRP rib. In this study, the mixed bilinear cohesive zone model, containing normal and shear components (see Fig), was chosen for computational convenience.

The quadratic stress criterion is defined in equation (4.15), where, σ_n is the cohesive tensile stress and τ_1 and τ_2 are the shear stresses in normal directions, 1 and 2, respectively (see Fig. 4.8b). Moreover, in equation 15, σ_n^0 is the cohesive tensile strength and τ_1^0 and τ_2^0 are the shear strengths in normal directions, 1 and 2, respectively.

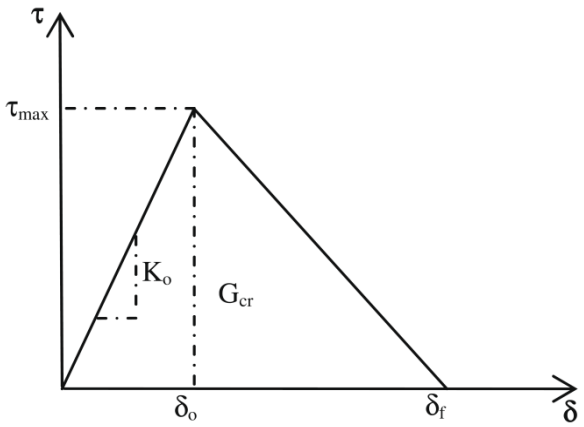

a)

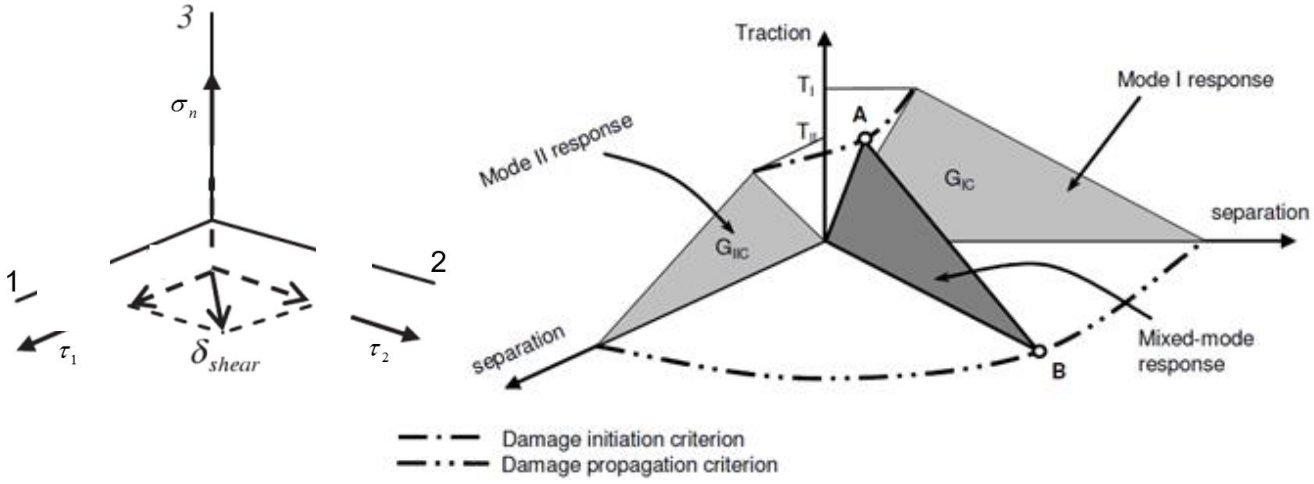

b)

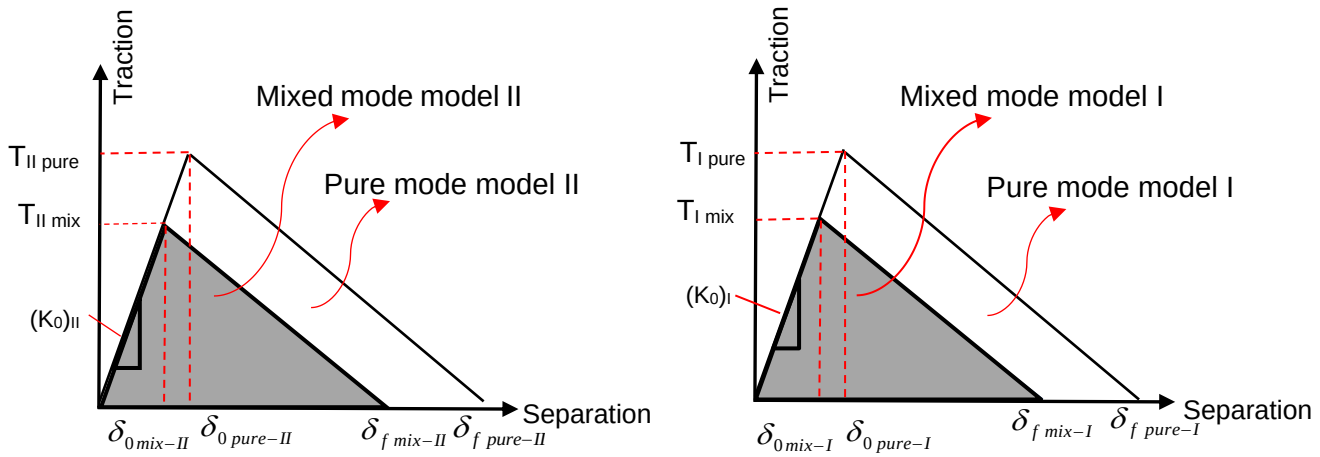

c)

Fig 4.8. a) Bilinear traction–separation constitutive law [6]; b) Mixed-mode bi-linear traction-separation law [17]; Triangular model of mixed-mode bi-linear traction-separation law [23]

Damage in the bilinear cohesive zone model was assumed to occur when a quadratic traction function involving the nominal stress ratios reaches the value one [18]. A typical mixed-mode response is depicted in Fig. 4.8b, in which points marked as A and B correspond to the initiation of damage and full failure conditions of mixed-mode response that are defined based on the mixed-mode damage initiation defined with equation (4.15) and propagation criteria defined with equation (4.16), respectively. The dependence of the fracture energy on the mode mix was based on the Benzaggah–Kenane (BK) damage evolution criterion. Equations (4.15) and (4.16) represent the Benzaggah–Kenane damage evolution criterion, where G_I, G_{II} and G_{III} refer to the fracture toughnesses and so that G_I is derived from the opening mode and G_{II} and G_{III} are related to sliding and tearing modes, respectively. Moreover, G_{IC} and G_{IIC} are the critical fracture energies for mode I and mode II, respectively. The critical fracture energies are represented by the area under the bilinear traction-separation curve for the representative mode, as indicated in Fig. 4.8b. The energy-based Benzeggah and Kenane (BK) damage evolution criterion was used as the propagation criterion [6], where, η in equation (4.16) is a BK material parameter, which respect to [19] this value was considered equal to 1.45 in this study. Damage propagation criterion under the mixed bilinear cohesive zone model expressed in terms of the total fracture energy release rates, G_T and single mode critical energy release of the interface, G_I, G_{II}, and G_{III} such that $G_T=G_I+G_{II}+G_{III}$ is given in equation (4.16).

$$\left(\frac{\sigma_n}{\sigma_n^{\,0}}\right)^2+\left(\frac{\tau_1}{\tau_1^{\,0}}\right)^2+\left(\frac{\tau_2}{\tau_2^{\,0}}\right)^2=1 \qquad (4.15)$$

$$G_I+G_{II}=G_{IC}+(G_{IIC}-G_{IC})\left(\frac{G_{shear}}{G_T}\right)^{\eta} \qquad (4.16)$$

$$G_{shear}=G_{II}+G_{III} \qquad (4.17)$$

$$G_T = G_I + G_{II} + G_{III} \tag{4.18}$$

The energy release rates under mixed-mode critical condition can be computed by the given equation (4.19) (see Fig. 4.8c):

$$G_I = \frac{1}{2}(K_0)_I \times (\delta_{0\,mix})_I \times (\delta_{f\,mix})_I \qquad G_{IC} = \frac{1}{2}(K_0)_I \times (\delta_{0\,pure})_I \times (\delta_{f\,pure})_I$$

$$G_{II} = \frac{1}{2}(K_0)_{II} \times (\delta_{0\,mix})_{II} \times (\delta_{f\,mix})_{II} \qquad G_{IIC} = \frac{1}{2}(K_0)_{II} \times (\delta_{0\,pure})_{II} \times (\delta_{f\,pure})_{II} \tag{4.19}$$

where, $(K_0)_I$ is the stiffness for mode I, $(K_0)_{II}$ is the stiffness for mode II, $(\delta_{0\,mix})_I$ is separation at the onset softening of the mixed-mode I, $(\delta_{f\,mix})_I$ is the ultimate separation in the mixed-mode I, $(\delta_{0\,mix})_{II}$ is separation at the onset softening of the mixed-mode II, $(\delta_{f\,mix})_{II}$ is the ultimate separation in the mixed-mode II, $(\delta_{0\,pure})_I$ is separation at the onset softening of the pure mode I, $(\delta_{f\,pure})_I$ is the ultimate separation in the pure mode I, $(\delta_{0\,pure})_{II}$ is separation at the onset softening of the pure mode II, and $(\delta_{f\,pure})_{II}$ is the ultimate separation in the pure mode II.

Various studies have been undertaken on the FRP–concrete bonded interfaces and there are available parameters in bilinear cohesive zone model, such as initial stiffness, the traction and an interval for fracture energy [15, 16].

To the authors' best knowledge, there is only one study reported on the literature related to the experimental bond response of GFRP shear connectors embedded in reinforced concrete hybrid structures [21], but there isn´t any work in the literature on the bond response between the proposed GFRP shear connectors and reinforced mortars, and also between foam core and reinforced mortars in hybrid structures. Thus, the bilinear CZM parameters are completely unknown, as they depend on the bond interaction between three materials (GFPR rib, foam core, and DHCC material) and no well-established the traction–separation curves are available.

Thus, an inverse analysis procedure was executed with ABAQUS software in order to obtain the unknown parameters of the bilinear cohesive zone model. This analysis was carried out to best-fit the experimental results in terms of force-deflection and force-strain relationships, and to well capture of the observed damages.

4.4.2. FEM mesh, loading and support conditions

Four-node constant strain tetrahedral elements (C3D4) with one integration point were used to model the DHCC materials. Mesh refinement was adopted in zones of expected high gradient of stress fields, such is the case around the GFRP shear connectors (see Fig. 4.9a). GFRP rib and skin were also simulated using 4-node constant strain tetrahedral elements.

Six-node linear triangular prism elements (C3D6) with two integration points were used to simulate the foam cores.

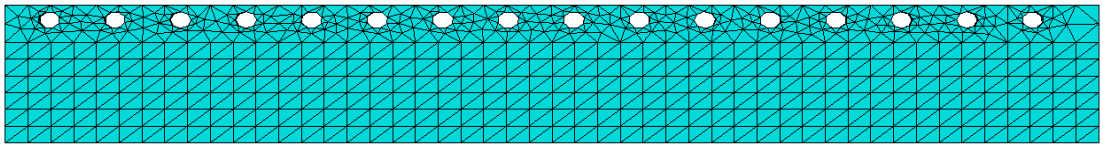

a) GFRP rib mesh

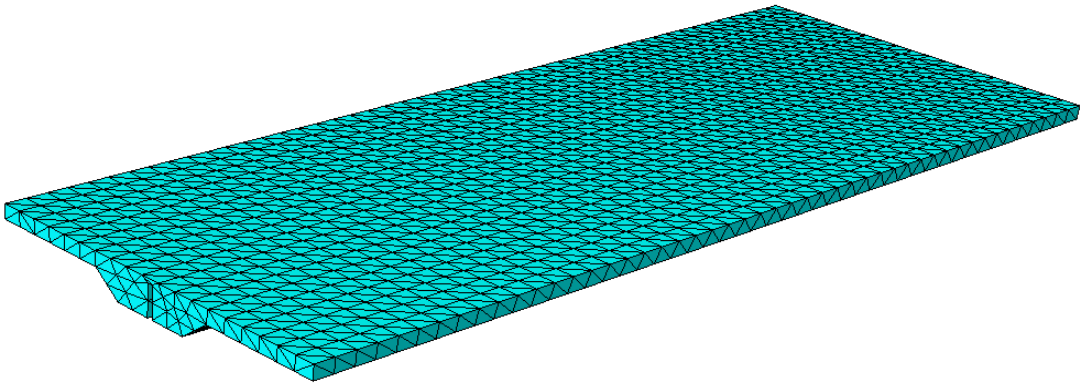

b) DHCC layer mesh

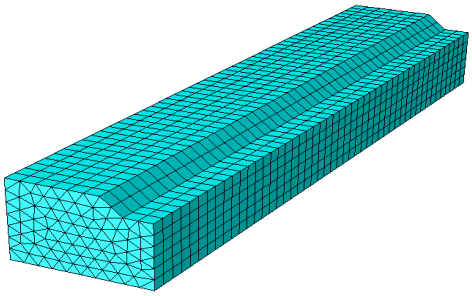

c) Foam core mesh

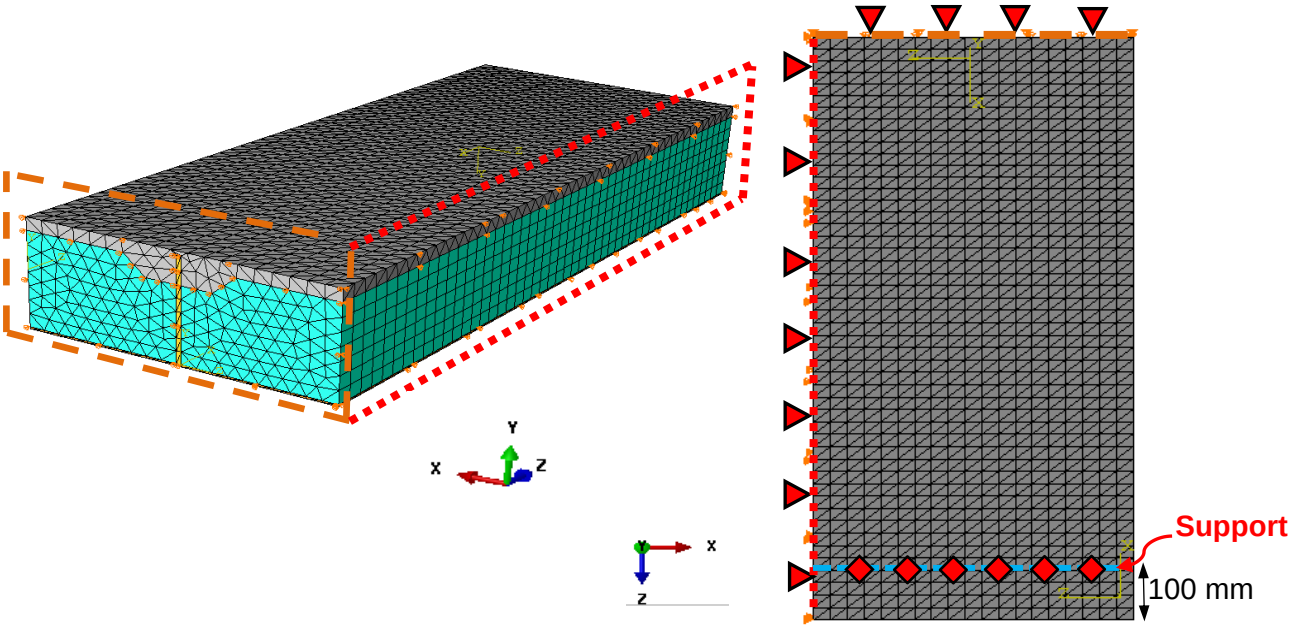

d) Boundary conditions

Fig 4.9. FE model of one quarter of the slab

The proposed hybrid slabs have double symmetry. Therefore, only one quarter of the slab was modeled. The DHCC layers, GFRP rib, GFRP skin, and foam cores of Slab 1 were respectively modeled with 16011, 4652, 8212, and 20272 elements, while in Slab 2 these elements were modeled with 17763, 3999, 7788, and 15120 elements, respectively.

As shown in Fig. 4.9a, a finer mesh was considered around the GFRP shear connectors to obtain results with sufficient accuracy, where relatively high stress gradients are expected to occur. The boundary conditions used in the numerical simulations are illustrated in Fig. 4.9d. The displacement in the X-axis is restricted on one surface of a quarter of slab and the displacement in direction of Z-axis is restricted on the other surface. Moreover, Fig. 4.9d illustrates the support condition, where diamond markers indicate the points with null displacement in the vertical direction (Y).

In the experimental tests, the flexural load was imposed to the hybrid slabs through two load lines. These dispositions were copied to the numerical model. The total applied deflection in each slab was divided into a series of deflection increments. Newton-Raphson incremental-iterative method was adopted by evaluating the tangent stiffness matrix in each iteration, having been adopted a tolerance of 0.001 for assuring convergence.

4.4.3. Failure criteria

Two types of failure were observed in the tested hybrid slabs: 1) Stability failure, based on local buckling in the ribs; 2) Material failure, e.g. DHCC under compression failure, shear failure in foam core, compression rib crushing or tension rib rupture. Stability failure was found when a very large displacement suddenly occurs in the slab. Material failure was found when the maximum stress measured on a specific component was higher than the ultimate tensile and compressive strengths of the corresponding material (see Table 2.4 and Table 4.1). It is worth stating that no damage was observed in the foam cores during the tests, therefore, material failure was considered only for exceeding the maximum stress measured in the DHCC layer, GFRP ribs, and GFRP skin from the ultimate tensile and compressive strengths of the corresponding material.

4.4.4. Results and discussion

In order to define the bilinear traction–separation constitutive law, three parameters need to be determined: the stiffness (K_0), the bond strength (τ_{max}), and the fracture energy (G_f). Moreover, to use the bilinear traction-separation constitutive law, it is necessary to define the parameters of damage initiation. As there is no data on the literature related to the bond behavior between the proposed GFRP shear connectors and reinforced mortars, the unknown

values of the CZM parameters were obtained by executing an inverse analysis. The unknown parameters of the bilinear traction–separation constitutive law and the parameters of damage initiation were determined for both tested hybrid slabs, by adopting the error of the force-deflection response of the numerical simulation lower than 8% and fitting as better as possible the force-strain relationship registered experimentally. Moreover, the damages observed in the numerical simulations should be consistent with the experimental results. Table 4.6 indicates the parameters of the bilinear traction–separation constitutive law and the damage initiation obtained from in the inverse analysis.

Table 4.6. Obtained parameters, stresses and fracture energy for the bi-linear traction-separation law through inverse analysis

		Slab 1		Slab 2	
		DHCC layer to GFRP rib	**DHCC layer to foam core**	**DHCC layer to GFRP rib**	**DHCC layer to foam core**
τ_{max}	[N/mm^2]	10.00	1.00	7.00	0.20
K_0	[N/mm^3]	2500.0	200.0	1658.0	162.0
G_{Gr}	[N/mm]	5.00	0.10	4.00	0.10
δ_0	[mm]	0.004	0.005	0.004	0.001
δ_f	[mm]	1.00	0.20	1.14	1.00
Normal stress (σ_n^0)	[N/mm^2]	30.0	5.0	25.0	10.0
Shear stress in the 1st direction (τ_1^0)	[N/mm^2]	10.0	1.0	7.0	0.2
Shear stress in the 2nd direction (τ_2^0)	[N/mm^2]	10.0	1.0	7.0	0.2
Normal fracture energy	[N/mm]	10.0	0.5	9.0	1.0
Fracture energy for shear in 1st direction	[N/mm]	5.0	0.1	4.0	0.1
Fracture energy for shear in 2nd direction	[N/mm]	5.0	0.1	4.0	0.1

Moreover, the force-deflection response of the numerical simulations of the hybrid slabs where perfect bond between components were assumed were compared with the results obtained in hybrid slabs that employed CZM in Fig. 4.10.

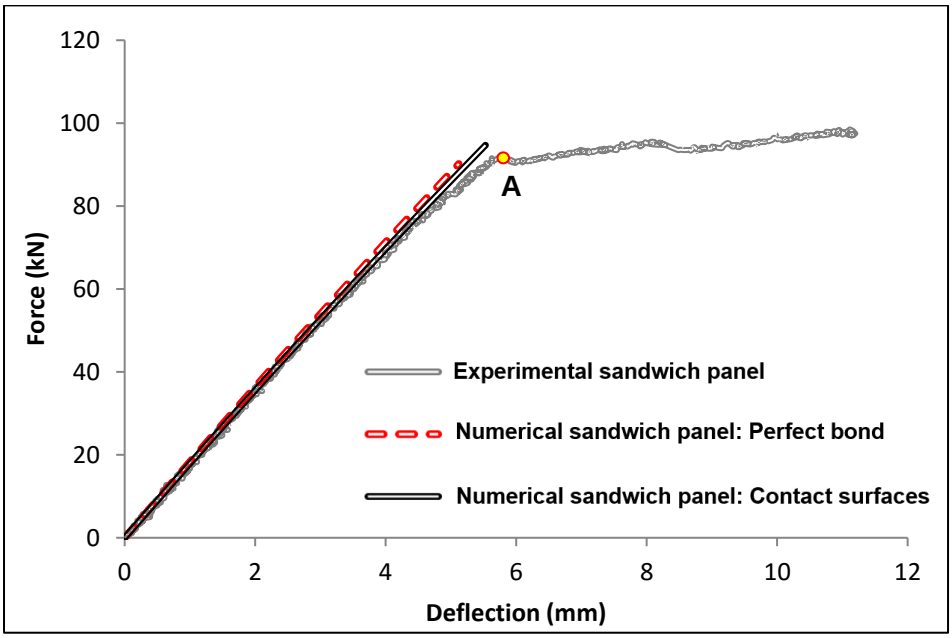

a) Slab 1

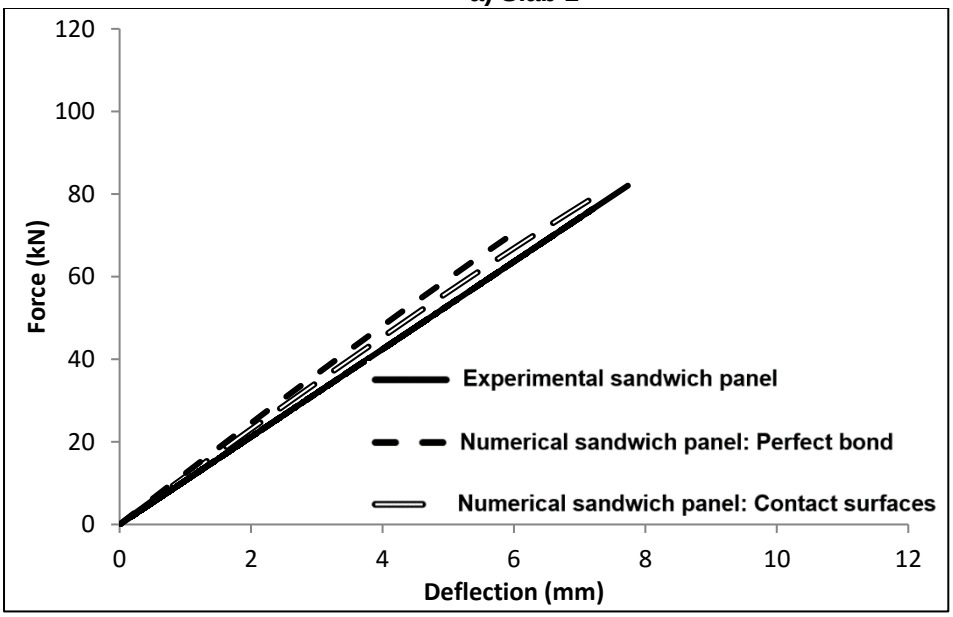

b) Slab 2

Fig 4.10. Comparison between experimental and numerical results

4.4.2.1. Failure modes

During the first cycle of the loading procedure applied in the experimental test of Slab 1, compressive damage in GFRP ribs was recorded, at a deflection of 5.5 mm, as described in chapter three. Above the deflection of 5.5 mm, a hardening stage began, caused by deflection hardening behavior of the reinforced mortar layer and the perforated shear connectors. Point A in Fig. 4.10a corresponds to the initiation of slip between GFRP ribs and DHCC layer.

During the first cycle of the loading procedure applied in Slab 2, in addition to compressive damage in GFRP ribs, splitting cracks were formed on the surface of DHCC layer. Moreover, slip and uplift movements were registered between the GFRP ribs and DHCC layer in Slab 2.

To assess the bond behavior of the interface surfaces introduced between the slab's components, the damage formed in the CZM was detected with the quadratic stress criterion defined by equation (15). Cohesive tensile stress (σ_n^0) and shear stresses in normal directions, 1 and 2 (τ_1^0 and τ_2^0) were defined through an inverse analysis and listed in Table 4.6 for Slab 1 and Slab 2.

In the numerical model developed for Slab 1, the maximum shear stress in the interface surface between the DHCC layer and the GFRP ribs was 9.08 MPa, while the shear strength in the defined CZM was 10 MPa. With respect to the defined damage evolution criterion in equation 4.15, damage is close to be initiated in the contact surface between the DHCC layer and the GFRP ribs.

In the numerical model developed for Slab 2, the maximum shear stress measured at the interface surface between the DHCC layer and the GFRP ribs was 7.67 MPa, which is higher than the shear strength established and shows the damage formed in the defined CZM (see Table 4.6). The FE model could also capture the uplift and the slip between DHCC layer and GFRP rib in Slab 2, as shown in Fig. 4.11a and Fig. 4.11c.

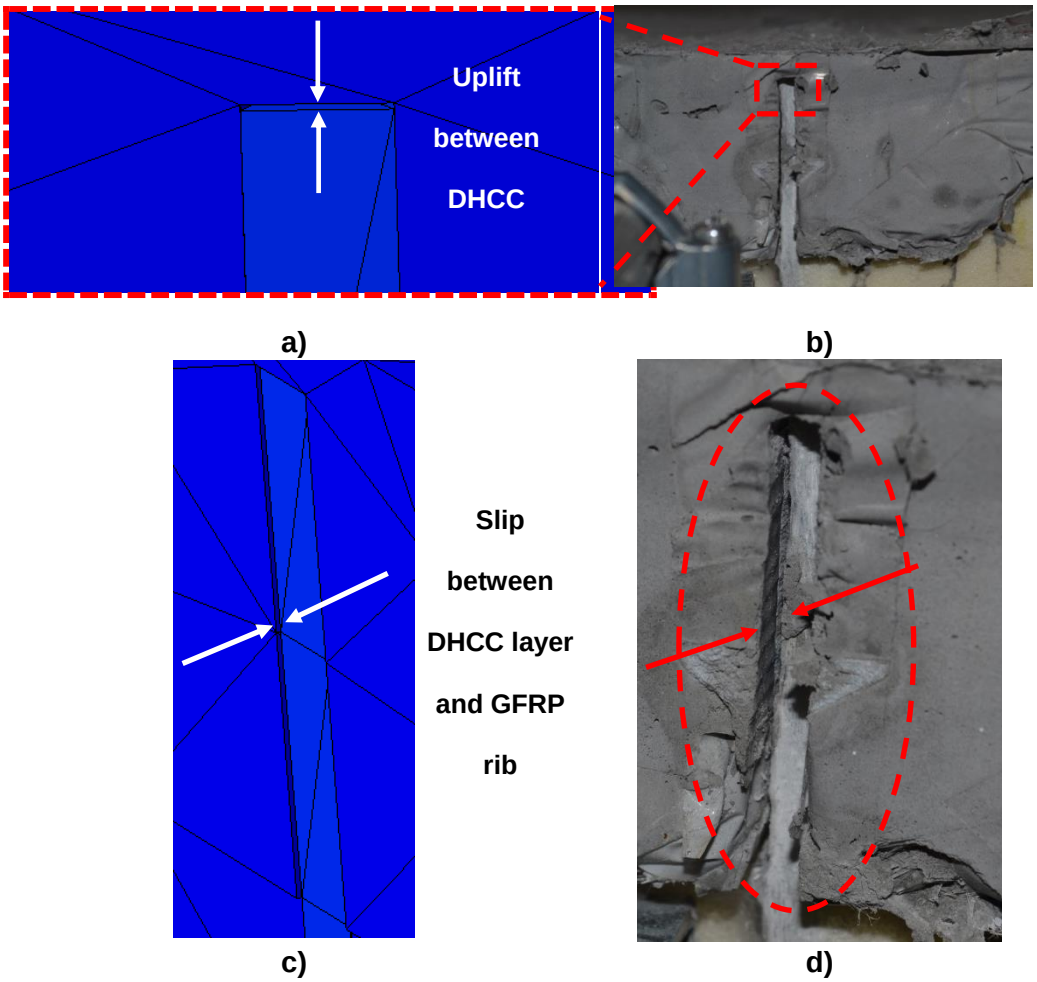

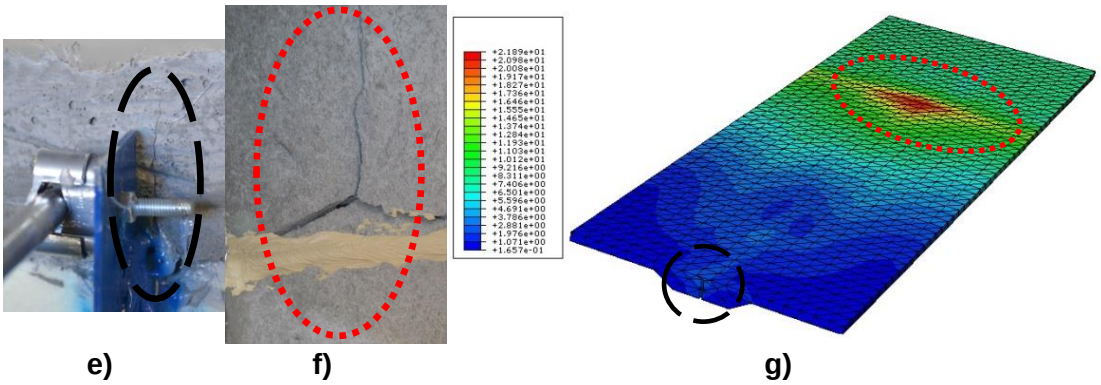

Fig 11. Slab 2 - Separation between DHCC layer and GFRP rib: a) Uplift in the numerical model and b) Uplift in the experimental tests; c) Slip in the numerical model and d) Slip in the experimental tests; e) Formed crack in the connection zone between DHCC layer and GFRP rib; f) Localized compression in the DHCC layer; g) Von Mises stresses in the DHCC layer

In ABAQUS software, it is not possible to provide a failure criterion for composite materials modeled with solid elements, therefore, the onset of damage in GFRP materials was detected through using the maximum stress and maximum strain criteria. In these criteria, material failure was detected when the maximum stress or the maximum strain measured on a specific component exceeds the respective strengths or the ultimate strain, respectively.

Thus, failures in the solid elements of GFRP materials were found by comparing the maximum stresses and strains obtained in the elements with the capacity of the materials in terms of stresses and strains, presented in Table 2.4. According to the recorded strains through installed strain gauges in the GFRP ribs, compressive damages occurred in GFRP ribs of Slab 1 and Slab 2 due to exceed compressive strains 00026 and 0.0003, respectively. The maximum compressive strains in the GFRP ribs (SG 1) obtained in the FE models were 0.0004 in Slab 1 and 0.0038 in Slab 2. In both cases, the strain values measured in the numerical models were higher than the strains measured in the corresponding experimental tests (see Fig. 4.13).

The DHCC material was experimentally evaluated and the corresponding results are presented in chapter three. Its compressive strength measured about 24 MPa. The maximum compressive stress obtained in the FE model was 23.8 MPa in Slab 1 and 26.7 MPa in Slab 2 under the load line (see Fig. 4.11g). According to the values mentioned, the DHCC layer was nearly damaged due to high compressive stresses in Slab 1, under the load line, while the DHCC layer in Slab 2 has entered in a post peak phase. Fig. 4.12 presents the distribution of longitudinal principal stresses and in-plane shear stresses in the GFRP ribs. The captured damages in the shear connectors and GFRP ribs of the numerical results are consistent with the experimental ones, as indicated in Fig. 4.12.

a) Damaged GFRP ribs after implementation of the experimental test in Slab 1

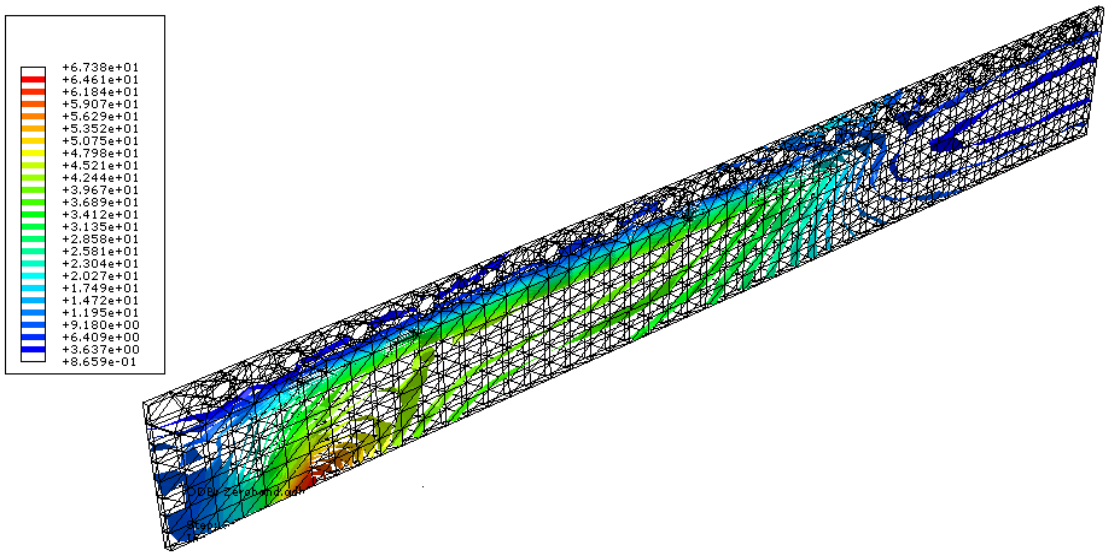

b) Distribution of longitudinal principal stresses in the GFRP rib of Slab 1

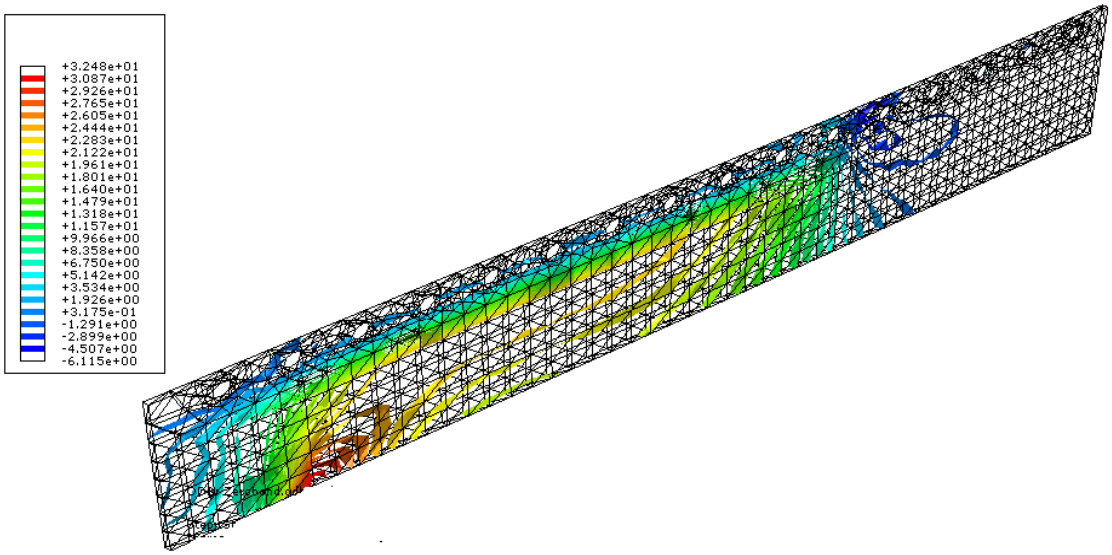

c) Distribution of shear stress in the GFRP rib of Slab 1

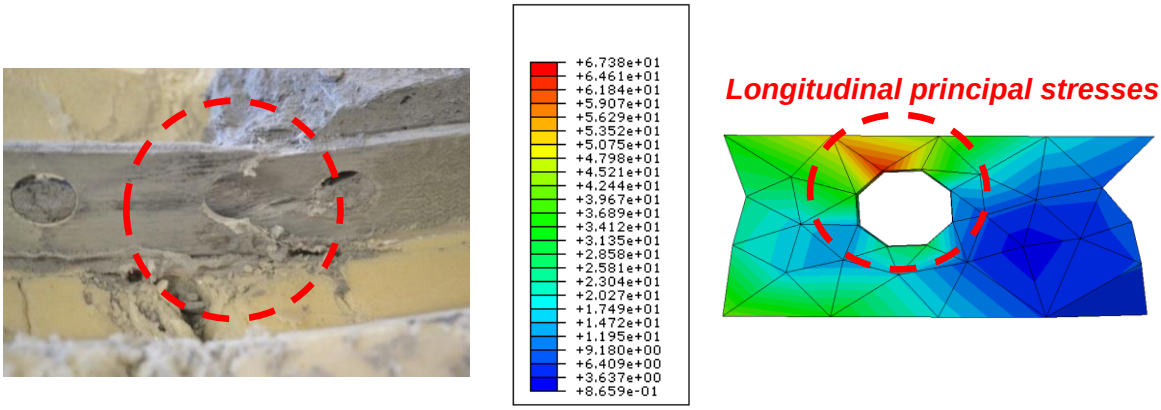

d) Experimental and numerical damage positions in the GFRP rib of Slab 1

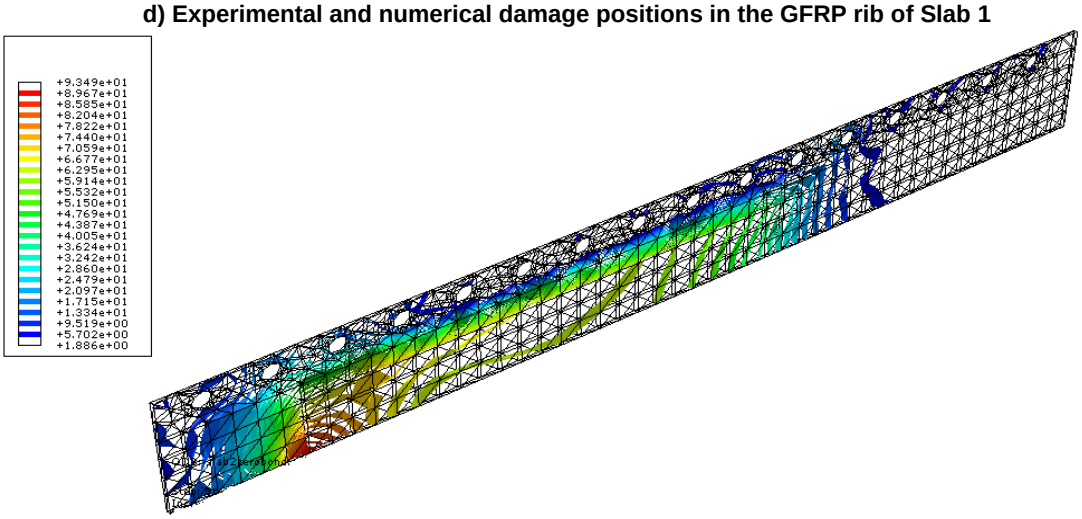

e) Distribution of longitudinal principal stresses in the GFRP rib of slab 2

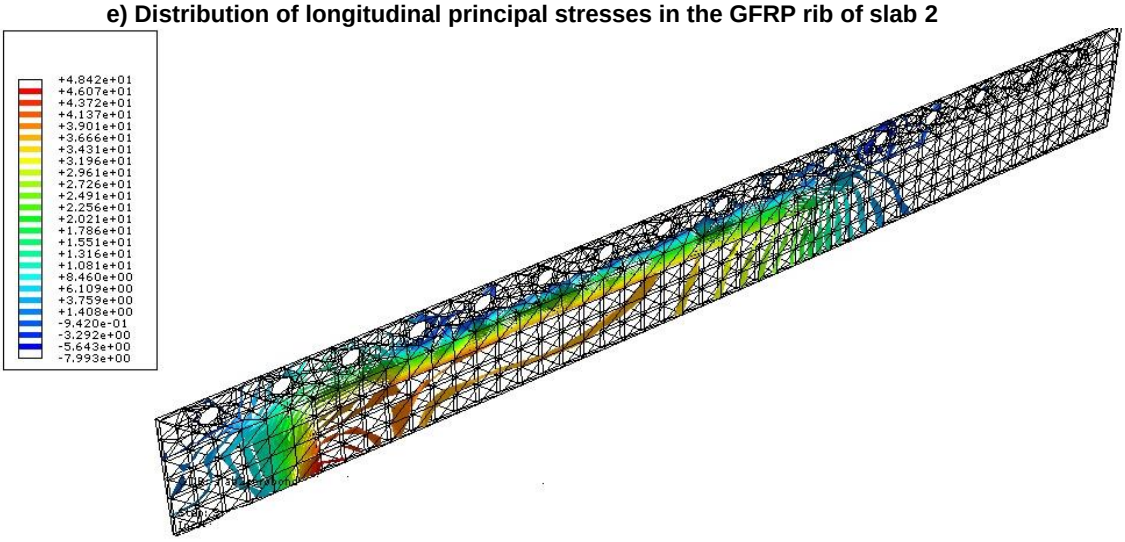

f) Distribution of shear stresses in the GFRP rib of Slab 2

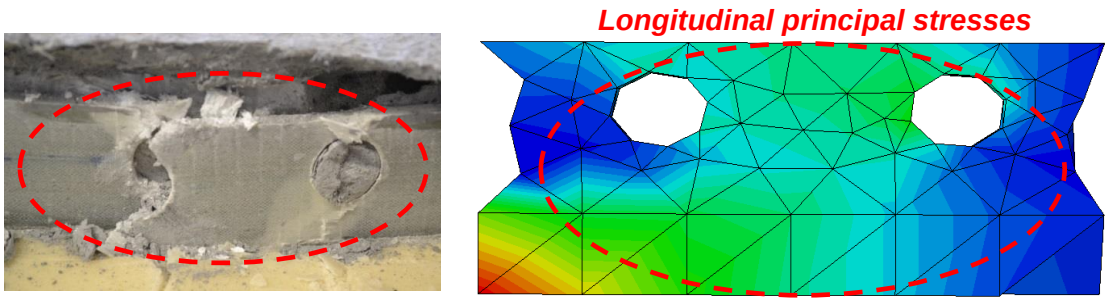

g) Numerical and experimental failure positions in the GFRP rib of Slab 2

Fig 4.12. Results obtained in the ribs of Slab1 and Slab 2

Concerning the presented results, it can be concluded that the developed 3D FE models can well capture the failure modes registered in the experimental tests, and have high potential to predict the flexural performance of the proposed hybrid slabs.

4.4.4.2. Load-deflection response

Fig. 4.10 depicts the load versus deflection responses obtained in the numerical simulations of the experimentally tested slabs. It can be observed that the results obtained in the numerical simulations have good agreement with the experimental ones. However, there is some tendency to overestimate stiffness in the FE simulation.

Equation (4.20) defines how to calculate the error percentages, which may be defined in terms of force, deflection, or stiffness. The corresponding results are listed in Table 4.7 and can be used to assess the accuracy of perfect bond or CZM as interface surfaces between slab's components,

$$Error\,in(\,force, deflection, stiffness) = \left(\frac{A_N - A_E}{A_E}\right) \times 100 \qquad (4.20)$$

where, A_N and A_E refer to values obtained from numerical and experimental results, respectively.

Table 4.7. Obtained error percentages due to use perfect bond and cohesive zone model

	Slab 1			Slab 2		
Bond type	**Error in force (%)**	**Error in deflection (%)**	**Error in stiffness (%)**	**Error in force (%)**	**Error in deflection (%)**	**Error in stiffness (%)**
Cohesive zone model (CZM)	+7.7	-2.8	+3.8	-3.3	-7.0	+3.5
Perfect bond	-18.1	-13.8	+4.7	-15.9	-28.4	+10.8

As was expected, using CZM as interface between slab's components led to attain smaller errors in force, deflection and stiffness values than using perfect bond between slab's

components. Errors are lower than 8% for force, 7% for deflection, and 5% for stiffness for CZM interface, while perfect bond presents an error lower than 20% for force, 30% for deflection, and 10% for stiffness. Since the use of CZM significantly increases the models' computational cost, it is concluded that the use of perfect bond also results in an acceptable response for pre-design purposes, with enough reasonable accuracy in engineering applications.

4.4.4.3. Load-strain response

The recorded experimental and numerical load-strain responses of the tested hybrid slabs are shown in Fig. 4.13. The tensile strains did not exceed 0.0012 in both slab skins, which is well below the tensile failure strain of 0.0222 in skin fibers oriented at 90º, and 0.0166 in skin fibers oriented at 0º. This fact confirms that no tensile failures occurred in the GFRP skin.

According to the results obtained, a good agreement was achieved between the experimental and the numerical simulations, with exception for the values registered by SG 3 and SG 2. The thicknesses of GFRP ribs and GFRP skin were increased in the connection zone to obtain a continuous uniform distribution of stresses and forces (see Fig. 4.14b). These higher thicknesses in the transition zone could be the cause for the differences between experimental and numerical strain values in SG 3 and SG 2 (see Fig. 4.14a).

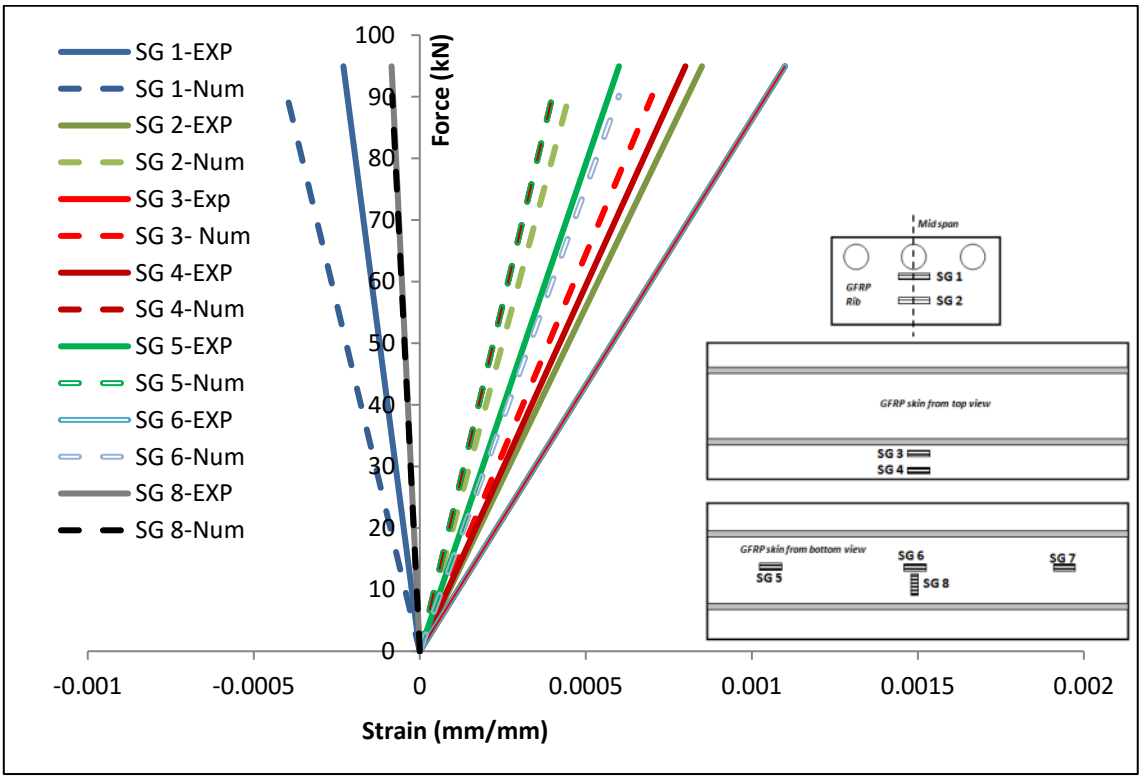

a) Slab 1

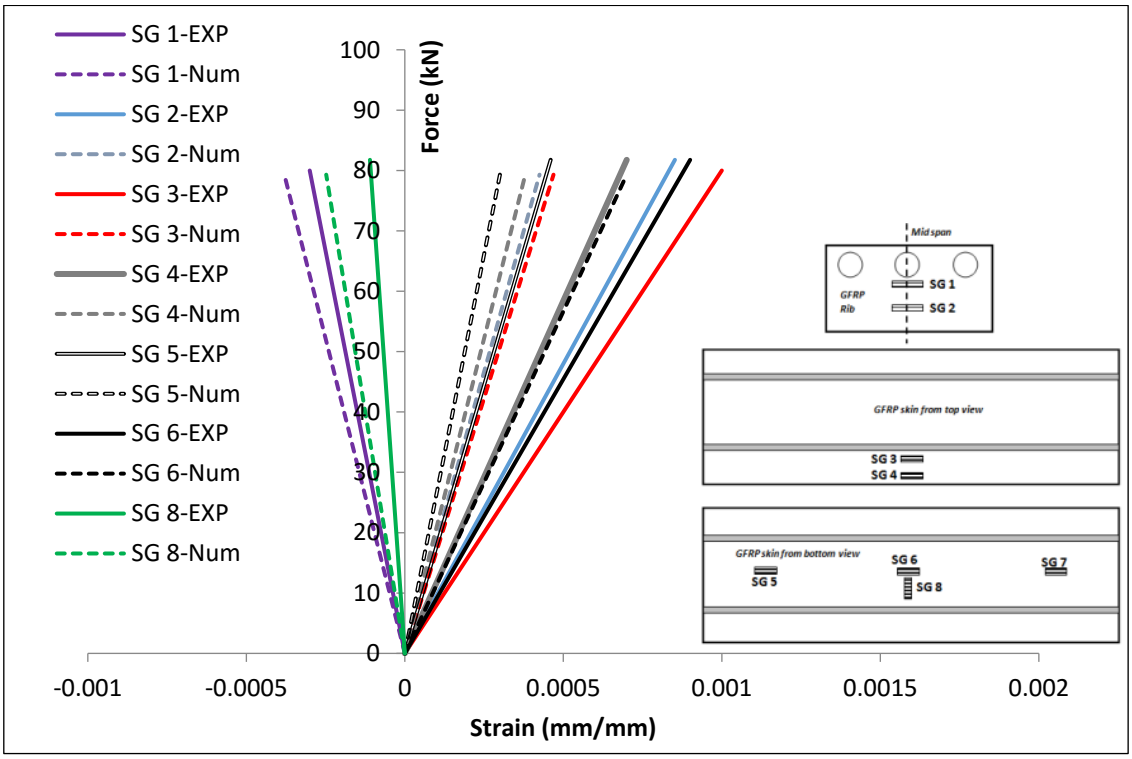

b) Slab 2

Fig 4.13. Comparison between strain values measured in the experimental tests and obtained in numerical simulations

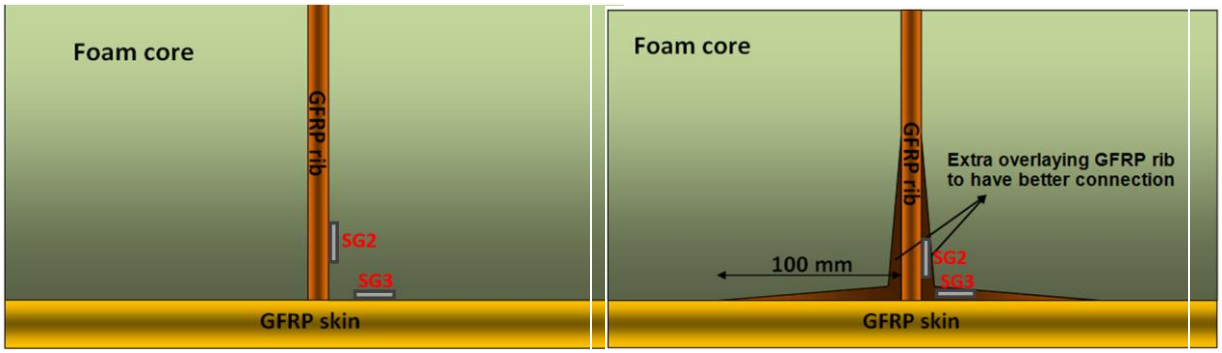

a) **b)**

Fig 4.14. a) Modeled slab's components in the FEM software; b) Thickening of GFRP ribs and GFRP skin in the connection zone

4.5. Efficiency of the proposed hybrid-panel

In order to assess the efficiency of the proposed hybrid sandwich panels, the FEM analysis was developed for two other sandwich panel systems including: 1) Simple sandwich panel with two GFRP skins placed on top and bottom with shear stresses transferred by a foam core in the middle of two skins; 2) GFRP sandwich panel with internal ribs: two GFRP skins are used as top and bottom skins and shear stresses are transferred by GFRP ribs together with the foam cores (the shear stress is mainly transferred with GFRP ribs). A schematic figure of slabs and slab's component placement that used to assess under four point bending test indicated in Table 4.8.

Table 4.8. Used different types of sandwich panels in the numerical simulations

Slab name	Schematic figures of slabs	Component placements	
Simple sandwich panel		Top	GFRP skin
		Middle	Foam core
		Bottom	GFRP skin
Sandwich panel with internal rib	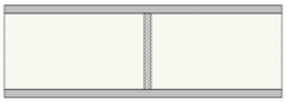	Top	GFRP skin
		Middle	GFRP rib
		Bottom	GFRP skin
Hybrid sandwich panel		Top	Reinforced mortar
		Middle	Foam core
		Bottom	GFRP skin

It is worth stating that in the modeling of the GFRP sandwich panel with internal ribs and simple GFRP sandwich panel, it was assumed that the thickness and material properties of GFRP sheets and foam cores are equal to hybrid slabs. For instance, the thickness of GFRP skin in the Slab 1 was equal to 3 mm, therefore, in the numerical simulation for both GFRP sandwich panel with internal ribs and simple GFRP sandwich panel the thickness of GFRP faces were considered equal to 3 mm. Moreover, the thickness of ribs in the GFRP sandwich panel with internal ribs was considered equal to 6 mm. As no slip was observed between the GFRP skin, the GFRP rib, and the foam cores during the experimental tests it was postulated that in the numerical FEM simulation, GFRP faces and ribs connect to foam core as perfect bond. It is worth mentioning that using equal thicknesses for slab's components of other typical sandwich panels is not fair, once the thicknesses of slab's components for other typical sandwich panels should be designed and then comparison should be executed. However, the results obtained provide a general idea of the structural performance of hybrid slabs.

The load-deflection curves obtained from FEM analysis for both proposed sandwich panels (with and without internal ribs) are depicted in Fig. 4.15. The results gathered from this FEM analysis, initially, confirmed the results of previous studies, where it was concluded that the internal ribs play an important role in increasing both the stiffness and the load carrying capacity of the sandwich panel system. Moreover, it demonstrates that using DHCC layer as top layer in the proposed hybrid sandwich panels result in significant increase of stiffness and load carrying capacity compare to both simple sandwich panels and sandwich panels with internal ribs.

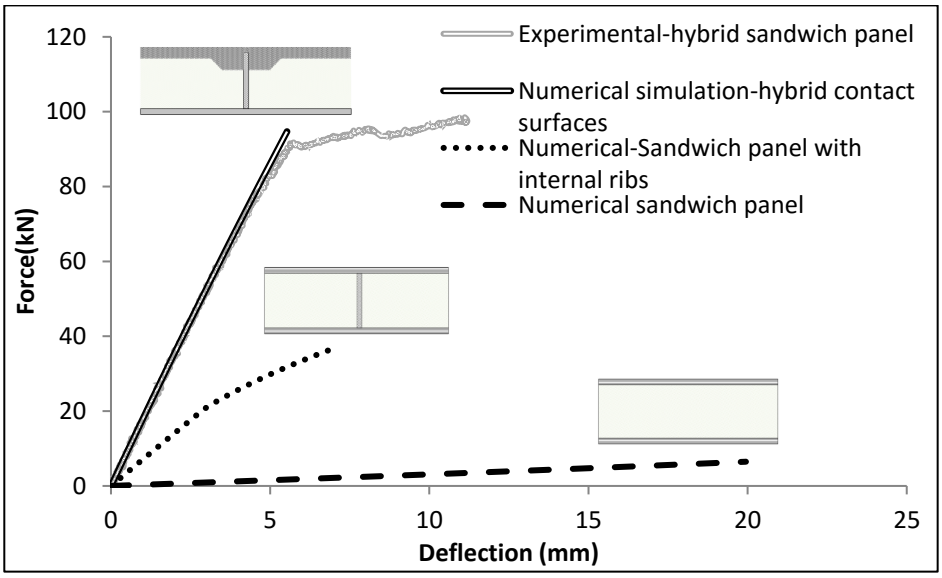

a) Slab 1

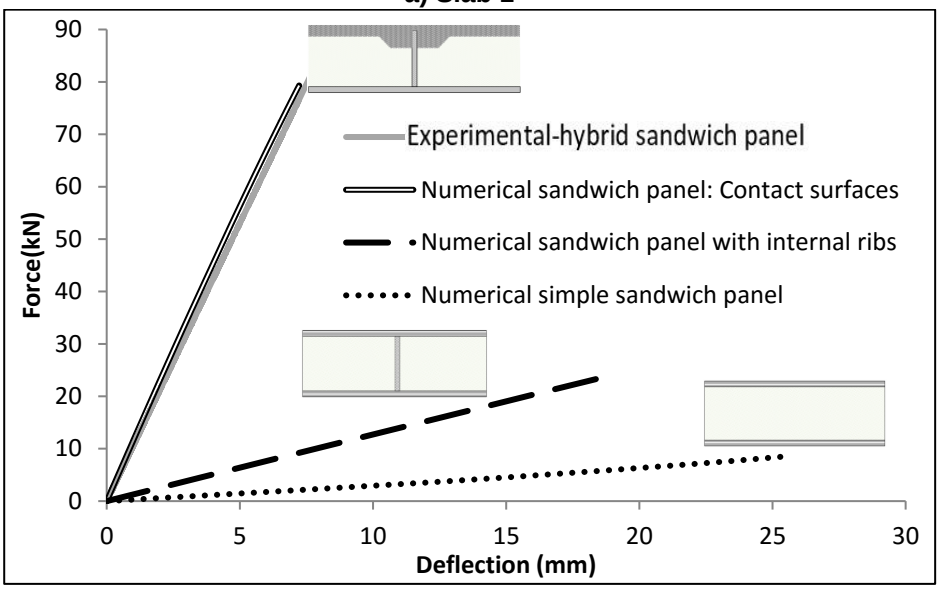

b) Slab 2

Fig 4.15. Load-deflection curves of the proposed hybrid: a) Slab 1; b) Slab 2

4.5.1. Prediction of stiffness

To predict the load-deflection response of the proposed hybrid slabs, a simplified assumption was adopted to predict the stiffness of simply supported hybrid slabs with the same cross sections as the one considered for Slab 1 and Slab 2 and submitted to four point bending load. Equation (4.21), presented in the manuscript and based on elementary sandwich theory, is able to predict the stiffness of hybrid slabs under FPB load, accounting for flexural and shear deformations.

In equation (4.21), P is the applied load, L is the beam span, EI is the flexural stiffness which was calculated using transformed cross-section analysis (in calculation of this value, effects

of all materials were considered, including foam cores, DHCC layer, GFRP ribs and GFRP skin), G_{rib} is the shear modulus of the GFRP ribs, and A is the cross section of the ribs.

$$\Delta = \frac{(23PL^3)}{(648EI)_{Total}} + (\frac{PL}{3KGA})_{Rib} \quad (4.21)$$

In equation (4.21), it was assumed that shear stresses are transferred between top and bottom skins by GFRP ribs while foam cores have no contribution within transferring shear stresses. Both experimental and analytical responses of the proposed hybrid slabs under four point bending test are indicated in Fig. 4.16. Respect to the indicated results, it is revealed that the analytical estimation has very good agreement with the experimental results in the linear stage.

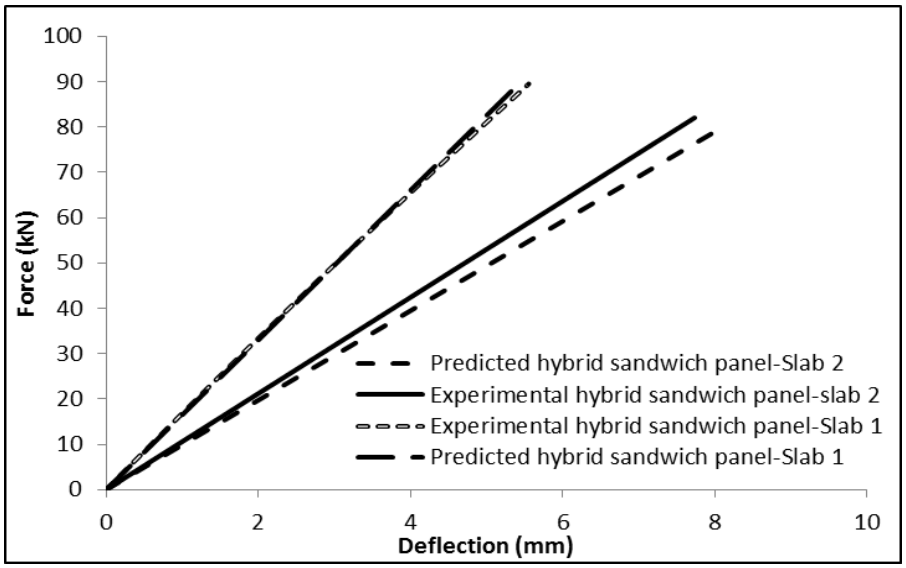

Fig 4.16. Comparison between experimental results and predicted results

based on the assumption that the maximum load carrying capacity of hybrid slabs is obtained for a predefined mid-span deflection that is equal to a serviceability limit state of δ= L/300. Regarding the results depicted in Fig. 4.18, it was revealed that equation (4.21) is a reliable equation to predict the stiffness and force-deflection of hybrid sandwich panel in linear stage. Therefore, this equation was developed for predicting the performance of hybrid sandwich panels under distributed load. Equation (4.22) represents deflections due to applied distributed load. This equation is functioned by the amplitude of the applied distributed loads, considering the span length, flexural stiffness, shear modulus of rib, and cross section of rib.

$$\Delta = \frac{(5qL^4)}{(384EI)_{Total}} + (\frac{qL^2}{8KGA})_{Rib} \quad (4.22)$$

where, q is the applied load, L is the beam span, EI is the flexural stiffness, G_{rib} is the shear modulus of the GFRP ribs, K is the Timoshenko shear coefficient or reduction factor of stiffness and equal to 0.833 and A is the cross section of the ribs. Using the calculated EI values, a deflection limit of δ = L/300 and considering now a span of 5.0 m that is commonly

found in many residential buildings and the self-weight of the slabs analyzed, it was possible to obtain a maximum load of 3.73 kN/m^2 for Slab 1 and 2.35 kN/m^2 for Slab 2. The values of the slab self-weight were discounted from the maximum load values presented (Slab 1 weight is equal to 86.4 kg/m^2 and Slab 1 weight is equal to 63.2 kg/m^2). These values are within the range of live load values usually considered in European design codes, for residential buildings.

4.6. Economy assessment of sandwich panels

Good structural performance of this type of new slabs besides low price can convince the users to use this type of hybrid slabs instead of the traditional ones. In this regard, a cost analysis was executed on the proposed hybrid slabs to indicate economic benefits. The calculated prices for one cubic meter of hybrid Slab 1 and Slab 2 listed in Table 4.9.

Table 4.9. Price of used materials in the hybrid slabs

	Resin	**Fiber (EBX 400)**	**Fiber (UNI 640)**	**Foam for Slab 1**	**Foam for Slab 2**	**DHCC**
	€/kg	**€/kg**	**€/kg**	**€/m**	**€/m**	**€/Lit**
Price	3.2	3.8	2.8	38.45	29.48	1
Price of slab's components (€/m^2)						
	Resin	**Skin**	**Rib**	**Foam**	**DHCC**	
Slab 1	22.40	12.92	51.96	38.45	28.00	
Slab 2	20.80	21.54	32.96	29.48	24.00	

Considering the presented prices of materials in Table 4.9 from their suppliers, cost of Slab 1 and Slab 2 computed about 192 €/m^2 and 161 €/m^2, respectively, while the price of concrete slabs for one cubic meter is around 140-180 Euro [22]. Comparing these two prices reveals that the price of the proposed hybrid slabs are approximately in range of conventional concrete slabs, but 2/3 lighter than concrete slabs used in residential buildings. Moreover, cost analysis was implemented for two other sandwich panel systems to compare the economic aspects of the prosed hybrid slabs with other sandwich panel systems. The results obtained from cost analysis of different sandwich panel systems presented in Fig. 4.17. According to the results attained, the minimum price was detected for simple sandwich panel, but due to low carrying capacity of this sandwich panel system, there is a low interest to use it. Therefore, the main comparison implemented between the sandwich panel with internal ribs and the proposed hybrid sandwich panel. Interestingly, the highest price assigned to rib's fiber and then foam cores for both sandwich panel with internal ribs and hybrid sandwich panel.

With respect to the presented results in Fig. 4.17, the proposed hybrid sandwich panels has lower price and better structural performance when compare to the sandwich panel with internal ribs. Hence, combination of good structural performance and lower price provides significant incentives for users to employ these new proposed hybrid slabs.

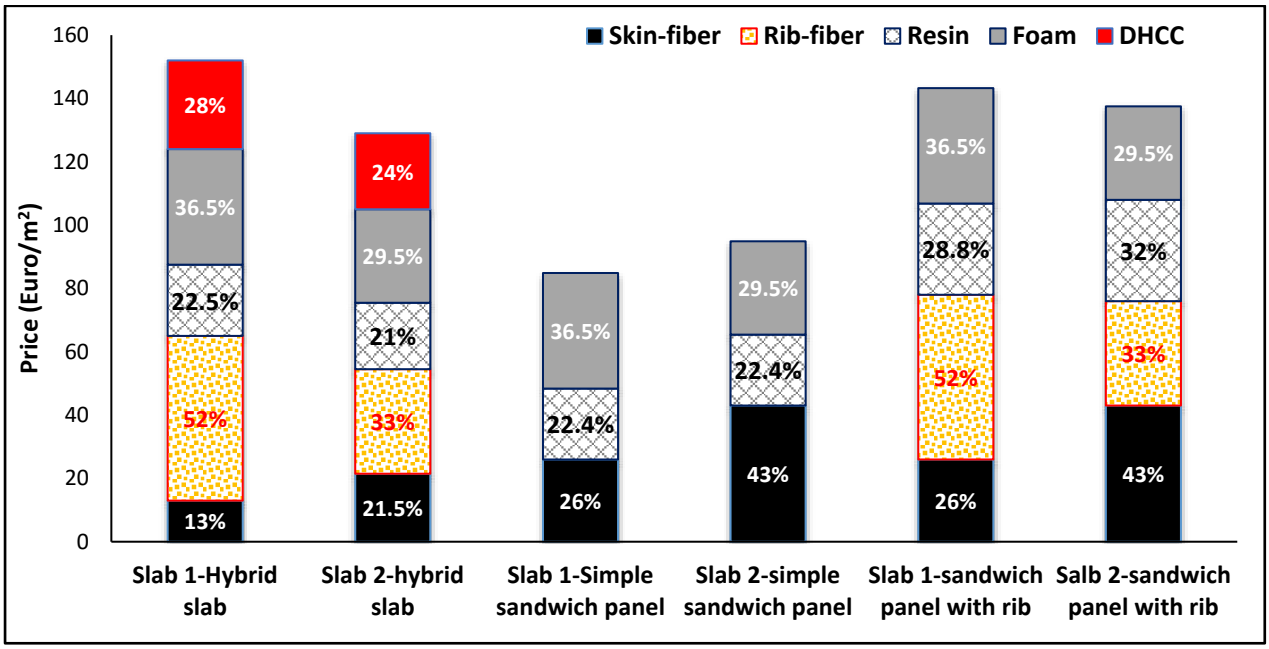

Fig 4.17. Comparing cost analysis of sandwich panel systems

4.5. Conclusions

In this study, an initial parametric study was carried out to reveal the influence of material properties and geometry on the global behavior of full-scale hybrid slabs. Then, some optimized slabs were proposed and analyzed and finally, two slabs were chosen. The two optimized slabs were previously manufactured and tested experimentally at University of Minho. Then, the obtained experimental specimens and results were considered in the development of FEM models that could well capture the observed damages, and predict the force/deflection or the force/strain responses of the hybrid sandwich panels. The main outcome results of this numerical study are herein presented:

1. The parametric study demonstrated that the GFRP rib thickness is the most important slab component in increasing the load carrying capacity of hybrid slabs.
2. The minimum height of hybrid slab should be 100 mm.
3. It is not possible to occur local buckling in the GFRP ribs under SLS.
4. Applying the interface constitutive model for bond behavior between the slab's components had significant importance in achieving a robust and more precise numerical simulation.
5. As there is no specific closed-form design code for hybrid slabs, using perfect bond between the slab's components can be a reliable and helpful option for pre-design purposes.
6. Using the interface constitutive model resulted in attaining more accurate results but increased significantly the computational cost and time. Therefore, using perfect bond

as interface between slab's components led to results with lower accuracy, in compare to the use of CZM. However, using perfect bond can reduce significantly the computational cost and time associated with these models.

References

[1]. Ziad K. Awad, Aravinthan T., Zhuge Y., 2012, "Experimental and numerical analysis of an innovative GFRP sandwich floor panel under point load", Journal of Engineering Structures, Vol. 41, pp: 126-135.

[2]. Raj S., Kumar R., Bharath Kumar B.H., Gopinath S., Iyer N.R., 2015, "Flexural studies on Basalt Fiber Reinforced Composite sandwich panel with profile sheet as core", Journal of Construction and Building Materials, Vol. 82, pp: 391-400.

[3]. Mostafa A., Shankar K., Morozov E.V., 2013, "Effect of shear keys diameter on the shear performance of composite sandwich panel with PVC and PU foam core: FE study", Journal of Composite Structures, Vol. 102, pp: 90-100.

[4]. Sharaf T., Fam A., 2013, "Analysis of large scale cladding sandwich panels composed of GFRP skins and ribs and polyurethane foam core", Journal of Thin-Walled Structures, Vol. 71, pp: 91-101.

[5]. Mastali M., Valente I.B., Barros J.A.O., Gonçalves D.M.F., 2015, "Development of innovative hybrid sandwich panel slabs: Experimental results" Journal of Composite Structures, Vol. 133, pp: 476-498.

[6]. Hibbitt, Karlsson, and Sorensen, Inc. ABAQUS Theory manual, User manual and Example Manual, Version 6.11., 2010, USA.

[7]. Barros J.A.O., Figueiras J.A., 2001, "Nonlinear analysis of steel fibre reinforced concrete slabs on grade", Journal of Computers and Structures, Vol. 79, pp: 97-106.

[8]. Pereira E.B., Barros, J.A.O., Camões A.F.F.L., 2008, "Steel fiber reinforced self-compacting concrete – experimental research and numerical simulation", ASCE Structural Engineering Journal, Vol. 134, pp: 1310-1321.

[9]. Barros J.A.O., Costa I. G., Ventura-Gouveia A., 2011, "CFRP flexural and shear strengthening technique for RC beams: experimental and numerical research", Journal of Advances in Structural Engineering, Vol. 14, pp: 559-581.

[10]. José Sena-Cruz, 2004, "Strengthening of concrete structures with near-surface mounted CFRP laminate strips", PhD thesis, Minho University, Portugal.

[11]. Selcom multiaxial technology company, Biaxial products. http://www.multiaxialfabricselcom.com/en/Products/

[12]. Ventura-Gouveia A., Barros J.A.O., Azevedo A.F.M., 2011, “Crack constitutive model for the prediction of punching failure modes of fiber reinforced concrete laminar structures”, Journal of Computers and Concrete, Vol. 8, pp: 735-755.
[13]. BS EN 1992-1-1:2004 Eurocode 2: Design of concrete structures – Part 1.1: General rules and rules for buildings; with UK National Annex to BS EN 1992-1-1:2004.
[14]. Bank L.C., 2006, “Composites for construction: Structural design with FRP materials”, John Wiley & Sons, New Jersey, pp: 413.
[15]. Mastali M., Valente I.B., Barros J.O.A., 2013, “New composite slab system for the structural rehabilitation of traditional buildings”, FRPRCS11, Guimaraes, Portugal.
[16]. Eurocomp, 1996, “Structural Design of Polymer Composites”, Eurocomp Design Code and Handbook (J. Clarke, ed.), E&FN Spon, London, UK.
[17]. Khoramishad H., Crocombe A.D., Katnam K.B., Ashcroft I.A., 2010, “Predicting fatigue damage in adhesively bonded joints using a cohesive zone model”, International Journal of Fatigue, Vol. 32, pp:1146-1158.
[18]. Corigliano A., Allix O., 2000, “Some aspects of interlaminar degradation in composites”, Journal of Computer Methods Application Mechanic Engineering, Vol. 185, pp: 203–224.
[19]. Taleb Obaidat Y., Susanne H., Dahlblom O., 2010, “The effect of CFRP and CFRP/concrete interface models when modelling retrofitted RC beams with FEM”, Journal of Composite Structures, Vol. 92, pp: 1391-1398.
[20]. Qiao P., Chen Y., 2008, “Cohesive fracture simulation and failure modes of FRP–concrete bonded interfaces”, Journal of Theoretical and Applied Fracture Mechanics, Vol. 49, pp: 213-225.
[21]. Lameiras R., Barros J.A.O., Valente I.B., Azenha M., 2013, “Development of sandwich panels combining fiber reinforced concrete layers and fiber reinforced polymer connectors. Part I: Conception and pull-out tests”, Journal of Composite Structures, Vol. 105, pp: 446-459.
[22]. Langdon D., 2014, “Spon’s Architects’ and Builders’ Price Book”, CRC Press, UK.
[23]. Lorenzis L., Fernandob D., Teng J., 2013, “Coupled mixed-mode cohesive zone modeling of interfacial debonding in simply supported plated beams”, International Journal of Solids and Structures, Vol. 50, pp: 2477-2494.

Chapter 5

Flexural performance of hybrid sandwich panels with special focus on the shear connection behavior

5.1. Introduction

Sandwich panels are an interesting solution for building floors due to their high strength to weight ratio. Low self-weight, high stiffness and improved durability have increased the demand for this type of composite structures and several studies have been dedicated to improve the mechanical properties of sandwich structures. Typical sandwich panels are composed of three different layers that include two thin, stiff and resistant composite material skins (such as FRP materials), separated by a layer of a low density material that is usually made with basalt, polyvinyl chloride (PVC), polystyrene (PS), polyurethane (PU), polymethacrylamide, polyetherimide (PEI) or styreneacrylonitrile (SAN). The proper combination of different core and skin materials may promote the merge of the most advantageous properties of each constituent material and even eliminate some negative characteristics. The combination of skins with appropriate cores leads to high stiffness-to-weight and high strength-to-weight ratios [1]. The development of new production techniques has made sandwich panels more affordable and their pre-fabrication allows an easier mounting, with greatly reduced construction times [1]. The main problems of this type of sandwich panels are related to a low load carrying capacity when compared to other structural elements (for example, the ones that use concrete), a low resistance to high temperatures and various possible failure modes, which make the acceptance of sandwich panels by the construction industry more difficult [1]. Therefore, wide studies have been carried out to compensate the proposed disadvantages and improve the sandwich panel behavior.

In the previous chapter, a FEM based analysis used to perform a parametric study on hybrid sandwich panels with GFRP bottom skin and ribs and top skin made with deflection hardening cementitious composites (DHCC). This preliminary FEM based study was developed to optimize the slab dimensions and reveal the contribution of each structural component to the global behavior of the hybrid sandwich slabs. The numerical findings wereconsistent with the experimental results attained in chapter three. In respect to the numerical findings, the hybrid sandwich slabs present high load carrying capacity, high span to weight ratio and high stiffness. However, these good structural aspects require providing good connection between GFRP shear connectors and DHCC layer. Since, previous experimental studies in [2, 3] and also Chapter 3 showed that there are some difficulties in transferring shear stresses from top skin to bottom skin of hybrid sandwich panels through shear connectors.

Thus, in this chapter all efforts are made to assess the flexural performance of hybrid sandwich panels with special focus on the shear connection behavior. The flexural assessment was executed by using four point bending tests. These bending tests aim to analyze the behavior of

shear connectors that are defined within the GFRP ribs and stay embedded in the DHCC (Deflection Hardening Cement Composites) layer after curing. Two types of shear connectors are used in the tested hybrid slabs: indented and perforated shear connectors.
Therefore, two hybrid slabs with indented shear connectors are manufactured and tested under Four Point Bending (FPB) test. In chapter 3, two other hybrid slabs with perforated shear connectors were previously tested under FPB test, and the corresponding experimental results are here used to implement a comparative analysis.

5.2. Dimensions of slab's components

Two optimized hybrid sandwich panels with heights of 140 mm and 180 mm were proposed in chapter two, which are depicted in Fig. 2.1. The dimensions of slab's components were obtained with execution of a parametric FEM-based analysis in chapter four. Table 2.1 lists the geometry of the components associated with the two types of sandwich panels developed, herein designated by Slab 1, with total height of 180 mm, and Slab 2, with total height of 140 mm.

The mechanical properties of materials used in the hybrid slabs like DHCC, GFRP sheets, and foam core were completely explored through execution of experimental tests and described in chapter two. Therefore, in the following, the geometry of the embedded GFRP shear connectors into DHCC layer, devices used to execute FPB test and adopted test setup for this purpose, and comparative results have been presented.

5.3. Geometry of the proposed shear connectors

The performance of three types of embedded GFRP connectors, including T shape profiled connectors, perforated connectors with circular holes and perforated connectors with elongated holes, was assessed by Lameiras et al. [4] with pull-out tests. Other types of connectors, like connectors adhesively bonded to steel fiber reinforced concrete block were also assessed but the observed failure was rather brittle. It was concluded that embedded connectors provide high load carrying capacity, significant deformation capacity after peak load and an appreciable residual strength [4]. Thus, it was initially decided to use perforated shear connectors in the hybrid slabs to establish the shear connection between the GFRP rib and the DHCC layer.

A first group of hybrid slabs comprising two hybrid slabs, with the geometry proposed in Fig. 2.1 and detailed in Table 2.1 was fabricated and tested. In these specimens, only perforated

connectors with circular openings were considered. The corresponding results are completely reported in chapter three. Respect to the presented results in chapters three and four, the nonlinearity observed in the response of the tested slabs was mainly caused by the damage occurred in the connection between GFRP ribs and DHCC layer due to high stress concentration around the perforated shear connectors. Therefore, in the present chapter, indented shear connectors are proposed with the objective of postponing the damage occurred in GFRP ribs and providing a higher load carrying capacity, which are obtained by increasing the sectional area of the DHCC dowels. The indented openings in the GFRP ribs filled with DHCC material form larger dowels that increase the mechanical anchorage between the GFRP connectors and the DHCC layer. The indented openings in the GFRP ribs also alter their stiffness.

In the present study, all efforts are made to assess the flexural performance of hybrid sandwich panels with indented shear connectors as well as to implement a comparative study regarding the experimental results attained from FPB tests conducted on the hybrid slabs with perforated shear connectors in chapter three. Considering this, two slabs with 2000 mm of length and 800 mm of width were built and experimentally tested under FPB test.

The details of the perforated and indented shear connectors used in the fabricated specimens are shown in Fig. 5.1b and Fig. 5.1c, respectively. To create shear connectors in GFRP ribs, simple circular holes with small diameter were cut on the top zone of the GFRP part that stays embedded in the DHCC layer after casting, with a rather economical procedure. To guarantee the embedment of the shear connectors in the DHCC layer and to reduce the formation of cracks in the surface of the DHCC layer, a haunch area was designed in the DHCC layer. This trapezoidal shape is also an adequate solution to create a larger compression flange in the DHCC layer (see Fig. 5.1a).

It is worth mentioning that the maximum length of discrete PAN fibers used in DHCC material is 12 mm while the hole diameters in the perforated GFRP shear connectors is 20 mm. Therefore, DHCC material can easily flow and fill the holes.

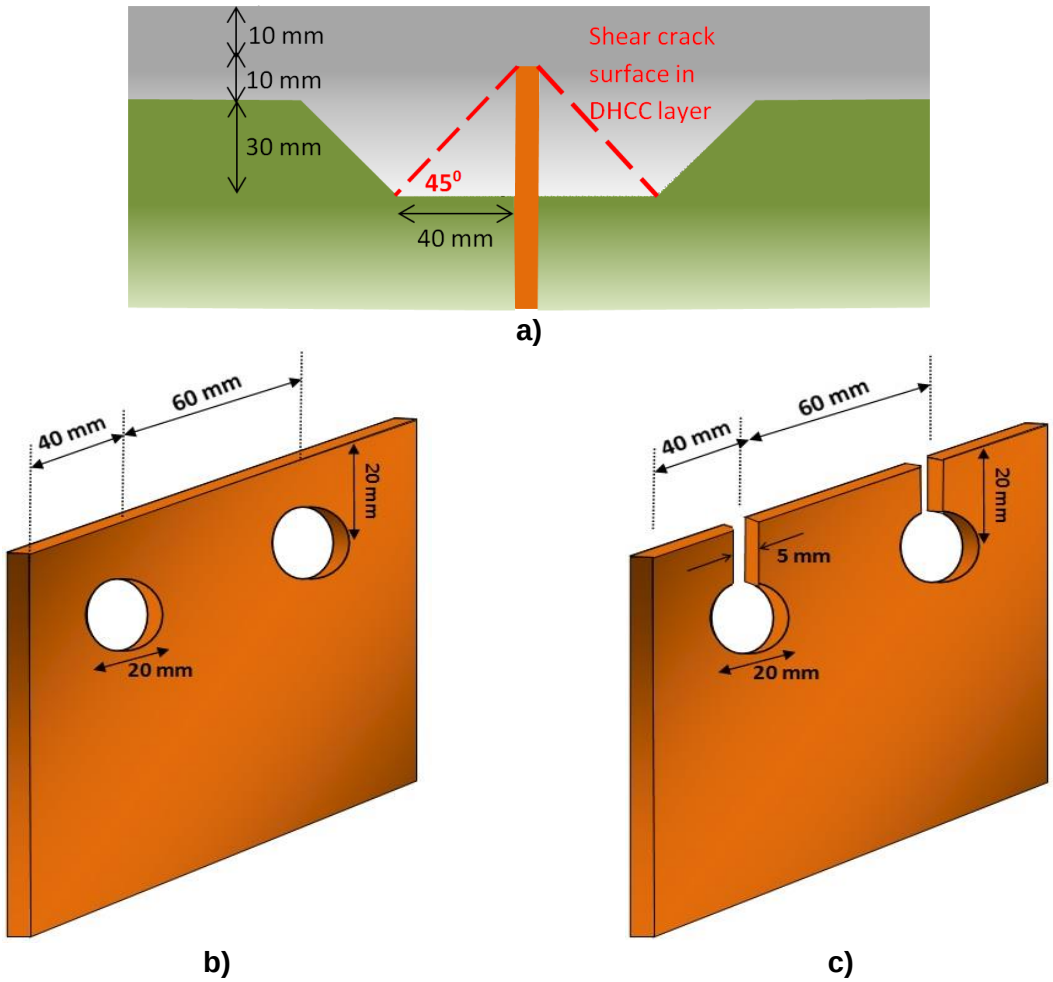

Fig 5.1. The proposed hybrid sandwich panel: a) Haunch area; b) Perforated shear connectors in GFRP ribs; c) Indented shear connectors in GFRP ribs

The manufacture process of hybrid slabs is schematically shown in Fig. 5.2. The ribs and skins were produced through VARTM process. More details about VARTM process can be found in chapter two. Afterwards, perforated shear connectors were created in the GFRP ribs with a simple drilling process. Finally, reinforced mortar was applied on the top layer.

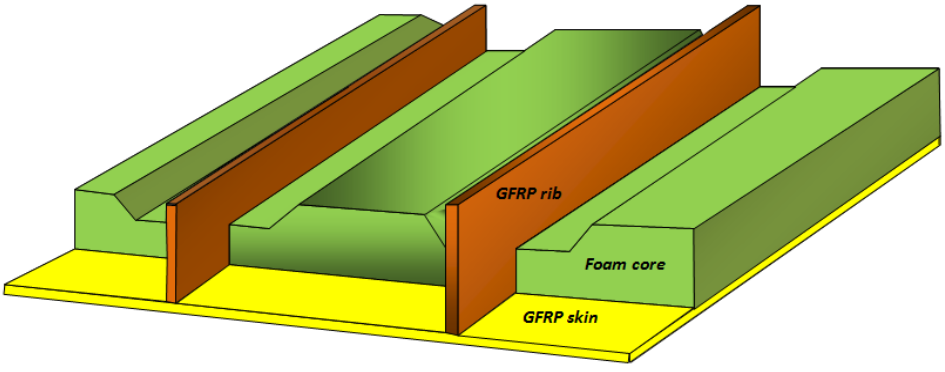

a)

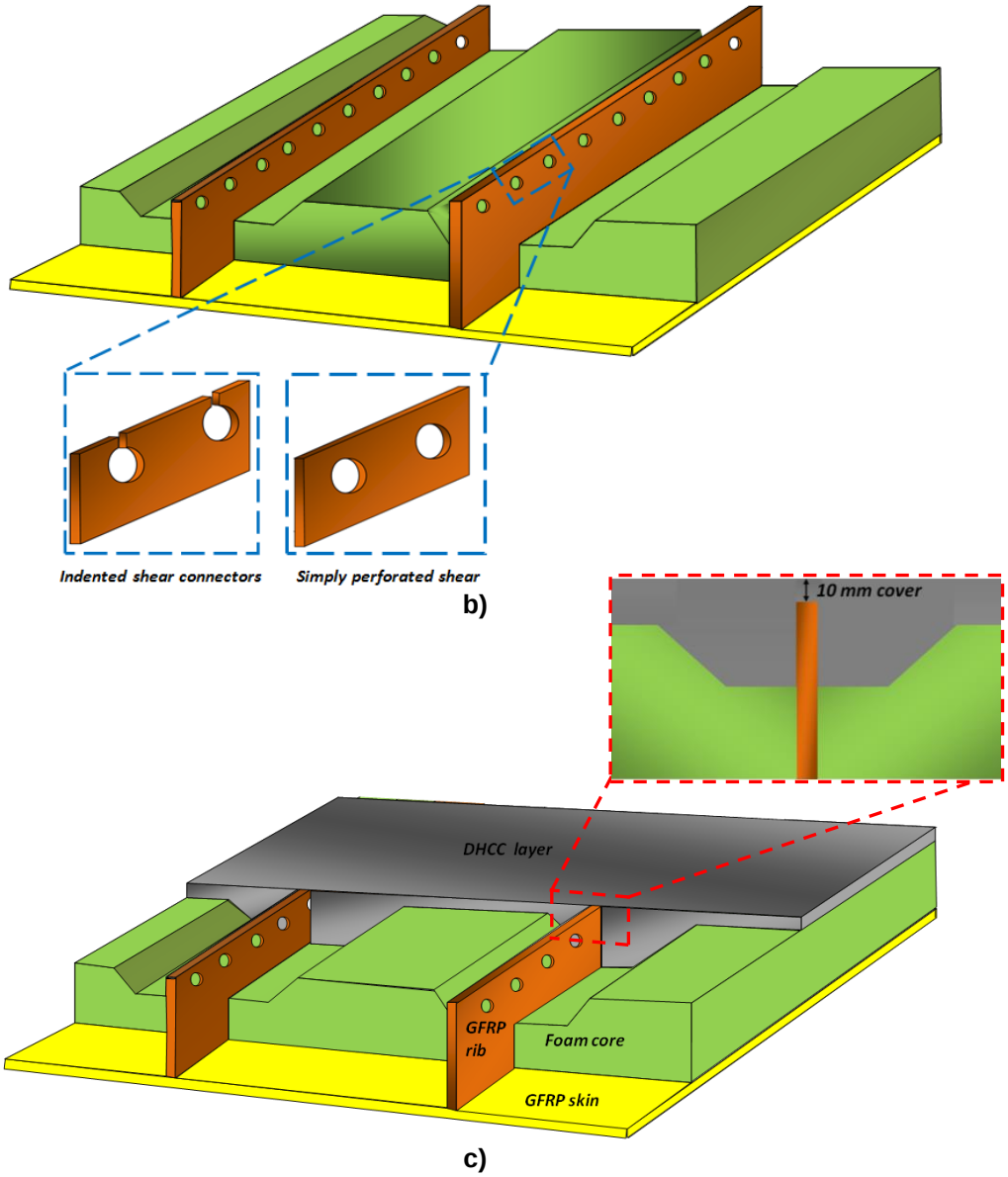

Fig 5.2. Manufacturing sequence of the GFRP-DHCC sandwich panels: a) GFRP skin and ribs produced through VARTM process; b) drilling of perforated connectors; c) Casting of DHCC layer

5.4. Test setup and instrumentation

Two slabs with indented shear connectors were tested under flexural FPB loading conditions to assess their flexural performance. Seven Linear Variable Differential Transformers (LVDTs) were used to measure displacements in the different positions of slabs, as indicated in Fig. 5.3. Three LVDTs were mounted to record vertical deflections (LVDT 3, LVDT 4, and LVDT 5), two LVDTs measured vertical displacements at two-side supports (LVDT 2 and LVDT 6), and two LVDTs registered slip between GFRP rib and DHCC layer (LVDT 1 and LVDT 7) at both end sides, as indicated in Fig. 5.3a and Fig. 5.3b.

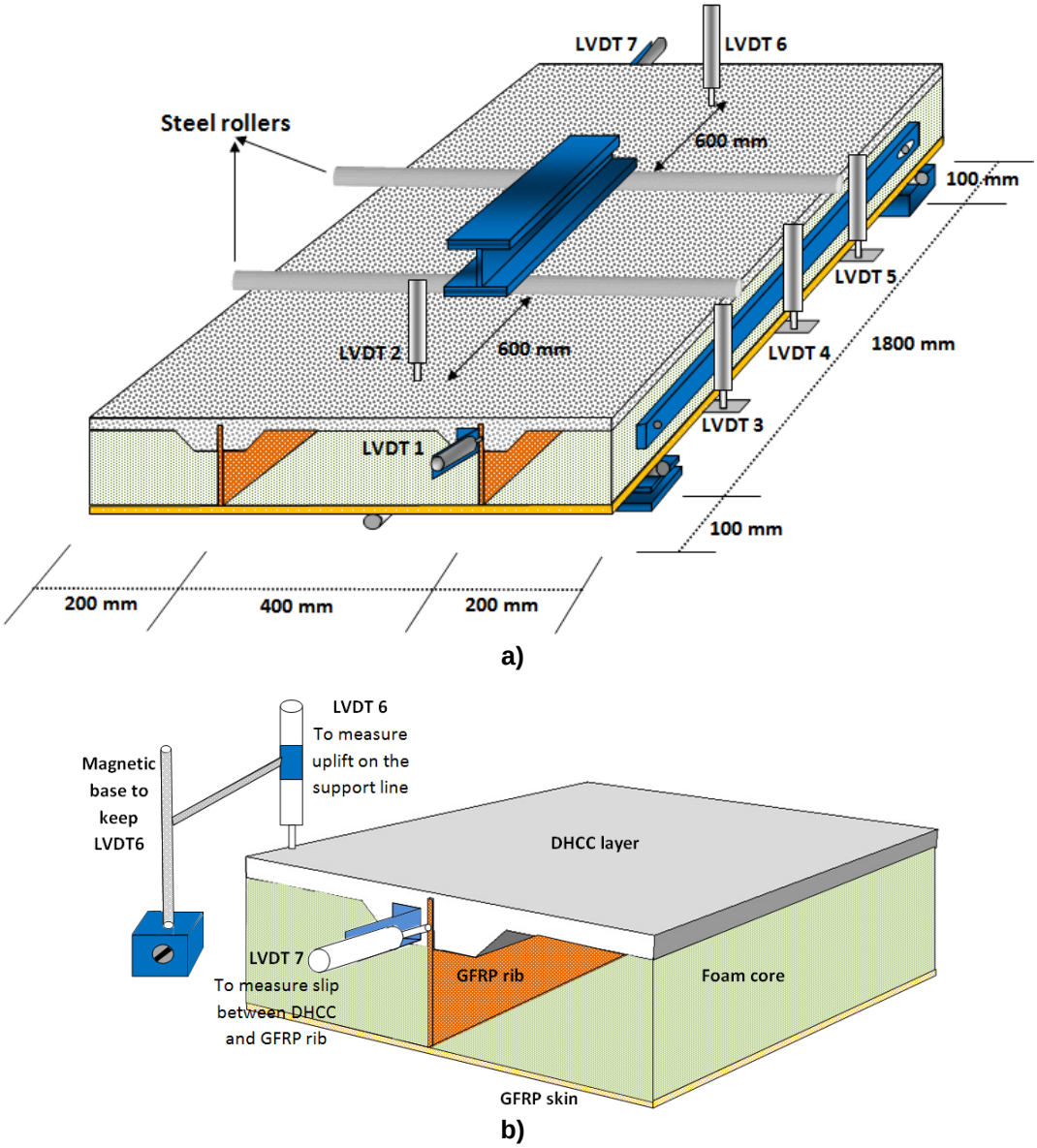

Fig 5.3. a) Used instrumentations for measuring displacements and test setup; b) 3D view of test setup and used instrumentation

The GFRP skin and ribs were instrumented with strain gauges, type BFLA-5-5 from TML and 5 mm measuring length. Two strain gauges were positioned in the GFRP rib, one strain gauge was installed at the bottom of GFRP skin, and one strain gauge with type PFL-30-11—3LT, from TML and 30 mm measuring length, was installed on top of DHCC layer, as shown in Fig. 5.4. The detailed positions of the strain gauges are illustrated in Fig. 5.4. The tests were carried under monotonic FPB loading by applying a displacement rate of 30 μm/sec to the slab at mid-span.

In order to compare the flexural performance of slabs with indented shear connectors and slabs with perforated connectors, it was important to adopt the same type of loading (FPB test),

LVDT's locations, and imposed displacement rate that were previously taken into account in chapter three. The behavior of the developed hybrid sandwich slabs with perforated shear connectors was assessed using two different flexural loading configurations: Three Point Bending (TPB), and Four Point Bending (FPB). Slab 1 was subjected to both TPB and FPB loading configurations, while Slab 2 was only submitted to FPB loading. According to the load procedures defined in Chapter 3, two cycles were applied in each sequence of loading, followed by a final monotonic loading up to a mid-span deflection of 100 mm (=L/18). In each cyclic loading sequence, the applied load was increased up to a certain deflection and then, after reaching the target deflection at the mid-span, it was maintained constant for one minute.

The first step of loading for Slab 1 was composed of the FPB test by applying two cycles with a maximum mid-span deflection of 14.4 mm (=2δ, which δ=L/250). After applying the first cyclic loading, Slab 1 has been unloaded and was subjected to a TPB cyclic loading with the same mid-span deflection. The third and the fourth loading steps were executed under FPB and TPB tests, respectively, by applying 21.6 mm deflection at mid-span. Then, in the last loading sequence to Slab 1, the mid-span deflection was increased up to 100 mm under FPB test up to failure. The mid-span deflections applied to Slab 1 and Slab 2 were different. Since, the experimental response of Slab 1 during the first load sequence has presented signs of damage, in order to have a first load sequence with a linear response, the increment of deflection adopted in the load sequences of the Slab 2 was limited to δ/2 (δ=L/250, with L = 1800 mm).

a) Strain gauge 1 positioned on the GFRP skin

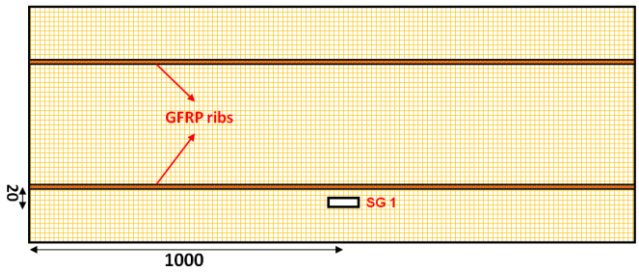

b) Strain gauges 2 and 3 positioned in the GFRP ribs

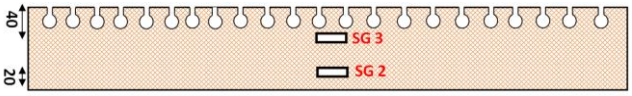

c) Strain gauge 4 positioned on the DHCC layer

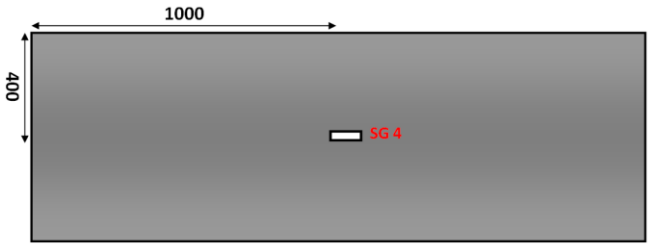

Fig 5.4. Positions of strain gauges in the hybrid sandwich panels tested

5.5. Experimental results and discussion

In order to assess the flexural performance of the tested hybrid slabs, flexural loading was applied and the damage sequences were recorded. According to the observations made during the execution of experimental tests, five damage events occurred and they were similar for all the tested specimens. With respect to the registered experimental results in this chapter and Chapter 3, damage sequences were independent of the shear connector type. The registered damage includes, in a sequential manner:

1) Loss of connection between DHCC layer and foam core (see Fig. 5.5a);

2) Damage in the GFRP ribs due to compressive stress concentration (see Fig. 5.5b);

3) Slip between DHCC layer and GFRP ribs due to loss of bond (see Fig. 5.5c);

4) Splitting cracks formed on the surface of DHCC layer in the alignment of the GFRP ribs (see Fig. 5.5d);

5) Crushing of foam cores around the applied load lines (see Fig. 5.5e).

a) Loss of connection between DHCC layer and foam core

b) Compressive damage in the GFRP ribs

c) Slip between DHCC layer and GFRP ribs

d) Splitting cracks in the alignment of the GFRP ribs

e) Crushing of foam cores

Fig 5.5. Damages observed during the execution of FPB tests

The only difference was detected in the damage level imposed to the GFRP ribs of slabs using perforated or indented shear connectors. Using indented shear connectors provides larger contribution of connectors in the imposed compressive damage to the GFRP ribs. As shown in Fig. 5.6, higher numbers of GFRP shear connectors crushed, when compared to the perforated shear connectors used in Chapter 3. This may be a consequence of different stiffness amongst the DHCC dowels, and/or uniform distribution of compressive stresses within the GFRP ribs.

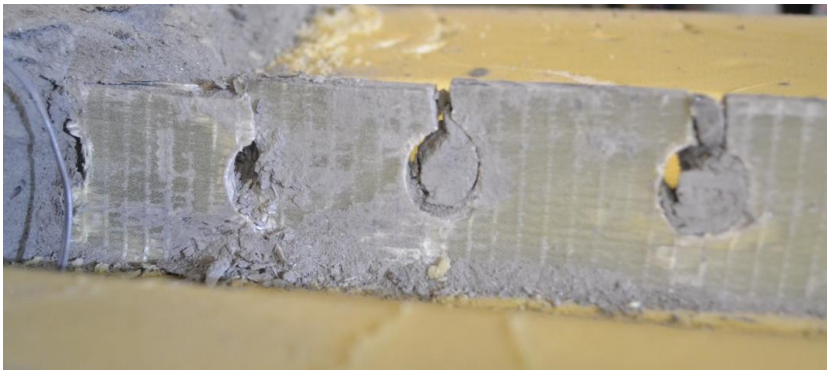

Fig 5.6. Larger contribution of shear connectors in the imposed damage to GFRP ribs

The flexural assessment was developed on hybrid sandwich panels by execution of four point bending (FPB) tests. The recorded force-mid span deflection response is presented in Fig. 5.7 for all the tested specimens.

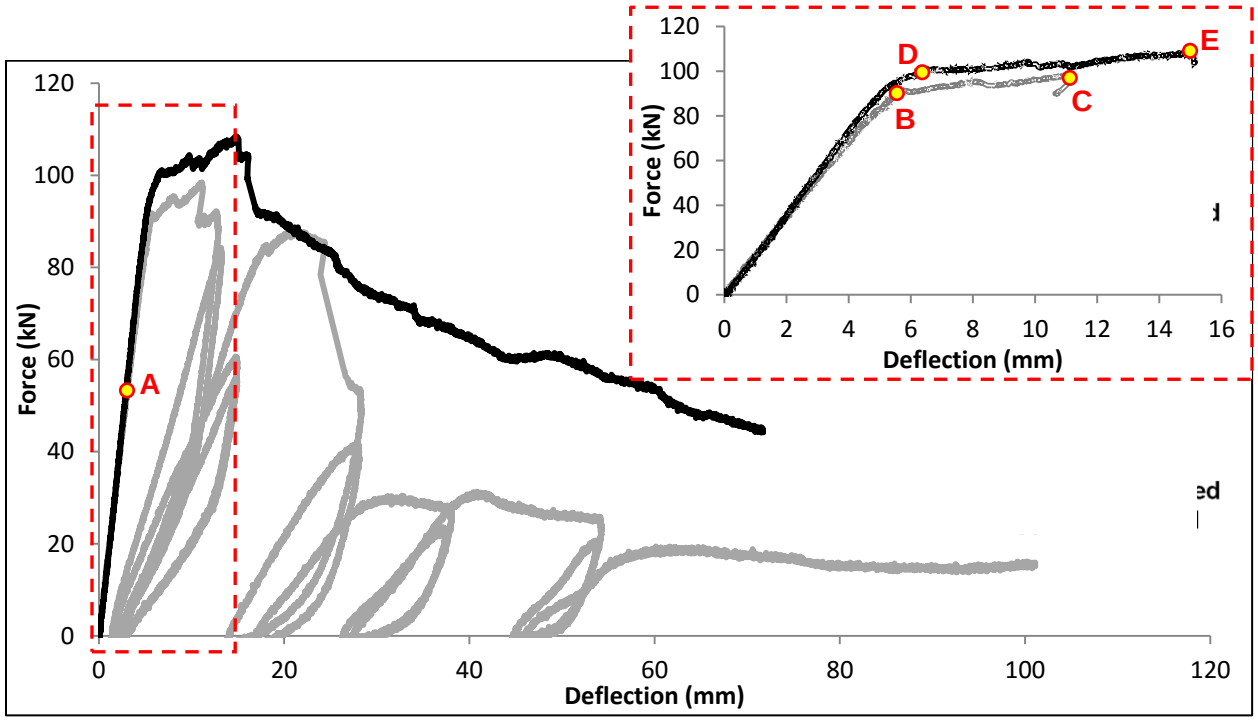

a) Type 1 slabs

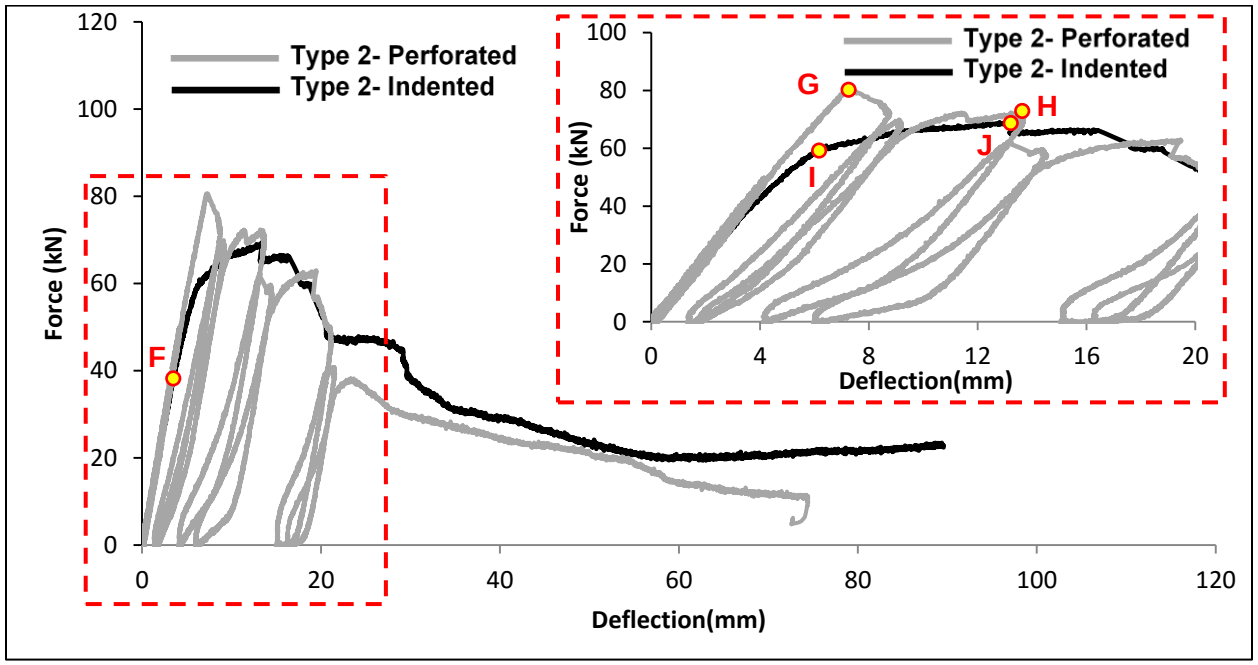

b) Type 2 slabs

Fig 5.7. Force-deflection responses of hybrid sandwich panels: a) Type 1; b) Type 2

Concerning the results indicated in Fig. 5.7a, the load carrying capacity and the residual strength are higher in Type 1 slab with indented shear connectors than in Type 1 slab with perforated shear connectors. Regardless of the type of shear connector used, Type 1 slabs lost connection between DHCC layer and foam core at a load of 53.00 kN (indicated as point A in Fig. 5.7a and corresponding to the damage identified in Fig. 5.5a). This detachment between DHCC layer and foam core did not have any impact in terms of changing the stiffness and the load carrying capacity of the tested slabs, which means that the shear forces are mainly transferred through the shear connectors and not through the link between the DHCC layer and foam core that is prematurely broken.

In Type 1 slab with perforated shear connectors, compressive damage in the GFRP ribs occurred at the load of 91.53 kN and a corresponding deflection of 5.63 mm (Point B in Fig. 5.7a and compressive damage in Fig. 5.5b). In Type 1 slab, with indented shear connectors, compressive damage in the GFRP ribs was registered at a load 99.97 kN and a corresponding deflection of 6.37 mm (Point D in Fig. 5.7a). Afterwards, a pronounced nonlinear behavior occurred due to the propagation of damage in both Type 1 slabs. Type 1 slab with perforated shear connectors presented a hardening stage for deflection above 5.63 mm and up to 10.61 mm deflection. This value of deflection occurred together with a peak load of 97.48 kN (Point C in Fig. 5.7a). In Type 1 slab with indented shear connectors, a hardening stage was observed above 6.37 mm of deflection and up to a deflection of 14.80 mm. This vertical deflection of 14.80 mm corresponds to a peak load of 108.53 kN, as represented by Point E in Fig. 5.7a.

A residual load carrying capacity about 45.00 kN was registered for Type 1 slab with indented shear connectors, at the end of loading (71 mm, ≈L/25), which is about 42% of peak load. Using perforated shear connectors in Type 1 slab led to attain a residual load carrying capacity about 18.00 kN at the end of loading (60 mm - 100 mm, ≈ L/30-L/18), which is about 19% of the peak load. It is verified that the residual strength is higher in Type 1 slabs with indented shear connectors than in perforated shear connectors.

A similar approach was implemented to assess Type 2 slabs with indented and perforated shear connectors under flexural loading. The registered results are presented in Fig. 5.7b. Regardless of the shear connector used, the connection between DHCC layer and foam core is lost at a vertical load of 40.00 kN without visible damage or significant impact in terms of loss of stiffness (Point F in Fig. 5.7b). This behavior was similar to the one previously observed in Type 1 slabs.

The first damage was detected in the GFRP ribs of Type 2 slab with perforated shear connectors, at a load of 80.58 kN and 7.02 mm of deflection (Point G in Fig. 5.7b), while Type 2

slab with indented connectors suffered compressive damage, at a load of 58.96 kN and 6.07 mm of mid-span deflection (see Fig. 5.5b). For Type 2 slab with perforated shear connectors, a hardening stage was observed above 7.02 mm of deflection, and a peak load was attained at 71.51 kN, corresponding to a deflection of 13.55 mm (Point H in Fig. 5.7b). At the end of loading, a load carrying capacity equal to 10.82 kN was registered (which is about 15% of the maximum load), with 72.66 mm of mid-span deflection.

Despite the compressive damage verified in GFRP ribs of Type 2 slab with indented shear connectors, a hardening stage was observed above 6.07 mm of deflection (Point I in Fig. 5.12b), and a peak load of 69.37 kN was attained for with a corresponding deflection of 13.36 mm (Point J in Fig. 5.12b). Above this deflection, the Type 2 slab with indented shear connectors entered in a softening phase. In the final stage of this softening phase, this slab presented a residual strength of 21.23 kN, which corresponds to 30% of the maximum load, at a deflection varying between 60 and 90 mm (≈L/30 and L/20).

Together with the results already presented, for Type 1 slabs, it can be concluded that indented shear connectors can be more effective on providing a higher residual strength than perforated ones. Using indented shear connectors resulted in increasing the sectional area of DHCC dowels in comparison to perforated shear connectors. This increase may have led to a more effective contribution of fiber reinforcement mechanisms in bridging the formed cracks. In addition, the indented shear connectors diminished the stiffness of the part of the GFRP rib that was embedded in the DHC layer, reducing the localized damage and crushing that occurred both in the GFRP rib and in the DHCC layer.

In terms of maximum load capacity, both Type 1 and Type 2 slabs present similar results. Table 5.1 summarizes the results obtained in the tested Type 1 and Type 2 slabs, where P_{max} is the peak load attained during the tests, d (P_{max}) is the corresponding vertical deflection at mid span and s (P_{max}) is the corresponding slip measured at the slabs' supports. Moreover, in Table 5.1, $P_{max,linear}$ is the maximum load attained during the initial phase of the tests when the specimens behave elastically and d ($P_{max,linear}$) is the corresponding vertical deflection at mid span. Moreover, the experimental moment of inertia was presented for each specimen using Equation (5.1):

$$(EI)_{equiva} = \frac{23PL^3}{648\delta} \tag{5.1}$$

where, P is the applied load, L is the span length, and δ is the mid span deflection. The values of the flexural stiffness are presented in Table 7. Based on the results obtained, using indented shear connectors instead of perforated shear connectors in Slab 1 increased the elastic flexural

stiffness in about 7%, while for Slab 2, using indented shear connectors instead of perforated shear connectors reduced the elastic flexural stiffness in about 16%.

Table 5.1. Summarized results obtained in hybrid slabs

Slab type	Shear connectors	P_{max} (kN)	d (P_{max}) (mm)	s (P_{max}) (mm)	$P_{max,linear}$ (kN)	d ($P_{max,linear}$) (mm)	$(EI)_{Exp}$ (kN.m^2)
Type 1	Perforated	97.48	10.61	0.014	91.53	5.63	3365
	Indented	108.53	14.80	3.83	99.97	6.37	3600
Type 2	Perforated	71.51	13.55	1.98	80.58	7.02	2376
	Indented	69.37	13.36	0.29	59.94	6.07	2044

Figs 5.8a and 5.8b present the force and slip measured between the DHCC layer and the GFRP ribs. In Type 1 slab with perforated shear connectors, it was verified that a sudden increment of slip occurred at the peak load of 97.48 kN, corresponding to a slip value of 0.014 mm. Above this slip, a softening behavior was observed. In Type 1 slab with indented shear connectors, an abrupt increment of slip was registered at load of 95.93 kN corresponding to slip of 0.014 mm. For slip values higher than 0.014 mm, a hardening force-slip stage was monitored and a peak load of 108.53 kN corresponding to a slip value of 3.83 mm were recorded. Due to increase of the sectional area of DHCC dowels, larger contribution of fiber reinforcement mechanisms bridging the formed cracks during of crack propagation was observed for indented shear connectors in Type 1 slab.

The force-slip diagrams for Type 2 slabs are presented in Fig. 5.8b. In Type 2 slab with perforated shear connectors, a sudden alteration in the evolution of slip was recorded, from 0.15 mm at 60.50 kN up to 1.98 mm at 72.2 kN (Point A in Fig 5.8b), corresponding to a hardening behavior. In Type 2 slab with indented shear connectors, an abrupt increment of slip was measured at a load of 60.85 kN and a slip of 0.07 mm. A hardening behavior was observed above 0.07 mm of slip, and at the peak load of 69.37 kN, a slip value of 0.29 mm was recorded (Point B in Fig. 5.8b). Above this slip, high post-peak residual slip capacity was attained. Comparing the force-slip and force-deflection responses of slabs, it is revealed that the stiffness, load carrying capacity, gradual decrease of load carrying capacity after peak load are mainly governed by the behavior of the shear connection between GFRP ribs and DHCC layer.

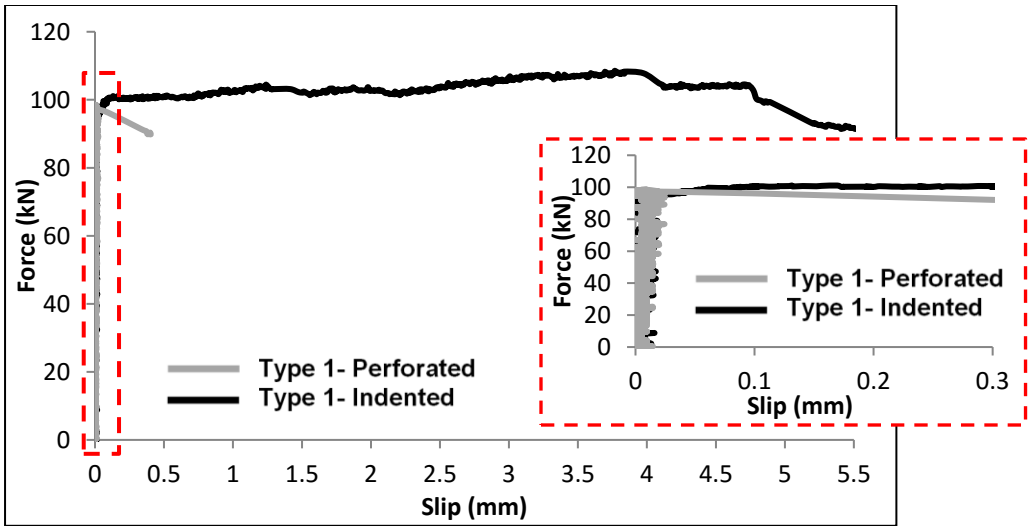

a) Type 1 slabs

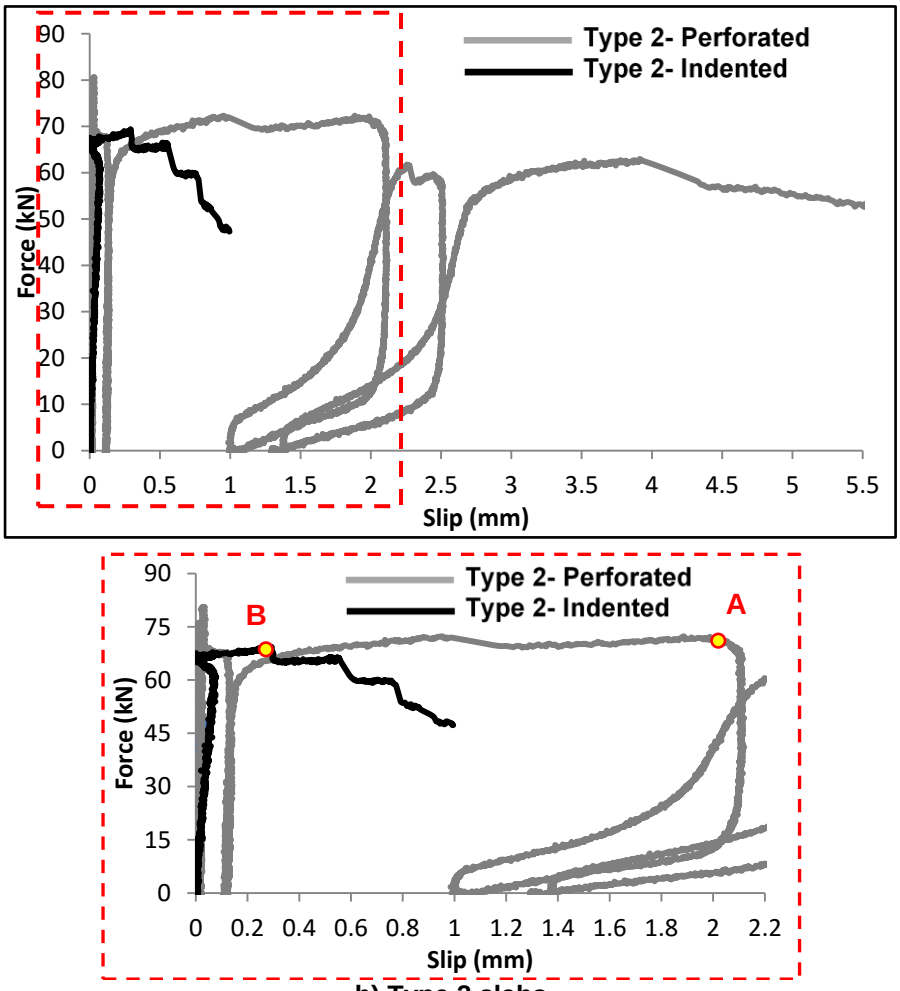

b) Type 2 slabs

Fig 5.8. a) Force-slip response between GFRP rib and DHCC layer for Type 1 slabs; b) Force- slip response between GFRP rib and DHCC layer for Type 2 slabs

As previously mentioned in Section 5.4 and represented in Fig. 5.4, hybrid slabs with indented shear connectors were monitored with one strain gauge at the bottom of the GFRP skin (SG 1), two strain gauges in the GFRP rib, and one strain gauge on the upper face of the DHCC layer. Fig. 5.9 illustrates the variation of strain during the loading process. Maximum tensile and compressive strains of 0.0013 (mm/mm) and -0.00033 (mm/mm) were registered in the GFRP skin (SG 1) and in the DHCC layer (SG 4), respectively, of Type 1 slab with indented connectors, as shown in Fig. 5.9a. The tensile strains measured in the GFRP skin were much lower than the ultimate strains recorded in the direct tensile tests carried out with specimens extracted from these components of the slab (see Table 2.4). Using indented shear connectors results in almost linear tensile strains in the GFRP skins even during the deflection hardening stage identified for Type 1 slab. This indicates that the damage is mostly concentrated in the connection between GFRP ribs and DHCC layer and the hardening behavior results from the slip developed in the interface of the two materials.

The strains recorded in the different positions of Type 2 slab with indented connectors are shown in Fig. 5.9b. A maximum tensile strain of 0.00086 (mm/mm) was recorded in the GFRP skin and a maximum compressive strain of -0.00058 (mm/mm) was measured in the GFRP rib while a compressive strain of -0.00023 (mm/mm) was recorded in the DHCC layer (SG 4). Again, the maximum tensile strains measured in the GFRP skin of Type 2 slab were much lower than the ultimate strains recorded in the direct tensile tests executed in the specimens extracted from these GFRP elements (see Table 2.4) and the same conclusions related to the hardening behavior that were stated before for Type 1 slab, can be here considered.

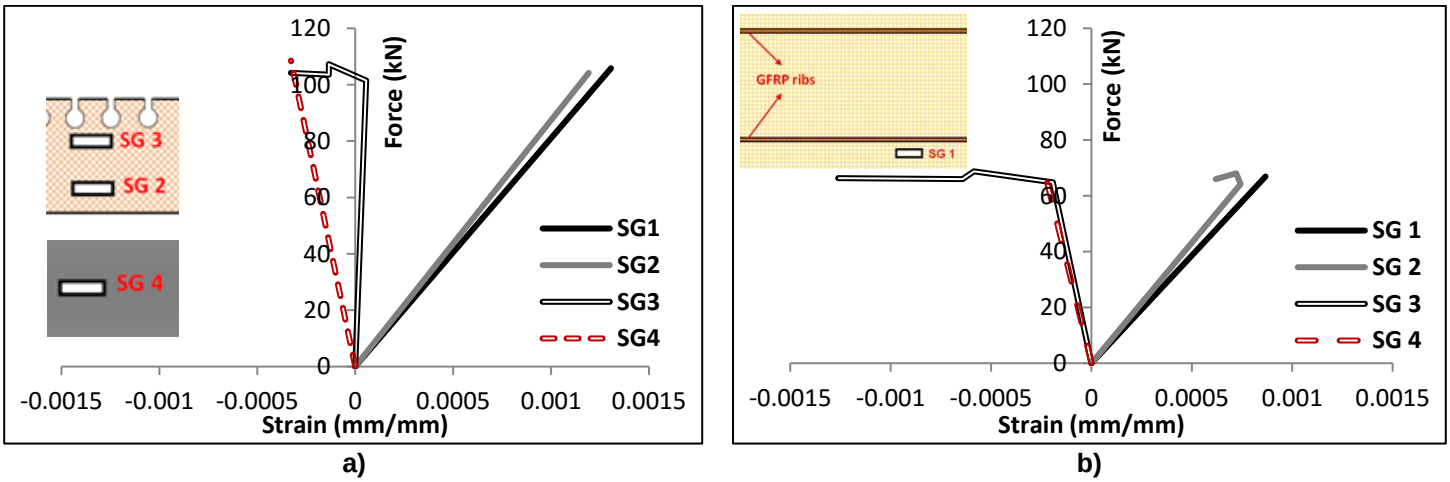

Fig 5.9. Recorded strains in hybrid slabs with indented connectors: a) Type 1; b) Type 2

The efficiency of the shear connectors used in this study was also evaluated by considering the strain distribution across the panel's thickness, at mid span. The curves represented in Fig. 5.10

correspond to different load levels that were established considering ratios between applied load and maximum load, resulting in the following: 20%, 40%, 60%, 80% and 100% of P_{max}.

It is worth mentioning that no strain gauge was installed on the top layer of DHCC material to measure compressive strains in slabs with perforated shear connectors.

As mentioned before, one strain gauge was installed on the top layer of DHCC material to measure compressive strains in the slabs with indented shear connectors. These strains were used to evaluate the efficiency of the indented shear connector, by analyzing the distribution of strains across the panels' thickness.

The author is aware that the distribution of strains obtained for maximum load, across the panels' thickness, are influenced by the significant slip values measured between the DHCC layer and the GFRP ribs at this load level. Additionally, the strain gauge installed on the top layer of the DHCC layer did not record the compressive strain precisely in the location of DHCC crushing at mid-span. Thus, as shown in Figs 5.10a and 5.10b, the compressive strains measured in the DHCC layer for maximum load cannot connect to other strain values recorded in GFRP ribs and skin. Even so, the results obtained provide a general idea of the composite action in slabs with indented shear connectors, at maximum load.

In a composite element, full composite action is attained when there is no slip between two or more elements connected. In this case, shear stresses are fully transmitted between layers and the strain diagram remain linear across the slab thickness. If the connection is not rigid, there is some slip between layers and the strain diagram is not continuous.

The distribution of strain across the panels' thickness in Type 1 and Type 2 slabs with indented shear connectors was analyzed to estimate the level of composite action.

Fig. 5.10a shows the distribution of strains across the panels' thickness in the different phases of loading for Type 1 slab with indented shear connectors. In the initial phase of loading, the strain diagram is continuous and linear, indicating that the slab is working as fully composite. For P_{max}, the strain diagram is not linear anymore, indicating a partial composite behavior. This means that between $0.8P_{max}$ and P_{max}, some damage occurred in the connection that altered the transmission of shear stresses. This effect was previously identified in Fig. 5.5 and Fig. 5.7, where non-linear behavior was observed for loads higher than 99.97 kN (this value corresponds to 0.92 P_{max}) due to compressive damage in the GFRP ribs.

Type 2 slab with indented shear connectors shows an almost fully composite behavior up to $0.8P_{max}$, as shown in Fig 5.10b. Due to propagation of damage, by applying loads that are higher than $0.8P_{max}$ a partial composite action is obtained.

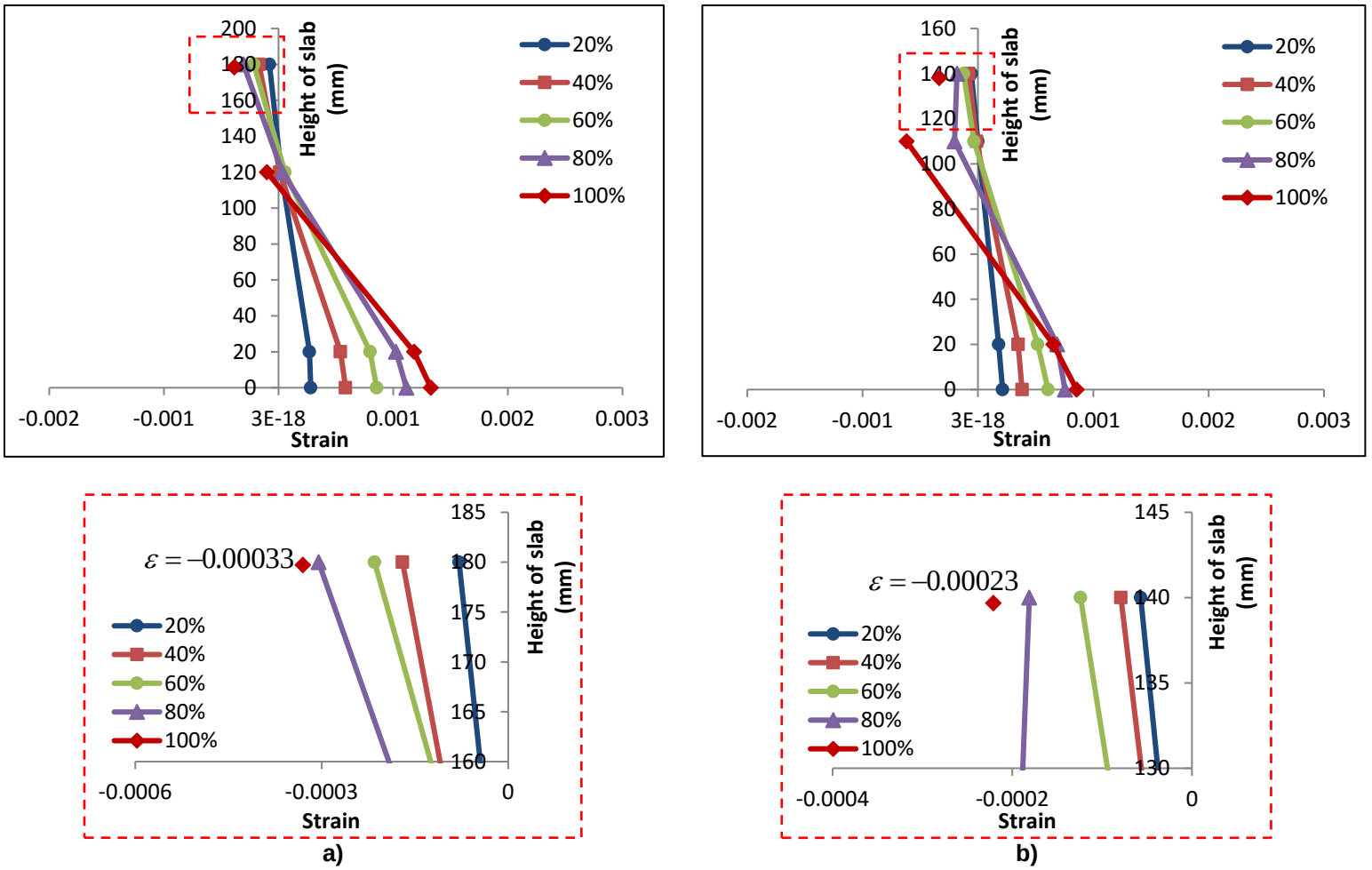

Fig 5.10. Strains in cross section of: a) Type 1 slab with indented shear connectors; b) Type 2 slab with indented shear connectors

The degree of composite action during the initial phase of loading was evaluated for each specimen. The method defined by Pessiki and MIynarczyk [5] was used together with the values of initial stiffness obtained in the experimental tests performed and the numerical models developed. The experimental moment of inertia was calculated for each specimen using Equation (5.1). The degree of composite action was calculated based on the experimental moment of the inertia of specimens (I_{exp}) and the corresponding numerical values for full-composite action (I_{fc}) and non-composite action (I_{nc}). Equation (5.2) is used to calculate the degree of composite action associated to the initial phase of loading.

$$\kappa = \frac{(I_{\exp} - I_{nc})}{(I_{fc} - I_{nc})} \times 100\,(\%) \qquad (5.2)$$

It is worth stating that the moment of inertia for full-composite action (I_{fc}) and non-composite action (I_{nc}) are calculated in slabs with no damage. To determine the moment of inertia of full-

composite action and non-composite action of hybrid slabs, a robust three dimensional nonlinear finite element model that can capture the force/deflection response of the hybrid sandwich panels was used. The three-dimensional FEM models developed within this study were calibrated with the experimental results previously presented in chapter four. The main objective of modeling the hybrid slabs with full-composite action and non-composite action is to determine the corresponding moment of inertia that is later used in calculating the degree of composite action.

Three different material models were introduced to model DHCC layer, polyurethane foam cores, and orthotropic GFRP material. To model the DHCC behavior, a plastic damage model was used that includes both tensile cracking and compressive crushing in the analysis. The stress–strain response to uniaxial tension has a linear elastic relationship. After forming the initial crack, a plastic response followed by strain-hardening under uniaxial tension loading. Polynomial curves were fitted to the experimental results in order to achieve the simplified DHCC behavior under tensile loading. Additionally, elastic modulus and Poisson's ratio were considered equal to 10.00 GPa and 0.20, respectively. A crushable foam plasticity model was used to represent the foam core behavior. In sandwich panels, core compaction is modeled by using a crushable foam plasticity model with volumetric hardening and strain-rate sensitivity [6]. In this model, a uniaxial elastic-plastic stress-strain relationship was defined for the foam core behavior under compressive loading [7]. The elastic modulus and Poisson's ratio were considered equal to 2.00 MPa and 0.183, respectively. In order to introduce orthotropic GFRP material, linear elasticity is defined by specifying the Engineering constants in FEM software. Engineering constants are used to define the elastic properties of GFRP materials in different directions [8].

Four-node tetrahedral elements were used to model the DHCC materials (Fig. 5.11a). The simplest three-dimensional solid element available in the finite element analyst is the 4-node constant strain tetrahedral element [9]. This element is used abundantly in practice, as the analyst is able to mesh almost any volume and regardless of its complexity or its robustness in contact analysis. The element matrices are inexpensive to calculate, and the resulting global stiffness matrix has a relatively small bandwidth. In order to enhance the stresses in localized regions of particular interest in this study, refined mesh with higher element numbers were used around the GFRP shear connectors. GFRP rib and skin were simulated using 4-node constant strain tetrahedral elements, while 6-node linear triangular prism elements used to simulate the foam cores. As the hybrid slabs had double symmetry, only one quarter of the specimen modeled to approach a lower computational cost and time in the numerical simulation, as shown

in Fig. 5.11b. Additionally, the boundary conditions used in the numerical simulations are illustrated in Fig. 5.11b. Two surfaces of a quarter of slab are restricted in the degrees of freedom associated with displacement in directions of X-axis and Z-axis, respectively, as shown in Fig. 5.11b. Moreover, Fig. 5.11b illustrates the support condition, where diamond markers indicate the points with null displacement in the vertical direction (Y). More details on the numerical simulation can be found in chapter four.

Slabs were numerically simulated and loaded under FPB conditions, considering both fully composite action and non composite action between DHCC layer and GFRP ribs and skin. The results obtained in experimental tests and in numerical simulations are indicated in Table 5.2. Considering Equation (5.1), the flexural stiffness (EI) of the hybrid slabs were computed and listed in Table 5.2.

Four-node tetrahedral elements ***Six-node linear triangular prism elements***

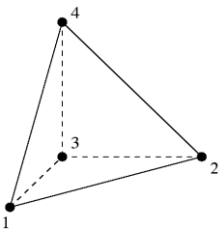

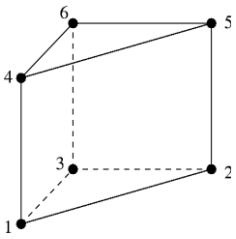

a)

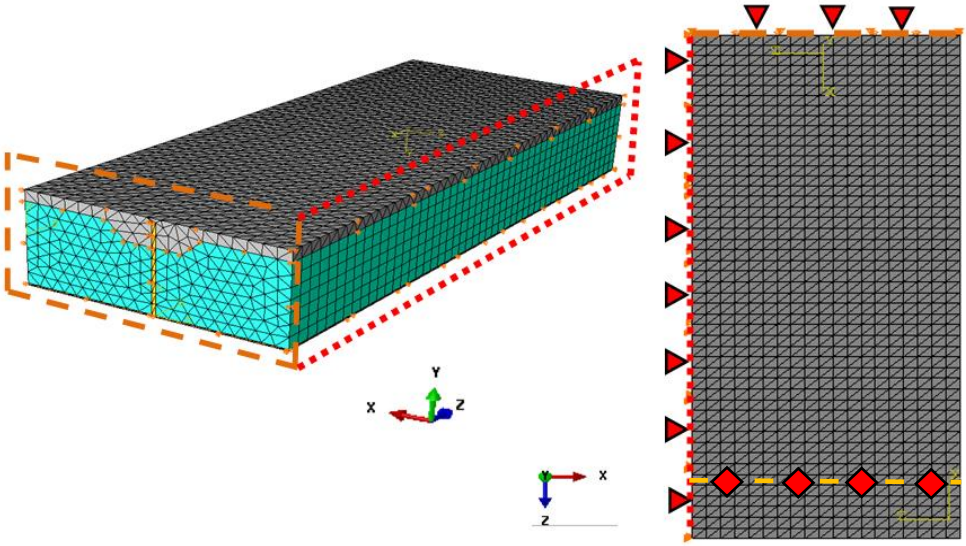

b)

Fig 5.11. a) Model of one quarter of the slabs and used elements; b) Boundary conditions

Using the values of flexural stiffness presented in Table 5.1 and applying equation (5.2), the degree of composite action for the Type 1 slabs with perforated and indented shear connectors were computed as 86.62% and 99.00%, respectively. Moreover, the degree of composite action in Type 2 slabs with perforated and indented shear connectors were calculated as 93.35% and 71.70%, respectively.

Table 5.2. Flexural stiffness (EI) of hybrid slabs

Slab type	Shear connectors	$(EI)_{Exp}$	$(EI)_{fc}$	$(EI)_{nc}$	$(EI)_{Exp} / (EI)_{fc}$	Degree of composite action
		Experimental	*Numerical*			
		(kN.m^2)	(kN.m^2)	(kN.m^2)		(%)
Type 1	**Perforated**	3365	3618	1727	0.94	86.62
	Indented	3600			0.99	99.00
Type 2	**Perforated**	2376	2475	985	0.96	93.35
	Indented	2044			0.82	71.70

5.6. Conclusions

Providing good shear connection between the GFRP ribs and the DHCC layer leads to attain an increase of load with a larger increment of deflection. Therefore, within the scope of this chapter, hybrid slabs using two types of shear connectors, including indented shear connectors were built and experimentally tested. Both indented and perforated shear connectors provide an effective connection between DHCC layer and GFRP ribs, a simple, but efficient technology was adopted by executing holes of small diameter on the top zone of the GFRP embedded in the

DHCC layer. To assess the structural performance of hybrid slabs under flexural loading, all slabs were loaded under four point bending tests. Then, the results obtained from experimental tests used to implement a comparative study. By comparing the results attained in this chapter from flexural performance of hybrid slabs with indented or perforated shear connectors, the following results can be pointed out:

1) Using different shear connectors at the ribs/DHCC connection influences the peak load, deflection corresponding to peak load, residual load carrying capacity, and degree of composite action;
2) Occurring damage sequences are independent of indented or perforated shear connectors;
3) Indented shear connectors in Type 1 slab provides about 15% higher degree of composite action in term of initial stiffness, when compared with perforated shear connectors. Using perforated shear connectors in Type 2 slab leads to about 30% higher degree of composite action;
4) Regardless of shear connector type, the maximum strain levels in the GFRP ribs and skin were much lower than the ultimate strain determined on the tensile tests carried out with GFRP coupons;
5) Load carrying capacity of hybrid slabs are mainly governed by the stiffness provided the connection of GFRP ribs/DHCC layer.
6) Regardless of shear connector type, slabs presented an almost linear force versus mid-span response up to peak load, followed by a smooth softening curve. Despite of weightless of hybrid slabs, they indicated high load carrying capacity and considerable stiffness.

References

[1]. Correia J.R., Garrido M., Gonilha J.A., Branco F.A., Reis L.G., 2012, "GFRP sandwich panels with PU foam and PP honeycomb cores for civil engineering structural applications: Effects of introducing strengthening ribs", International Journal of Structural Integrity, Vol. 3, pp: 127 – 147.

[2]. Norton T.M., 2004, “3D Orthogonal Woven Glass Fiber Reinforced Polymeric Bridge Deck: Fabrication and Experimental Investigation”, Master thesis, North Carolina State University, USA.

[3]. Charles M.J., Tarek S., Rizkalla S.H., 2007, “Behavior of Three-Dimensionally Woven Glass Fiber Reinforced Polymeric Bridge Deck”, Composites Research Journal, Vol. 1, pp: 27-42.

[4]. Lameiras R., Barros A.O. Joaquim, Valente I.B., Azenha Miguel A.D., 2013, “Development of sandwich panels combining fiber reinforced concrete layers and fiber reinforced polymer connectors. Part I: Conception and pull-out tests”, Journal of Composite Structures, Vol. 105, pp: 446-459.

[5]. Pessiki S., Mlynarczyk A., 2003, “Experimental evaluation of the composite behavior of precast concrete sandwich wall panels”, Journal of PCI, Vol. 48,pp: 54–71.

[6]. Xiaoding Wei, Phuong Tran, Alban de Vaucorbeil, Ravi Bellur Ramaswamy, Felix Latourte, Horacio D. Espinosa, 2013, “Three-dimensional numerical modeling of composite panels subjected to underwater blast”, Journal of the Mechanics and Physics of Solids, Vol. 61, pp: 1319-1336.

[7]. ABAQUS Theory Manual and Users Manuals. Version 6.9-3, 2010, Hibbitt, Karlsson and Sorensen, Inc., USA.

[8]. Venu Gopala Rao G., Mahajan P., Bhatnagar N., 2007, “Micro-mechanical modeling of machining of FRP composites – Cutting force analysis”, Journal of Composites Science and Technology, Vol. 67, pp: 579-593.

[9]. Daniel Jose P., Klaus-Jürgen B., 2011, “Improved stresses for the 4-node tetrahedral element”, Journal of Computers and Structures, Vol. 89, pp: 1265-1273.

Chapter 6

Shear performance of hybrid sandwich slabs using indented shear connectors

6.1. Introduction

Sandwich panels are commonly composed of two top and bottom skins, separated by foam core. Shear stresses between top and bottom skins are transferred by the foam core. The low shear load carrying capacity is usually a weakness of this type of sandwich panel. Taking this into account, various studies have been developed on the improvement of the sandwich panels structural performance.

Lanssens *et al,* in 2014, presented the results of a computational and experimental study on the mechanical behavior of a 3D GFRP sandwich panel with through thickness fiber insertions [1]. Samples of the GFRP skin and glass fiber insertions were cut out from larger scale panels and tested to determine the material mechanical characteristics. The experimental results obtained on the components were used to create a nonlinear finite element model that could predict the large-scale mechanical deformation of the sandwich panels. The model can accurately predict the force–displacement behavior of the panel, under a variety of experimental conditions. Then, the finite element model was used to determine the bending capacity of sandwich panels with various span lengths with the objective of creating a load table for engineering applications. This model can also be used to predict the mechanical performance and failure load of sandwich panels for specific load conditions [1].

Thanoon *et al*. worked on a semi-precast floor slab, which consists of a precast reinforced concrete layer that acts initially as formwork and is connected in situ with another concrete layer by using shear connectors [2]. Steel reinforcement (shear link, studs and/or steel truss) is commonly used to transfer the longitudinal shear forces that arise between the two composite layers. Longitudinal shear failure is the most common type of failure in a composite floor slab. These authors proposed a new composite slab based on interlocking concept and that does not require any shear reinforcement [2]. The concept of interlock is indicated in Fig. 6.1. The composite floor slab used to illustrate the interlocking concept consists of a precast inverted ferrocement layer interconnected with the cast in situ brick–mortar layer, as indicated in Fig. 6.1. Ferrocement is a system of reinforced mortar applied over layers of metal such as chicken wire or woven or expanded metal (iron) mesh or fibers and possibly closely spaced small-diameter steel rods such as rebar. It is used to form relatively thin, hard and strong forms for such applications as shell roofs and water tanks.

The efficiency of the interlocking mechanism of the proposed slab in transferring the stresses developed due to the applied load was investigated. Eleven composite slabs with different shear connectors were fabricated and tested under pure shear

loading (push-off test). In the tested specimens, different interlocking mechanisms, continuous truss shear connectors and no shear connection between the two layers was considered. The results indicate that the interlocking mechanism proposed is as effective as the steel trusses in resisting shear stresses and can be used to replace the steel trusses, which in turn will reduce the global cost of the composite slab.

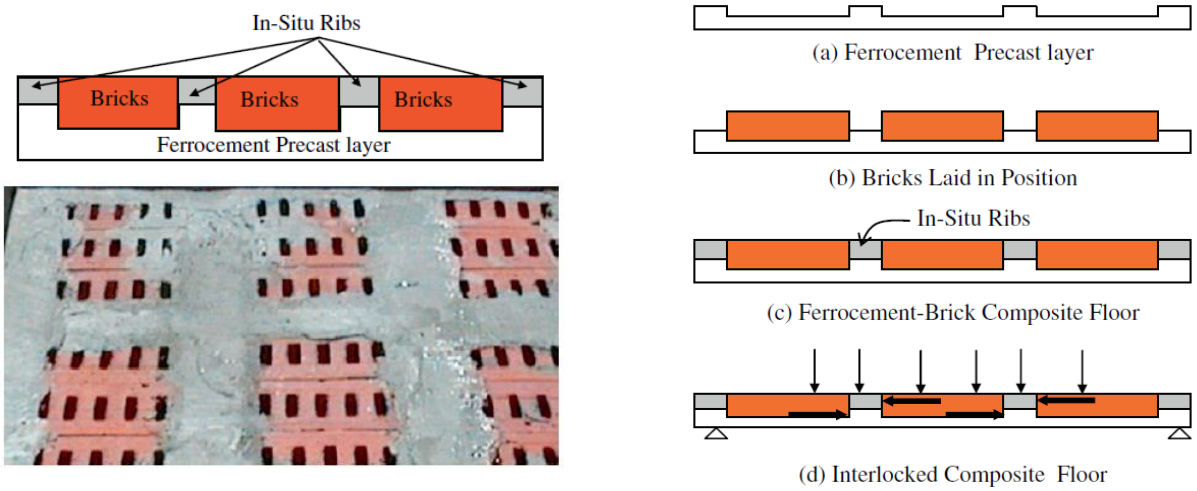

Fig 6.1. Interlocking composite ferrocement–brick floor slab

Mathieson *et al*., in 2015, tested 18 sandwich beam specimens under three and four point bending [3]. The specimens are composed of low-density polyurethane core and glass fiber-reinforced polymer (GFRP) skins on the upper and the bottom sides [3]. The shear span-to-depth (a/h) ratio was varied from 1.33 up to 4.67. Two different skin thicknesses were used to provide beam depth-to-skin thickness (h/t) ratios of 47 and 94. It was found that, in sandwich beams with an h/t ratio of 94, the ultimate bending moment was reduced by approximately one third as the a/h ratio increased from 1.33 to 4.67. In beams with an h/t ratio of 47, the ultimate bending moment decreased by about one quarter, in the same situation. Doubling the skin thickness [i.e., from h/t of 94–47] increased the bending moment capacity significantly. The increase on the ultimate bending moment ranged from 55 to 95% as a/h increased from 1.33 to 4.67. Failure of sandwich beams occurred by skin wrinkling in compression, mostly symmetrically, where skins move out-of-plane [3].

Choi *et al.,* in 2015, used a CFRP grid as the shear transfer element in order to assess the effect of different parameters on the shear flow capacity of concrete sandwich panels [4]. The parameters included grid embedment length, insulation type and thickness, shear grid density (spacing), and the effect of repeated loading. The results obtained indicate that the shear grid density, the type and thickness of insulation type have a major importance on the shear strength of the system [4].

It can be concluded that the shear performance of sandwich panels is influenced by the following parameters: thickness of skins, depth of the embedded shear connectors into concrete, shear span-to-depth ratio, thickness and shape of shear connectors, and spacing of shear connectors.

In this chapter, the main aim is to investigate the structural performance of hybrid sandwich slabs with shear span-to-depth (a/h) ratios that varies from 2 to 0.77. Six hybrid slabs with different lengths were manufactured and experimentally tested.

In the chapter three and five, hybrid composite slabs were built and experimentally tested under flexural loading. Slabs presented an almost linear force versus mid-span response up to pick load, followed by a smooth load carrying degradation in the structural softening phase. The nonlinearities observed in the response of the tested slabs were mainly caused by the damage occurred in the connection between the GFRP ribs and the DHCC layer. Using indented shear connectors, instead of perforated connectors, leads to postpone the damage in GFRP ribs and provides a higher residual load carrying capacity and deflection. Furthermore, it was concluded that the stiffness and load carrying capacity of the hybrid slabs is mainly governed by the connection of GFRP ribs/DHCC layer. Six specimens, with different lengths that provide different shear span-to-depth ratios, were tested to assess the shear performance of hybrid slabs. The attained experimental results and their interpretation are presented in the following.

As mentioned in the previous chapters, the proposed hybrid sandwich panel comprises four components that include DHCC material as top layer, GFRP skin as bottom layer, GFRP rib to transfer shear stresses from DHCC layer to GFRP skin, and polyurethane foam core positioned between the bottom GFRP skin and the DHCC layer, as shown in Fig. 2.1.

The DHCC layer connects the GFRP ribs through indented shear connectors. A simple technique was adopted to create the indented shear connectors in the GFRP ribs: holes of small diameter were executed on the top zone of the GFRP rib that is later embedded in the DHCC layer. Fig. 5.1 shows the dimension and disposition of the indented shear connectors. The dimensions of the slab's components were equal to the slabs (Slab 1 and Slab 2) used in Chapter 2, as presented in Fig. 2.1. and Table 2.1.

6.2. Experimental plan

6.2.1. Materials

Extensive experimental tests were carried out in Chapter 2 to develop the DHCC material and characterize the mechanical properties of the GFRP components. A brief summary on the mechanical properties of the materials used in the hybrid slabs is here presented.

6.2.2. Manufacturing process

Fabrication of GFRP body (GFRP ribs and skin) was done using vacuum assisted resin transfer molding (VARTM) process on a formwork with pre-installed foam cores (see Fig. 6.2a, b, c). The fabrication process of hybrid sandwich panels includes: 1) Preparation of mold and fiber layers lay-up for GFRP skins and ribs on a metallic table (see Fig. 6.2a); 2) Sealing the mold and creating vacuum (see Fig. 6.2b). The air is evacuated from the porous material prior to admitting the resin. 3) Preparation and degassing of the resin; 4) Resin impregnation (see Fig. 6.2c). The prepared resin is injected into the mold at a very slow rate and the flow is controlled with a peristaltic pump. The resin is first allowed to flow in the distribution medium for some distance and then the inlet is shut off, giving the resin time to flow through the thickness. The distribution medium is a green mesh laid at the bottom of laid skin fibers; 5) Demolding the prototypes. At least 24 hours of resin curing are required before demoulding the specimens. 6) Trimming is executed to separate extra parts as well as creating holes in the GFRP ribs to define the shear connectors, as shown in Fig. 6.2d and Fig. 6.2e. In manufacturing process of slabs through VARTM, for ensuring proper infusion of resin, GFRP skins and ribs produced in larger dimensions than the designed dimensions. Finally, slabs are cast using DHCC material on the top layer and the specimens are left to be cured for 28 days (see Fig. 6.2f).

6.2.3. Hybrid slabs

The experimental program executed in this chapter comprises six hybrid slabs. Table 6.1. lists the spans and loading schemes of different hybrid slabs. With respect to the listed six slabs in Table 6.1., one slab with cross section of Slab 1 and the other one with cross section of Slab 2 and a span length equal to 500 mm were used to be assessed under shear load with span ratio 1.39 (=(A/H), where letter of A in Fig. 6.3 depicts the arm of load and H is slab's height) for Slab 1 and 1.78 of span ratio for Slab 2, where herein designated by ST1 and ST2, respectively. Moreover, two slabs with cross sections of Slab 1 and Slab 2, and 900 mm span length evaluated under shear loading, considering of span ratio of 2, where specimens designated by SS1 and SS2, respectively. Finally, two slabs with cross sections of Slab 1 and Slab 2, and 500 mm span length were assessed under shear loading, considering of shear span ratio of 0.77, where specimens designated by SL1 and SL2, respectively.

Table 6.1. Summarized details about the slabs assessed under shear loading

Slab name	Cross section	Span length	Height (H)	The arm of load (A)	(A/H)
SS1	Slab 1	900	162.5	325	2.00
SS2	Slab 2	900	130.0	260	2.00
ST1	Slab 1	500	162.5	226	1.39
ST2	Slab 2	500	130.0	231	1.78
SL1	Slab 1	500	162.5	125	0.77
SL2	Slab 2	500	130.0	100	0.77

a)

b)

c)

d)

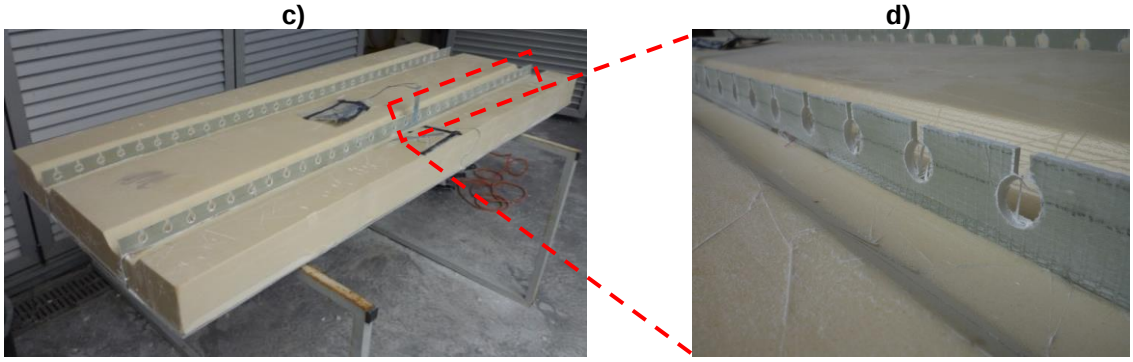

e)

f)

Fig 6.2. Manufacture process of hybrid slabs: a) fiber layers lay-up; b) sealing the mold; c) resin impregnation; d) trimming; e) creating shear connectors; f) casting of DHCC layer

The main aim in this chapter is to assess the structural performance of shear connectors in specimens with reduced shear span to depth ratios, where the proportion of shear stress is subsequently increased.

6.2.4. Test setup and instrumentations

Seven linear variable differential transformer (LVDT) were installed on the slab specimens to measure the displacements in different positions, as shown in Fig. 6.3. LVDT 3, LVDT 4, and LVDT 5 measured deflections in the mid-span zone and LVDT 2 and LVDT 6 were used to record the vertical displacements on the DHCC layer, at both end sides over the supports, as shown in Fig. 6.3. Additionally, LVDT 1 and LVDT 7 used for registering slip between the DHCC layer and the GFRP ribs at both end sides.

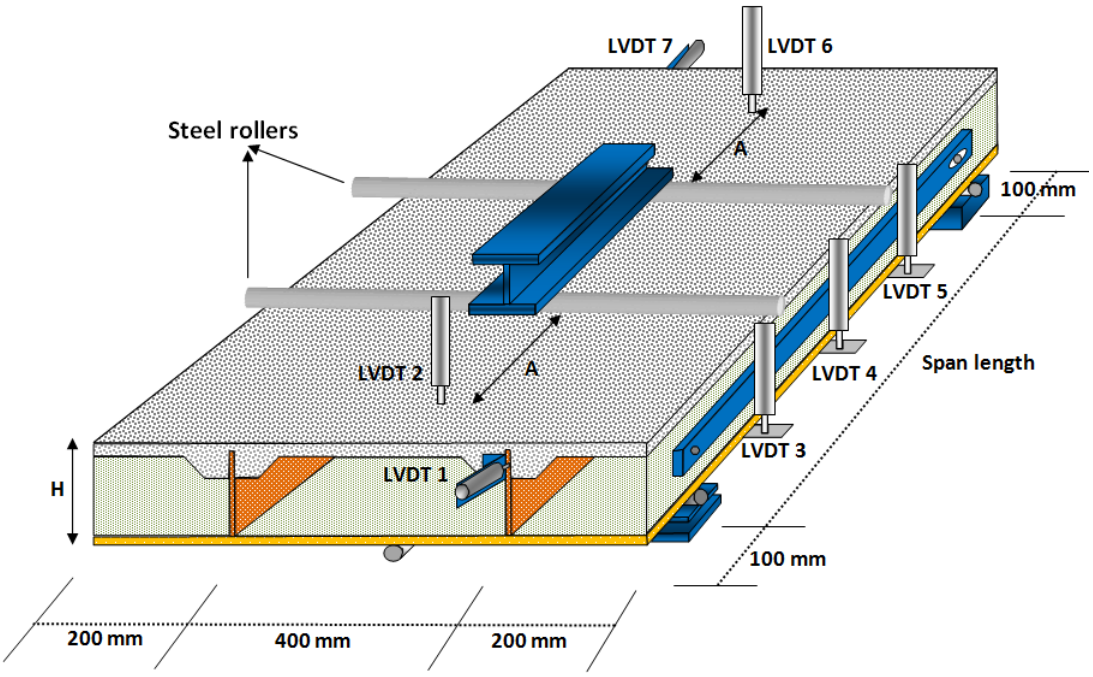

Fig 6.3. Setup for the shear tests on hybrid slabs

Depending on the type of loading, one or two steel rigid rollers were used to apply line loads across the width of specimens. Four strain gauges were used to measure strain across the panel's thickness at mid-span, including one strain gauge at the GFRP skin, two strain gauges at the GFRP ribs, and one strain gauge at the top surface of the DHCC layer, as shown in Fig. 5.4. Strain gauges, type BFLA-5-5, from TML, with a 5 mm measuring length were used in the GFRP ribs and skins. One strain gauge, Type PFL-30-11—3LT, from TML with 30 mm measuring length, was installed on the top of the DHCC layer. All tests were controlled by displacement. A displacement rate of 30 μm/sec was applied on the slab mid-span.

6.3. Results and discussion

Damages occurred in the hybrid slabs in several sequences. No sudden failure was observed in the damage sequences identified during the tests. The following damage sequences recorded in specimens SF1, SF2, SS1, SS2, ST1, ST2, and SL2 as:

1) Loss of connection between the foam core and the DHCC layer (see Fig. 6.4a);
2) Damage in the GFRP ribs due to high compressive stress (see Fig. 6.4b);
3) Loss of bond between the GFRP rib and the DHCC layer (see Fig. 6.4c);
4) Splitting cracks formed on the surface of DHCC layer, aligned with the shear connectors (see Fig. 6.4d);
5) Some shear cracks formed in the foam core (see Fig. 6.4e).

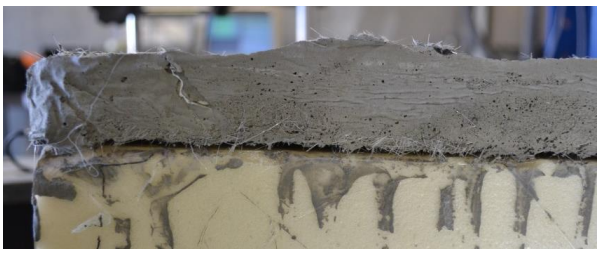

a) Loss of connection between the foam cores and the DHCC layer

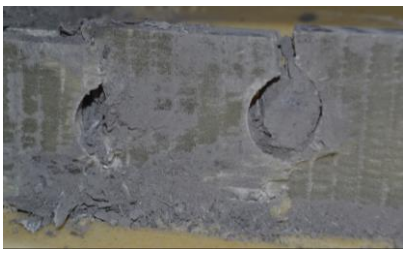

b) Compressive damage in the GFRP rib

c) Loss of bond between the GFRP rib and the DHCC layer

d) Splitting and crushing cracks formed on the surface of DHCC layer

e) Forming shear cracks in foam cores

Fig 6.4. Sequence of observed failure modes in specimens SS1, SS2, ST1, ST2, and SL2

Specimen SL1 showed a different damage sequence due to reduction of shear span to depth ratio. The damage sequence observed in specimen SL1 includes:

1) Loss of connection between the foam core and the DHCC layer (Fig. 6.5a);
2) Ply delamination of GFRP rib layers (Fig. 6.5b);
3) Local buckling in the GFRP ribs (Fig. 6.5c);
4) Splitting cracks formed on the surface of DHCC layer, aligned with the shear connectors (Fig. 6.5d);
5) Ply delamination of GFRP rib layers in the connection zone with GFRP skin (Fig. 6.5e);
6) Formation of shear cracks in the foam cores (Fig. 6.5f).

a) Loss of connection between the foam cores and the DHCC layer

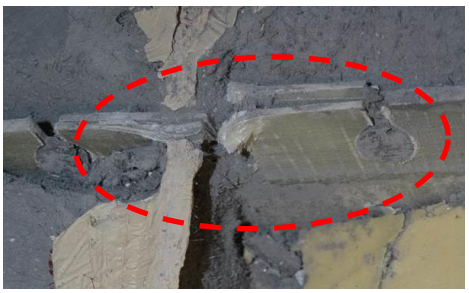

b) Ply delamination of GFRP rib layers

c) Local buckling in GFRP ribs

d) Splitting cracks formed on the surface of DHCC layer

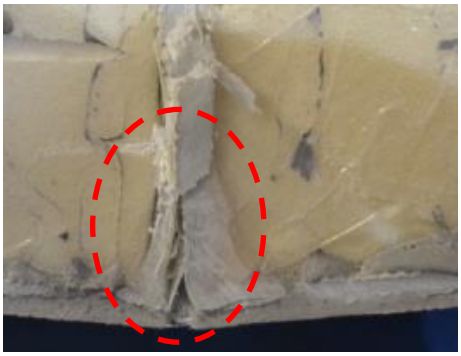

e) Ply delamination of GFRP rib layers at connection zone with GFRP skin

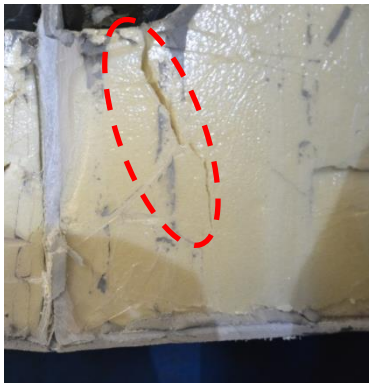

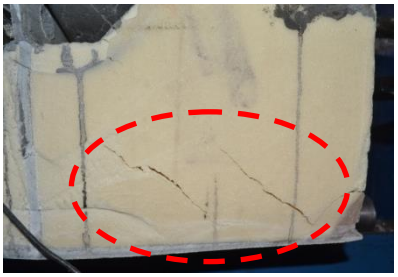

f) Forming shear cracks in the foam cores

Fig 6.5. Sequence of damage observed in specimen SL1

The following paragraphs present the results obtained in the experimental tests. Diagrams that relate the force applied and the corresponding deflection, the force applied and the slip measured between the GFRP rib and the DHCC layer, the force applied and the corresponding strain response and the composite action for different load levels were considered. Interestingly, it was observed that applying shear loads to slabs with different span to depth ratios resulted in recording different structural behaviors and damages. Table 6.2. presents the summarized results obtained from imposing shear loads to slabs in terms of the ultimate load carrying capacity, deflection and slip corresponding to the end of hardening structural behavior of slabs. In general, regarding the recorded results, higher maximum force was registered for specimens ST1, SS1, and SL1, compared to specimens ST2, SS2, and SL2. The recorded deflection and slip at pseudo hardening stage were governed by the connection between the GFRP ribs and the DHCC layer.

In the following sections, all details are presented about the structural behavior of the assessed slabs under the shear loads with different span to depth ratios.

Table 6.2. The summarized results recorded from applying shear loads to slabs

Slab name	Maximum force (kN)	Deflection corresponding to the end of hardening behavior (mm)	Slip corresponding to the end of hardening behavior (mm)
SS1	159.42	5.37	3.64
SS2	109.76	5.12	1.14
ST1	150.66	2.05	1.28
ST2	91.16	6.47	0.45
SL1	228.41	4.89	0.22
SL2	172.92	5.39	4.08

6.3.1. Shear loading in specimens with span to depth ratio of 2.0

Fig. 6.6 shows the relation between the applied load and the deflection measured at the slabs' mid span for the various specimens and different load levels applied. Figs 6.6a and 6.6b indicate the response of slabs SS1 and SS2 under shear loading, respectively. Specimen SS1 presents an almost linear force-deflection response up to 120.7 kN, when a deflection of 1.6 mm was registered (Point B in Fig. 6.6a). Although the first evidence of damage was detected for a load level of about 80 kN (Point A in Fig. 6.6a), with loss of contact between the foam and the DHCC layer (Fig. 6.4a), the value of stiffness is more or less constant up to point B (120.7 kN). At point B, damage increased significantly, mainly due to high compressive stress in the GFRP ribs (see Fig. 6.4b). Specimen SS1 was able to endure an increase of load up to 160 kN. Then, load capacity was maintained and larger deflection values were developed, expressing a hardening behavior (a load of 149.4 kN and a deflection of 9 mm, $=L/100$, where L is equal to span length, were registered at Point C of Figure 6.6a). By further increasing the deflection, more deterioration on the connection between the ribs and the DHCC layer was observed, and a splitting crack started to be visible in the top surface of the DHCC layer, along the alignment of the GFRP ribs (Fig. 6.4d). According to the experimental results, an almost constant residual load carrying capacity of about 50 kN was registered up to a deflection value of 28.15 mm (≈L/32), which is about 33% of the load recorded in point C. Afterwards, shear cracks also began to appear in the foam core due to large residual deflection (see Fig. 6.4e).

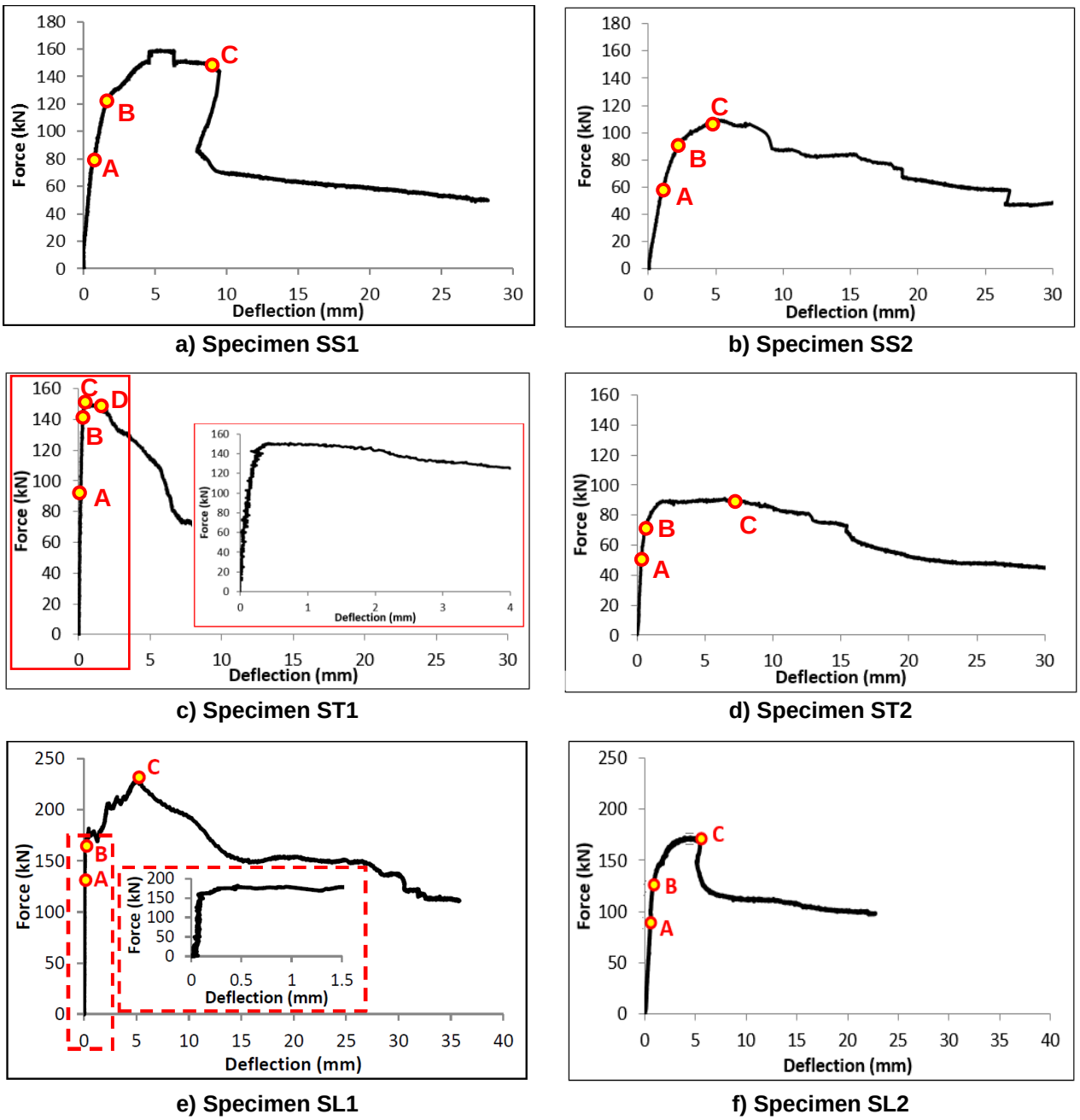

a) Specimen SS1 b) Specimen SS2

c) Specimen ST1 d) Specimen ST2

e) Specimen SL1 f) Specimen SL2

Fig 6.6. Force and corresponding deflection measured in the tested specimens

Fig. 6.7 shows the slip values between the DHCC layer and the GFRP ribs recorded by LVDT 1 during the test. In specimen SS1, a nonlinear increment of slip occurred at the end of the linear response, corresponding to a force of 125.7 kN and a slip value of 0.022 mm, as shown in Fig. 6.7a. For values of slip higher than 3.64 mm (where the load is equal to 143.2 kN), and sudden reduction of load takes place (Point A in Fig. 6.7a) caused by the loss of contact between the GFRP shear connectors and the DHCC layer. Fig. 6.8a shows a faster increment of slip from this moment on. A linear correlation between deflection and slip is verified, beginning in point A and up to 3.64 mm of slip (branch of AB in Fig. 6.8a). Afterwards, specimen SS1 experiences a new phase, where the vertical deflection grows

faster. The diagrams presented indicate that the stiffness and the load carrying capacity of specimen SS1 are mainly governed by the connection between the GFRP ribs and the DHCC layer.

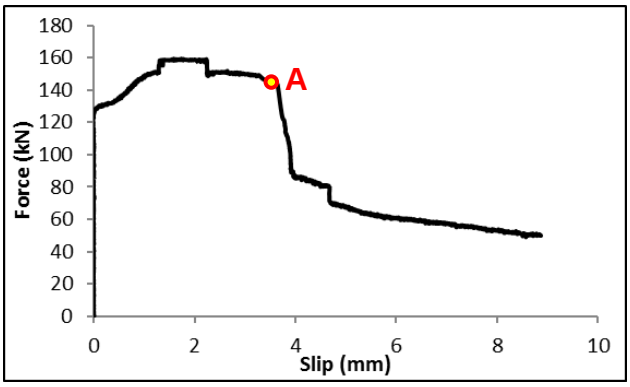

a) Specimen SS1

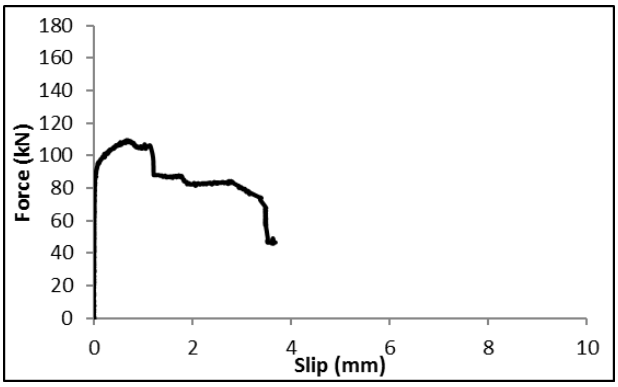

b) Specimen SS2

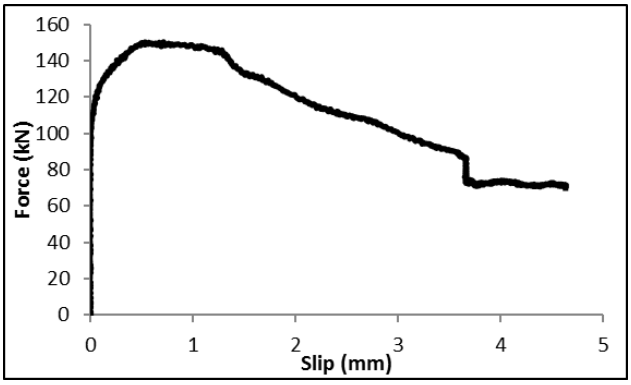

c) Specimen ST1

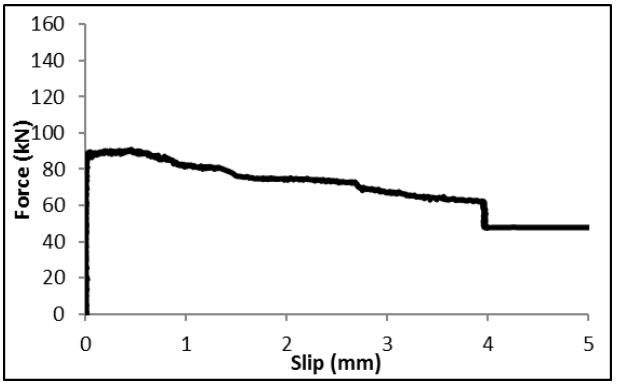

d) Specimen ST2

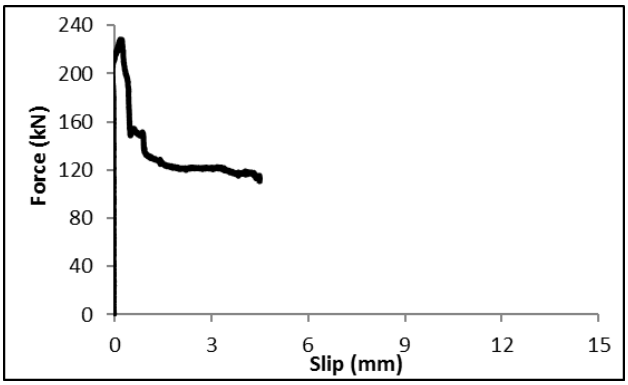

e) Specimen SL1

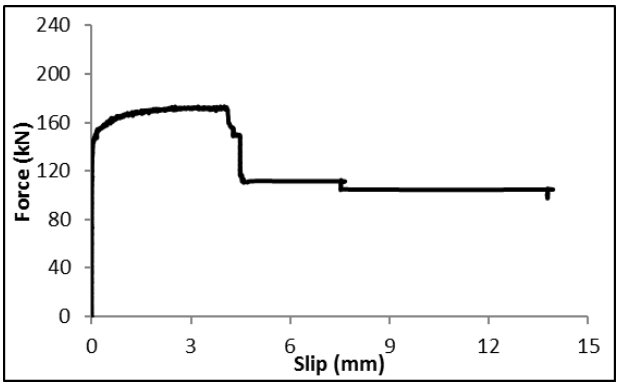

f) Specimen SL2

Fig 6.7. Force and corresponding slip measured in the tested specimens

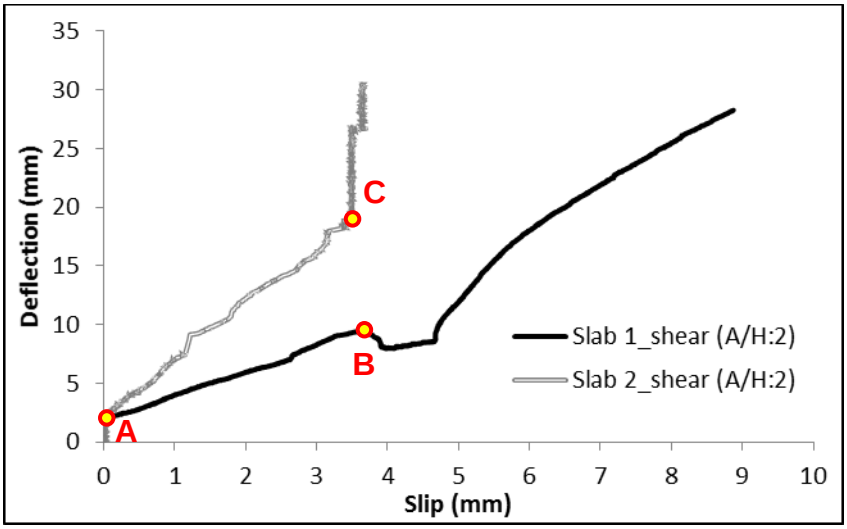

a)

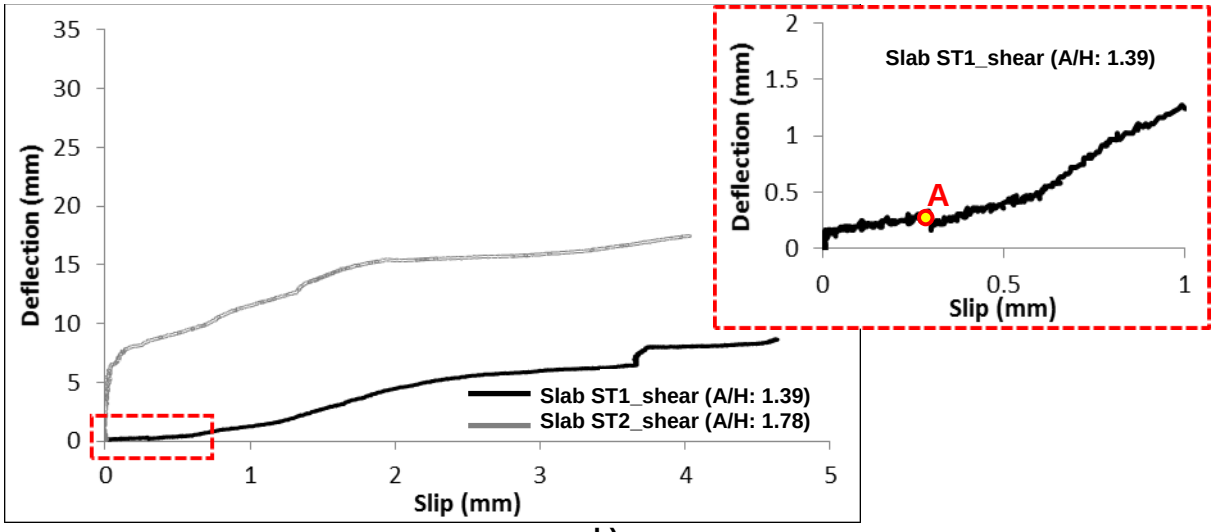

b)

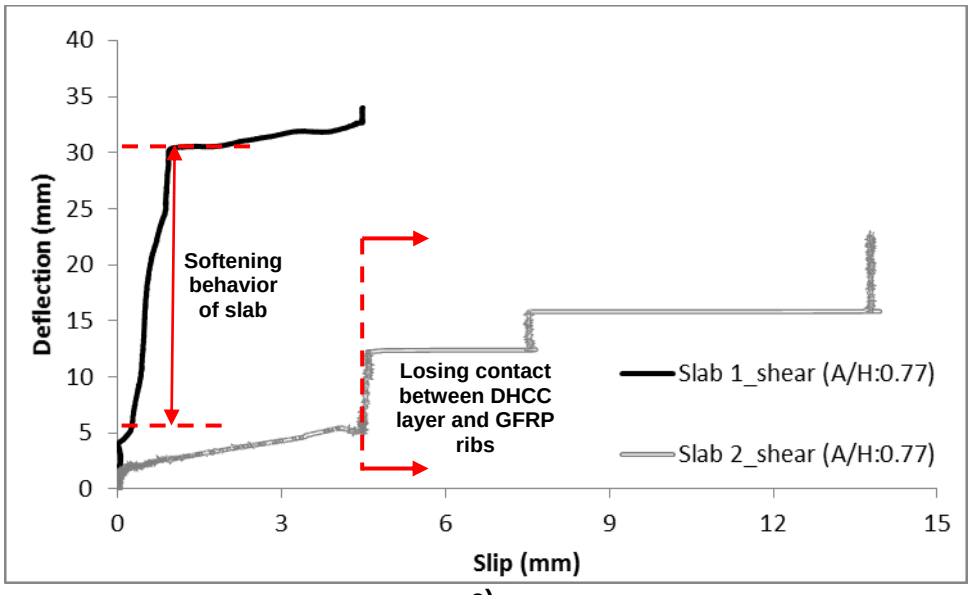

c)

Fig 6.8. Relationship between deflection versus slip for specimens loaded under shear with span rations of: a) 2; b) 1.39 for Slab 1 and 1.78 for Slab 2; c) 0.77

Fig. 6.9 presents the strains values registered at the mid span cross section of all the tested specimens, during the loading process. According to the results shown in Fig. 6.9a, a maximum compressive strain of -1100×10^{-6} (m/m) was recorded at the top of the DHCC layer (SG4), while a maximum tensile strain of 1822×10^{-6} (m/m) was registered in the GFRP skin (SG1). The tensile strains measured in the GFRP ribs and skin of specimen SS1 were much lower than the ultimate strains recorded in the direct tensile tests carried out on specimens extracted from these components of the slab (see Table 2.4). During the deflection hardening stage of specimen SS1, the vertical compressive stress in the GFRP ribs increased significantly due to the deterioration of the shear connection between the ribs and the DHCC layer.

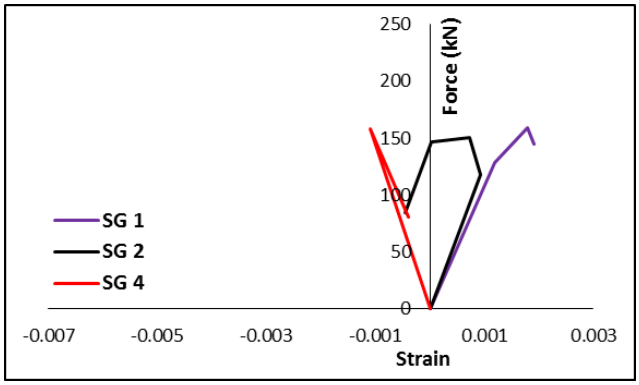

a) Specimen SS1

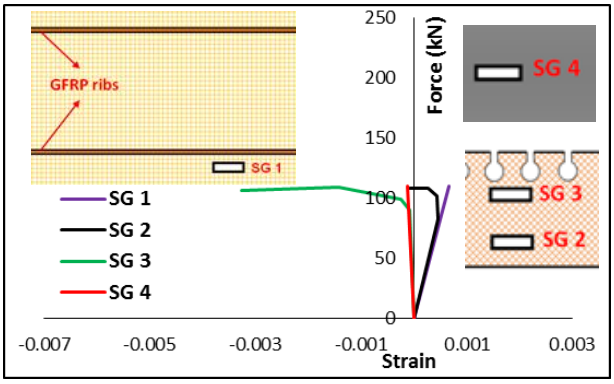

b) Specimen SS2

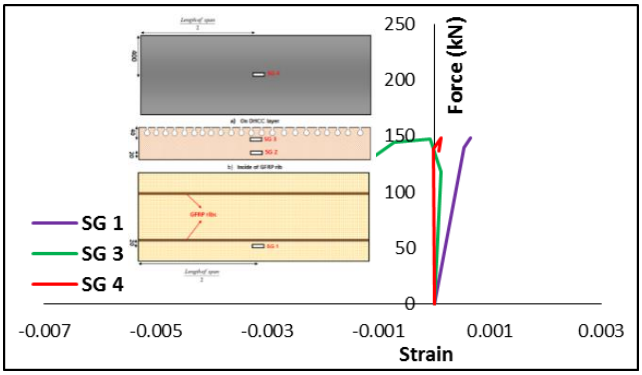

c) Specimen ST1

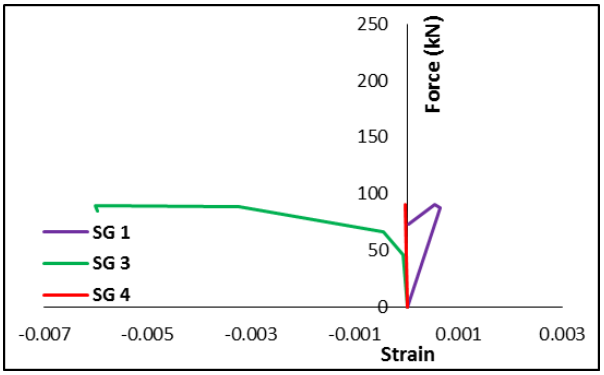

d) Specimen ST2

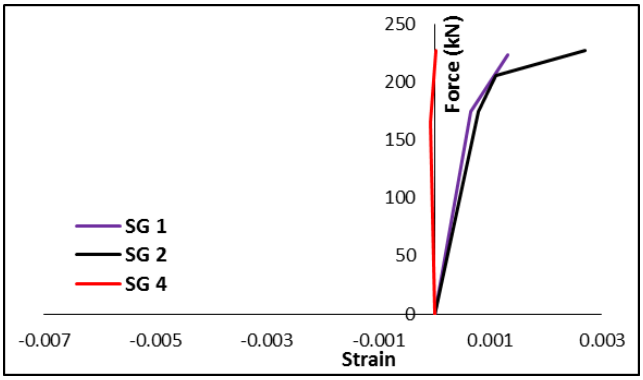

e) Specimen SL1

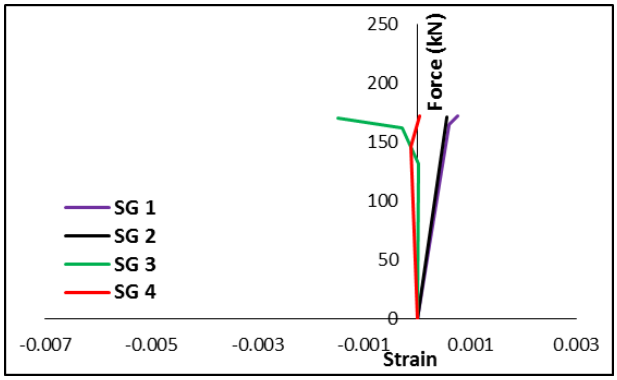

f) Specimen SL2

Fig 6.9. Strain values recorded in different positions of the tested specimens

The efficiency of shear connectors under different load conditions was also evaluated by analysing the strain distribution at mid span cross section. Fig. 6.10 illustrates the strains in the mid-span cross section. The represented diagrams correspond to the following load levels: $0.2P_{max}$, $0.4P_{max}$, $0.6P_{max}$, $0{,}8P_{max}$ and P_{max}. These strains diagrams are used to evaluate the efficiency of the indented shear connector. The distribution of strains obtained for the maximum load, across the panels' thickness, is altered by the significant slip values measured between the DHCC layer and the GFRP ribs at this load level. Three different levels of composite action were defined to assess the efficiency of shear connectors under different load conditions: full composite action, partial composite action, and non-composite action. Full composite action is attained when there is no slip between slab's components. In this case, the strain diagram remains linear and continuous across the slab thickness. If the connection is not rigid, there is some slip between slab's layers and the strain diagram is not continuous.

As aforementioned, one strain gauge with 30 mm length was installed on the top layer of DHCC material to measure compressive strains in the slabs. The strain gauge installed on the top layer of the DHCC layer did not record the compressive strain precisely in the location of DHCC crushing. Additionally, if the strain gauge is not in a position close to the crushing area, it tends to "unload" back to low values when the shear connection between the GFRP body and the DHCC layer is lost. Thus, as shown in Fig. 6.10, the compressive strains measured in the DHCC layer for maximum load may not be representative of the maximum strain in the location of crushing. Even so, the results obtained provide a general idea of the composite action in slabs with indented shear connectors. The pattern of the strain distribution across the panel's thickness was analysed to estimate the composite action achieved.

The results presented in Fig. 6.10a show that, in the initial phase of loading, the strain diagram is almost continuous, while significant difference in the distribution of strains across the panels' thickness was found for loads higher than $0.6P_{max}$ (equal to 95.65 kN), indicating that the strain diagram is not linear and slab behaves as partially-composite. Increasing of the load from $0.6P_{max}$ to $0.75P_{max}$ (equal to 120.70 kN, where non-linear behaviour was observed for slab due to excessive compressive stress in the GFRP ribs occurred) led to some damage in the connection between ribs and DHCC layer. This damage is almost totally concentrated in the connection between ribs and DHCC layer when the load is increased from $0.75P_{max}$ up to P_{max} (159.42 kN).

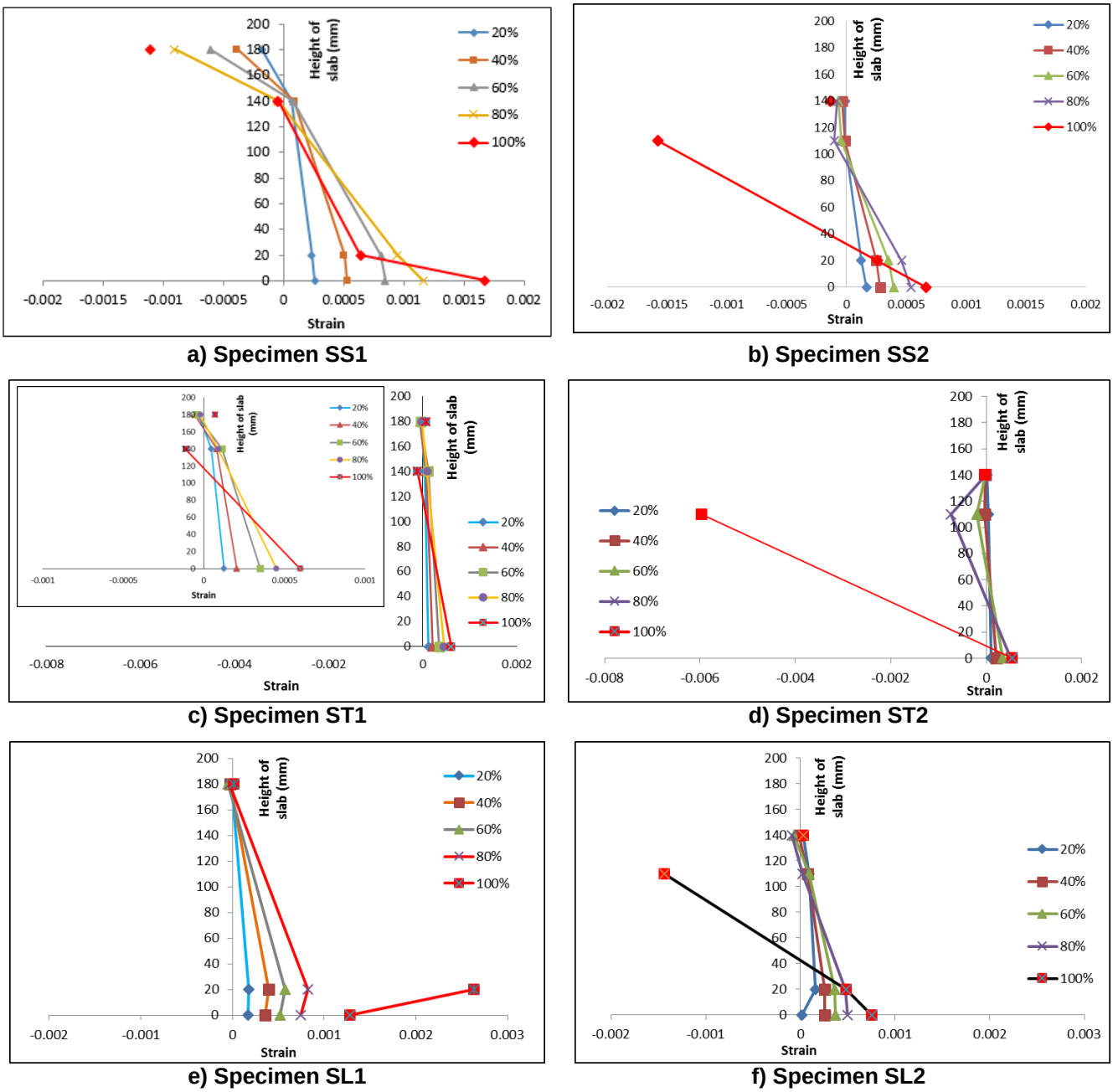

a) Specimen SS1

b) Specimen SS2

c) Specimen ST1

d) Specimen ST2

e) Specimen SL1

f) Specimen SL2

Fig 6.10. Strain distribution of the tested specimens, at the mid-span cross section

Specimen SS2 was tested based on shear load conditions and span to height ratio of 2. All details about measurement devices and test setup were described in section of 3.4. The load versus deflection response registered for specimen SS2 is depicted in Fig. 6.6b, where specimen SS2 presented a linear-elastic behaviour up to load of 92.51 kN and 1.96 mm of deflection (Point B in Fig. 6.6b), at which compressive damage has occurred in the GFRP ribs (Fig. 6.4b). Loss of contact between DHCC layer and foam was also observed in specimen SS2, when the load was equal to 60 kN (Point A in Fig. 6.6b), but again this had no significant impact in term of loss of stiffness for the slab. A hardening stage was observed above 2.32 mm of deflection due to damage in the GFRP ribs. Damage began to propagate in specimen SS2, and a load of 106.58 kN for a corresponding deflection of 7.48 mm

(≈L/120) were recorded in Point C (see Fig. 6.6b). Above deflection of 7.48 mm, specimen SS2 entered in a softening structural stage with smooth reduction of the load carrying capacity, so that this slab presented a load carrying capacity of 47.9 kN at deflection of 29.98 mm (≈L/30), which is about 45% of the peak load. The relationship between the applied load and the measured slip between the DHCC layer and the GFRP ribs for specimen SS2 is shown in Fig. 6.7b, where a nonlinear increment of slip occurred at the end of the linear response of specimen SS2, corresponding to a force of 81.79 kN and 0.011 mm of slip. Fig. 6.8a shows an abrupt increment of slip in point A, with 1.96 mm of deflection, where a splitting crack started to be visible on the top surface of the DHCC layer along the alignment of the GFRP ribs (see Fig. 6.4d). A linear correlation between slip and deflection can be found up to 3.50 mm of slip (branch of AC in Fig. 6.8a). Specimen SS2 experienced a high residual load carrying capacity of about 48 kN (Fig. 6.6b).

According to the results presented in Fig. 6.9b, a maximum compressive strain of -1600×10^{-6} m/m was recorded in the GFRP ribs (SG3), and a maximum tensile strain of 660×10^{-6} m/m was measured in the GFRP skin (SG1). The maximum registered compressive strain on the top surface of DHCC layer was equal to -140×10^{-6} m/m (SG 4), which is a low strain value when compared to the ultimate compressive strain of DHCC material (equal to 2400×10^{-6} m/m). After occurring compressive damage in GFRP ribs, both the strain gauges installed in the GFRP ribs (SG2 and SG3) indicated an increase in the compressive strains. This increase may be justified by a local buckling in the GFRP ribs, developed at large residual deflection and load carrying capacity. Additionally, the strains recorded in GFRP ribs and skin of specimen SS2 were much lower than the ultimate tensile strains recorded in the direct tensile tests executed in specimens extracted from these GFRP elements (see Table 2.4).

Fig. 6.10b shows the distribution of strain across the panels' thickness in different phases of loading for specimen SS2. In the initial phase of loading, the strain diagram is continuous and almost linear, indicating that the slab is working as fully composite. For P_{max} (109.76 kN), the strain diagram is not linear anymore, indicating a partial composite behaviour. This means that between $0.8P_{max}$ (87.80 kN) and P_{max} (109.76 kN), some damage occurred in the connection and altered the transmission of shear stresses. This effect was previously identified in Fig. 6.6b and Fig. 6.7b, where non-linear behaviour was observed for loads higher than 92.51 kN due to compressive damage in the GFRP ribs.

6.3.2. Shear loading in specimens with span to depth ratio of 1.39 (Slab ST1) and 1.78 (Slab ST2)

Two slabs with 500 mm span length were built and designated as ST1 and ST2. A concentrated load was imposed in the mid-span of Slab ST1 and Slab ST2 to assess their shear performance. The loading conditions chosen provide shear span ratios of 1.39 for Slab ST1 and 1.78 for Slab ST2. Both slabs were monotonically loaded and the following results were obtained. By reducing shear span to depth ratio, the shear stress is increased in a distance between support and where the load imposed (the arm of load) to the hybrid slabs. Therefore, these tests with $1\langle\frac{A}{H}\langle 2$ were established to investigate the structural performance of hybrid slabs under higher portion of shear load.

Fig. 6.6c depicts the relationship between force and deflection on specimen ST1. This slab presents a linear-elastic behaviour up to a load of 140 kN and a corresponding deflection of 0.25 mm - Point B in Fig. 6.6c - where compressive damage occurred in the GFRP ribs (Fig. 6.4b). Like specimens SS1 and SS2, the first damage occurred due to loss of contact between the foam and the DHCC layer (Fig. 6.4a), when the imposed load was equal to 90 kN (Point A in Fig. 6.6c). This damage had no significant impact the stiffness of the slab. A plateau stage was measured above 0.25 mm of deflection (branch of CD in Fig. 6.6c), and an almost constant peak load of 146.6 kN for a deflection of 1.8 mm was recorded in Point D (Fig. 6.6c). Above this deflection, the specimen ST1 entered in a structural softening stage, where a residual load carrying capacity of 70 kN was measured at the deflection of 8.64 mm (≈L/58), which is about 48% of peak load.

Fig. 6.7c depicts the slip measured between the DHCC layer and the GFRP rib for specimen ST1. According to the results obtained, abrupt sudden slip occurred at a load of 100 kN and 0.0071 mm of slip. As shown in Fig. 6.8, most of the tested slabs registered large mid-span deflections and low slip values in the linear-elastic stage, which did not occur in specimen ST1. Due to damage at the connection between the GFRP rib and the DHCC layer, large slip values were recorded, as shown in Point A in Fig. 6.8b. Above the deflection value of 0.25 mm, due to concentration of damage in connection zone and deterioration of the shear connection between the ribs and the DHCC layer, a faster increment of deflection is measured.

According to the results indicated in Fig. 6.9c, a maximum compressive strain of -670×10^{-6} m/m was recorded in the GFRP ribs (SG3) and a maximum tensile strain of 620×10^{-6} (m/m) was measured in the GFRP skin (SG1). Due to the deterioration of the shear connection between the ribs and the DHCC layer in the plateau stage, the compressive stress in GFRP ribs (SG3) increased significantly. The strains registered in the

GFRP ribs and skin of specimen ST1 were much lower than the ultimate strains recorded in the direct tensile tests executed in specimens extracted from these GFRP elements (see Table 2.4). Moreover, based on Fig. 6.10c, specimen ST1 behaved as fully composite up to 0.8 P_{max} (117.28 kN). When the load was increased from 0.8P_{max} to P_{max} (146.60 kN), non-composite action was attained, which means that severe damage occurred in this load interval. Specimen ST1 presents a nonlinear behaviour at a load of 0.95P_{max} that results from high compressive stress in the GFRP ribs. Thus, it can be concluded that specimen ST1 presented a fully composite behaviour up to 0.95P_{max} and above this load, the slab behaved as non-composite with occurring compressive damage in the GFRP ribs (Point B in Fig 6.6c).

Fig. 6.6d represents the force versus deflection response of specimen Slab 2 under shear loading, considering span to height ratio of 1.78. Like other tested slabs, in specimen ST2 the first damage consisted on loss of contact between foam and DHCC layer (Fig. 6.4a), when the imposed load was equal to 50 kN (Point A in Fig. 6.6d) and its impact in term of stiffness was almost imperceptible. By further increasing the deflection, a second damage was observed in the GFRP ribs due to excessive compressive stress (Fig. 6.4b), when the load was equal to 69.67 kN and the corresponding deflection was 0.62 mm. A hardening stage was registered above the vertical deflection of 0.62 mm. The peak load of 90.03 kN and the corresponding deflection of 7.32 mm (≈L/68) were recorded in Point C (Fig. 6.6d). Above this deflection, the slab entered into a structural softening stage and subsequently, its load carrying capacity was smoothly decreased. The slab's load carrying capacity at the ultimate deflection (about 30 mm, ≈L/17) was approximately 44.5 kN, which is about 50% of the peak load. It is interesting to observe that the residual load carrying capacity is around 50% of the corresponding peak load in both tested slabs with low span to height ratio, ST1 and ST2.

According to Fig. 6.7d, a nonlinear increment of slip started to be measured when the force applied was 88.28 kN and the corresponding slip was 0.008 mm. At this slip, the deflection in slab ST2 was equal to 1.89 mm, as shown in Fig. 6.8b. It is worth stating that compressive damage in GFRP ribs of slab ST2 occurred at a deflection of 0.62 mm and a linear increment was recorded for slip in slab ST2 up to deflection of 1.89 mm. This exhibits that damage in the connection zone, between ribs and DHCC layer, is intensified for a deflection of 0.62 mm up to 1.89 mm. Increasing the deflection above 1.89 mm led an abrupt increment of slip.

According to the results indicated in Fig. 6.9d, a maximum tensile strain of 660×10^{-6} m/m was measured in the GFRP skin (SG1), and a maximum compressive strain of -5900×10^{-6} m/m was recorded in the GFRP ribs (SG3). Additionally, the strain distribution across the panel's thickness, at mid-span indicates that specimen ST2 behaves as fully

composite up to 0.4P_{max} (36.01 kN), partially composite at a load of 0.6P_{max} (54.02 kN), and non-composite action at 0.8P_{max} (72.02 kN) and P_{max} (90.03 kN), as shown in Fig. 6.10d.

6.3.3. Shear loading in specimens with span to depth ratio of 0.77

Two slabs with 500 mm span length were built and designated as SL1 and SL2. The load was imposed to these slabs with a shear span ratio of 0.77. This configuration provides an equilibrium condition where an inclined compression strut runs directly from the load application point to the support (through the GFRP ribs and the foam core), the GFRP skin is loaded as tension tie, and a top horizontal compressive strut is developed in the DHCC layer.

Figs 6.6e and 6.6f indicate the force versus deflection responses of Slab SL1 and Slab SL2. Specimen SL1 presents an almost linear force-deflection response up to 153.17 kN, when a deflection of 0.1 mm is recorded in Point B (Fig. 6.6e). The first damage observed occurred at a load level of 120.68 kN (Point A in Fig. 6.6e), due to loss of contact between foam and DHCC (Fig. 6.5a), whose effect on stiffness was reduced. Then, at Point B, ply delamination was observed in the GFRP ribs when subjected to in-plane compressive loads, when a load of 151.28 kN and a deflection of 0.107 mm were registered (Fig. 6.5b). Above this deflection, an increase of load was observed in the slab, until a peak load of 228.07 kN and a deflection of 4.89 mm (≈L/102) were measured at Point C, and splitting cracks started to appear in the top surface of the DHCC layer along the alignment of the GFRP ribs (Fig. 6.5d). In the hardening stage (branch BC in Fig. 6.6e), the delaminated area in the GFRP ribs locally buckled (delamination buckling) and the damage propagate at the connection zone between GFRP ribs / DHCC layer, as shown in Fig. 6.5c. Above a deflection of 4.89 mm, specimen SL1 entered into a softening structural behavior, and subsequently the deterioration intensified between the GFRP ribs and the DHCC layer, at the connection zone, and at the connection between the GFRP rib and the GFRP skin (see Fig. 6.5e). According to the experimental results obtained, shear cracks appeared in the foam core due to large residual deflection (Fig. 6.5f). An almost constant residual load carrying capacity of 110.39 kN was registered at a deflection of 35.72 mm (≈L/14), which is about 48% of the peak load, measured to point C.

As shown in Fig. 6.7e, it is indicated that abrupt sudden increment of slip was recorded at a force of 210.38 kN and 0.057 mm of slip. The relationship between deflection and slip in Fig. 6.8c indicates that an abrupt increment of slip led to record a deflection of 30 mm.

According to the results are shown in Fig. 6.9e, a maximum tensile strain of 2700×10^{-6} (m/m) was registered in the GFRP rib (SG 2). Due to problems in recording strain values with SG 3, compressive strains in the GFRP ribs were not measured.

The efficiency of shear connectors in Slab SL1 was evaluated by analysing the strain distribution across the panel's thickness at mid-span. The strain distribution across the slab's thickness presented in Fig. 6.10e, shows that specimen SL1 behaved as partially composite up to $0.6P_{max}$ (136.84 kN), and a non-composite action was verified afterwards. Unfortunately, during the test, SG 3 disconnected and therefore, strain values were not recorded in the upper part of the GFRP ribs.

The force versus deflection response of Slab SL2 under shear loading is shown in Fig. 6.6f. According to the experimental results obtained and like other hybrid slabs tested, an almost linear force-deflection response was measured, up to a force equal to 140.04 kN and a deflection of 1.14 mm (Point B in Fig. 6.6f). Despite no severe damage in the linear response of the slab, the first damage observed was caused by loss of contact between DHCC layer and foam cores, for a load of 95.54 kN, and a deflection of 0.63 mm (Point A of Fig. 6.6a). This damage had no significant effect on the stiffness of slab. Nonlinear damage in specimen SL2 mainly resulted from high compressive stress in the GFRP ribs (Fig. 6.4b) that occurred for a force of 140.04 kN and a deflection of 1.14 mm in Point B (Fig. 6.6f). By increasing the deflection, a hardening behavior was observed, up to a peak load of 170.95 kN and a deflection of 5.37 mm (≈L/93), corresponding to Point C. In the hardening stage (branch BC in Fig. 6.6f), some splitting cracks began to form on the top surface of the DHCC layer along the alignment of the GFRP ribs (Fig. 6.5d).

Above the deflection of 5.37 mm, a softening structural behavior was registered, and an almost constant residual load carrying capacity of 97.75 kN was recorded at deflection of 22.50 mm (≈L/22), which is about 57% of the peak load. Furthermore, shear cracks were formed in the foam core resulting from large residual deflection (Fig. 6.5e).

A sudden increment of slip was recorded at a force of 119.62 kN and 0.005 mm of slip (Fig. 6.7f). Softening structural behaviour in specimen SL2 began at a deflection of 5.37 mm, the connection between DHCC layer and GFRP ribs lost (Fig. 6.4c) and subsequently large values of slip were registered, as shown in Fig. 6.8c.

In respect to the results indicated in Fig. 6.9f, during the deflection hardening stage of the slab SL2 (see Fig. 6.9f), the compressive strain in the GFRP rib (SG 3) increased significantly from -110×10^{-6} (m/m) to -1500×10^{-6} (m/m), caused by the deterioration of the shear connection between the ribs and the DHCC layer A maximum tensile strain of 770×10^{-6} (m/m) was measured in the GFRP skin (SG 1). Tensile strains in the GFRP ribs and skin did not experience higher strains than the ultimate strains recorded in the direct tensile tests carried out in specimens extracted from these components of the slab.

As shown in Fig. 6.10f, the strain distribution across the panel's thickness was used to depict the efficiency of the indented shear connectors in providing composite action to hybrid slab

SL2 under shear loading. Specimen SL2 behaved as fully composite up to 0.8P_{max} (136.76 kN). Increasing the load up to P_{max} (170.95 kN) led to a non-composite behaviour.

In general, according to the experimental results, the stiffness provided at the GFRP ribs-DHCC layer connection significantly affects the global behaviour of hybrid slab under shear loading, which is reflected in its force, deflection, and slip response.

In this chapter, the experimental tests assessed the structural performance of hybrid slabs under different shear load conditions, considering different shear failures caused by different dimensions, geometries, type of loadings, mechanical properties of slab's components.

According the experimental results obtained, the hybrid slabs exhibited a linear behaviour up to peak load, regardless of shear span to depth ratio. Then, hybrid slabs entered to a nonlinear structural phase. Imposing higher load leads to observe a hardening structural behaviour in the slabs. After occurrence of several damages in different positions of slabs, the hybrid slabs entered to a softening structural behaviour with large residual load carrying capacity.

In addition, the experimental results revealed a local buckling in the GFRP ribs of specimen SL1 due to reduction of shear span to depth ratio to a value equal to 0.77, while for shear span to depth ratio with higher values than 0.77, no local bucking was observed in the GFRP ribs.

6.4. Conclusions

In this chapter, six hybrid slabs with different lengths were built and experimentally tested under different shear load conditions. Indented shear connectors were used in the upper zone of the GFRP ribs to guarantee an effective load transfer from DHCC layer to GFRP skin and also to provide high load carrying capacity. Considering the need for an efficient shear connection, an efficient and simple technology was adopted here in this study by executing holes of small diameter in the top zone of the GFRP ribs that was embedded in the DHCC layer.

The shear performance of the hybrid slabs was assessed by executing experimental monotonic shear tests with span ratios in the range of 0.77 to 2. The following results can be concluded, based on the relevant observations:

1. The stiffness provided at the connection between the GFRP ribs and the DHCC layer strongly influences the load carrying capacity, stiffness, and absorbed energy of the hybrid panel.
2. Regardless of shear span ratios, large residual load carrying capacity was registered in the post peak response. On average, around 45% and 50% of the peak load was obtained for slabs (SS1, ST1, SL1) and slabs (SS2, ST2, SL2), respectively;

3. The observed damages in the tested slabs showed that the slabs did not experience a sudden failure due to tensile rupture in GFRP skin, because the GFRP skin layers remained almost undamaged.
4. Reduction of shear span ratios to a value lower than 0.77 increases the possibility of occurring local buckling in the GFRP ribs (SL1), while for shear span to depth ratio with higher values than 0.77, no local bucking was observed in the GFRP ribs.
5. Regardless of shear span ratios, slabs entered to a pseudo-plastic stage after occurring compressive damage in GFRP ribs.

References

[1]. Lanssens T., Tanghe C., Rahbar N., Okumus P., Van Dessel S., El-Korchi T., 2014, “Mechanical behavior of a glass fiber-reinforced polymer sandwich panel with through-thickness fiber insertions”, Journal of Construction and Building Materials, Vol. 64, pp: 473-479.

[2]. Thanoon Waleed A., Yardim Y., Jaafar M.S., Noorzaei J., 2010, “Development of interlocking mechanism for shear transfer in composite floor”, Journal of Construction and Building Materials, Vol. 24, pp: 2604–2611.

[3]. Mathieson H., Fam A., 2015, “In-Plane bending and failure mechanism of sandwich beams with GFRP skins and soft polyurethane foam core”, Journal of Composites for Construction, 10.1061/(ASCE)CC.1943-5614.0000570, 04015020.

[4]. Choi I., Kim J.H., Kim H., 2015, “Composite behavior of insulated concrete sandwich wall panels subjected to wind pressure and suction”, Materials, Vol. 8, pp: 1264-1282.

Chapter 7

The effects of load history on shear and flexural performance of hybrid sandwich panel slabs

7.1. Introduction

During the last decade, the employment of Fiber Reinforced Polymer (FRP) materials increased significantly and it is now possible to find various applications in civil engineering structures. Indeed, some unique properties such as high strength, low self-weight, high insulation properties, ease of installation, and corrosion resistance make this material very attractive for a wide range of applications [1–3]. Sandwich panel structures are one of the best examples of FRP materials used in civil engineering applications. Sandwich panels usually include FRP materials on top and bottom skins. Despite their brittle behavior, new solutions for sandwich panel structures were developed, with various configurations and material properties. Some innovative solutions were proposed by different researchers, such as the use of internal GFRP ribs to connect the top and bottom GFRP skins [4], stitching the top and bottom skins with through-thickness fibers to provide a better composite action between structural components [5], or the addition of corrugated GFRP sheets inside the sandwich panels to connect both GFRP skins [6]. These solutions resulted in a significant increase of stiffness and strength of the slabs. In 2015, Mastali et al. proposed an innovative hybrid sandwich panel that uses a high ductile reinforced mortar on the top layer. An indented shape was cut in the upper part of the GFRP ribs and later embedded in the high ductile reinforced mortar (DHCC) layer to act as shear connector. The GFRP ribs transfer shear stress from the top DHCC layer to the GFRP bottom skin [7]. The studies developed demonstrated that the proposed solution has high potential to increase the load carrying capacity, the stiffness, and the ductility of the hybrid slab solution, in comparison to other typical sandwich panel systems [8]. The results presented in [4-7] were obtained in tests developed under monotonic loading.

However, the proposed system was not validated in terms of its long-term behavior. As the proposed innovative solution is supposed to be used as a structural element that is submitted to real loading conditions, assessment of the long-term deformability of the proposed solution is required. Considering the lack of studies on the subject, the present study is dedicated to investigate the effect of load history on the structural performance of hybrid sandwich panels.

Creep phenomenon varies significantly in GFRP materials with the type of solicitation, i.e., compression, tension, flexure and shear [9].

Gonilha et al. found that creep phenomenon in GFRP materials varies significantly with the load conditions and type of internal stresses such as bending, shear, tension, and compression [12]. Researches indicated that creep phenomenon is more critical under compression in comparison to tension for GFRP materials [10, 11].

In the present study, the hybrid sandwich panel slabs comprise an upper layer of Deflection Hardening Cement Composite (DHCC) material in compression, GFRP ribs and a bottom GFRP skin in tension. This combination can be useful in reducing not only the instantaneous deformability but also the magnitude of GFRP creep deformation, thereby reducing the long-term deformability in the slab [9].

Few studies have been found in the literature about the creep response of GFRP-concrete hybrid structures (hybrid GFRP-reinforced concrete bridges) [9, 12], while no studies have been reported on the creep response of hybrid sandwich panels. Therefore, this study is established in two stages to provide the creep response of hybrid sandwich panels and also to obtain the effects of load history on the flexural and shear performance of hybrid sandwich panels.

The first part of this chapter describes the test setup for creep tests to assess the long-term flexural and shear deformability, and presents numerical and/or analytical predictions for the creep response of hybrid sandwich panels. In a second part, the hybrid sandwich panel slabs were loaded under long-term flexural and shear deformability. In the last part, after assessing hybrid slabs under long-term deformability, the slabs were unloaded and then again, the slabs were tested under monotonic static shear and flexural loadings. In this third part, it is also necessary to describe the test setup and test procedure of the static shear and flexural tests, and also to present the corresponding experimental results registered. The final part of the chapter includes comprehensive interpretations on the effects of the loading history on the flexural and shear performance of hybrid sandwich panels.

7.2. Creep response of hybrid sandwich panels

7.2.1. Structural concepts and characteristics of the hybrid sandwich panels

The tested hybrid DHCC-GFRP sandwich panels were produced at the Civil Engineering Department of Minho University, in 2015. Fig. 5.1 presents the proposed hybrid sandwich panel slabs.

Efficiency of the proposed hybrid sandwich panels were discussed in Chapter 3, Chapter 4, Chapter 5 and Chapter 6. The dimensions of the hybrid sandwich panels components considered in Chapter 2 are also considered in the creep tests here presented. The dimensions and geometrical properties of the hybrid slabs are listed in Table 2.1 and represented in Fig. 2.1.

DHCC material was developed as a high ductile material under flexural loading with 4% hybrid short discrete PAN fibers (3% of PAN12 and 1% of PAN6). The PAN fibers used in this study are produced by FISIPE Company. An average flexural strength of 7.82 MPa was recorded at 3 mm mid-span deflection. More details on mixture ingredients, mixing process

and test setup of the DHCC can be found in [7]. Additionally, Table 2.3 summarizes the results gathered from characterization of GFRP materials. Information on fiber layout of GFRP ribs and skins, manufacturing process and test setup for measurement of mechanical properties can be found in Chapter 2. In the design process of the hybrid sandwich slabs, the contribution of foam core on the panel load carrying capacity was ignored [7]. The results recorded from compressive tests on polyurethane foam core showed that the plastic response was followed by strain-hardening at large strains, with excessive compressive deformations. Density of the polyurethane foam cores, pseudo yield compressive stress, and compressive modulus measured were 42.5 kg/m^3, 0.18 MPa, and 2.5 MPa, respectively.

The specimens were manufactured using Vacuum Assisted Resin Transfer Molding (VARTM) technique process in PIEP institute. More details about manufacturing process can be found in Chapter 2.

7.2.2. Experimental creep test

All the experimental tests presented in this chapter were executed at the Civil Engineering Laboratory of Minho University and at Civitest Company. Four sandwich panels were tested under long-term loading conditions. The total length of the sandwich panels tested under flexural long-term loading was 2.0 m. This length was reduced to 1.1 m for evaluating the slab behavior under long-term shear deformability.

The proposed hybrid sandwich panels are used as slabs. It is expected that the hybrid slabs are loaded at a Serviceability Limit State (SLS) level during their operating life. Considering the serviceability limit state, a total load equal to 3.75 kN/m^2 was applied to the slabs. Based on Eurocode 1, the uniformly distributed load proposed for residential applications is 1.5 kN/m^2, and the uniformly distributed load proposed for walls and covering is 1.5 kN/m^2. The slab dead load was taken as 0.75 kN/m^2 [13]. The slabs were simply supported over a span of 1.8 m, and loaded according to a uniformly distributed loading pattern, by using 15 cement bags. Each bag weighted 40 kg (see Fig. 7.1). Supports placed at one end side of slabs could slide.

Additionally, the smaller slabs were simply supported over a 0.9 m span. In this case, two rigid steel bars were employed with 360 mm and 280 mm distance from each support side in Slab 1 (S1) and Slab 2 (S2), respectively, in order to provide the adequate shear loading conditions (see Fig. 7.2b and Fig. 7.2c). Shear span to height ratios for both hybrid slabs under shear loading were considered equal to 2. To apply shear load in serviceability limit state, thirteen bags were loaded on the hybrid slabs, each one weighting 25 kg. The loading was performed manually, by placing the bags, one by one, on the slabs. These operations

were implemented as fast as possible, while guaranteeing a smooth application of the load, and took approximately 2 minutes for each slab.

Two types of gauges were employed for monitoring and measurement of various displacements in the hybrid slabs. Measurements of vertical displacement and slip between DHCC layer and GFRP ribs were measured with analogical deflection gauges from Mahr Company with (i) a 10 mm stroke and 0.01 mm precision for the measurement of vertical deflections and (ii) a 5 mm stroke and a 0.001 mm precision for the monitoring the slip between the DHCC layer and the GFRP ribs (see Fig. 7.2a). One analogical deflection gauge was mounted at mid-span of the slab (LVDT 3 and LVDT 7 in Fig. 7.1c and Fig. 7.2d) to measure and monitor the vertical deflection and other analogical deflection gauge to measure deflection was installed at 100 mm distance from the mid-span of the slab (LVDT 2 and LVDT 6 in Fig. 7.1c and Fig. 7.2d). Slip between DHCC layer and GFRP ribs was monitored by using the minimum stroke and maximum precision deflection gauge. During the test period, variations of temperature and relative humidity were also recorded continuously. The device used for recording temperature and relative humidity could measure temperature between 0-100 ^{0}C and relative humidity between 0-100%.

As shown in Fig. 5.4, four strain gauges were installed in different components of the slab. Strain gauge 1 (SG 1) was installed at the bottom GFRP skin and underneath one of the GFRP ribs, in order to measure tensile strain. Furthermore, strain gauge 2 (SG 2) and strain gauge 3 (SG 3) were employed to record strains in the GFRP ribs. The GFRP ribs and skin were instrumented with type BFLA-5-5 strain gauges from TML, with 5 mm measuring length. Strain gauge 4 (SG 4) was applied to measure compressive strain on top DHCC layer. In order to record the compressive strain on the DHCC layer, a type of PFL-30-11 strain gauge with 30 mm measuring length was used. Since creep is a long-term phenomenon, and recording the strains requires an electrical data logger connection during the test period, it was decided not to measure strains during the creep test period.

The flexural and shear creep tests were carried out in Civitest Company and in the Civil Engineering Laboratory of Minho University, respectively. The hybrid slabs were loaded for 1540 hours and 1454 hours under long-term flexural and shear deformability, respectively. Stabilization of deflection and slip were taken into account as the stop criteria for the long-term loading tests. Due to the relative large size of the slabs, it was not possible to use a climatic chamber to control temperature and humidity of the environment.

The flexural creep tests (Slabs F1 and F2) were carried out between Jun 2nd and August 6th, 2014, i.e., during 64 days. Afterwards, the shear creep tests (slabs S1 and S2) were executed between September 24th and November 26th, 2014, i.e., during 62 days. When the bags were applied to the slabs, the DHCC layers age was 30 days for flexural tests and 145 days for shear tests.

a) The hybrid slabs loaded for flexural creep test

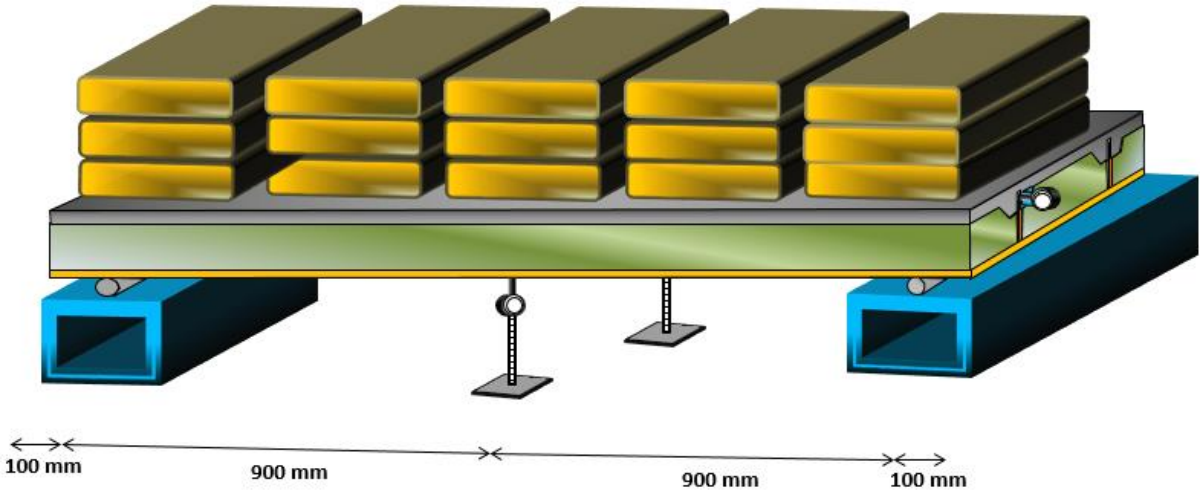

b) 3D view of loaded hybrid slabs and LVDT's positions

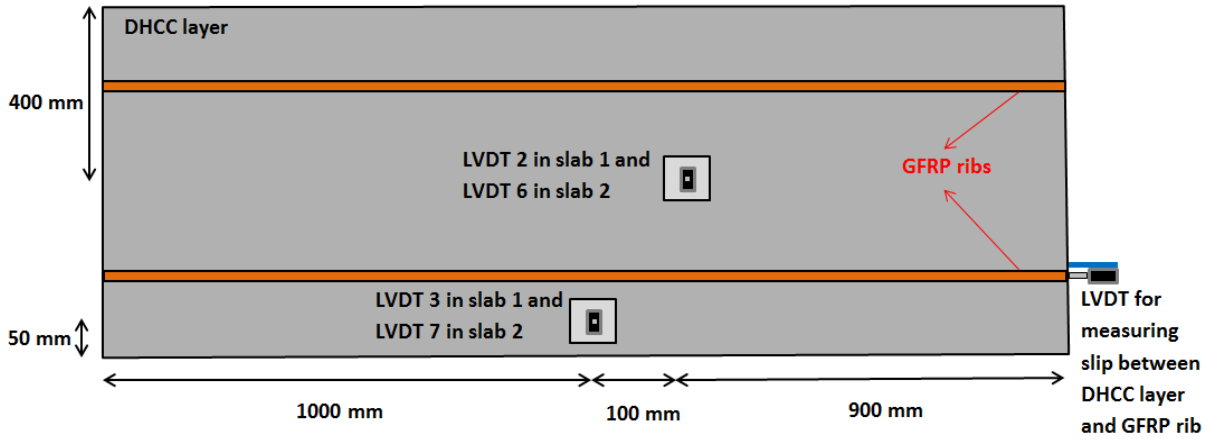

c) Top view of LVDT's positions

Fig 7.1. Loaded hybrid slabs and mounted monitoring instruments to hybrid slabs for flexural creep test

a) The hybrid slabs loaded for shear creep test

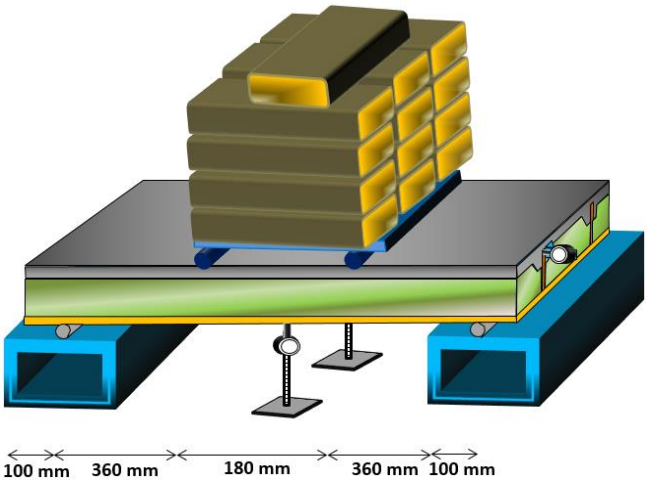

b) Loaded hybrid slab S1 and LVDT's positions

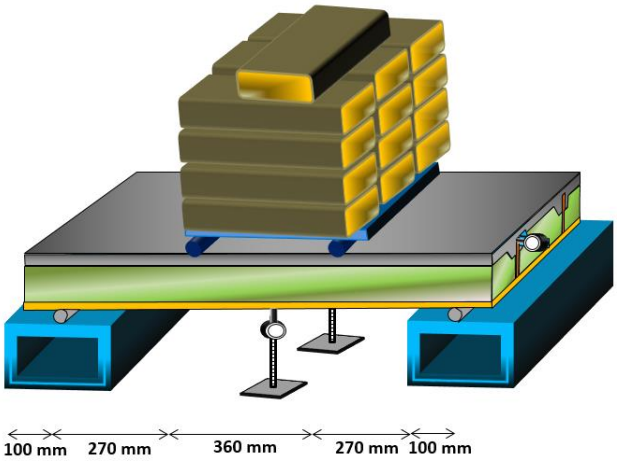

c) Loaded hybrid slab S2 and LVDT's positions

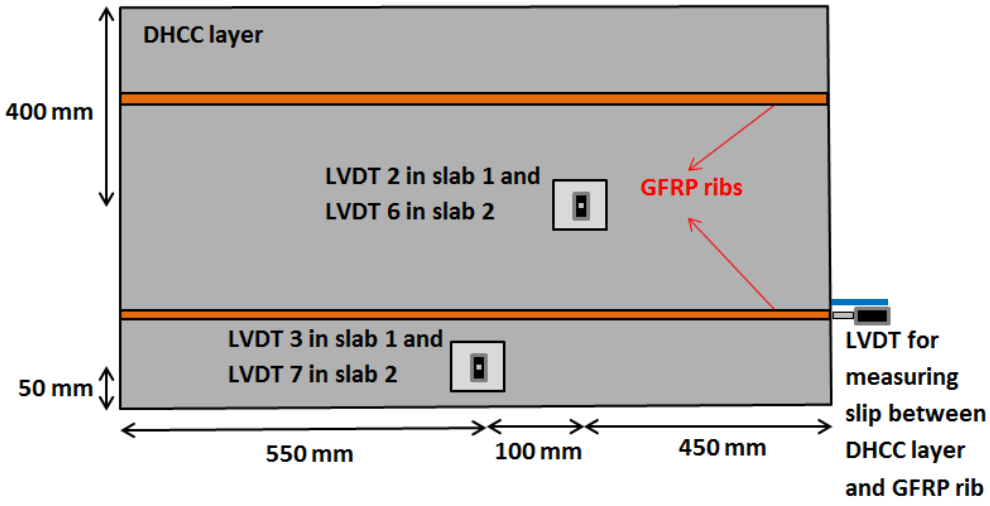

d) Top view of LVDT's positions

Fig 7.2. Loaded hybrid slabs and mounted monitoring instruments to hybrid slabs for shear creep test

7.2.3. Experimental results of creep test

7.2.3.1. Flexural loading

Relative humidity and temperature were recorded in Civitest Company (location of the hybrid slabs that were assessed under flexural creep test) during the testing period. This data is shown in Fig. 7.3. During this period, the temperature was moderate (with an average value of 23.6 °C) and humidity was approximately high (with an average value of 60.1%). In general, temperature increase was associated with humidity decrease during this period (Summer in Portugal).

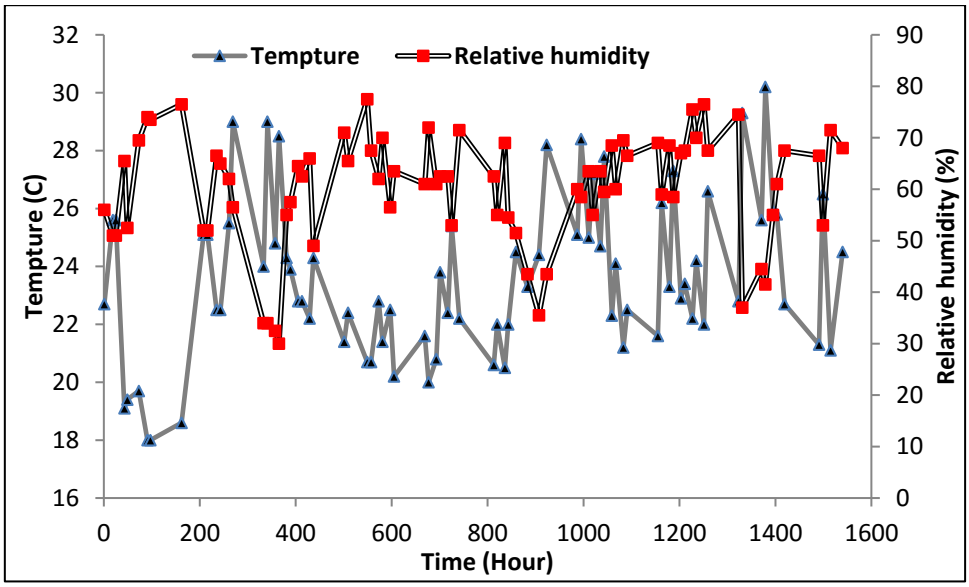

Fig 7.3. Temperature and relative humidity during the flexural creep tests

Fig. 7.4 shows the relation between time, vertical deflection and slip for hybrid Slab F1 and hybrid Slab F2, under long-term loading.

The instantaneous mid-span deflection measured in Slab F1 was 1.16 mm and 1.35 mm in Slab F2. The instantaneous mid-span deflection of Slab F1 was 14.1% less than that of Slab F2. However, the values of instantaneous mid-span deflection measured in both slabs are close and the difference between them can result from differences in the stiffness of the hybrid slabs.

At the end of the flexural creep test, the mid-span deflection of Slab F1 was 2.53 mm and the mid-span deflection of Slab F2 was 2.58 mm. The difference between the instantaneous mid-span deflection and the deflection measured in the end of the creep test can be derived from the viscoelastic nature of some of the materials used in this type of slab, such as polymeric adhesives, resins, foams, fiber reinforced mortar. Again, the vertical deflection values measured in both slab specimens at the end of the creep tests are close and reflect the similar behavior observed in these tests.

Fig. 7.4b and Fig. 7.4d show the values of slip measured in each slab specimen during the corresponding creep tests. It is possible to observe that the maximum slip measured in Slab F1 is 0.048 mm and the maximum slip measure in Slab F2 is 0.118 mm, after 64 days of loading. The slip measured between the GFRP rib and the DHCC layer in Slab F2 was 2.45 times the slip measured in Slab F1, at the end of the flexural creep test.

Although the mentioned difference, the obtained results show that slip values were very small, which means that the shear connection proposed is effective and stiff, guaranteeing high interaction between the GFRP rib and the DHCC layer.

Fig. 7.5 illustrates the normalized vertical deflection for Slab F1 and Slab F2. The vertical deflection was normalized by its instantaneous values. It could be concluded that the creep phenomenon was more effective on increasing vertical deflections in Slab F1, compared to Slab F2, so that flexural long-term deformability led to 2.18 and 1.9 times increase in mid-span deflection in Slab F1 and Slab F2, respectively.

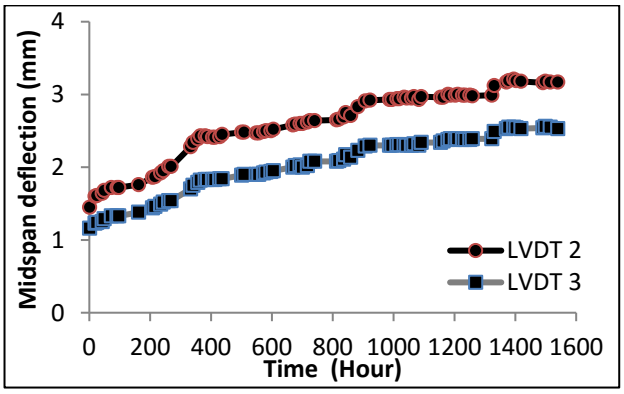

a) Slab F1: Vertical deflections

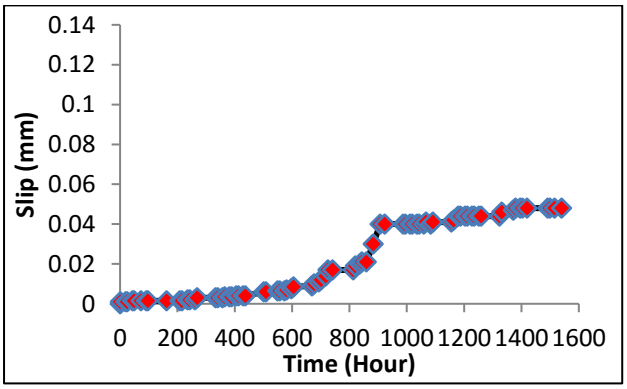

b) Slab F1: Slip between GFRP rib and DHCC layer

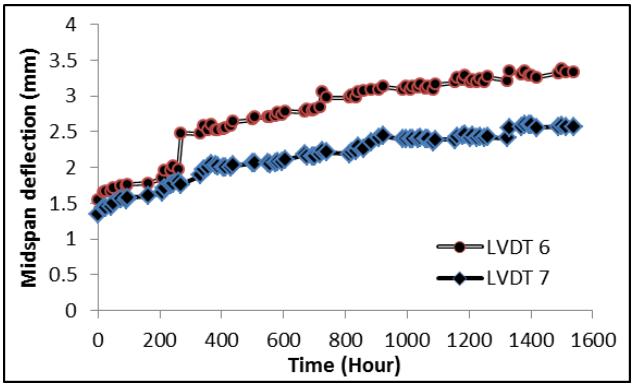

c) Slab F2: Vertical deflections

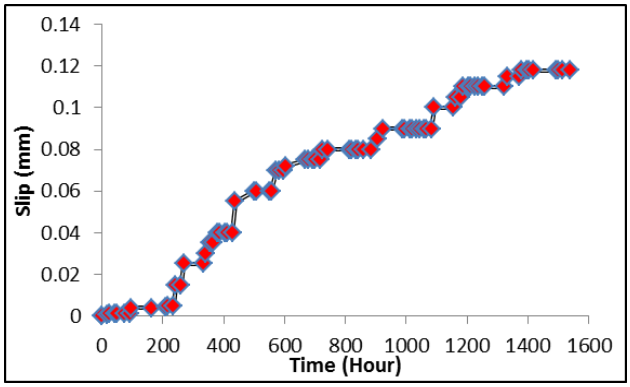

d) Slab F2: Slip between GFRP rib and DHCC layer

Fig 7.4. Recorded time-vertical deflection relationship and time-slip relationship for hybrid slabs under flexural creep test

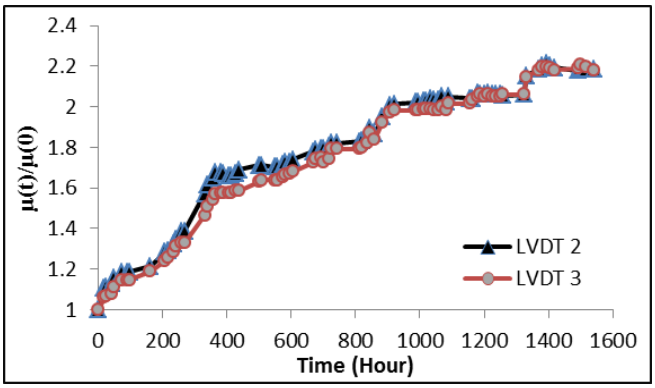

a) Slab F1: Normalized vertical deflections

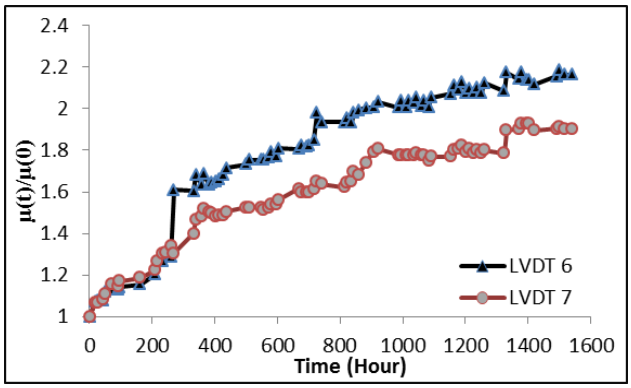

b) Slab F2: Normalized vertical deflections

Fig 7.5. Recorded time-normalized deflection relationship for hybrid slabs under flexural creep test

7.2.3.2. Shear loading

As mentioned before, the shear creep tests on the hybrid slabs were carried out at the Laboratory of the Civil Engineering Department, at University of Minho. Temperature and relative humidity were monitored during these tests (Fig 7.6). The temperature was moderate (with an average value of 21.9 °C) and relative humidity was approximately high (with an average value of 62.9%). The values recorded show that temperature and relative humidity had smaller variations in shear creep tests than in flexural creep tests.

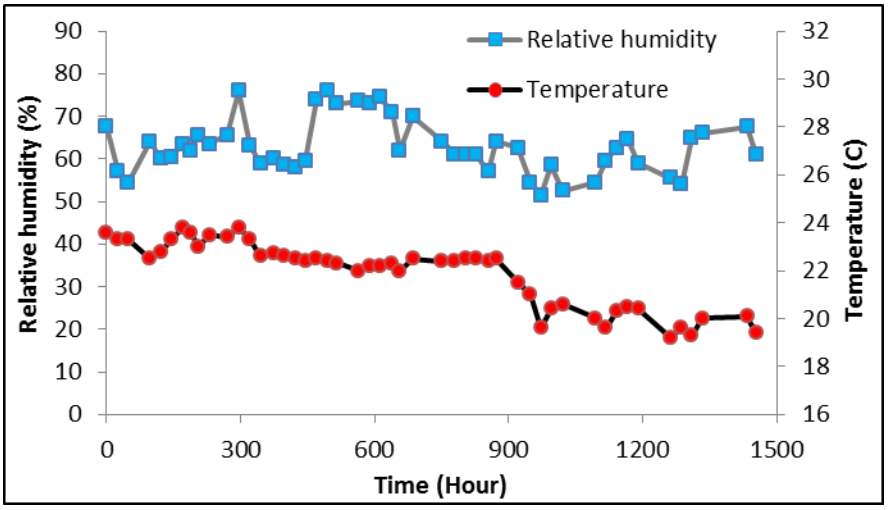

Fig 7.6. Temperature and relative humidity during the shear creep tests

According to the results indicated in Fig. 7.7, the instantaneous mid-span deflection measured in Slab S1 was 0.69 mm and 0.44 mm in Slab S2.

At the end of shear creep test, the mid-span deflections measured 1.22 mm in Slab S1 and 0.66 mm in Slab S2, respectively. These results show that there was 77.1% and 49.1% increment of instantaneous deflections in Slab S1 and Slab S2, respectively (see Figs 7.8a and 7.8c).

Under the imposed shear long-term deformability, slip in Slab S1 and Slab S2 increased 2.20 and 8.00 times, respectively (see Figs 7.7b and 7.7d). Despite recording higher slip in

Slab S2 in comparison Slab S1, the recorded deflection in Slab S1 was higher than that of Slab S2, due to the applied long-term shear deformability. This fact is due to viscoelastic nature of slab´s components and the slip between the GFRP shear connectors and the DHCC layer. Regarding the importance of the viscoelastic nature of the slab components, viscoelastic deflections of the hybrid sandwich panels were obtained and shown in Fig. 7.9, under long-term flexural and shear deformability. It was assumed that viscoelastic contributions source from (1) the glass-fiber reinforced polymer ribs in shear and (2) the glass-fiber reinforced polymer skin in tension (3) the fiber reinforced mortar in compression. Since the rate of viscoelastic deformation of slabs was high during the first hours of the tests, the first monitoring from analogical deflection gauges executed after passing one hour from applying cement bags to slabs.

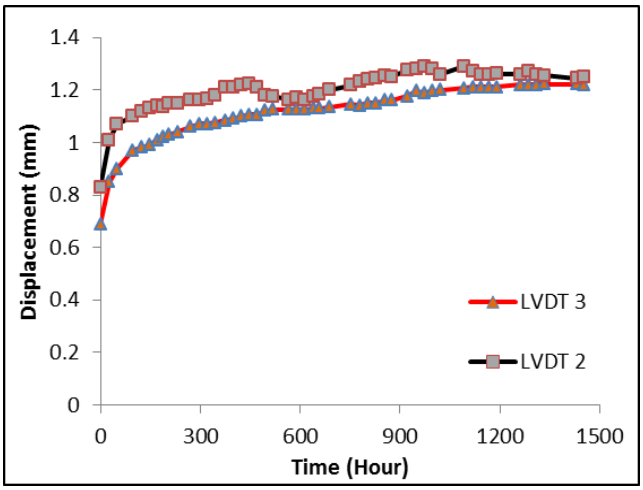

a) Slab S1: Vertical deflections

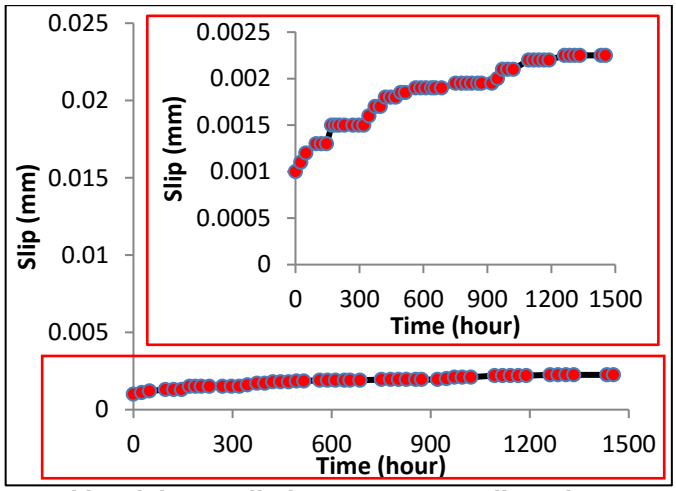

b) Slab S1: Slip between GFRP rib and DHCC layer

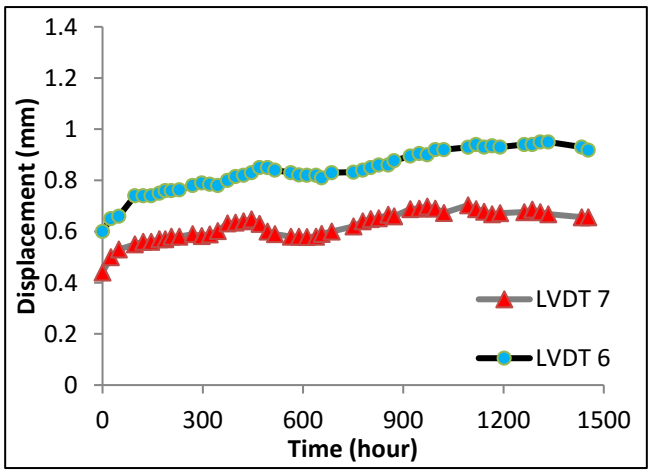

c) Slab S2: Vertical deflections

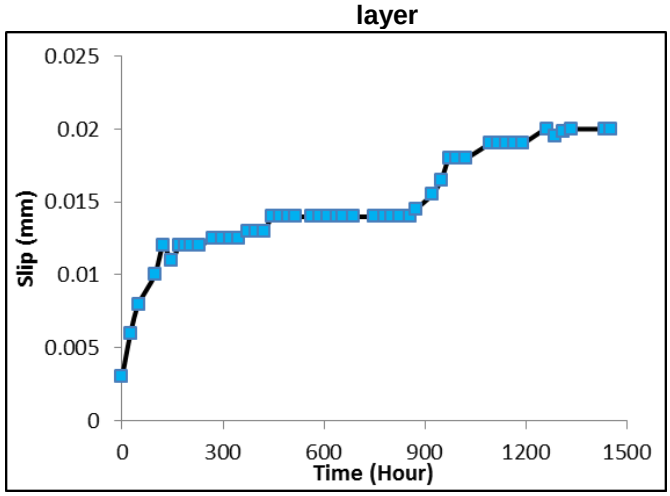

d) Slab S2: Slip between GFRP rib and DHCC layer

Fig 7.7. Recorded time-vertical deflection relationship and time-slip relationship for hybrid slabs under shear creep test

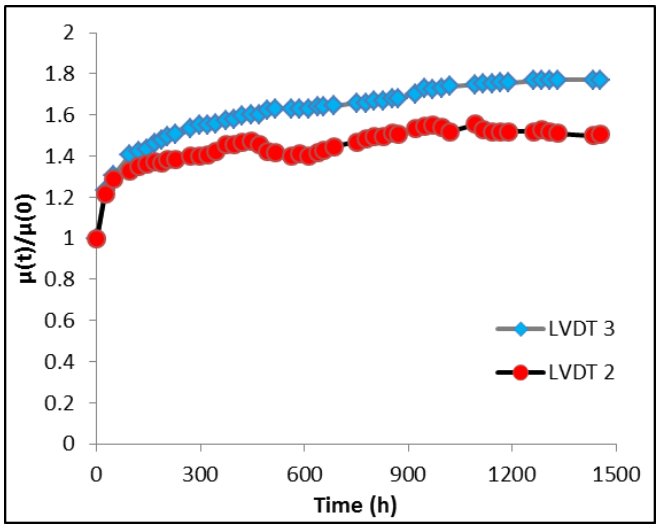

a) Slab S1: Normalized vertical deflections

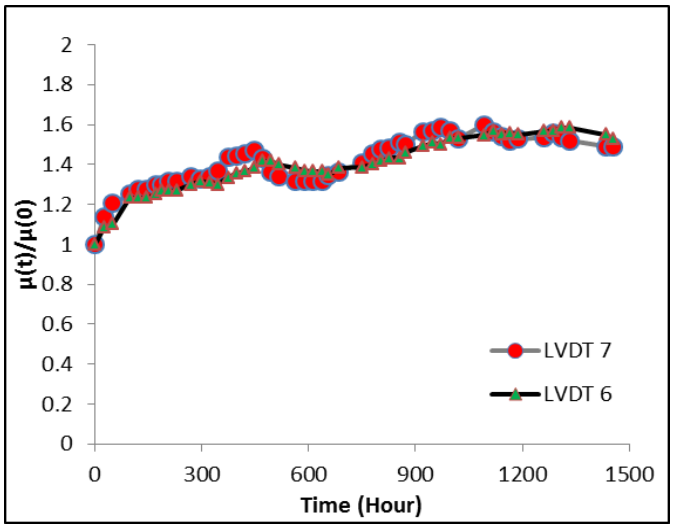

b) Slab S2: Normalized vertical deflections

Fig 7.8. Recorded time-normalized deflection relationship for hybrid slabs under shear creep test

The structural behavior of viscoelastic materials is time-dependent. Environmental conditions, such as age, temperature, or moisture, can significantly influence the viscoelastic response and properties of the materials used in the hybrid sandwich panels proposed. Based on the results shown in Fig. 7.9, it is possible to observe that the viscoelastic increase in deformations of hybrid slabs during the first hours of the tests was significantly high, but reduced gradually and converged into a lower rate.

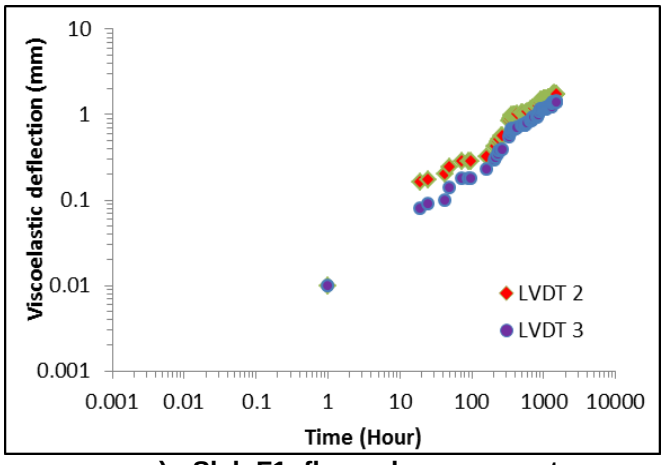

a) Slab F1: flexural assessment

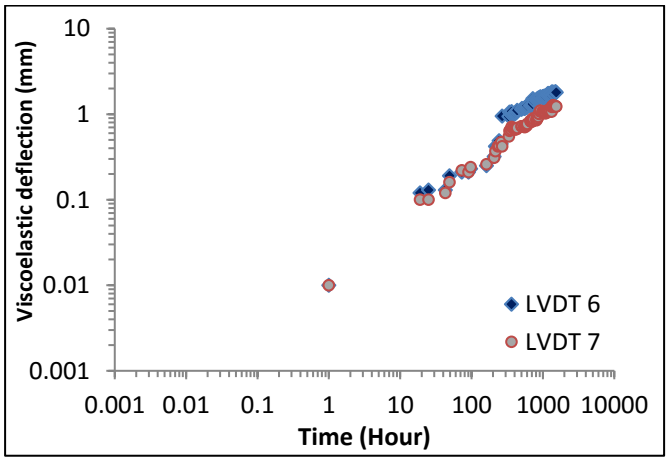

b) Slab F2: flexural assessment

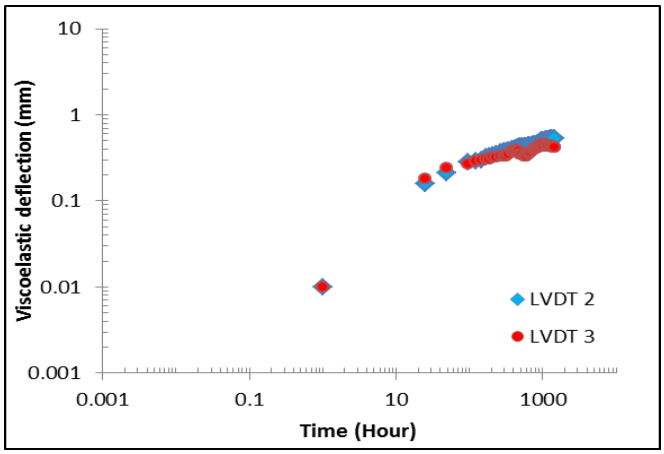

c) Slab S1: shear assessment

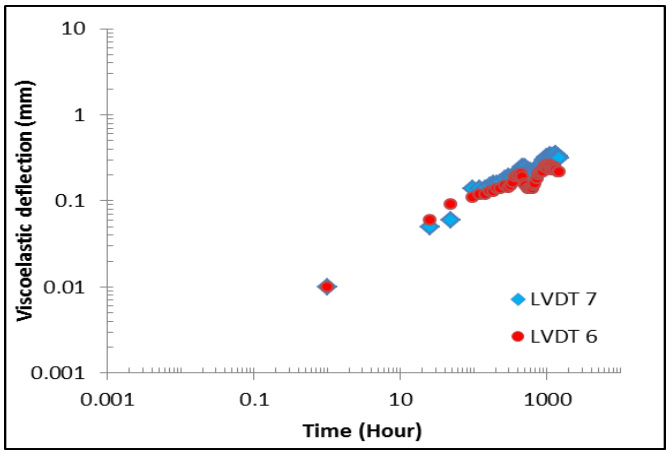

d) Slab S2: shear assessment

Fig 7.9. Viscoelastic deflection (log_{10} plot) at mid-span section throughout the duration of the creep test on the sandwich panel

The recorded vertical deflections, which occur due to the creep phenomenon, can be influenced by the viscoelastic nature of the slab components and also by the slip between the GFRP shear connectors and the DHCC layer. Hence, it was important to determine the effects of slip on viscoelastic deflections of hybrid slabs. It is worth mentioning that slip between the DHCC material and the GFRP ribs may depend on viscoelastic nature of materials, but here it was postulated that slip behaves independently.

Fig. 7.10 displays the relationship of viscoelastic deflection at mid-span versus slip between the GFRP shear connectors and the DHCC layer for the hybrid slabs. According to the results depicted in Fig. 7.10, regardless of the applied load conditions, the slopes of slip versus viscoelastic deflection responses are higher for Slab 2, compared to Slab 1. Additionally, for both shear and flexural load conditions, the viscoelastic deflection at the end of creep test of Slab 1 was more than that of Slab 2. Recording higher slip values and smaller viscoelastic deflections in Slab 2 indicate a better mechanical interlock between DHCC materials and GFRP shear connectors, when compared to Slab 1 with smaller slip values and larger viscoelastic deflections. Concerning this observation, it may be concluded that utilizing effective shear connectors would result in decreasing both instantaneous and viscoelastic deflections. Providing a stiffer bond between the DHCC layer and the GFRP shear connectors would reduce both instantaneous and viscoelastic deflections.

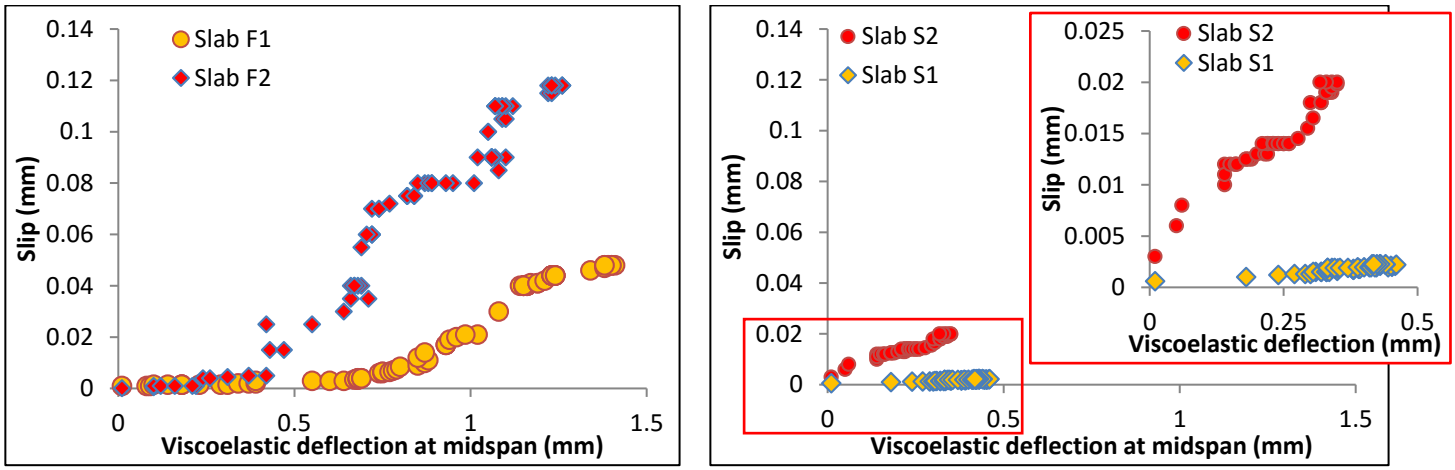

a) Flexural creep test **b) Shear creep test**

Fig 7.10. Viscoelastic deflection at mid span-slip relationship for the hybrid slabs

In addition to analyzing the results gathered from experimental creep tests, it is required to establish an analytical creep model to predict the slab behaviors for short-term and long-term deflections. Therefore, models that are used to implement the predictions in short-term and long-term will be further explained in the following sections.

7.2.3.3. Creep response of constituent materials

The viscoelastic behavior of GFRP materials is often predicted by Findley's power law, as presented in equation (7.1),

$$\Delta(t) = \Delta_0 + m.t^n \qquad (7.1)$$

where, $\Delta(t)$ is the time-dependent general deformation (strain or deflection), Δ_0 is the instantaneous general deformation, *t* indicates time, *m* is a stress-dependent coefficient and *n* is a stress independent coefficient. Findley's power law was computed based on nonlinear regression. Fig. 7.11 plots the analytical evolution of the mid-span deflections (δ_3, and δ_7, where subscripts indicate the nominations of LVDTs that were used to record vertical deflections at mid-span, as indicated in Fig. 7.1c and Fig. 7.2d), together with Findley's power law regression (Equation (7.1)) for each slab. The coefficients of determination (denoted R^2) in nonlinear regression were computed and presented in Fig. 7.11a for Slab F1 and the value of 0.93 on the coefficient of determination was obtained for δ_3. The coefficient of determination in nonlinear regression was also computed for Slab F2. The corresponding value of 0.94 for δ_7, is presented in Fig. 7.11b.

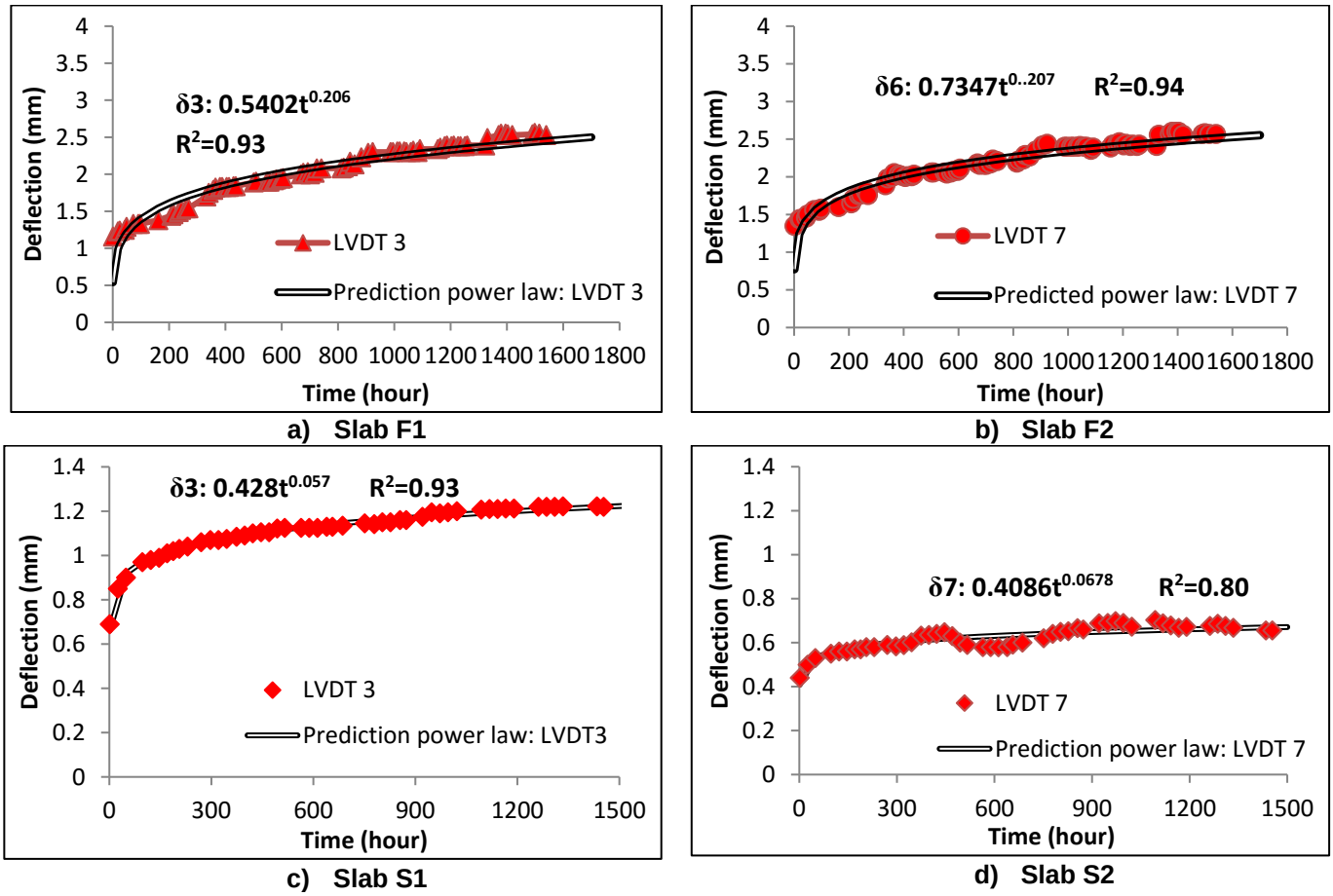

Fig 7.11. Evolution of mid-span deflections and Findley's power law regressions for: a) Slab F1; b) Slab F2; c) Slab S1; d) Slab S2

Time-dependent Young's modulus was used to predict the stiffness reduction in the material for a given time period during loading. The constants of Findley's power law can be used to predict the reduction of stiffness, but the equation does not consider the stress dependency [14]. On the other hand, the stiffness reductions in the Findley's power law are considered independent of the applied load conditions. Indeed, the Findley's power law is not capable of accounting the deflections and stiffness reductions in long-term behavior of hybrid structures. These deflections could be due to: 1) creep behavior of cementitious materials; 2) differences in considering the position of the neutral axis in the section. Neutral axis changes with a constant rate in the Findley's power law, while in the hybrid structures the neutral axis could change the logarithmic slope of the curve representing the structural response [12]. Therefore, an analytical study was developed to predict the creep behavior of hybrid slabs under both shear and flexural loading. Gonilha *et al*. proposed an analytical model based on the Timoshenko beam model, utilizing the material modulus provided by empirical creep models of the constituent materials as input and taking into account their actual stress state and overall environmental conditions [12]. Gonilha *et al*. validated the proposed analytical model with results gathered from experimental tests for GFRP–concrete hybrid structures

under flexural loading [12]. Therefore, in the present study, DHCC material was employed instead of concrete, and also the proposed analytical model is validated for hybrid sandwich panel slabs under shear load conditions. Since the mechanical properties of the fiber-reinforced mortar used were different from plain concrete, the analytical model is modified based on properties of the fiber-reinforced mortar. Thus, the creep response of constituent materials, such as DHCC and GFRP materials, are provided as an input of the numerical models. These issues are briefly explained in the following sections.

7.2.3.4. GFRP material

To approach the elasticity (or shear) modulus over the time, the Findley's power law can be rewritten using equations (7.2) and (7.3),

$$E(t) = \frac{E_0}{1 + \left(\frac{E_0}{E_t}\right) t^{n_E}} \qquad (7.2)$$

$$G(t) = \frac{G_0}{1 + \left(\frac{G_0}{G_t}\right) t^{n_G}} \qquad (7.3)$$

where, $E(t)$ is the time-dependent elasticity modulus (or shear modulus – $G(t)$), E_0 is the instantaneous elasticity modulus (or shear modulus – G_0), E_t is known as the creep elasticity modulus (or shear modulus – G_t) and n_E and n_G are Findley's law stress-independent parameters for bending and shear, respectively. The creep elasticity modulus (E_t or G_t) may be determined empirically from creep tests and these modulus are dependent to the applied stress. For the flexural creep behavior, Bank proposed the values of E_t = 1241.06 GPa, G_t = 186.16 GPa, and $n_E = n_G$ = 0.30 [15]. Furthermore, some studies corresponding to the creep response of GFRP flexural members indicate that an appropriate value for n_E would be within the range of 0.30 to 0.36 [1, 16].

7.2.3.5. DHCC (Deflection Hardening Cement Composite) material

The creep response of fiber-reinforced mortar depends on various parameters such as the matrix or the fiber properties, including: creep behavior of matrix, elastic modulus of fiber and matrix, fiber orientation characteristics, fiber effective aspect ratio, and fiber content. As no cracks were formed during the creep test due to low stress levels, it can be assumed that fibers did not have any contribution within the induced load level. Thus, the cementitious layer can be modeled as regular concrete. Since the creep model proposed by Eurocode 2 is used for regular concrete, this analytical model can also be applied to the DHCC layer [17]. In this model, the creep behavior is influenced by some parameters, including

equivalent thickness of the element (h_0), compressive strength of the concrete at 28 days of age (f_{cm}), age of the concrete during loading (t_0), temperature (T), and relative humidity (RH). The effect of each parameter is considered on the creep model proposed by Eurocode 2 [17]. Equation (7.4) is used in the proposed creep model to determine the elasticity modulus of DHCC layer along time,

$$E_C(t,t_0) = \frac{E_{c,28}}{1+\chi(t,t_0)\times\varphi(t,t_0)} \qquad (7.4)$$

where, $\varphi(t,t_0)$ is the creep coefficient along time, $\chi(\mathrm{t},\mathrm{t}_0)$ is Trevino's ageing coefficient, $E_{c,28}$ is the concrete elasticity modulus at age of 28 days. The creep coefficient along time is computed based on equation (7.5),

$$\varphi(t,t_0) = \varphi_0 \times \beta_c(t,t_0) \qquad (7.5)$$

where, φ_0 is a constant creep coefficient and $\beta_c(t,t_0)$ represents the creep behavior along time. The constant creep coefficient (φ_0) can be calculated with equations (7.6) to (7.10),

$$\varphi_0 = \varphi_{RH} \times \beta(f_{cm}) \times \beta(t_0) \qquad (7.6)$$

where,

$$\varphi_{RH} = \left[1+\frac{RH/100}{0.1\times\sqrt[3]{h_0}}\right] \qquad f_{cm} \langle 35MPa \qquad (7.7)$$

$$\beta(f_{cm}) = \frac{16.8}{\sqrt{f_{cm}}} \qquad (7.8)$$

$$\beta(t_0) = \frac{1}{(0.1+t_0{}^{0.2})} \qquad (7.9)$$

$$h_0 = \frac{2A_c}{u} \qquad (7.10)$$

and *Ac* is section area of the concrete; *u* is the perimeter of the section edge exposed to the environmental conditions. Relative humidity in equations (7.7-7.10) is in percentage (%), h_0 is in (mm), compressive strength of concrete (f_{cm}) is in (MPa), t_0 is in days. Additionally, $\beta_c(t,t_0)$ is defined based on equation (7.11) and (7.12):

$$\beta_c(t,t_0) = \left[\frac{t-t_0}{\beta_H + t - t_0}\right]^{0.3} \qquad (7.11)$$

where, t is the concrete age based on days, (t-t_0) is the load period, and

$$\beta_H = 1.5\left[1+(0.012RH)^{18}\right]\times h_0 + 250 \le 1500 \qquad (7.12)$$

β_H in equation (7.12) represents the environmental conditions for compressive strength lower than 35 MPa. To determine the elasticity modulus of DHCC layer over the time in equation (7.4), it is required to calculate the Trevino's ageing coefficient. This coefficient can be evaluated with equation (7.13),

$$\chi(t,t_0) \cong \chi(t_0) = \frac{\sqrt[3]{t_0}}{1+\sqrt[3]{t_0}} \qquad (7.13)$$

where, t_0 is age of the concrete when loaded, in days.

By computing Young's modulus and shear modulus of GFRP materials over the time, based on the time-dependent modulus in shear proposed by Bank and Young's modulus of DHCC layer over the time based on the time dependent modulus in flexure proposed by Eurocode 2 [17], the mid-span deflections can be calculated based on Timoshenko's beam theory under flexural and shear loading, through equations (7.14) and (7.15), respectively.

$$\Delta = \frac{5ql^4}{384E(t)I} + \frac{ql^2}{8\mathrm{G(t)KA}} \qquad (7.14)$$

$$\Delta = \frac{Pa^2(3l-4a)}{6E(t)I} + \frac{PL}{3\mathrm{G(t)}KA} \qquad (7.15)$$

where *q* is distributed load, *l* is length of span, *E(t)* is Young's modulus over the time, *G(t)* is shear modulus over time, and *a* is length of the support arm of concentrated load, being 360 mm and 270 mm, for Slab 1 and Slab 2, respectively. In equations (7.14) and (7.15), *A* is the shear area and the value of *K* was considered 0.85. Shear area in equations (7.14) and (7.15) is the total area of GFRP ribs. Equations (7.2) to (7.13) provide the creep response of constituent materials under flexural and shear load conditions, with equations (7.14) and (7.15) assigned particularly to compute the mid-span deflection of slabs under flexural and shear load conditions, respectively. The analytically obtained results are shown in Fig. 7.12 for Slab F1, Slab F2, Slab S1, and Slab S2 under shear and flexural loading.

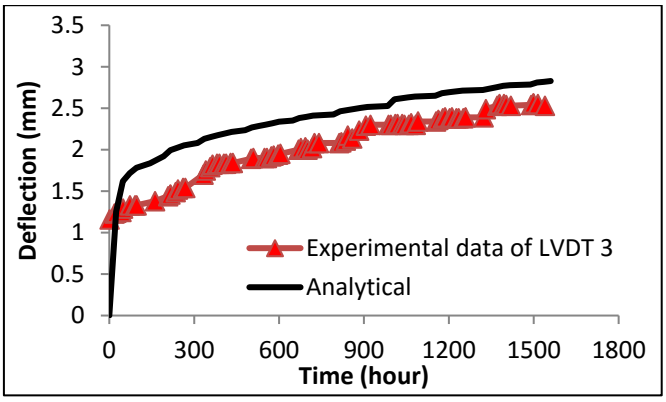

a) Slab F1

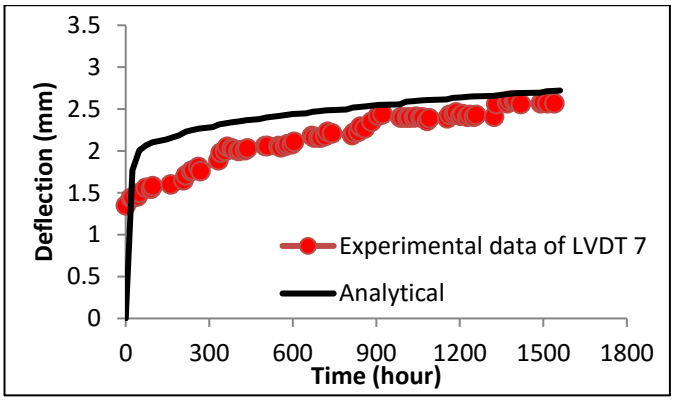

b) Slab F2

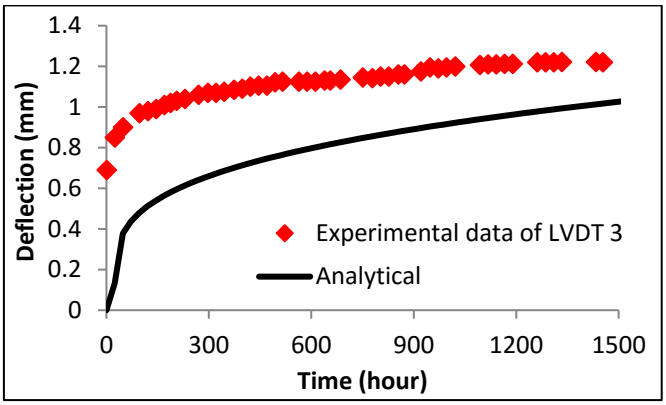

c) Slab S1

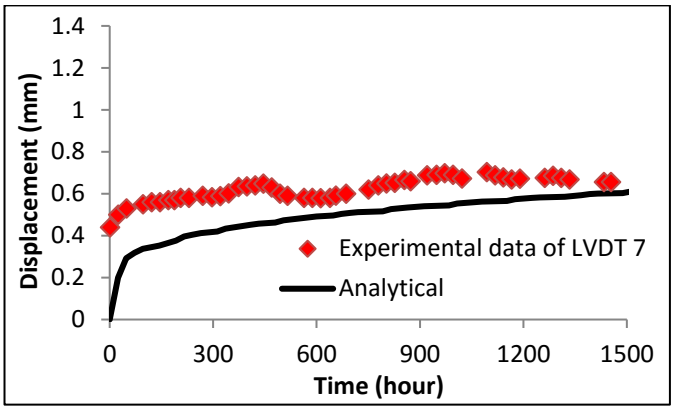

d) Slab S2

Fig 7.12. Evolution of mid-span deflections and analytical model for: a) Slab F1 under flexural loading; b) Slab F2 under flexural loading; c) Slab S1 under shear loading; d) Slab S2 under shear loading

The illustrated results reveal that the proposed analytical models are capable to predict the creep behavior of constituent materials under flexural and shear load conditions. According to the results shown in Fig. 7.12, the results presented from the proposed analytical models for predicting creep behavior of slabs indicate good agreement with the experimental results recorded, which demonstrate good accuracy of the analytical model in predicting the creep behavior of hybrid sandwich panel slabs. The analytical model was also applied to predict the creep response of hybrid slabs in long-term deformability. Since service life of normal residential buildings is 50 years, long-term deformability period of hybrid slabs under creep response was considered 50 years. Fig. 7.13 illustrates long-term deformability responses of hybrid slabs, predicted by Findley's power law and the analytical creep model. According to the results indicated in Fig. 7.13, the divergence in the results of the analytical model and Findley's power law under flexural and shear load conditions is significantly high. These results show that, although it is possible to adjust Findley's power law to the creep behavior of a hybrid slab, this method may not be very accurate, especially for long-term predictions based on short-term tests.

Hence, using the parameters obtained from Findley's power law to predict the long-term creep response of hybrid slab structures may lead to unreliable results. It seems that this method is inadequate to predict the creep behavior of the hybrid sandwich panel slabs. The validation of the analytical model used in long-term deformability prediction of hybrid slabs was approved by authors in [18].

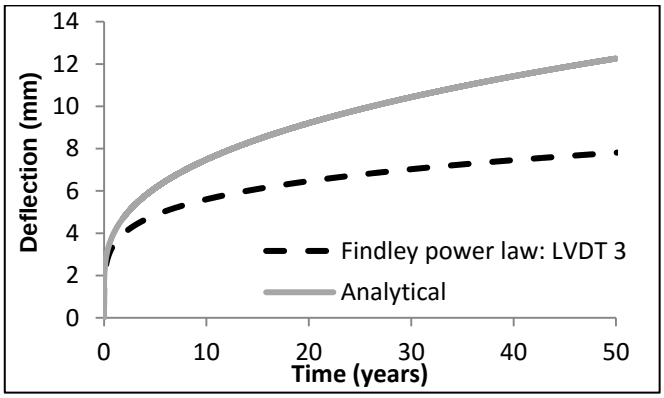

a) Slab F1

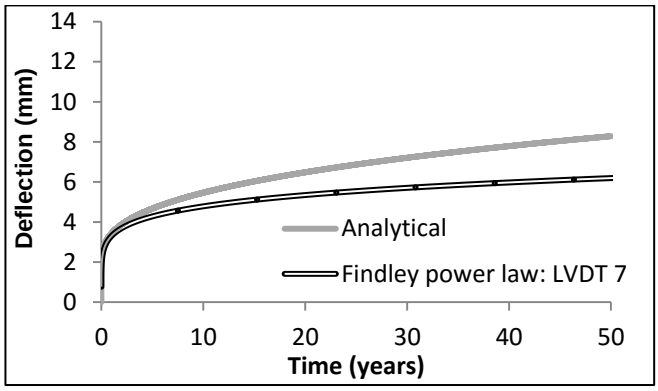

b) Slab F2

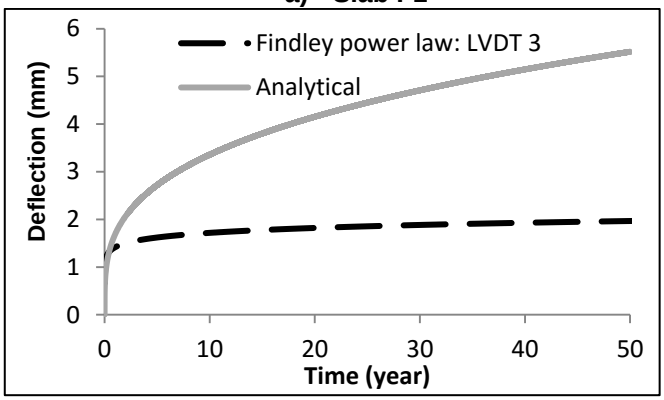

c) Slab S1

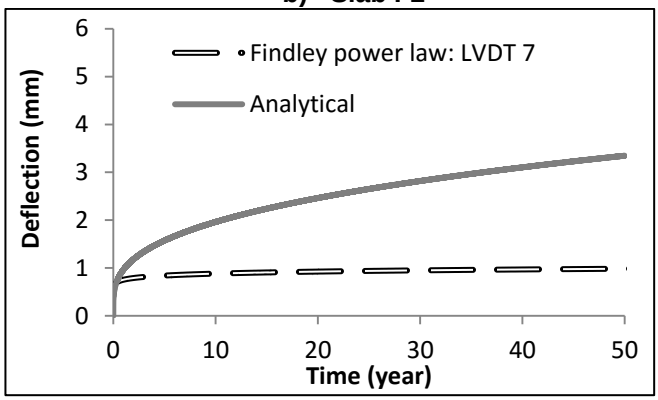

d) Slab S2

Fig 7.13. Long-term creep behavior of: a) Slab F1 under flexural loading; b) Slab F2 under flexural loading; c) Slab S1 under shear loading; d) Slab S2 under shear loading

7.3. Responses of the hybrid sandwich panels under flexural and shear tests

In the second stage of the present investigation, the effect of load history on flexural and shear performance of hybrid slabs will be studied. Thus, after imposing long-term loadings during the creep tests, the sandwich panels were unloaded. During the unloading process, the bags applied on the slabs were uniformly and slowly removed. Afterwards, the hybrid sandwich panels were prepared for monotonic flexural and shear loading tests. It is worth mentioning that the maximum duration between unloading the hybrid slabs and performing the static shear and flexural tests was less than 24 hours.

Therefore, the second stage of this study is dedicated to clarify the effect of load history on shear and flexural performance of the hybrid sandwich panel slabs. It is important to keep in mind that the results gathered in chapter five present the structural performance of the hybrid slabs under monotonic shear and flexural loads, which did not experience long-term deformability. Finally, the effects of creep will be revealed by comparing the results gathered from the structural performance of hybrid slabs in the current study and the structural performance of hybrid slabs presented in chapter five. To implement a comparison, the test conditions assumed in the current study are equal to the ones considered in chapter five: 1)

test setup; 2) loading conditions; 3) equipment used for measuring deflection and slip; 4) hydraulic jack used to apply the load; 5) applied load speed rate.

As shown in Fig. 7.14, seven linear variable differential transformers (LVDT) and four strain gauges were used to measure displacement and strain in various positions. Fig. 7.14 illustrates the test setup and positions of LVDTs. Length of slabs varied based on flexural and shear assessment objectives. LVDT 3, LVDT 4, and LVDT 5 were employed to measure vertical deflection along the slab's span. LVDT 2 and LVDT 6 were used to record the vertical displacements of slabs at both side supports. As shown in Fig. 7.14, LVDT 1 and LVDT 7 measured the slip between DHCC layer and GFRP ribs at both end sides. All four hybrid slabs were assessed under monotonic flexural and shear displacement control with loading rate of 30 µm/sec. The hybrid slabs were tested under conditions that are similar to the ones considered for the static tests. The results gathered will be further discussed in the following sections.

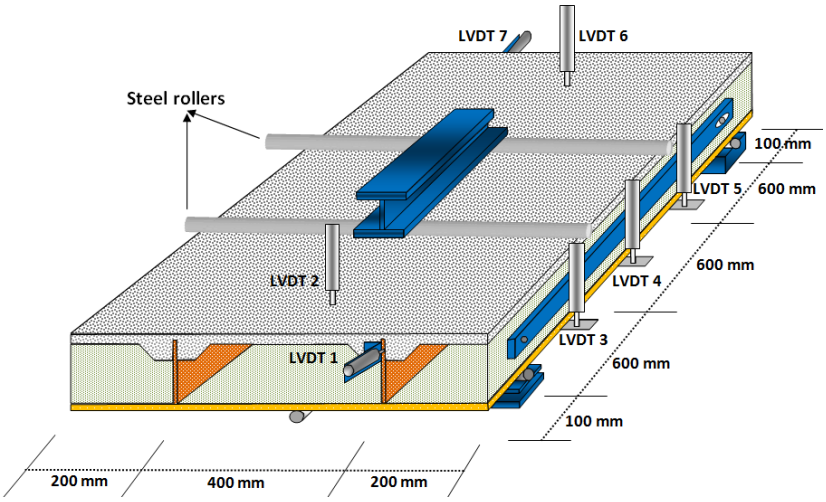

a) Flexural assessment

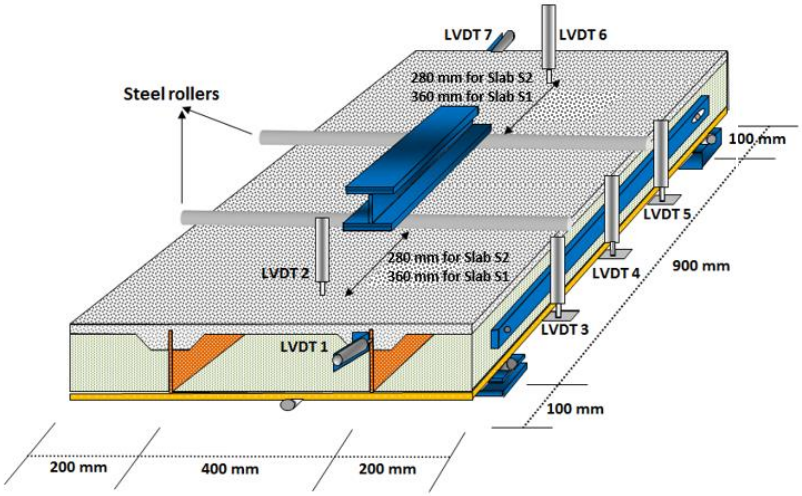

b) shear assessment

Fig 7.14. Test setup and disposition of LVDTs during static flexural and shear load tests

7.3.1. Observed damages

Various damages were observed after implementation of the static shear and flexural loadings on the tested hybrid slabs. The sequence of the observed damages is:

1. Losing connection between foam cores and DHCC layer (see Fig. 7.15a)
2. Compressive damage in GFRP ribs (see Fig. 7.15b)
3. Losing adhesive bond between the GFRP ribs and the DHCC layer (see Fig. 7.15c)
4. Splitting cracks formed on the surface of DHCC layer (see Fig. 7.15d)
5. Formation of shear cracks in the foam cores (see Fig. 7.15e)

The only difference in the observed damages of hybrid slabs that experienced long-term deformability and hybrid slabs, which were loaded statically, was formation of shear cracks in the foam cores. This fact is may result from the increase in the load carrying capacity of the hybrid slabs over time. Regarding this point, more energy is absorbed by the hybrid slabs, which experienced long-term deformability. The increase in the absorbed energy leads to form of shear cracks in the foams.

a) Losing connection between foam cores and DHCC layer

b) Compressive damage in GFRP ribs

c) Losing adhesive bond between GFRP ribs and DHCC layer

d) Splitting cracks on the surface of the DHCC layer

e) **Shear cracks in the foam core**

Fig 7.15. Damages observed during the static shear and flexural tests on hybrid slabs

7.3.2. Results and discussion

7.3.2.1. Force-Deflection response

Fig. 7.16 presents the relation between force and deflection obtained in the tested hybrid slabs under flexural and shear loadings. The red lines correspond to the results obtained in specimens loaded monotonically up to failure after imposing long-term loadings while the black lines correspond to specimens loaded monotonically up to failure without imposing any previous loading conditions. The results that correspond to the black lines were previously presented in Chapters five and six, and here are added for comparison purposes.

Long-term deflection led to an increase of load carrying capacity in all hybrid slabs. The deflection corresponding to the ultimate load carrying capacity in the most hybrid slabs that experienced long-term deformability reduced compare to the hybrid slabs that did not experience long-term deformability. The main results obtained in the tests, which are presented in Table 7.1 and Fig. 7.16, concern the maximum attained load, the corresponding slip and the deflection at initiation of softening behavior. These results are also summarized and presented in percentage in Fig. 7.18. The long-term loading led to an increase of 19.7% and 21.8% on the load carrying capacity in Slab F1 and Slab F2 tested under flexural loading, respectively. This increment of load carrying capacity also occurred under shear loading, with 19.7% and 38.7% increase in Slab 1 and in Slab 2, respectively. However, the deflection at initiation of softening behavior (see points A and B in Figs 7.16a and 7.16b) increased 23.0% in Slab F1 and decreased 14.7% in Slab F2, due to flexural loadings. Deflections at initiation of the softening behavior on hybrid Slab S1 and Slab S2 (see points A and B in Figs 7.16c and 7.16d), under shear creep loadings, decreased 55.6% and 60.2%, respectively.

Furthermore, an increase of stiffness was observed in all hybrid slabs. However, the hybrid slabs became stiffer but present lower ductility after implementation of creep tests. These results can be justified by the DHCC layer ageing and the hydration degree of fly ash. All details about composition of DHCC material and its mechanical properties can be acquired in chapter 2. Since degree of hydration in fly ash is low and some particles remained without

reaction in early stages, it can be concluded that fly ash particles that remained without reaction in early stages may have reacted gradually over time in hybrid slabs submitted to creep tests.

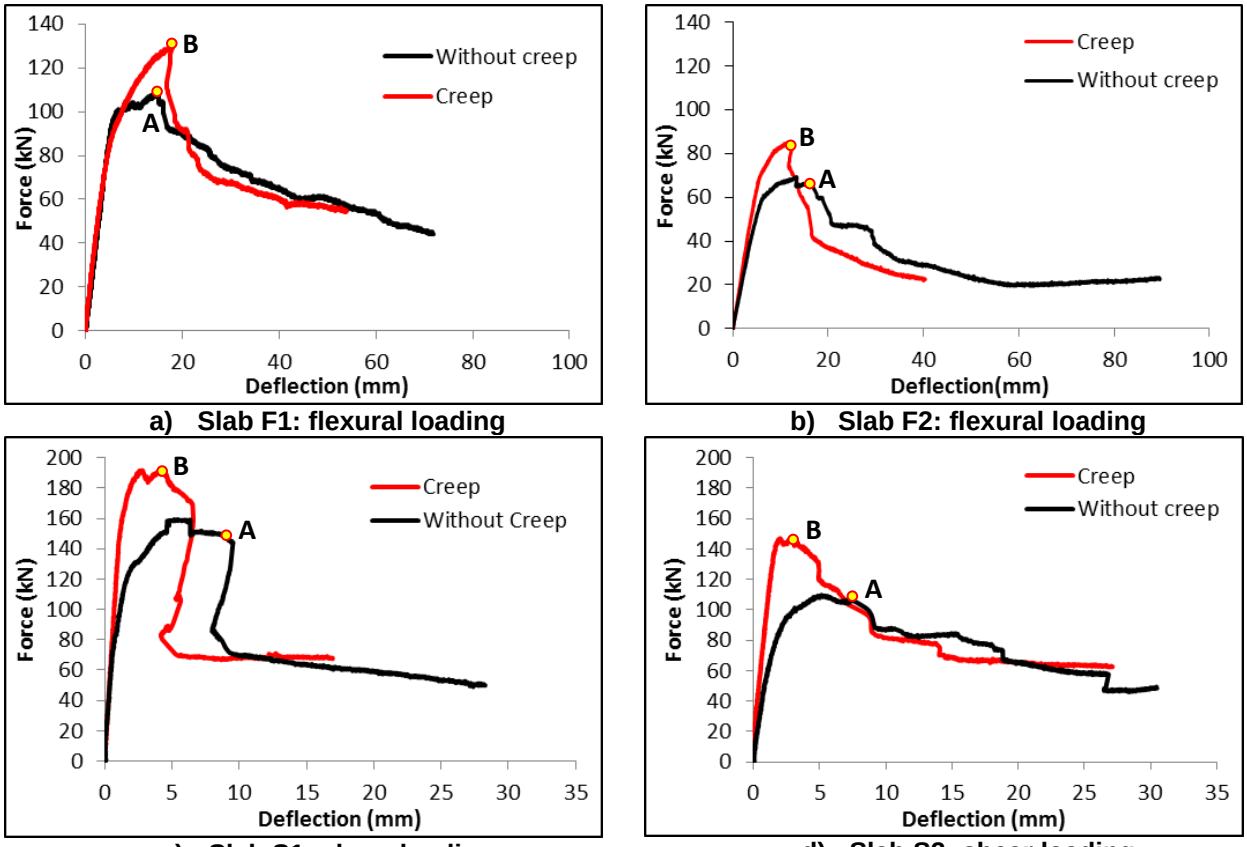

a) Slab F1: flexural loading

b) Slab F2: flexural loading

c) Slab S1: shear loading

d) Slab S2: shear loading

Fig 7.16. Force versus deflection response of hybrid slabs under flexural and shear loadings

7.3.2.2. Force-Slip response

Fig. 7.17 depicts slip versus deflection response of hybrid slabs under flexural and shear loadings. According to the results displayed in Fig. 7.17, Fig. 7.18, and Table 7.1, the bond between DHCC material and GFRP ribs of the hybrid slabs tested under creep loads, is lost under higher loads, than in slabs, which did not experience long-term loadings. The recorded measurements indicate a reduction in slip between DHCC material and GFRP ribs at the initiation of the softening behavior of the most hybrid slabs experienced creep test (see points A and B in Fig. 7.17).

Slip at initiation of softening behavior of Slab F1 and Slab F2 is 20.2% and 89.7% smaller than slip at softening behavior measured in slabs that were not previously submitted to creep loading. Slip at initiation of softening behavior of Slab S1 is 90.2% smaller and slip at initiation of softening behavior of Slab S2 is 27.6% higher than the corresponding slip measured in slabs that were not previously submitted to creep loading. Considering the results depicted in Fig. 7.17, it seems that reaction of fly ash particles over time results in providing a stiffer bond between the embedded indented shear connectors and the DHCC

layer. Since the holes of indented shear connectors were filled by DHCC material, the bond between GFRP ribs and DHCC layer is increased due to reaction of fly ash particles over time. Reaction of fly ash particles in DHCC material leads to increase of flexural and compressive strengths of DHCC layer.

Table 7.1. Maximum force, deflection at initiation of softening behaviour and slip in hybrid slabs under static and creep tests

			Maximum applied force (kN)	Deflection at initiation of softening behaviour (mm)	Slip (mm)
Flexural	**Slab F1**	**Creep**	129.63	17.84	2.89
		Without creep	108.28	14.50	3.62
	Slab F2	**Creep**	84.96	11.39	0.007
		Without creep	69.73	13.36	0.069
Shear	**Slab S1**	**Creep**	189.97	3.77	0.60
		Without creep	158.66	8.50	3.07
	Slab S2	**Creep**	147.22	2.91	1.25
		Without creep	106.11	7.31	0.98

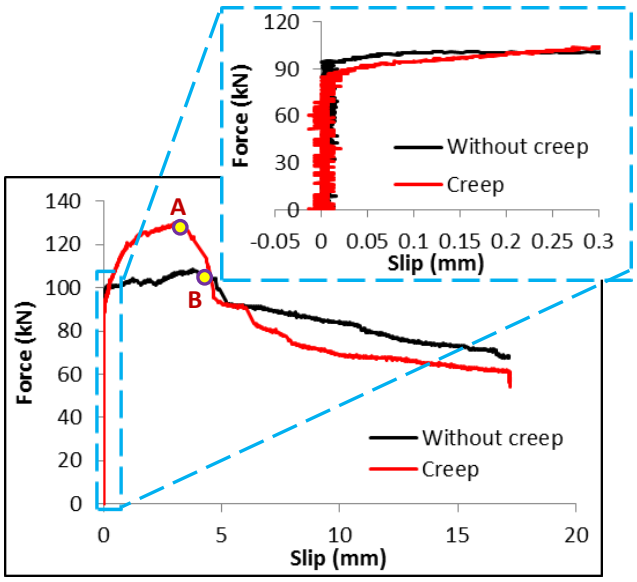

a) Slab F1: flexural loading

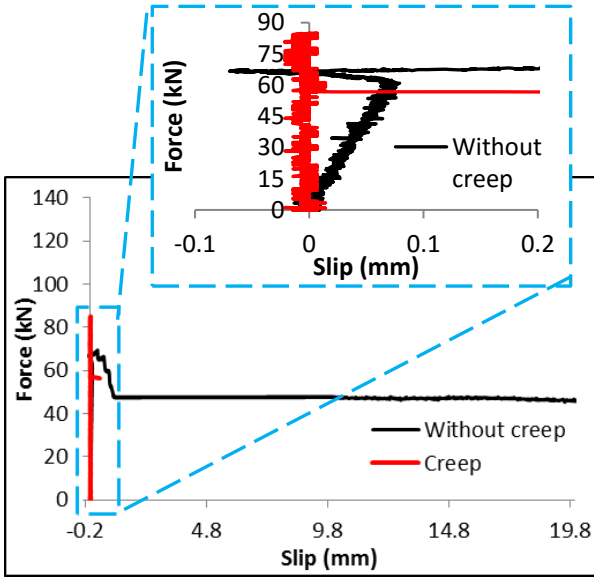

b) Slab F2: flexural loading

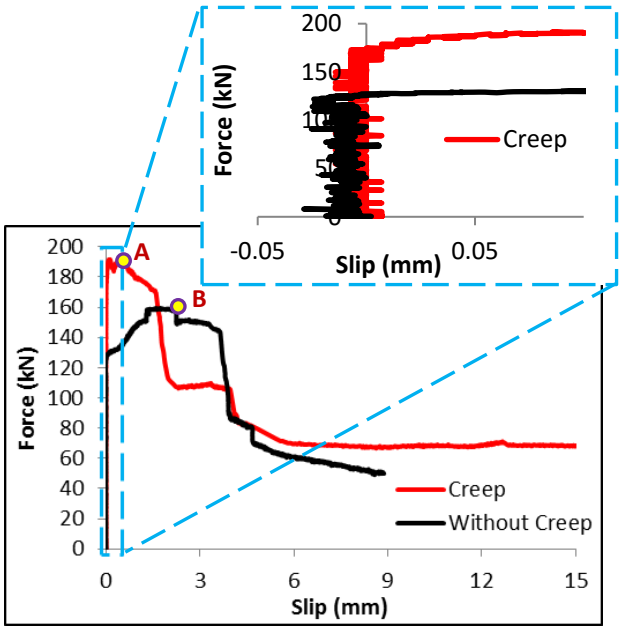

c) Slab S1: shear loading

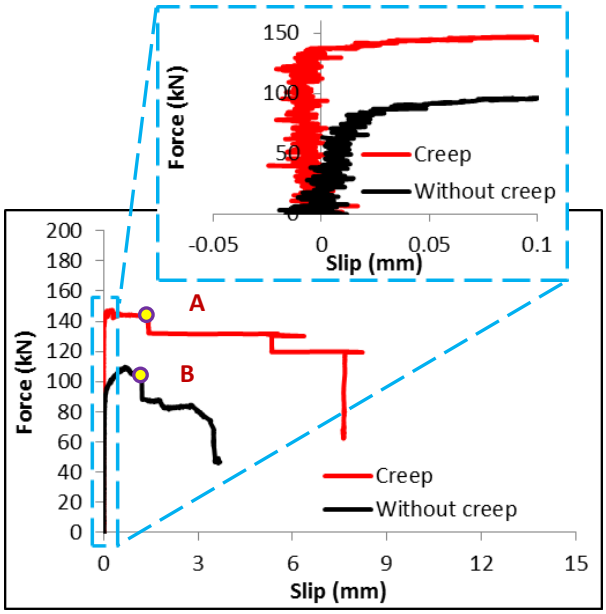

d) Slab S2: shear loading

Fig 7.17. Measured force versus slip responses of hybrid slabs under both shear and flexural loadings

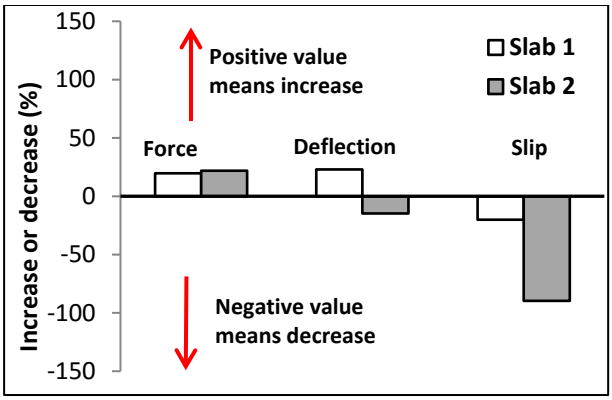

a) Under flexural creep loading

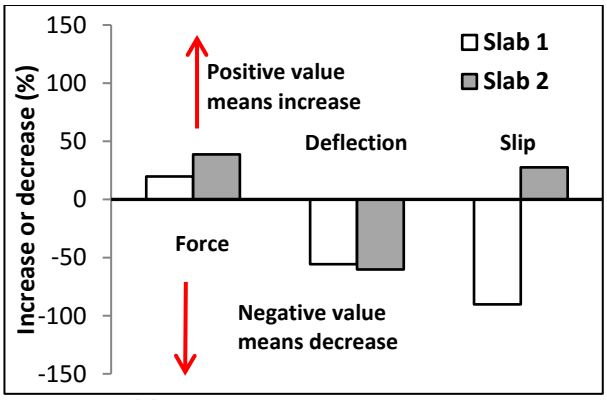

b) Under shear creep loading

Fig 7.18. Effects of long-term deformability on the maximum applied force, deflection at initiation of the softening behavior in slab, and slip

7.3.2.3. Force-Strain response

Fig. 7.19 presents the measurements recorded with the strain gauges installed on different slab´s components. According to the results indicated in Figs 7.19a and 7.19b, the maximum tensile strains in the flexural test measured by SG1 in Slab F1 and Slab F2 were 1700×10^{-6} m/m and 1000×10^{-6} m/m, respectively. Additionally, the maximum compressive strains recorded in Slab F1 and Slab F2 (by SG3 or SG4) were -360×10^{-6} m/m and -170×10^{-6} m/m, respectively.

In the shear tests, the position of the maximum tensile strains is the same as was determined. The maximum tensile strains in Slab S1 and Slab S2 at the position of SG1

measured 1100×10^{-6} m/m and 530×10^{-6} m/m, respectively. The results depicted in Figs 7.19c and 7.19d show that the maximum compressive strains in Slab S1 and Slab S2 measured with SG3 were -940×10^{-6} m/m and -60×10^{-6} m/m, respectively.

Strain gauges were all installed on the same cross section for the hybrid slabs loaded under long-term loading and the hybrid slabs assessed just under monotonic static loadings (see Fig. 5.4). The strain values recorded on different components of hybrid slabs, the effect of load history on the composite action and the efficacy of shear connectors can be investigated by considering the strain distribution across the panel's thickness, at mid span. The curves represented in Fig. 7.20 correspond to different load levels that were established according to predefined ratios between applied load and maximum load. The considered ratios are the following: 20%, 40%, 60%, 80% and 100% of P_{max}.

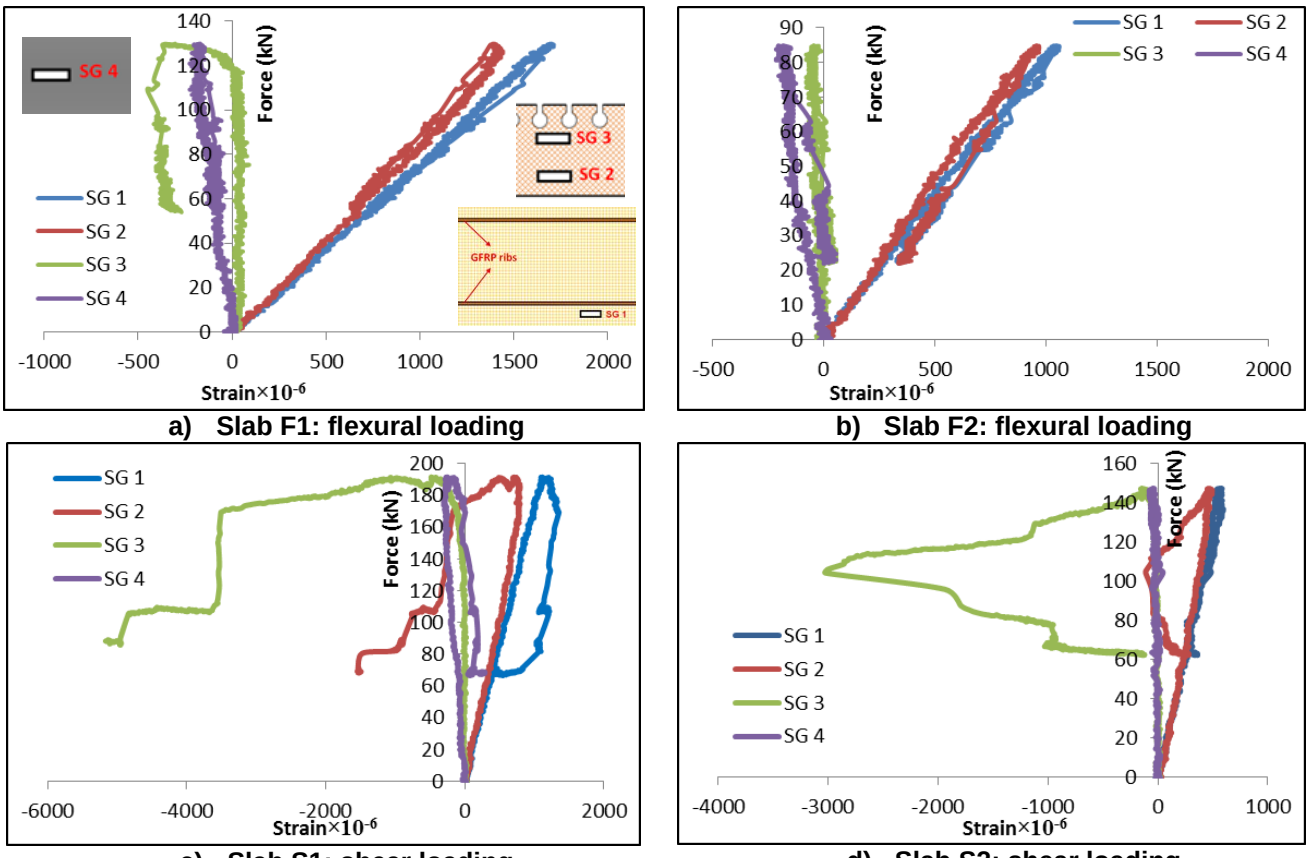

Fig 7.19. Recorded strains in different positions of the hybrid slabs under both shear and flexural loadings

The distribution of strain obtained for maximum load, across the panels' thickness, is influenced by the significant slip values measured between the DHCC layer and the GFRP ribs at this load level. These high values of slip show that there is loss of bond between the GFRP ribs and the DHCC layer which results in a loss of composite action. Therefore, there is a decrease on the concrete compressive strain values and an increase on the GFRP

strain values. The loss of composite action takes place between 80% and 100% of P_{max}, for most of the specimens tested.

The strain gauge installed on the top of the DHCC layer did not record the compressive strain precisely in the location of crushing.

In a composite element, full composite action is obtained when there is no slip between two or more elements connected. In this case, shear stresses are fully transmitted between layers and the strain diagram remains linear across the slab thickness. If the connection is not rigid, semi-composite or non-composite, there is some slip between layers and the strain diagram is not continuously linear. The distribution of strain across the panels' thickness in the hybrid slabs was analyzed to estimate the level of composite action.

Figs 7.20a and 7.20b show the distribution of strains across the panels' thickness in the different phases of loading for Slab 1 and Slab F1 (previously under long-term flexural loadings) during the application of monotonic loadings up to failure.

During the initial phase of loading of Slab 1 under flexural loading, the strain diagram is continuous and linear, indicating that the slab is working as fully composite. No strain gauge was installed on the top layer of DHCC material to measure compressive strains, but there is significant difference in the distribution of strain across the panels' thickness for loads higher than $0.8P_{max}$ (equal to 86.8 kN for Slab 1), indicating that the strain diagram is not linear and slab behaved as partially-composite. Increasing of the load from $0.8P_{max}$ to $0.93P_{max}$ (equal to 91.8 kN), led to some damages in the connection between ribs and DHCC layer (Losing adhesive bond between GFRP ribs and DHCC layer as well as compressive damage in GFRP ribs). This damage is almost totally concentrated in the connection between the ribs and the DHCC layer when the load is increased from $0.93P_{max}$ (91.8 kN) up to P_{max} (98.5 kN).

In Slab F1 (Fig. 7.20b), the strain diagram is continuous and linear up to $0.6P_{max}$ (equal to 77.8 kN), showing that up to this load level, the slab is working as fully composite. Above $0.6P_{max}$, Slab F1 behaves as semi-composite. While increasing the load from $0.6P_{max}$ to $0.67P_{max}$ (equal to 87.7 kN), non-linear behavior was observed due to excessive compressive strain in the GFRP ribs) of Slab F1 which led to some damage in the connection between ribs and DHCC layer. This damage is almost concentrated in the connection between ribs and DHCC layer when the load is increased from $0.67P_{max}$ (87.7 kN) up to P_{max} (129.6 kN).

Figs 7.20c and 7.20d indicate the distribution of strain across the panels' thickness in the different phases of loading applied to Slab 2 and Slab F2 (previously submitted to long-term flexural loadings). Slab 2 under flexural loading presented a continuous and linear strain diagram, showing that the slab is working as fully composite in the initial phase of loading. The main alteration in the distribution of strains across the panels' thickness was found for

loads higher than 0.8P_{max} (equal to 55.5 kN), indicating that the strain diagram is no longer linear and slab begins to behave as partially-composite. Moreover, when the load was increased from 0.8P_{max} to 0.83P_{max} (equal to 57.4 kN), non-linear behavior was observed due to excessive compressive strain in the GFRP ribs which led to some damage in the connection between ribs and DHCC layer. This damage is almost concentrated in the connection between ribs and DHCC layer when the load is increased from 0.83P_{max} (57.4 kN) up to P_{max} (69.4 kN). In Slab F2, the strain diagram is continuous and linear up to 0.4P_{max} (equal to 34.0 kN) showing that this slab is working as fully composite. For a higher load level, an almost partial-composite behavior was monitored for Slab F2. Increasing of the load level from 0.4P_{max} to 0.7P_{max} (equal to 59.4 kN, a non-linear behavior was observed due to excessive compressive strain in the GFRP ribs, resulting in damages located in the connection between ribs and DHCC layer. The damage between ribs and DHCC layer occurs mostly when the load is increased from 0.7P_{max} (59.4 kN) up to P_{max} (85.0 kN).

Figs 7.21a and 7.21b depict the distribution of strain across the panels' thickness in the different phases of loading for Slab 1 (without long-term deformability effects) and Slab S1 submitted to long-term shear loading.

In the initial phase of shear loading applied to Slab 1, the strain diagram across the panels' thickness for loads higher than 0.2P_{max} (equal to 31.9 kN) does not indicate linear behavior and it can be observed that Slab 1 behaved almost partially-composite. While increasing the load from 0.2P_{max} to 0.8P_{max} (equal to 128.47 kN), non-linear behavior was observed due to excessive compressive strain in the GFRP ribs resulting in some damage in the connection between ribs and DHCC layer. This damage is almost concentrated in the connection between ribs and DHCC layer when the load is increased from 0.8P_{max} (128.5 kN) up to P_{max} (158.5 kN).

Under long-term shear loadings, the strain diagram is continuous and linear up to 0.8P_{max} (equal to 153.3 kN), showing that the slab is working as fully composite. Due to apply higher load level, Slab S1 behaved almost partially-composite. Imposing a load equal to 0.74P_{max} (equal to 142.7 kN) a non-linear behavior was observed due to excessive compressive strain in the GFRP ribs leading to some damage in the connection between ribs and DHCC layer. This damage is almost concentrated in the connection between ribs and DHCC layer when the load is increased from 0.74P_{max} (142.7 kN) up to P_{max} (191.7 kN).

The distribution of strains across the panels' thickness in the different phases of loading for Slab 2 and Slab S2 previously submitted to long-term shear loading is depicted in Figs 7.21c and 7.21d, respectively. During the initial phase of imposing load to Slab 2 (under shear loading), the strain diagram is continuous and linear, indicating that the slab is working as fully composite. The main alterations in the distribution of strain across the panels' thickness occur for loads higher than 0.6P_{max} (equal to 65.85 kN), indicating that the strain diagram is

not linear and slab behaves almost partially-composite. Increasing of the load from 0.6P_{max} to 0.83P_{max} (equal to 91.3 kN, where non-linear behavior was observed for slab due to excessive compressive strain in the GFRP ribs occurred) in the Slab 2 led to some damage in the connection between ribs and DHCC layer. This damage is larger and mostly concentrated in the connection between ribs and DHCC layer when the load is increased from 0.83P_{max} (91.3 kN) up to P_{max} (109.8 kN). In Slab S2, the strain diagram is continuous and linear up to 0.4P_{max} (equal to 59.0 kN) showing that the slab is working as fully composite up to this load level. While increasing of the load from 0.4P_{max} to 0.94P_{max} (equal to 139.4 kN), non-linear behavior was observed due to excessive compressive strain in the GFRP ribs leading to some damages in the connection between ribs and DHCC layer. This damage is almost concentrated in the connection between ribs and DHCC layer when the load is increased from 0.94P_{max} (139.4 kN) up to P_{max} (147.6 kN). The obtained results about composite actions in the hybrid slabs were summarized in Table 7.2.

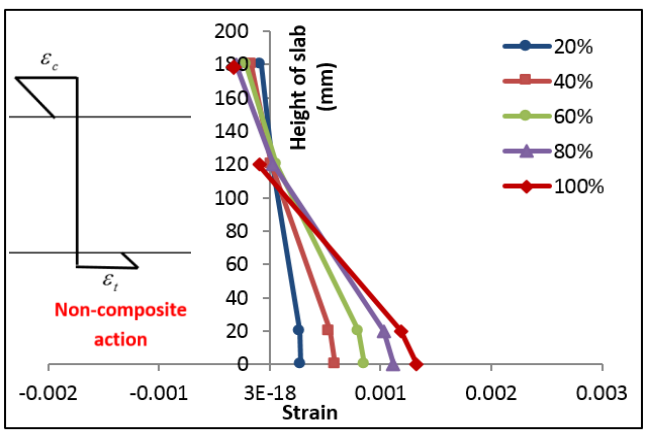

a) Slab 1: Without creep effects

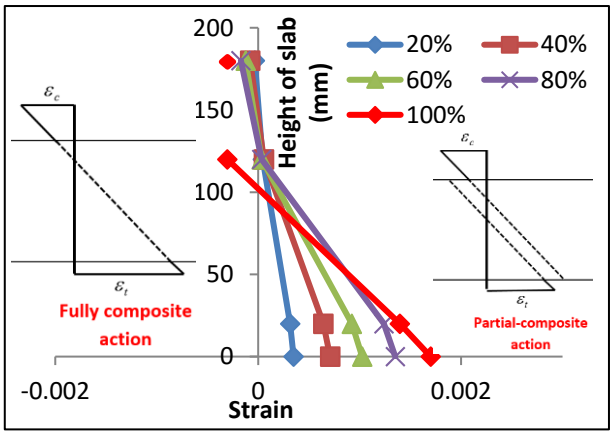

b) Slab F1: With creep effects

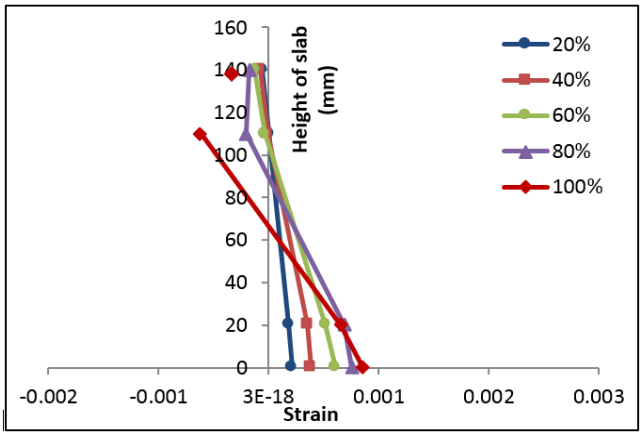

c) Slab 2: Without creep effects

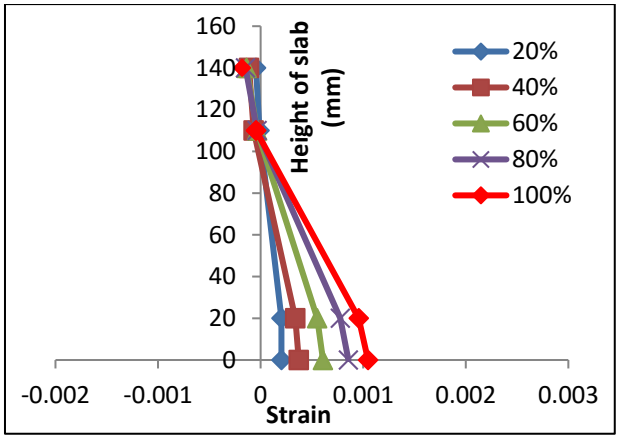

d) Slab F2: With creep effects

Fig 7.20. Variations of strains across the height of hybrid slabs tested under flexural loadings

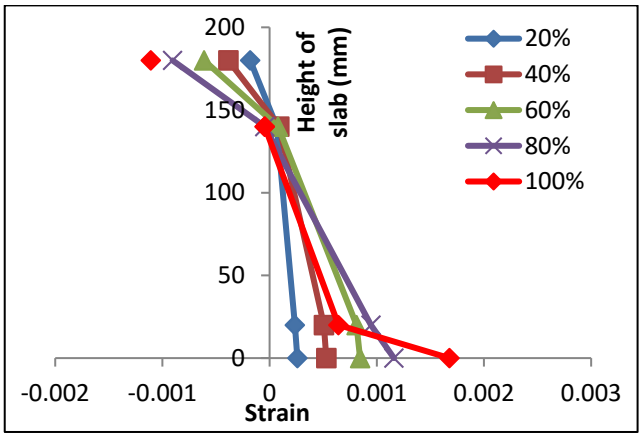

a) Slab 1: Without creep effects

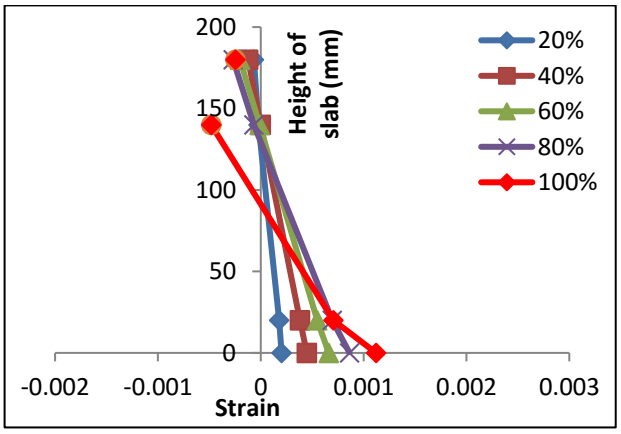

b) Slab S1: With creep effects

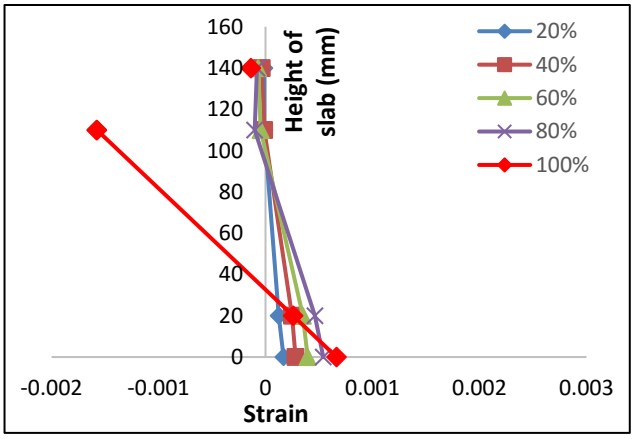

c) Slab 2: Without creep effects

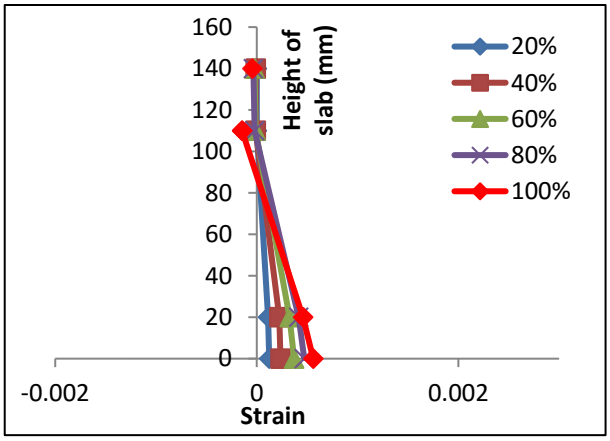

d) Slab S2: With creep effects

Fig 7.21. Variations of strains across the height of hybrid slabs tested under shear loadings

Table 7.2. Summarized results for comparing the composite action in the hybrid slabs

		Full composite action	Partial composite action	Non-composite
Flexural	**Slab 1**	0.8P_{max} (86.8 kN)	0.8-1P_{max} (108.5 kN)	---
	Slab F1	0.6P_{max} (77.8 kN)	0.6-1P_{max} (129.6 kN)	---
	Slab 2	0.8P_{max} (55.5 kN)	0.8-1P_{max} (69.4 kN)	---
	Slab F2	0.4P_{max} (34.0 kN)	0.4-1P_{max} (85.0 kN)	---
Shear	**Slab 1**	0.2P_{max} (31.9 kN)	0.2-0.8P_{max} (127.6 kN)	0.8-1P_{max} (159.5 kN)
	Slab S1	0.8P_{max} (153.3 kN)	0.8-1P_{max} (191.6 kN)	---
	Slab 2	0.6P_{max} (65.8 kN)	0.6-1P_{max} (111.4 kN)	---
	Slab S2	0.4P_{max} (59.0 kN)	0.4-1P_{max}(147.5 kN)	---

7.4. Conclusions

In this chapter, four hybrid sandwich panel slabs were tested under long-term shear and flexural deformability. After executing the tests and recording the experimental data of creep test, an analytical model was developed to predict the hybrid slab behavior under long-term loading. Then, the hybrid slabs that experienced long-term loading were subjected to shear and flexural static loads that were applied up to failure in order to clarify the load history

effects on the shear and flexural performance of hybrid slabs. The following results came out:

1. The DHCC material contains fly ash particles within the mixture composition. The results showed that fly ash particles reacted in the DHCC material over time. After completing the reaction of all fly ash particles in the DHCC material, there was an increase in load carrying capacity, stiffness provided by shear connectors, and composite action between different layers of the hybrid panels.
2. Over the time, the stiffness provided by shear connectors between the embedded GFRP ribs in the DHCC layer increased and resulted in reduction of viscoelastic deflections of hybrid slabs under long-term deformability.
3. The results manifest the possibility to adjust Findley's power law to the creep behavior of a hybrid slab, this method may not be very accurate, especially for long-term predictions based on short-term tests.
4. Utilizing efficient shear connectors between the embedded GFRP ribs in the DHCC layer results in decreasing both instantaneous and viscoelastic deflections.
5. Implementation of creep test did not change significantly the damage sequences that occur in the hybrid slabs tested up to failure.

References

[1] Correia JR., 2008, "GFRP pultruded profiles in civil engineering: hybrid solutions, bonded connections and fire behavior", PhD thesis in Civil Engineering, Instituto Superior Técnico, Technical University of Lisbon.

[2] Liao K., Schultheisz CR., Hunston DL., 1999, "Effects of environmental aging on the properties of pultruded GFRP", Composite: part B, Vol. 30, Issue 5, pp: 485–93.

[3] Cabral-Fonseca S., Correia JR., Rodrigues MP., Branco FA., 2012, "Artificial accelerated ageing of GFRP pultruded profiles made of polyester and vinylester resins: characterization of physical-chemical and mechanical damage", Strain, Vol. 48, pp: 162–173.

[4]. Sharaf T., Fam A., 2010, "Flexural performance of sandwich panels comprising polyurethane core and GFRP skins and ribs of various configurations", Composite Structures, Vol. 92, pp: 2927-2935.

[5]. Engin M. Reis, Sami H. Rizkalla, 2008, "Material characteristics of 3-D FRP sandwich panels", Construction and Building Material, Vol. 22, pp: 1009-1018.

[6]. Sopal G., Rizkalla S., Solomon G., 2012, "Performance of new 3D GFRP sandwich panels with corrugated GFRP sheets", Conference on FRP Composites in Civil Engineering, CICE, Rome, Italy.

[7]. Mastali M., Valente IB, Barros A.O.J., Gonçalves D., 2015, “Development of innovative hybrid sandwich panels: Experimental results”, Composite Structures, Vol. 133, pp: 476-498.
[8]. Mastali M., Valente IB, Joaquim A.O. Barros, 2016, “Development of innovative hybrid sandwich panel slabs - part II: advanced numerical simulations and parametric studies”, Journal of Composite Structures, Vol. 152, pp: 362-381.
[9]. Dutta P.K., Hui D., 2000, “Creep rupture of a GFRP composite at elevated temperatures”, Computer Structure, Vol. 76, pp: 153–61.
[10]. Scott DW., Lai JS., Zureick A-H., 1995, “Creep behavior of FRP composites: a review of technical literature”, Reinforced Plastic Composite, Vol.14, pp: 588–617.
[11]. Clarke JL, editor. Structural design of polymer composites – EuroComp design code and handbook. London: E&FN Spon; 1996.
[12]. Gonilha J., Correia J.R., Branco F.A., 2013, “Creep response of GFRP–concrete hybrid structures: Application to a footbridge prototype”, Composite: Part B, Vol. 53, pp: 193-206.
[13]. Eurocode 1: Actions on structures - Part 1-1: General actions-Densities, self-weight, imposed loads for buildings, Brussels: European Committee for Standardization (CEN); 2002.
[14]. Garrido M., Correia J.R., Fernando A Branco, Keller T., 2013, “Creep behaviour of sandwich panels with rigid polyurethane foam core and glass-fibre reinforced polymer faces: Experimental tests and analytical modelling”, Composite Materials.
[15]. Bank LC., 2006, “Composites for construction: structural design with FRP materials”, New Jersey: John Wiley & Sons Inc.
[16]. Sá MF, Gomes AM, Correia JR., Silvestre N., 2011, “Creep behavior of pultruded GFRP elements – part 1: literature review and experimental study”, Composite Structure, Vol. 93, pp: 2450–9.
[17]. Eurocode 2: Design of concrete structures - Part 1-1: General rules and rules for buildings, Brussels: European Committee for Standardization (CEN); 2004.
[18]. Gonilha A. J., Barros A.O.J., Correia J.R., Sena-Cruz J., Branco F.A., Ramos L.F., Gonçalves D., Alvim M.R., Santos T., 2014, “Static, dynamic and creep behavior of a full-scale GFRP-SFRSCC hybrid footbridge”, Composite Structures, Vol. 118, pp: 496-509.

Chapter 8

Conclusions

8.1. General obtained results and conclusions

The main purpose of this thesis was to develop an innovative hybrid DHCC-GFRP sandwich panel to be used in the replacement of degraded floors. Therefore, in the first phase of this study a parametric study was implemented to understand the effect of each geometrical or material parameter on the global behavior of slabs, by considering three approaches: a) Linear-elastic-isotropic behavior for all the constituent materials; b) Linear-elastic-orthotropic behavior for the GFRP and linear-elastic-isotropic behavior for DHCC; c) Linear-elastic-orthotropic behavior for the GFRP and material nonlinear behavior for the DHCC. The parametric studies developed showed that the thickness of the GFRP ribs has the highest impact in increasing the load carrying capacity of the panels. In addition, a more complete numerical analysis was developed, by considering two slabs that were selected based on the best structural performance and optimized economic aspects. Then, a fiber reinforced layer, with high ductile behavior, was developed. It includes 4% hybrid PAN fibers, of which 3% are PAN fibers with 12 mm length and 1% is PAN fibers with 6 mm length. According to the obtained results, the energy absorption recorded in the fracture process, up to a CMOD=2.5 mm, was 18.56 N/mm and 14.27 N/mm in the TPB and FPB tests, respectively, while the flexural strength was 7.77 MPa and 8.66 MPa, respectively. In the FPB tests with un-notched DHCC specimens, an average flexural strength of 7.82 MPa was obtained at a mid-span deflection of 3 mm, and multiple cracks were formed due to the deflection hardening character of this composite. Mechanical properties of GFRP coupons that were used for ribs and skin were characterized through direct tensile tests. In the hybrid slabs, the polyurethane foam core was included in order to support the deflection-hardening cement based layer and to provide lateral support for GFRP ribs by preventing their local buckling. It was also important to avoid premature failures in the foam cores, and therefore, the mechanical properties of the used polyurethane foam were evaluated under compressive load conditions.

The hybrid slabs were manufactured by VARTM process. A simple and efficient solution was adopted to guarantee the composite action between the GFRP elements and the DHCC layer. The solution found was to cut holes or openings in the GFRP ribs, in order to create a perforated or indented shear connector that was able to transfer shear stresses from top DHCC layer to bottom GFRP skin. DHCC layer was cast and the slabs were cured with spraying water at ambient lab temperature for 28 days. In the preliminary experimental program, panels with 1800 mm span lengths were assessed under flexural load conditions. It was revealed that for deflections equal to L/20 and L/24 (where L was equal to 1800 mm), in Slab 1 and Slab 2, respectively, the residual load carrying capacity after peak load was around 15% of the peak load. Furthermore, experimental results indicated that the developed hybrid slab presented different bond responses between the slab's components. Considering the results, a simplified assumption was adopted to predict the maximum load carrying capacity

of simply supported hybrid slabs with the same cross sections as the one considered for Slab 1 and Slab 2 and submitted to uniformly distributed loads, based on the assumption that the maximum load carrying capacity of hybrid slabs is obtained for a predefined mid-span deflection that is equal to a serviceability limit state of $\delta = L/300$. Regarding the calculated flexural stiffness and a deflection limit of $\delta = L/300$, it was found that slabs were adequate to be used in residential buildings with span length of about 5 m.

Considering this, the tested hybrid slabs were numerically simulated in ABAQUS software and the bond properties between slab's components were determined through an inverse analysis. Concerning the results obtained from numerical simulations, it was revealed that by using cohesive zone models to simulate the bond behavior between slab's components leads to more precise results, in comparison to the use of perfect bond. However, the use of cohesive zone models requires more computational time. Since there is no code with specific rules to apply in the design of the proposed slabs, it was found that using perfect bond could be suitable for pre-design purposes with a maximum error of 20% error in the value of initial stiffness. The numerical results show that high stress concentration is formed around the perforated shear connectors. This stress concentration was confirmed in the experimental tests and led to the formation of longitudinal cracks aligned with the GFRP ribs. When these cracks were formed, the panels' load carrying capacity suffered a sudden decrease. It was not possible to maintain the panel's load capacity for higher deflection values. In order to postpone the formation of these cracks, it was decided to alter the shear connectors shape.

Thus, it was proposed to use indented shear connectors instead of perforated shear connectors. By conducting flexural tests on slabs with indented shear connectors, it was possible to verify that the use of indented shear connectors has no significant impact in term of the panel's stiffness, but ductility, load carrying capacity and residual load carrying capacity could be increased. This increment is governed to the slab's height and thickness of slab's components. When comparing the tests performed on specimens with perforated shear connectors and on specimens with indented shear connectors, it was found that the damage sequences were independent of the shear connector types. Regardless of the shear connector type, the maximum strain levels in the GFRP ribs and skin were much lower than the ultimate strain values determined on the tensile tests carried out with GFRP coupons. Furthermore, slabs presented an almost linear relation between the force applied and the mid-span response, up to the peak load, followed by a smooth softening curve. The tested hybrid slabs presented high load carrying capacity and considerable stiffness, despite their low weight.

Afterwards, the proposed slabs were evaluated under shear load conditions with different span to height ratios. In this stage, six hybrid slabs with different span length were experimentally tested. Regardless of shear span to height ratios, large residual load carrying capacity was registered in the post peak response of the tested slabs. This residual load carrying capacity

is around 45% and 50% of the peak load on average for slabs (SS1, ST1, SL1)and slabs (SS2, ST2, SL2), respectively. Moreover, hybrid slabs indicated fully composite action up to 80% P_{max}, while imposing higher loads, up to P_{max} leads to attain a semi-composite or even a non-composite action in the hybrid slabs.

Since the hybrid slabs are proposed for the replacement of degraded building floors, an assessment on the structural performance under shear and bending loading conditions of these slabs under long-term loading was carried out. Four slabs were loaded under shear and flexural long-term deformability associated with serviceability limit state (SLS) load levels. The SLS load level defined was equal to 375 kg/m^2. The hybrid slabs were loaded for 1540 hours and 1454 hours under flexural and shear long-term deformability, respectively. Stabilization of deflection and slip were the stop criteria for long-term flexural and shear loading conditions. During the development of the creep tests, analogical deflection gauges were disposed in specific positions of the sandwich panels to monitor and evaluate deflection and slip between the GFRP ribs and the DHCC layer. Afterwards, the slabs were unloaded from the imposed long-term load of 375 kg/m^2 and then again loaded under static flexural and shear monotonic load conditions in order to investigate the effects of shear and flexural long-term deformability on their structural performances.

The results obtained in the creep tests showed that the fly ash particles used in the DHCC layer reacted over time and this led to an increase in compressive strength, tensile strength, and flexural strength of the DHCC material used in the upper layer of the panels.

Imposing long-term deformability results in a reduced the ultimate load carrying capacity in RC elements. Unlike RC elements, the ultimate load carrying capacity measured in hybrid slabs increased under long-term shear and flexural load conditions. Moreover, the results indicated the possibility to adjust Findley's power law to the creep behavior of a hybrid slab, this method may not be very accurate, especially for long-term predictions based on short-term tests. Additionally, it was verified that long-term loading had no significant effect on the damage sequences observed during the monotonic tests performed in the hybrid specimens, after the long-term loading.

8.2. Recommendations for future works

The proposed work provides a comprehensive experimental and numerical study on the development of an innovative hybrid sandwich panel system. This work tries to contribute to an increased knowledge on structural applications of sandwich panel systems. However, several aspects deserve to be further investigated in a near future:

- **Execution of direct tensile pullout tests to obtain bond properties between DHCC material and GFRP shear connectors**

  In the developed experimental tests, it was observed that the stiffness of the proposed hybrid slabs was largely influenced by the connection between the DHCC layer and the GFRP ribs. The development of pullout tests would be important in order to obtain the bond properties of different GFRP shear connectors embedded in a DHCC material slab. Since there is no experimental data on the bond properties of GFRP shear connectors embedded in DHCC, it would be an advantage to have an analytical bond model for this connection.

- **Imposing long term direct tensile pullout force to GFRP laminates to investigate the structural performance of the embedded GFRP shear connectors under long term loading**

  The creep tests performed on hybrid panels indicated that the GFRP shear connectors embedded in the DHCC layer have significant impact on the slab's performance under shear and flexural long-term deformability. In this regard, it would be interesting to investigate the performance of the GFRP shear connectors embedded into a DHCC layer and submitted to long-term loading.

  Afterward, analytical models could be developed and then used to for predicting the slip evolution in hybrid panels.

- **Assessment of structural performance of hybrid DHCC-GFRP sandwich panels under fire**

  This study tested and evaluated the behavior of hybrid slabs under shear and flexural load conditions, including monotonic and long-term loadings. All the results were obtained for ambient temperatures under 35 ^{0}C. Increasing temperature can significantly affect the structural performance of hybrid slabs, because viscoelastic materials which are influenced by environmental conditions, such as age, temperature, or moisture. Considering this, more investigations are still needed to understand the performance of slabs under elevated temperatures.

- **Development of hybrid sandwich panels with two-way bending behavior**

  In this thesis, the hybrid slabs proposed present a one-way principal bending behavior. Further research is required to develop hybrid slabs with two-way bending behavior. Developing hybrid slabs with two-way bending behavior includes some practical and important issues related to the intersection of GFRP ribs. Moreover, assessment of full-

scale slabs with two-way bending behavior under distributed load (the distributed loads could be imposed by disposing a water tank or cement bags.